Evaluation of the 7-km GEOS-5 Nature Run

Ronald Gelaro[1], *William M. Putman*[1], *Steven Pawson*[1], *Clara Draper*[2,1], *Andrea Molod*[3,1], *Peter M. Norris*[2,1], *Lesley Ott*[1], *Nikki Privé*[4,1], *Oreste Reale*[2,1], *Deepthi Achuthavarier*[2,1], *Michael Bosilovich*[1], *Virginie Buchard*[2,1], *Winston Chao*[1], *Lawrence Coy*[6,1], *Richard Cullather*[5,1], *Arlindo da Silva*[1], *Anton Darmenov*[1], *Ronald M. Errico*[4,1], *Marangelly Fuentes*[6,1], *Min-Jeong Kim*[4,1], *Randal Koster*[1], *Will McCarty*[1], *Jyothi Nattala*[6,1], *Gary Partyka*[6,1], *Siegfried Schubert*[1], *Guillaume Vernieres*[6,1], *Yuri Vikhliaev*[2,1] *and Krzysztof Wargan*[6,1]

[1] *NASA Goddard Space Flight Center, Greenbelt, MD*
[2] *Universities Space Research Association, Columbia, MD*
[3] *University of Maryland, College Park, MD*
[4] *Morgan State University, Baltimore, MD*
[5] *Earth System Science Interdisciplinary Center, College Park, MD*
[6] *Science Systems and Applications, Inc., Lanham, MD*

October 2014

Abstract

This report documents an evaluation by the Global Modeling and Assimilation Office (GMAO) of a two-year 7-km-resolution non-hydrostatic global mesoscale simulation produced with the Goddard Earth Observing System (GEOS-5) atmospheric general circulation model. The simulation was produced as a *Nature Run* for conducting observing system simulation experiments (OSSEs). Generation of the GEOS-5 Nature Run (G5NR) was motivated in part by the desire of the OSSE community for an improved high-resolution sequel to an existing Nature Run produced by the European Centre for Medium-Range Weather Forecasts (ECMWF), which has served the community for several years. The intended use of the G5NR in this context is for generating simulated observations to test proposed observing system designs regarding new instruments and their deployments. Because NASA's interest in OSSEs extends beyond traditional weather forecasting applications, the G5NR includes, in addition to standard meteorological components, a suite of aerosol types and several trace gas concentrations, with emissions downscaled to 10 km using ancillary information such as power plant location, population density and night-light information.

The evaluation exercise described here involved more than twenty-five GMAO scientists investigating various aspects of the G5NR performance, including time mean temperature and wind fields, energy spectra, precipitation and the hydrological cycle, the representation of waves, tropical cyclones and midlatitude storms, land and ocean surface characteristics, the representation and forcing effects of clouds and radiation, dynamics of the stratosphere and mesosphere, and the representation of aerosols and trace gases. Comparisons are made with observational data sets when possible, as well as with reanalyses and other long model simulations. The evaluation is broad in scope, as it is meant to assess the overall realism of basic aspects of the G5NR deemed relevant to the conduct of OSSEs. However, because of the relatively short record and other practical considerations, these comparisons cannot provide a definitive, statistically sound assessment of all model deficiencies, or guarantee the G5NR's suitability for all OSSE applications. Differences between the observed and simulated behavior also must be judged in the context of basic internal atmospheric variability which can introduce variations that are not necessarily controlled by the prescribed sea surface temperatures used in generating the G5NR.

The results show that the G5NR performs well as measured by the majority of metrics applied in this evaluation. Particular benefits derived from the 7-km resolution of G5NR include realistic representations of extreme weather events in both the tropics and extratropics including tropical cyclones, Nor'easters and mesoscale convective complexes; improved representation of the diurnal cycle of precipitation over land; well-resolved surface-atmosphere interactions such as katabatic wind flows over Antarctica and Greenland; and resolution of orographically generated gravity waves that propagate into the upper atmosphere and influence the large scale circulation. Obvious deficiencies in the G5NR include a "splitting" of the inter-tropical convergence zone, which leads to a weaker-than-observed Hadley circulation and related deficiencies in the depiction of stationary wave patterns. Also, while the G5NR captures global cloud features and radiative effects well in general, close comparison with observations reveals higher-than-observed cloud brightness, likely due to an overabundance of cloud condensate; less distinct cloud minima in subtropical subsidence zones, consistent with a weak Hadley circualtion; and too few near-coastal marine stratocumulus clouds.

Contents

List of Tables **vi**

List of Figures **vii**

1 Overview **1**

1.1 Observing System Simulation Experiments (OSSEs) 1

1.2 Model Aspects 2

1.3 Resolved Features 4

1.3.1 Extratropical Cyclones 4

1.3.2 Tropical Cyclones 6

1.3.3 Mesoscale Convective Complexes 7

1.3.4 Aerosols 8

1.3.5 Carbon 9

2 Wind and Temperature **30**

2.1 Zonal and Time Means 30

2.2 Energy Spectra 32

2.3 Extratropical Synoptic Waves 33

2.3.1 Overall Wave Activity 33

2.3.2 Wave Characterics 34

2.4 Stratospheric Overview 35

2.4.1 Quasi-Biennial Oscillation 35

2.4.2 Annual Cycle 35

2.4.3 Planetary Waves 36

2.4.4 Resolved Gravity Waves 37

3 Humidity and Precipitation **67**

3.1 Verification Data Sources 67

3.2 Mean Atmospheric Humidity . . . 68
3.3 Cloud Condensate . . . 69
3.4 Second Moments of Total Water . . . 69
3.5 Precipitation . . . 70
3.6 NEWS Global and Regional Water Budgets . . . 71
3.7 NEWS Global Energy Budget . . . 71
3.8 Selected Results on Monsoonal and Diurnal Precipitation Variability . . . 72
3.8.1 Tropical waves . . . 72
3.8.2 South and East Asia . . . 73
3.8.3 Africa and South America . . . 73
3.8.4 North America . . . 74
3.8.5 Summary . . . 74
3.9 Specific Humidity (QV) and Total Surface Precipitation Flux (PrFLX): . . . 75
3.9.1 PDF of OMEGA500 and Composite PrFLX Anomaly . . . 75
3.9.2 Composite QV Anomaly . . . 76
3.9.3 Covarying Anomaly Patterns of QV and PrFLX . . . 76
3.10 Precipitation Flux and Condensate . . . 77
3.10.1 Verification Data . . . 77
3.10.2 Rainy Area Fraction . . . 78
3.10.3 Probability Distribution of Surface Precipitation . . . 78
3.10.4 Convective Precipitation vs. Stratiform Precipitation . . . 78
3.10.5 Vertical Distribution of Precipitation . . . 79
3.10.6 Summary . . . 79

4 Tropical Cyclones and Related Phenomena 113
4.1 Tropical Cyclone Activity and Structure in Previous Nature Runs . . . 113
4.2 Tropical Cyclone Activity and Structure in the G5NR . . . 114
4.2.1 Tropical Cyclones in the Atlantic . . . 114
4.2.2 Tropical Cyclones in the Eastern Pacific . . . 117
4.2.3 Tropical Cyclones in the Northern Indian Ocean . . . 118
4.2.4 Tropical Cyclones in the Southern Indian Ocean . . . 119
4.3 Other Significant Weather Phenomena . . . 120
4.3.1 Example of Tropical-Extratropical Transition . . . 120
4.3.2 Ongoing Validation of Other Mesoscale Features . . . 120
4.4 Summary . . . 121

5 Surface Characteristics **153**
5.1 Land Surface - Hydrological Processes . . . 153
5.1.1 Relationship of G5NR Land Surface Hydrological Data to LDAS Products . . 153
5.1.2 Hydrological Land Surface Forcing . . . 154
5.1.3 Inconsistency Between Land-Only and Total-Grid Diagnostics . . . 156
5.1.4 Singularities in Parameter Estimation . . . 157
5.1.5 Snowfall Forcing . . . 157
5.1.6 Reduction of Solar Radiation During Rainfall Events . . . 159
5.1.7 Evaporation Instabilities . . . 159
5.1.8 Occasional High Levels of Rainfall Forcing . . . 160
5.2 Land Surface - Energy Processes . . . 167
5.2.1 Surface Energy Budget . . . 167
5.2.2 Land Surface Temperatures . . . 167
5.3 Ocean Surface . . . 172
5.3.1 Ocean Energy Budget . . . 172
5.3.2 Ocean Winds . . . 173
5.4 Polar Regions . . . 182
5.4.1 Polar Atmospheric Moisture and Energy Budgets . . . 182
5.4.2 Near-Surface Wind Field Over Polar Ice Sheets . . . 184

6 Clouds and Radiation **192**
6.1 June 2005 Validation Against CERES SSF: Not Diurnally Averaged . . . 193
6.1.1 TOA Outgoing Longwave Radiation . . . 193
6.1.2 TOA Outgoing Shortwave Radiation . . . 193
6.1.3 Cloud Properties . . . 194
6.1.4 Albedo vs. OLR Joint Histograms . . . 196
6.2 Diurnally-Averaged Validation Against CERES EBAF . . . 197
6.2.1 TOA Outgoing Longwave Radiation . . . 198
6.2.2 TOA Outgoing Shortwave Radiation . . . 198
6.3 CERES Validation Summary . . . 199
6.4 Cloud Top Pressure and Cloud Fraction Validation Against CALIPSO . . . 200
6.4.1 Data and Sampling . . . 201
6.4.2 Mean Cloud Height . . . 201
6.4.3 Spatial Distribution of Cloud Fraction . . . 202
6.5 CALIPSO Validation Summary . . . 203

7 Aerosols and Trace Gases **244**

7.1 Aerosols 244

7.1.1 Residence Times of Aerosols 245

7.1.2 Aerosol Optical Thickness 245

7.1.3 Spatial Patterns of AOT 247

7.1.4 Aerosol Speciation 248

7.1.5 Vertical Distribution 249

7.1.6 Comparison with CALIOP Retrievals 250

7.1.7 Summary and Recommendations 251

7.2 Trace Gases 252

7.2.1 CO 252

7.2.2 CO_2 254

7.2.3 O_3 257

References **279**

List of Tables

3.1 Comparison of global energy budget terms from the NEWS project and G5NR. . . . 81
3.2 Comparisons of rainy area fraction and mean surface rainrate between TRMM Precipitation Radar data and the G5NR. . . . 82
3.3 Comparison of convective and stratiform precipitation fractions between TRMM Precipitation Radar data and the G5NR. . . . 82

5.1 Comparison of G5NR and the NEWS project annual mean surface energy budget terms over continental regions. . . . 169
5.2 Comparison of G5NR and NEWS project annual mean surface energy budget terms over oceans. . . . 174

6.1 OLR validation against CERES EBAF for 2005 . . . 204
6.2 OSR validation against CERES EBAF for 2005 . . . 204
6.3 OSR validation against CERES EBAF for 2006 . . . 204
6.4 G5NR global TOA energy balance . . . 205
6.5 CERES EBAF global TOA energy balance . . . 205
6.6 SCF validation against CERES EBAF for 2005 . . . 205

7.1 Residence times of aerosol species. . . . 246
7.2 Global aerosol scaling factors . . . 247

List of Figures

1.1 Flow chart describing OSEs and OSSEs. 10
1.2 City lights and total precipitable water at the 50-km MERRA resolution. 11
1.3 City lights and total precipitable water at the 7-km G5NR resolution. 12
1.4 Visible clouds from MERRA and GEOS-5 at 3.5 km. 13
1.5 Extratropical cyclone locations as detected in the 7-km G5NR for DJF 2005–2006. . 14
1.6 As in Figure 1.5 but for DJF 2006–2007. 15
1.7 Change in snow mass over North America from January 13 to January 21, 2007 in the 7-km G5NR. 16
1.8 50m-wind speeds and SLP, and snow/ice/rain rates and 1000-500 hPa thickness in the 7-km G5NR at 12Z January 18, 2007. 17
1.9 As in Figure 1.8 at 00Z January 19, 2007. 18
1.10 As in Figure 1.8 at 012Z January 19, 2007. 19
1.11 As in Figure 1.8 at 00Z January 20, 2007. 20
1.12 As in Figure 1.8 at 18Z January 20, 2007. 21
1.13 Global distributions of tropical cyclone tracks detected in the 7-km G5NR for the annual period from June 2005 to May 2006. 22
1.14 As in Figure 1.13 for June 2006 to May 2007. 23
1.15 Clouds and surface winds speeds at 2130Z on September 10, 2006 during the 7-km G5NR. 24
1.16 MCCs in AHRR imagery and in the 7-km G5NR. 25
1.17 Distribution of MCCs from May–June of 2005 and 2006 in geostationary IR observations and in the 7-km G5NR. 26
1.18 Global distribution of aerosols in the 7-km G5NR at 12Z on September 23, 2006. . . 27
1.19 Concentrations of SO_2 and SO_4 in the 7-km G5NR at 02Z on October 27, 2005. . . . 28
1.20 Concentrations of CO_2 and CO in the 7-km G5NR at 07Z on January 20, 2007 . . . 29

2.1 Time mean zonal mean of the G5NR zonal wind and streamfunction. 39

2.2 Monthly time mean zonal mean maximum strength of the tropospheric zonal wind and location of the maximum in G5NR, ERA-I and CFSR. 40
2.3 As for Figure 2.2, but for the maximum streamfunction of both Hadley cells. 41
2.4 As for Figure 2.2, but for the location of the maximum streamfunction of the two Hadley cells. 42
2.5 Time mean zonal mean of the G5NR for temperature. 43
2.6 As for Figure 2.5, but for the zonal mean meridional wind. 44
2.7 As for Figure 2.2, but for the tropical upper tropospheric zonal mean meridional wind maximum and tropical tropopause temperature minimum. 45
2.8 Multi-year seasonal mean horizontal wind speed at 300 hPa. 46
2.9 Multi-year seasonal mean zonal wind averaged between 10N and 10S. 47
2.10 Power spectra of kinetic energy on the 250 hPa level. 48
2.11 Multi-year seasonal standard deviation of 200 hPa meridional wind. 49
2.12 Individual seasonal standard deviation of 200 hPa meridional wind along latitudinal bands. 50
2.13 Phase-spectra decomposition of 200 hPa meridional wind, contours of power. 51
2.14 Phase-spectra decomposition of wave packets of 200 hPa meridional wind, contours of power. 52
2.15 G5NR monthly averaged zonal wind component averaged zonally and between 10°S and 10°N. 53
2.16 Monthly average 10 hPa temperatures at 90°N for the G5NR and MERRA. 54
2.17 Monthly average 10 hPa zonally averaged zonal wind component at 60°N for G5NR and MERRA. 55
2.18 Daily zonally averaged zonal wind at 10 hPa and 60°N for G5NR and MERRA. . . . 56
2.19 As in Figure 2.16 but for 90°S. 57
2.20 As in Figure 2.17 but for 60°S. 58
2.21 Meridional heat flux due to stationary waves at 200 hPa and 60°N for G5NR and MERRA. 59
2.22 Meridional heat flux due to stationary waves at 200 hPa and 60°S for G5NR and MERRA. 60
2.23 G5NR absolute value of EPV for 15 July 2005 and 15 January 2006. 61
2.24 G5NR absolute value of EPV for 16 January 2007. 62
2.25 Longitude-height cross sections of potential temperature, vertical velocity and zonal wind component over Greenland. 63

2.26 G5NR 10 hPa EPV fields during 2005 at 12 hr intervals. 64
2.27 G5NR horizontal divergence field and vorticity field at 10 hPa. 65
2.28 Mesospheric GW vertical momentum flux on 1 Jan 2006 00 UTC. 66

3.1 Seasonal mean specific humidity in G5NR, MERRA and ERA-I. 83
3.2 Seasonal mean relative humidity in G5NR, MERRA and ERA-I. 84
3.3 Seasonal mean total precipitable water in G5NR, MERRA and ERA-I. 85
3.4 Annual mean cloud ice content in G5NR and CloudSat. 86
3.5 Annual mean cloud liquid water content in G5NR and CloudSat. 87
3.6 Subgrid scale variance of total water and critical relative humidity in G5NR. 88
3.7 Seasonal mean total precipitation in G5NR, MERRA and ERA-I. 89
3.8 Seasonal mean total precipitation over land only in G5NR, MERRA and ERA-I. . . 90
3.9 Graphical depiction of the Global Water Cycle for G5NR and NEWS. 91
3.10 Monthly hydrological quantities in G5NR and NEWS. 92
3.11 Graphical depiction of the NEWS constrained merged satellite energy balance and G5NR energy components. 93
3.12 Hovmöller diagrams of daily mean precipitation for G5NR and CMORPH observations. 94
3.13 Northward progression of the Indian monsoon precipitation in G5NR and CMORPH observations. 95
3.14 Monthly mean precipitation maps for G5NR and CMORPH observations. 96
3.15 Northward progression of the East Asian monsoon precipitation in G5NR and CMORPH observations. 97
3.16 Wind vectors and speed at 850mb over southern Asia for G5NR and CMORPH observations. 98
3.17 Precipitation over Africa for G5NR and CMORPH observations. 99
3.18 Wind vectors and speed over Africa for G5NR and MERRA. 100
3.19 Precipitation over South America for G5NR and CMORPH observations. 101
3.20 Wind vectors and speed over South America for G5NR and MERRA. 102
3.21 Simulated and observed monthly mean precipitation for June-August 2005. 103
3.22 Simulated and observed 850mb winds for June-August 2005. 104
3.23 Time mean simulated diurnal cycle of precipitation over North America. 105
3.24 Time mean observed (CMORPH) diurnal cycle of precipitation over North America. 106
3.25 Probability distribution function of diurnal mid-tropospheric vertical velocity composite precipitation flux anomaly for CFSR and G5NR. 107
3.26 Composite specific humidity anomaly for CFSR and G5NR. 108

3.27 Leading CCA patterns of specific humidity and precipitation flux anomaly for CSFR and G5NR. 109
3.28 Colocation of TRMM Precipitation Radar data and G5NR precipitation. 110
3.29 Comparisons of probability distribution of surface rain rates between the G5NR and TRMM PR data. 111
3.30 Comparison of vertical distribution of precipitation between the G5NR and TRMM Precipitation Radar data. 112

4.1 Zonal and meridional vertical cross-sections of winds and temperature for the strongest Atlantic tropical cyclone in the ECMWF NR. 122
4.2 Vertical meridional cross section of zonal wind at 0° longitude in G5NR and MERRA. 123
4.3 Hovmöller plots of meridional winds at 700 hPa in the G5NR. 124
4.4 Hovmöller plots of meridional winds at 700 hPa in MERRA. 125
4.5 Tropical cyclone activity over the Atlantic in 2005 in the G5NR. 126
4.6 Same as in Figure 4.5, but from the NHC, 2005 season (observed best tracks). 127
4.7 Same as Figure 4.5, but for 2006. 128
4.8 Same as Figure 4.5, but from the NHC, 2006 season (observed best tracks). 129
4.9 Zonal vertical cross-sections of winds and temperature for an Atlantic hurricane in the G5NR. 130
4.10 Same as in Figure 4.9, but for an Atlantic hurricane at an early development stage. . 131
4.11 Same as in Figure 4.9, but for an Atlantic hurricane at a mature development stage. 132
4.12 Tropical cyclone activity over the Eastern Pacific in 2005 in the G5NR. 133
4.13 Same as Figure 4.12, but from the NHC, 2005 season (observed best tracks). 134
4.14 Same as Figure 4.12, but for 2006. 135
4.15 Same as Figure 4.12, but from the NHC, 2006 season (observed best tracks). 136
4.16 Hovmöller diagram of equatorial low-level zonal wind in the G5NR and MERRA. . . 137
4.17 900 hPa wind in July 2006 across the Indian Ocean in the G5NR. 138
4.18 Same as Figure 4.17, but for MERRA. 139
4.19 Vertical meridional cross section of the Somali Jet in July 2006 in the G5NR. 140
4.20 Same as Figure 4.19, but for MERRA. 141
4.21 Tropical cyclone activity over the Northern Indian Ocean in 2005 in the G5NR. . . . 142
4.22 Same as Figure 4.17, but from the JTWC, 2005 season (observed best tracks). . . . 143
4.23 Same as Figure 4.17, but for 2006. 144
4.24 Same as Figure 4.17, but from the JTWC, 2006 season (observed best tracks). . . . 145
4.25 Tropical cyclone activity over the Southern Indian Ocean in 2005-2006 in the G5NR. 146

4.26 Same as Figure 4.25, but from the JTWC, 2005-2006 season (observed best tracks). 147
4.27 Same as Figure 4.25, but for 2006. 148
4.28 Same as Figure 4.25, but from the JTWC, 2006-2007 season (observed best tracks). 149
4.29 Zonal vertical cross-sections of winds and temperature for a Southern Indian Ocean tropical cyclone in the G5NR. 150
4.30 Near-surface wind speed at various stages of a tropical cyclone's life-cycle in the G5NR. 151
4.31 Extra tropical transition of a tropical cyclone in the G5NR. 152

5.1 Dryness index distribution as determined from observations and the G5NR. 155
5.2 Illustration of a situation that leads to an inconsistency in the 0.5 degree output diagnostics of the G5NR. 156
5.3 Locations where the output diagnostics for land surface runoff and precipitation are found to be inconsistent in G5NR. 157
5.4 Amount of snow reaching the surface during a 16-day period in May. 158
5.5 Time series of various quantities at a grid cell in northern Mexico. 161
5.6 Downward shortwave radiation and precipitation in MERRA and observations near Gainesville, Florida. 162
5.7 As in Figure 5.6, but for a representative high resolution grid cell in the G5NR. . . . 162
5.8 Time series of precipitation, downward solar radiation and latent heat flux in a G5NR high-resolution grid cell. 163
5.9 Locations where evaporation instabilities are found in the G5NR during a representative 14-day period during summer. 164
5.10 Locations where evaporation instabilities are found in two offline land surface model simulations. 165
5.11 Locations for which the maximum of half-hourly precipitation totals during a representative 2-week period in summer exceeds 4 cm. 166
5.12 Monthly mean T_{2m} and locations of ISH T_{2m} stations. 169
5.13 Monthly mean T_{2m} from the G5NR, ISH station observations and ERA-I, by continent. 170
5.14 G5NR minus ERA-I mean temperature differences. 171
5.15 Annual mean net surface shortwave and longwave radiation in G5NR and SRB data. 175
5.16 Annual mean latent and sensible heat flux in G5NR and GSSTF data. 176
5.17 Implied ocean heat transport in PetaWatts. 177
5.18 CCMP 10 meter wind rose from May 2005 to May 2007. 178
5.19 Same as 5.18 but for the G5NR 10 m winds. 179

5.20 Zonal wind speed, meridional winds speed and wind speed from the G5NR, SCOW and CCMP. . . . 180
5.21 Average wind stress magnitude from the G5NR and SCOW. . . . 181
5.22 Net surface energy flux components for the North Polar Cap from the G5NR and atmospheric reanalyses. . . . 186
5.23 Comparison of G5NR 2m temperature and corresponding station temperature for the South Pole and Barrow. . . . 187
5.24 Average annual cycle for net surface moisture flux from G5NR and corresponding values from reanalyses. . . . 188
5.25 G5NR surface mass balance for Greenland and Antarctica. . . . 189
5.26 G5NR 10 m wind vectors and contours of vector magnitude over the Antarctic. . . . 189
5.27 G5NR 10 m wind vectors and contours of vector magnitude over the Ross Sea. . . . 190
5.28 G5NR near-surface wind field over Greenland. . . . 190
5.29 Daily-averaged G5NR 10 m wind field over Greenland and surrounding area. . . . 191

6.1 Zonal average OLR validation against CERES SSF . . . 206
6.2 Global map OLR validation against CERES SSF . . . 207
6.3 Zonal average OSR validation against CERES SSF . . . 208
6.4 Global map OSR validation against CERES SSF . . . 209
6.5 Zonal average cloud fraction validation against CERES SSF . . . 210
6.6 Global map cloud fraction validation against CERES SSF . . . 211
6.7 Frequency distribution of cloud fraction . . . 212
6.8 Cumulative frequency distribution of cloud fraction . . . 213
6.9 Global map cloud top pressure comparison against CERES SSF . . . 214
6.10 Zonal average in-cloud cloud optical thickness validation against CERES SSF . . . 215
6.11 Zonal average corrected in-cloud cloud optical thickness validation against CERES SSF . . . 216
6.12 Global map corrected in-cloud cloud optical thickness comparison against CERES SSF . . . 217
6.13 Zonal average condensed water path validation against CERES SSF . . . 218
6.14 Global map condensed water path validation against CERES SSF . . . 219
6.15 Zonal average cloud fraction validation against CERES SSF (native G5NR resolution) 220
6.16 Global map cloud fraction validation against CERES SSF (native G5NR resolution) 221
6.17 Zonal average in-cloud condensed water path validation against CERES SSF . . . 222
6.18 Global map in-cloud condensed water path validation against CERES SSF . . . 223

6.19 Joint histogram of TOA Cloud Albedo vs. OLR (Tropical oceans) 224
6.20 Joint histogram of TOA Cloud Albedo vs. OLR (Mid-latitude oceans) 225
6.21 Joint histogram of TOA Cloud Albedo vs. OLR (Higher-latitude oceans) 226
6.22 Joint histogram of TOA Cloud Albedo vs. OLR (Global oceans) 227
6.23 Zonal average OLR validation against CERES EBAF (June 2005) 228
6.24 Zonal average OLR validation against CERES EBAF (September 2005) 229
6.25 Global map OLR validation against CERES EBAF (September 2005) 230
6.26 Zonal average OSR validation against CERES EBAF (September 2005) 231
6.27 Global map OSR validation against CERES EBAF (September 2005) 232
6.28 NEWS analysis of TOA energy balance 233
6.29 Zonal average TOA albedo validation against CERES EBAF (June 2005) 234
6.30 Global map TOA albedo validation against CERES EBAF (June 2005) 235
6.31 Zonal average SCF validation against CERES EBAF (June 2005) 236
6.32 Zonal average normalized SCF validation against CERES EBAF (June 2005) 237
6.33 Global map average normalized SCF validation against CERES EBAF (June 2005) . 238
6.34 Cloud Top Pressure Validation against CALIPSO 239
6.35 Cloud Fraction Validation against CALIPSO (all clouds) 240
6.36 Cloud Fraction Validation against CALIPSO (high clouds) 241
6.37 Cloud Fraction Validation against CALIPSO (mid-level clouds) 242
6.38 Cloud Fraction Validation against CALIPSO (low‘clouds) 243

7.1 Time series of global monthly mean aerosol optical thickness. 259
7.2 Annual-mean AOT from the MERRAero aerosol reanalysis and the G5NR simulation. 260
7.3 Seasonal-mean AOT from the MERRAero aerosol reanalysis and the G5NR simulation. 261
7.4 Seasonal variations of aerosol speciation. 262
7.5 Zonal mean mass concentrations of OC, BC and sulfate aerosols. 263
7.6 Zonal mean mass concentrations of sea salt and dust aerosols. 264
7.7 Vertical profile of attenuated backscatter coefficient over the African dust region. . . 265
7.8 Vertical profile of attenuated backscatter coefficient over the southern Africa biomass burning region. 265
7.9 Global distribution of aerosol optical thickness on 8 Aug 2005 00UTC. 266
7.10 Map of surface stations used in CO and CO_2 evaluation. 267
7.11 Time series of simulated and observed surface CO at select sites 268
7.12 Monthly mean simulated and observed CO at all surface stations. 269
7.13 Simulated and observed mid-tropospheric CO for April and October, 2006. 270

7.14 Simulated and observed zonal mean CO from MOPITT TIR and NIR measurements. 271
7.15 Time series of simulated and observed surface CO_2 at select sites. 272
7.16 Monthly mean simulated and observed CO_2 at all surface stations. 273
7.17 Simulated and observed XCO_2 for February and August. 274
7.18 Simulated and observed zonal mean XCO_2. 275
7.19 Ozone and potential vorticity at 100 hPa on January 1, 2006. 276
7.20 Monthly mean difference between G5NR ozone and OMI climatology. 277
7.21 G5NR and MLS ozone for June. 278

Chapter 1

Overview

William M. Putman

High-resolution global atmospheric models provide a unique tool for resolving the regional features of weather within the global climate system. While global models like the Goddard Earth Observing System, version 5 (GEOS-5) model are regularly applied in seasonal-to-decadal climate simulations at coarse resolutions (50 to 200 km), GEOS-5 is also uniquely adaptable for application as a global mesoscale model in pursuit of global cloud resolving applications at horizontal resolutions even finer than the highest resolution global weather models used around the world. These global mesoscale simulations with GEOS-5 represent multiple scales of regional weather from clusters of deep convection and mesoscale convective complexes, to hurricanes and large midlatitude storm systems, all within a cohesive simulation of the global circulation. This chapter provides an overview of a two-year global mesoscale simulation with GEOS-5 intended as a *Nature Run* for conducting observing system simulation experiments (OSSEs). Subsequent chapters address in detail the climatology and variance of this simulation.

1.1 Observing System Simulation Experiments (OSSEs)

The global mesoscale capability of GEOS-5 enhances our ability to maximize the impact of satellite observations in climate, weather and atmospheric composition prediction. Exploring the impact of new observations is a key element of this mission. OSSEs (e.g., Errico et al. 2012) are powerful tools for estimating the usefulness of various configurations of envisioned observing systems. Their utility stems from their being conducted in an entirely simulated context, with realistic simulated errors

included in the observations and a known truth with which to evaluate any algorithm or observation impact. For OSSEs, a high-resolution model simulation that is validated against nature, usually referred to as a *Nature Run*, produces the most useful simulated observations

OSSEs are designed to mimic the process of data assimilation in which real imperfect observations are used to produce estimates of global atmospheric states, or analyses, at sequences of time. Like observing system experiments (OSEs) in which real observations may be added or withheld from a data assimilation system to assess their impact on the analysis or forecast (left side of Figure 1.1), in an OSSE, *simulated* observations can be added or withheld from the assimilation system to assess their impact on the estimated Nature Run states (right side of Figure 1.1). Moreover, since the OSSE deals entirely with simulations, it is not restricted to using only observations that already exist, but also proposed future observations.

A non-hydrostatic 7-km global mesoscale simulation with GEOS-5 has been used to produce over two-years of high-resolution weather and chemistry data at 30-minute intervals for the period May 2005 to June 2007 (Putman et al., 2014). This simulation is intended to serve as a Nature Run, referred to as the 7-km GEOS-5 Nature Run or 7-km G5NR, for conducting OSSEs at NASA, NOAA and partner institutions such as the Joint Center for Satellite Data Assimilation (JCSDA). In addition to standard meteorological fields, the 7-km G5NR includes a suite of aerosol types (dust, seasalt, sulfate, black and organic carbon) and trace gas concentrations (O_3, CO and CO_2), with emissions downscaled to 10-km using ancillary information such as power plant location, population density and night-light information. The 7-km G5NR develops its own weather around the Earth in an environment constrained only by surface boundary conditions for sea-surface temperatures and sea-ice, daily volcanic and biomass burning emissions, as well as high-resolution inventories of anthropogenic sources. The output from this computation totaled nearly 4 Petabytes and was produced in just over 75 days of dedicated computation on the Discover cluster at the NASA Center for Climate Simulation (NCCS).

1.2 Model Aspects

At 7-km global resolution, GEOS-5 executes on more that 12 million horizontal grid cells. Compared with the Modern-Era Retrospective Analysis for Research and Applications (MERRA, Rienecker et al., 2011) performed at 50-km global resolution, the 7-km G5NR includes 64 additional horizontal grid cells within each 50-km MERRA cell. This increase in resolution effectively moves the resolved scales from the synoptic scale, to the local scale. A snapshot of city lights across the eastern United States from the NASA black marble image highlights this increase in resolved scales. While the 50-km MERRA resolution coarsely resolves only the largest cities (Figure 1.2), the 7-km G5NR resolves the local towns connecting these larger cities (Figure 1.3).

At 50 km, cloud processes and vertical motions are very coarsely resolved (Figure 1.4, left) and GEOS-5 is highly dependent on the statistical estimation (parameterization) of these processes over the large grid cells. In the 7-km G5NR these parameterizations are relaxed, but not completely

eliminated. Even at 7 to 3.5 km, local updrafts and deep convection cannot be explicitly resolved. However, the mesoscale organization of these systems is resolved including cloud features such as the broken marine stratocumulus in the Pacific Ocean, shallow convection over the Amazon, and organized convection throughout the inter-tropical convergence zone and within large-scale mid-latitude cyclones (Figure 1.4, right). Specific details of clouds and their radiative properties in the 7-km G5NR are presented in Chapter 6.

Atmospheric models with horizontal resolutions in the range of 15 to 1 km are very much in the "gray zone" of parameterizations. The gray zone defines a region where physical processes such as deep convection and cloud micro-physics are being resolved to some degree by the explicit algorithms of the model, but not completely, thus still requiring some level of parameterization. This is uniquely challenging in the case of global models that not only must accurately represent the processes occurring in the midlatitudes, but at the same time they must resolve the very different convective regimes of the equatorial tropics while propagating these small scale processes correctly into the global circulation.

Computational capability has increased dramatically in recent years, but remains at a level that will require global models to execute in this gray zone for several years to come. GEOS-5 has been designed to automatically adapt to this regime through scale-aware dynamics and physical parameterizations, as described below.

The hydrostatic formulation of the finite-volume (FV) dynamics (Lin, 2004) has been extended to the fully compressible non-hydrostatic flow (essentially the unapproximated Euler equations on the sphere). To maintain the advantages of the vertically Lagrangian discretization of the hydrostatic system, an explicit sound wave solver based on the conservation of Riemann invariants was developed. Due to the vertical Courant-Friedrichs-Lewy (CFL) condition imposed by the vertically propagating sound waves, the Riemann solver for the non-hydrostatic FV dynamics is consistently Lagrangian, such that the time step is not severely limited by vertically propagating sound waves. The non-hydrostatic dynamics becomes suitable for use at resolutions of 25 km and finer.

Convection is parameterized in GEOS-5 using the Relaxed Arakawa-Schubert (RAS) scheme of Moorthi and Suarez (1992). RAS is a mass flux scheme with an updraft-only detraining plume cloud model and a quasi-equilibrium closure. As resolution is increased, the convection parameterization is restrained using a stochastic, resolution-dependent limit on deep convection (Tokioka et al., 1988). As resolution increases, approaching cloud resolving scales in the gray zone, the large-scale moist processes begin to explicitly resolve some of the deep convection. This stochastic limiting scheme essentially restrains the deep convection parameterization from stabilizing instabilities within the column and restricts RAS to act as a shallow convection scheme.

The prognostic cloud cover and cloud water and ice scheme is from Bacmeister et al. (2006), with the total water probability distribution function (pdf) of Molod (2012). The critical relative humidity within the pdf increases (approaching 1.0) as resolution increases to account for the shrinking region being parameterized. This accounts for the decreased area being parameterized

and requires a larger fraction of the grid cell to become saturated before vapor if converted to liquid.

The gravity wave parameterization computes the momentum and heat deposition into the grid-scale flow due to orographic (McFarlane, 1987) and non-orographic (after Garcia and Boville, 1994) gravity wave breaking. Mountain waves are forced by the sub-grid orographic variability, where the variance of the orography is scaled down with increasing resolution to account for the better resolved topographically induced gravity waves due to increased resolution in the dynamics. This variance is adjusted within the model as resolution increases to account for the increase in resolved topography and the explicitly resolved gravity waves being generated by the high-resolution dynamics.

1.3 Resolved Features

The 7-km G5NR is capable of resolving robust weather systems and high-impact events critical for simulating observations. Because the 7-km G5NR is a free running simulation, meaning there are no constraints to the observed meteorology, it will not produce the specific weather events of the period 2005–2007. However, it must produce similar weather events with realistic variability and climatology representative of nature. The variability and climatology for the 7-km G5NR must fall within a statistically acceptable level of variance for the climate of Earth.

The 7-km resolution of the G5NR is 16-times finer than the highest resolution operational version of GEOS-5 used within the GMAO to date. This means that weather features will be resolved to a level not typically produced in standard GEOS-5 products. As a result, we can closely examine the fidelity of significant weather events that would be of importance to the OSSE community. These include, but are not limited to, extratropical cyclones, tropical cyclones and mesoscale convective complexes.

In addition to increased resolution, this Nature Run is unique to the OSSE community with the inclusion of radiatively active aerosols and trace gases. A version of the Goddard Chemistry, Aerosol, Radiation and Transport model (GOCART, Chin et al., 2002) is run online, with coupling to the GEOS-5 radiation code (Colarco et al., 2010). GOCART treats the sources, sinks, and chemistry of dust, sulfate, sea salt, and black and organic carbon aerosols. The inclusion of carbon monoxide (CO), carbon dioxide (CO_2) and sulfur dioxide (SO_2) provides a distinct capability to examine potential observing systems for these important trace gases.

1.3.1 Extratropical Cyclones

Large midlatitude cyclones are significant drivers of local weather around the globe. These extratropical cyclones are well resolved by global models even at much coarser resolutions than the 7-km

G5NR. However, fine scale regional and local details of these storms due to improved topographical resolution and better-resolved mesoscale properties contribute to the improved representation of these significant synoptic events in the 7-km G5NR.

The 7-km G5NR output has been searched for cyclones, and a catalogue of all instances at 30-minute intervals throughout the two-year period has been made including locations and intensities (in terms of sea level pressure field (SLP), 850 hPa winds, 10-meter winds and precipitation rates). The detection algorithm follows that of Murray and Simmonds (1991) and Simmonds et al. (1999) by first applying a Gaussian smoothing on the SLP. The Laplacian of this smoothed SLP (LSLP) field is then searched for any local maxima with a threshold value greater than 2.5. All locations of LSLP maxima are searched for a local SLP minimum which, if found, is marked and classified as a closed-low cyclone. If no local SLP minimum is found surrounding the LSLP maxima, then a search is performed to find the minimum pressure gradient and the cyclone is marked as an open system. This methodology detects both tropical and extratropical cyclones; a separate methodology is used to distinguish tropical cyclones by searching for additional characteristics unique to their warm-core structure.

The results of this cyclone detection scheme for the two northern hemisphere December-January-February (DJF) seasons are displayed in Figures 1.5 and 1.6. Intensities of extratropical cyclones are shown in these plots based on SLP minimum: points marked in shades of blue range from 1005–975 hPa, and shades of yellow-to-red range from 975 to <950 hPa. These plots clearly show the regions of primary cyclogenesis off the coast of Japan and the eastern United States. In several cases these cyclones rapidly deepen into major winter storms with minimum pressures in the range 1005 to <975 hPa before making landfall along the Siberian Peninsula or the Canadian Maritimes. The highest concentration of very intense extratropical cyclones is observed throughout the North Atlantic Ocean and into the Greenland and Norwegian Seas where storms that intensify over the North Atlantic eventually dissipate or make landfall in northern Europe or Scandinavia. The Bering Sea and Gulf of Alaska is another region of high concentration for these mature extratropical cyclones.

Several of these extratropical storms occur off the US east coast in the 7-km G5NR, with some developing into major Nor'easter winter storms having significant impacts on the mid-Atlantic and Northeast US. From January 17–21, 2007 in the 7-km G5NR a low-pressure system formed along the Gulf coast, drawing large amounts of moisture from the Gulf of Mexico, then tracked off the Carolina coast where it rapidly intensified into a major Nor'easter. This storm produced a wide swath of heavy snow from the southern Appalachians through the mid-Atlantic and into the northeast US (Figure 1.7), and is a classic representation of a major winter storm in this region.

A series of snapshots at 12-hour intervals show the evolution of this major winter storm over a two-day period from 12Z January 18, 2007 through 12Z January 20, 2007 (Figures 1.8–1.12). This storm forms from a surface low moving along the gulf coast with a central pressure of 1005 hPa, digging southward along a deep trough in the central US (Figure 1.8). An intense line of storms is present along the frontal boundary through the Gulf of Mexico feeding large amounts of moisture into the system. By 00Z January 19 as the storm moves across the southeast, this moisture begins

to override the cold air filling into the Appalachians, producing heavy snows along the mountains and rain along the coastal regions and into the mid-Atlantic (Figure 1.9). The storm begins to intensify as it moves off the mid-Atlantic coast at 12Z January 19 as cold air has pushed into this region now producing heavy snows along the eastern seaboard through the major metropolitan areas from Washington DC to New York City into the northeast US (Figure 1.10). Lines of 1000-500 hPa thickness less than 5400 m (blue) indicate a deep layer of cold air in this region of falling precipitation supporting heavy snowfall rates up to two-inches per hour in many locations. A band of icy mixed precipitation, typical of winter storms in this region, develops in areas where the surface is at or below freezing while the upper levels have enough warm air intruding to prevent the column from supporting snow. By 00Z on January 20 the storm reaches a central pressure of 975 hPa as it moves off the New England coast. This rapid intensification is known as "bombogenesis" as the pressure drops by 25 hPa in less than 24 hours (Figure 1.11). Heavy snows and frozen precipitation continue across New England with gale force winds in excess of 40 knots wrapping around the storm. Strong winds behind the storm lead to lake-effect snow bands across the upper midwest, New York and the mid-Atlantic. As the storm moves into the Canadian Maritimes at 12Z January 20 with a central pressure of 968 hPa, lake-effect snows continue across the Ohio Valley and into the northeast (Figure 1.12). Meanwhile, a strong extratropical cyclone moves into the Pacific Northwest with a central pressure of 984 hPa. These tightly wrapped cyclones are typically heavy snow producers throughout the Cascades of northern California, Oregon and Washington.

1.3.2 Tropical Cyclones

Improved resolution in the 7-km G5NR may have the most significant impact on the ability to develop very intense tropical cyclones. These synoptic scale features rely heavily on the development of mesoscale convection within favorable large-scale environments. Thus, it is critically important that as resolution increases, the parameterizations in the model adapt to this increased resolution to permit the feedbacks of these small-scale convective features in developing these important synoptic-scale storms.

The global distributions of tropical cyclone activity in the 7-km G5NR for the two annual tropical seasons from June–May (2005–06 in Figure 1.13, and 2006–07 in Figure 1.14) highlight the realistic variability between seasons and within individual basins across the globe. The very active 2005 Atlantic hurricane season is complemented by a less active 2006 season, while the east Pacific sees increased activity in 2006. Not only are tropical cyclone tracks and seasonal variability well represented, but also the ability to produce major hurricanes and super typhoons categorized as category 3 and higher based on near-surface wind speeds in excess of 112 mph using the Saffir-Simpson scale.

Multiple tropical cyclones in multiple basins are resolved simultaneously in the 7-km G5NR (Figure 1.15). In September of 2006 a major hurricane makes landfall along the US Gulf Coast while another major hurricane moves northward in the east Pacific basin. A weak tropical storm is dissipating in the north Atlantic, and the surface circulation of the remnants of another east Pacific storm

spins northward off Baja California. The diagnostic cloud optical thickness as represented in the 7-km G5NR highlights the intense banding structure of the mature tropical cyclones feeding into the deep convection surrounding the well defined eye-walls with their strong surface wind speeds. Specific details of the tropical atmosphere in the 7-km G5NR are presented in Chapter 4.

1.3.3 Mesoscale Convective Complexes

A mesoscale convective complex (MCC) is a large thunderstorm complex easily observed as cold cloud tops in infrared (IR) satellite imagery or outgoing long wave radiation from models. These large clusters of convection can be identified as continuous areas of cold IR brightness temperatures cooler than 225 K (-48 C) or outgoing longwave radiation (OLR) less than 150 Wm^{-2} , with surface areas larger than 100,000 km^2 . In North America, these complex nocturnal clusters of thunderstorms typically form over the eastern slopes of the Rockies and travel eastward across the Midwest maintaining their structure and intensity over long distances. Their development is driven by temperature and moisture advection from a strong low-level jet, typically forming along a weak shortwave trough or surface front. These systems commonly produce heavy rainfall, strong winds, frequent lighting, hail and often tornadoes. Over the central US, MCCs are responsible for a significant fraction of the May-June-July rainfall.

While MCCs occur globally, primarily over land, they are well known to be severe weather producers across the central United States during spring and summer months. An observed MCC on April 28, 2014 at 02Z, as seen by Advanced Very High Resolution Radiometer (AVHRR) imagery, shows the classic large circular cloud shield of an MCC (Figure 1.16, top). This MCC produced tornadoes in the region of the coldest overshooting cloud tops, seen as white to purple shades over southeastern Missouri. A similar storm system is observed from OLR in the 7-km G5NR on May 19, 2006 at 04Z (Figure 1.16, bottom). This merging pair of MCCs in the 7-km G5NR also produces the classic large circular cloud shield, and similar overshooting tops are observed over southern Nebraska and south-central Oklahoma.

The 7-km G5NR and composite geostationary IR brightness temperature observations have been sampled for occurrences of MCCs. MCCs detected over the US from May–July for both seasons 2005 and 2006 are plotted with circles representing the relative size of the MCC (from 100,000 km^2 to >500,000 km^2), and colored by the local solar hour of their occurrence (Figure 1.17). Not only does the 7-km G5NR produce a realistic number of MCCs, but the timing of their formation in the late afternoon and evening hours (hours 18 to 23) over the eastern slopes of the Rockies and growth during the nighttime hours (hours 00 to 06) over the central Midwest is very well represented. While MCCs in the 7-km G5NR tend to be slightly smaller than observed ones, several large MCCs occur over Kansas, Nebraska, Missouri and Iowa. This is a substantial improvement in capability for global models, which typically struggle to resolve these systems leading to substantial rainfall deficits in spring and summer totals from May–July across the central US.

1.3.4 Aerosols

Aerosols play an important role in both weather and climate. They are transported around the globe far from their source regions, interacting with weather systems, scattering and absorbing solar and terrestrial radiation, and modifying cloud micro- and macro-physical properties. They are recognized as one of the most important forcing agents in the climate system. Several missions in the Decadal Survey portfolio, such the Aerosol-Cloud-Ecosystem (ACE) and Geostationary Coastal and Air Pollution Events (Geo-CAPE) missions, as well as the Cloud-Aerosol Transport System (CATS) mission which will fly on the International Space Station (ISS), aim to gather new information on aerosol distributions and properties. The specific properties of aerosols are discussed in detail in Chapter 7, while brief highlights of the global distribution of aerosols from snapshots of the 7-km G5NR (Figures 1.18 and 1.19) are presented here.

Seasalt is lifted from the ocean surfaces around the globe within the strong winds of surface lows moving through the Southern Ocean, in the marine boundary layer within the stratocumlus regions of the east Pacific and southern Indian Oceans, and highly concentrated within the strong surface winds of tropical waves and hurricanes in the north Atlantic.

Dust from Africa fill the regions surrounding these developing Atlantic tropical storms, and can play a significant role in the limiting intensification of tropical waves in these regions while also providing an indication of where dry air may be intruding into these moist tropical cyclones.

Organic and black carbon species in smoke plumes are included from the Quick Fire Emissions Dataset (QFED) that has been downscaled to 0.1 degrees; this produces realistic individual fire plumes over southern Africa and Australia as well as large-scale features from fires in the Americas and Indonesia.

Sulfur dioxide (SO_2), produced during the burning of fossil fuels and from volcanic eruptions, is a short-lived gas which can act as a pollutant near the surface with detrimental health and acidifying effects. With a mean lifetime of just a couple of days in the troposphere, emitted SO_2 is quickly converted to sulfate aerosol (SO_4) through oxidation by OH or by reaction with H_2O_2 within clouds. The resulting SO_4 exerts a direct radiative effect on the atmosphere. The 7-km G5NR includes these important constituents and produces a realistic distribution of their concentrations around the globe. A snapshot of SO_2 and SO_4 as seen at 02Z on 27 October 2005 (Figure 1.19) highlights the fidelity of these emissions and the transport within the prevailing meteorology of the 7-km G5NR. A large ash plume can be seen in the eastern Pacific Ocean emitted from the eruption of the Sierra Nerga volcano on the Galapagos Islands beginning on 25 October 2005. Meanwhile, volcanic emissions can be seen throughout the ring of fire around the north and west Pacific and from active emissions in the Hawaiian Islands. Large concentrations from fossil fuel emissions are evident throughout Asia and from industrial sources over North America. Details of the aerosol simulation in the 7-km G5NR are presented in Chapter 7.

1.3.5 Carbon

Carbon exists in many forms—e.g., carbon dioxide (CO_2), carbon monoxide (CO)—and continually cycles through Earth's atmosphere, ocean and terrestrial ecosystems. CO_2 variations are largely controlled by fossil fuel emissions and seasonal fluxes of carbon between the atmosphere and land biosphere. CO_2 concentrations are enhanced by carbon sources, mainly from human activities. During Northern Hemisphere spring and summer months, plants absorb a substantial amount of CO_2 through photosynthesis, thus removing CO_2 from the atmosphere. This annual cycle of CO_2 production and absorption, as well as the two-year trend, is well captured as observed from surface concentrations sampled from the 7-km G5NR at Mauna Loa, Hawaii (Figure 1.20, inset). The global distribution of CO_2 varies substantially with high surface concentrations near local emission sources, and column concentrations distributed within the prevailing large-scale circulation. Figure 1.20 shows high column concentrations of CO_2 over North America, Europe and Asia, with local maximums wrapped up along frontal systems and mid-latitude cyclones in these regions. In this snapshot, a strong cold front has moved off the east coast of the United States while a deep cyclone drifts up the eastern seaboard into Canada. The gradient in CO_2 concentrations along these synoptic features pushes higher concentrations off-shore behind the front wrapping up into the cyclonic circulation of the storm, while lower concentrations are lifted out of the tropical Atlantic ahead of the front. Similar features are seen throughout the northern hemisphere. Details of the trace gas and constituent properties of the 7-km G5NR are presented in Chapter 7.

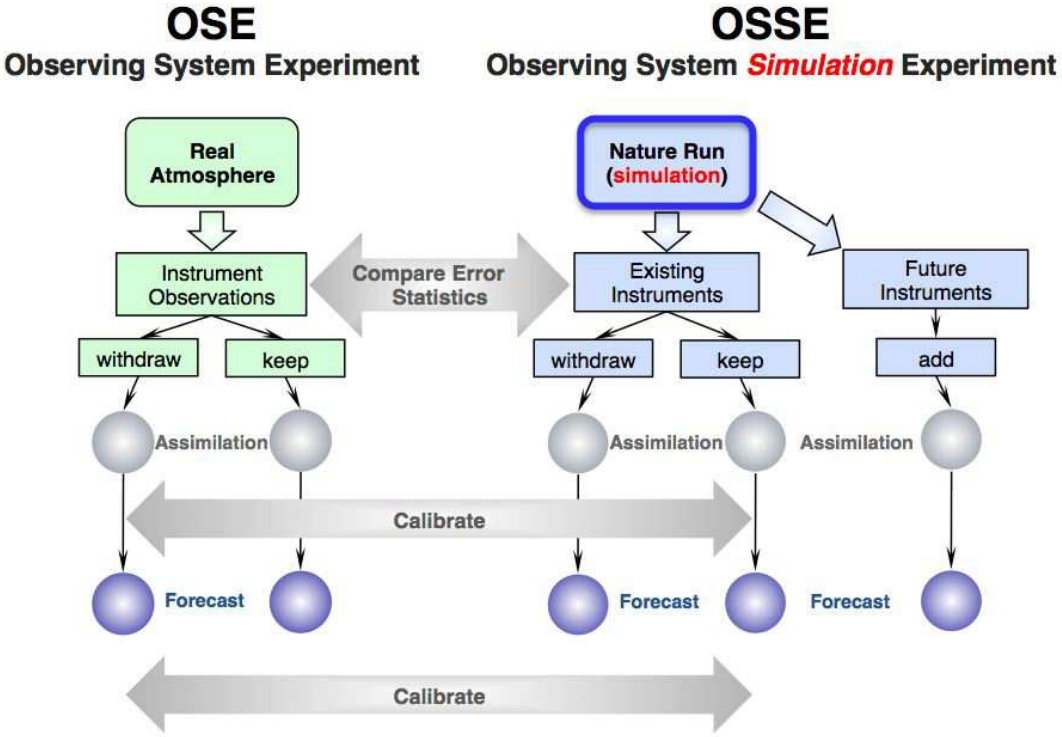

Figure 1.1: Flow chart describing the process of performing OSSEs by replacing observations of the real atmosphere as used in an OSE with simulated observations from a Nature Run simulation like the 7-km G5NR.

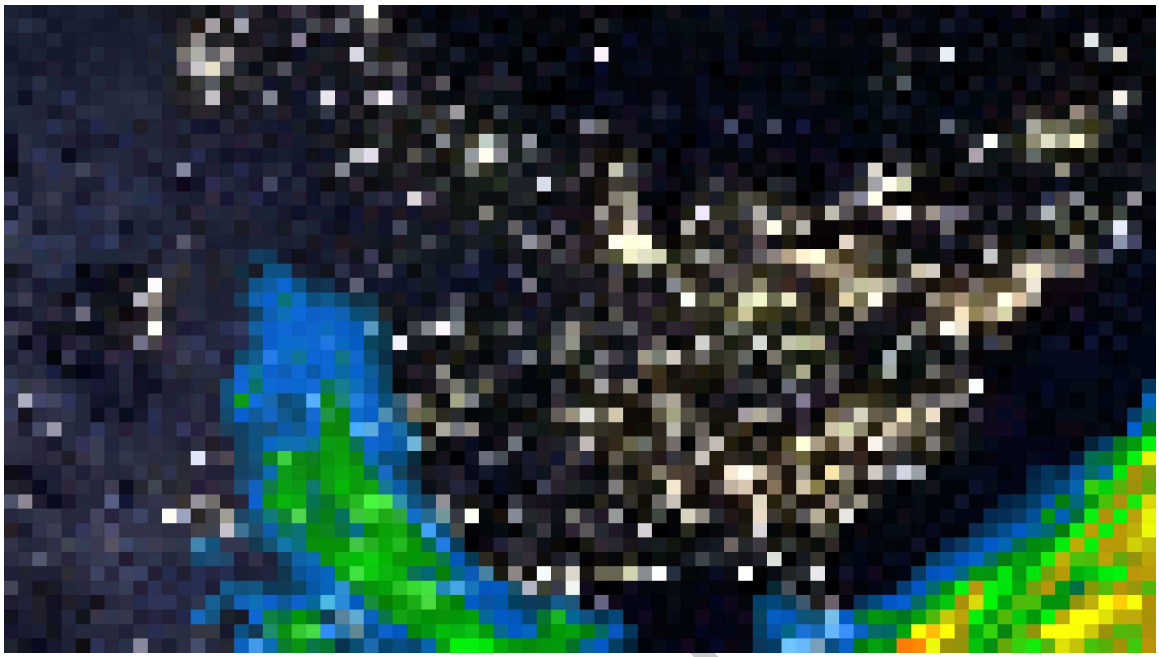

Figure 1.2: City lights over the eastern United States from the NASA black marble image and total precipitable water (colors) at the 50-km MERRA resolution.

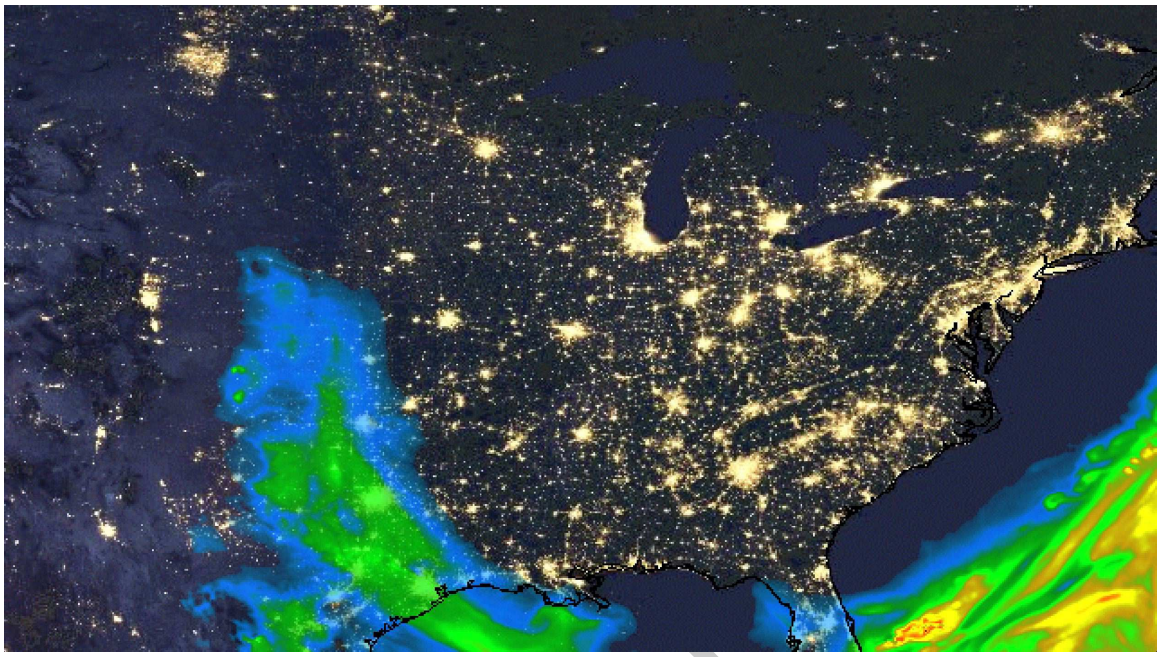

Figure 1.3: City lights over the eastern United States from the NASA black marble image and total precipitable water (colors) at the 7-km G5NR resolution.

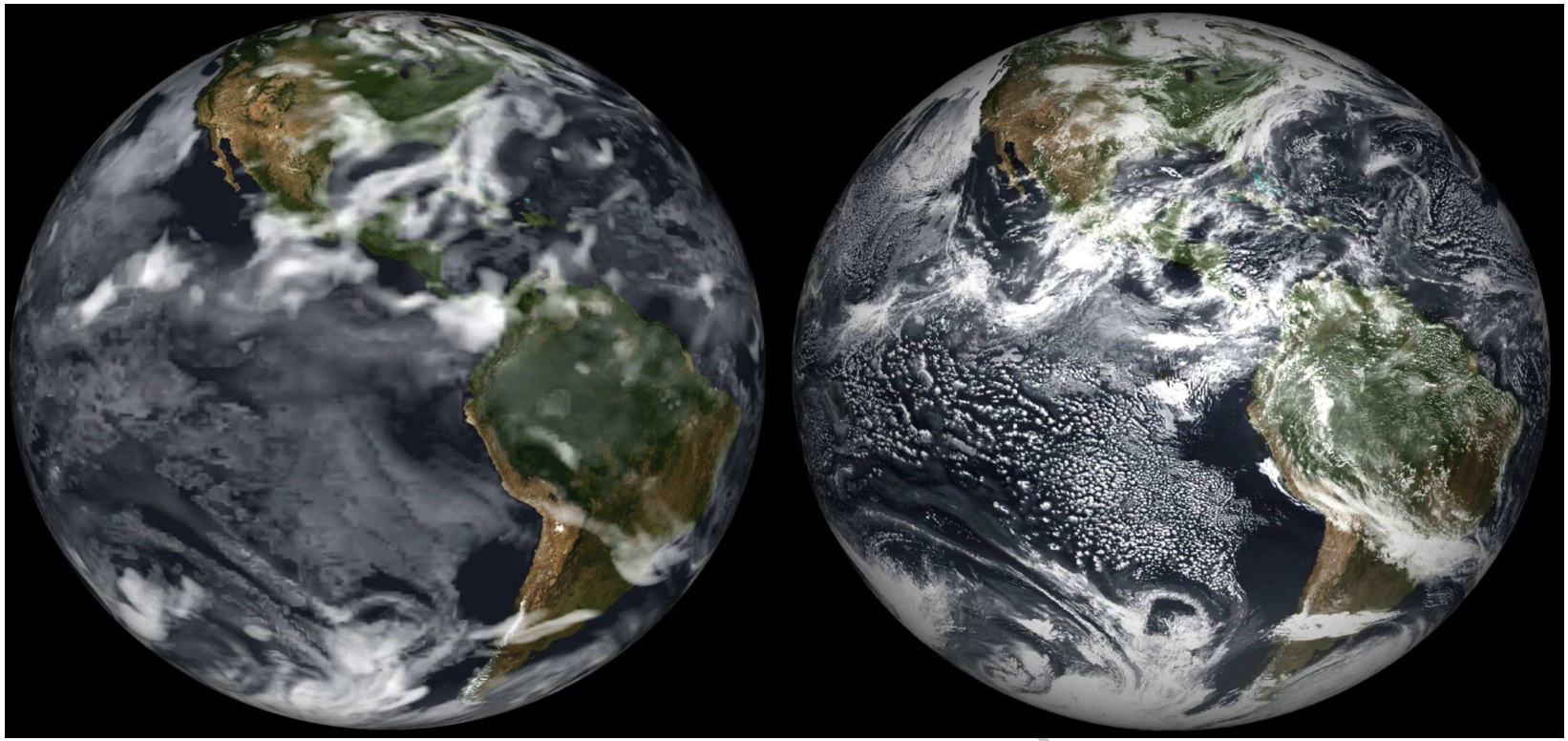

Figure 1.4: Western hemisphere view of visible clouds at 18z on 27 July, 2009 from MERRA at 50 km (left) and GEOS-5 at 3.5 km (right).

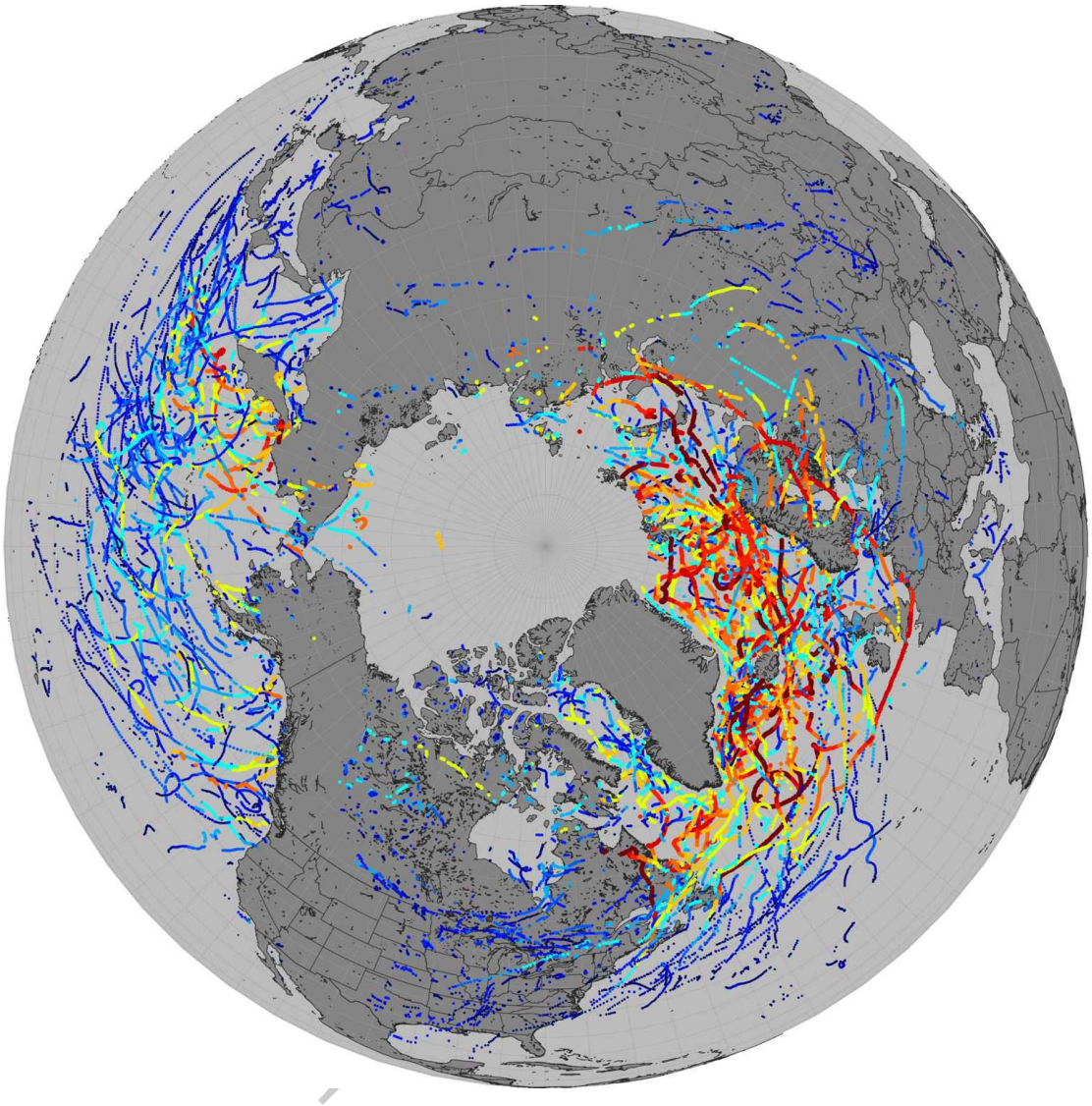

Figure 1.5: Extratropical cyclone locations as detected in the 7-km G5NR for December-January-February (DJF) 2005–2006. Intensity of these cyclones is denoted based on SLP minimum; points marked in shades of blue range from 1005–975 hPa, and shades of yellow-to-red range from 975 to <950 hPa.

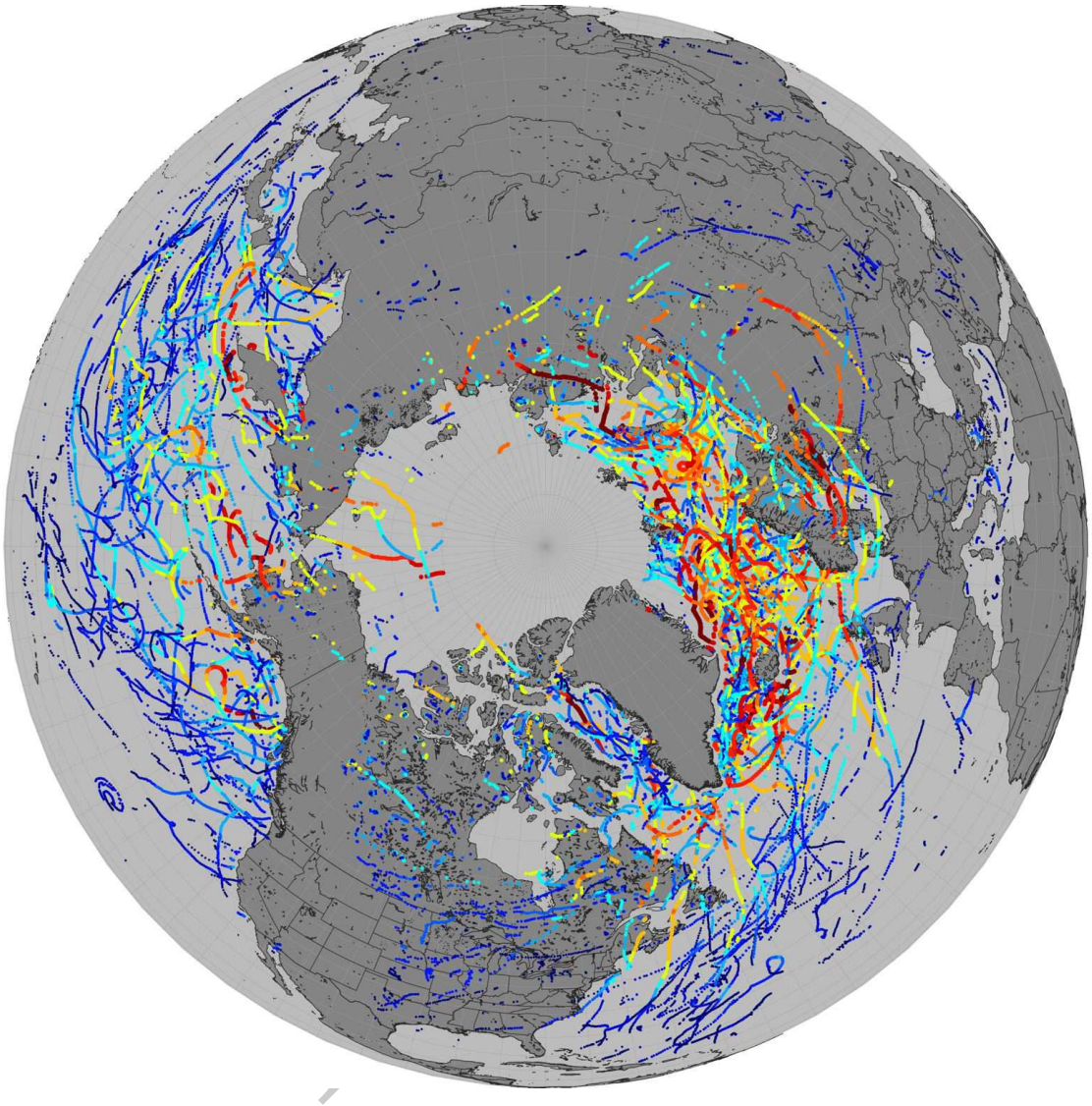

Figure 1.6: As in Figure 1.5 but for DJF 2006–2007.

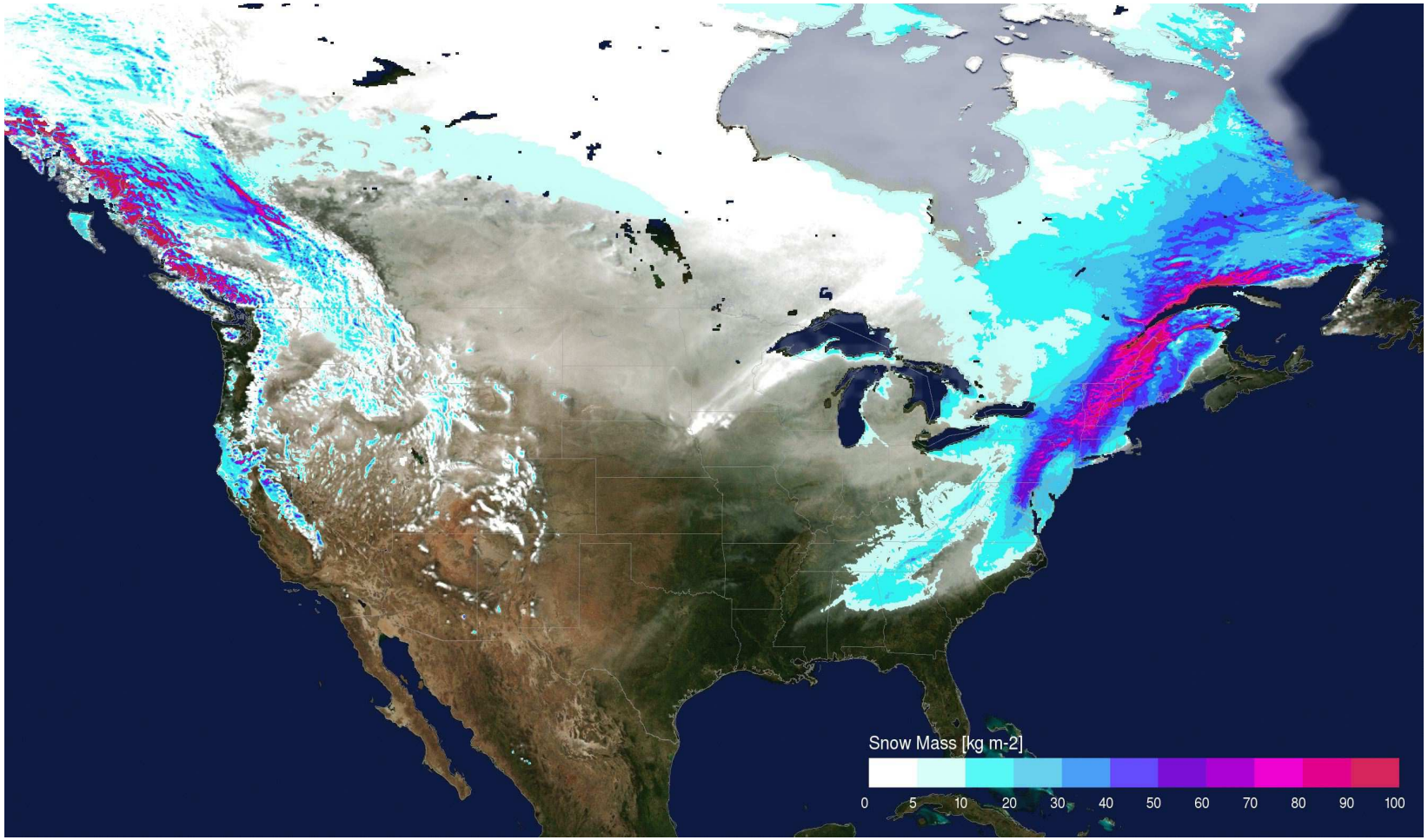

Figure 1.7: Change in snow mass over North America from January 13 to January 21, 2007 in the 7-km G5NR showing the heavy snow accumulation along the US east coast from a major Nor'easter that developed and intensified over this period.

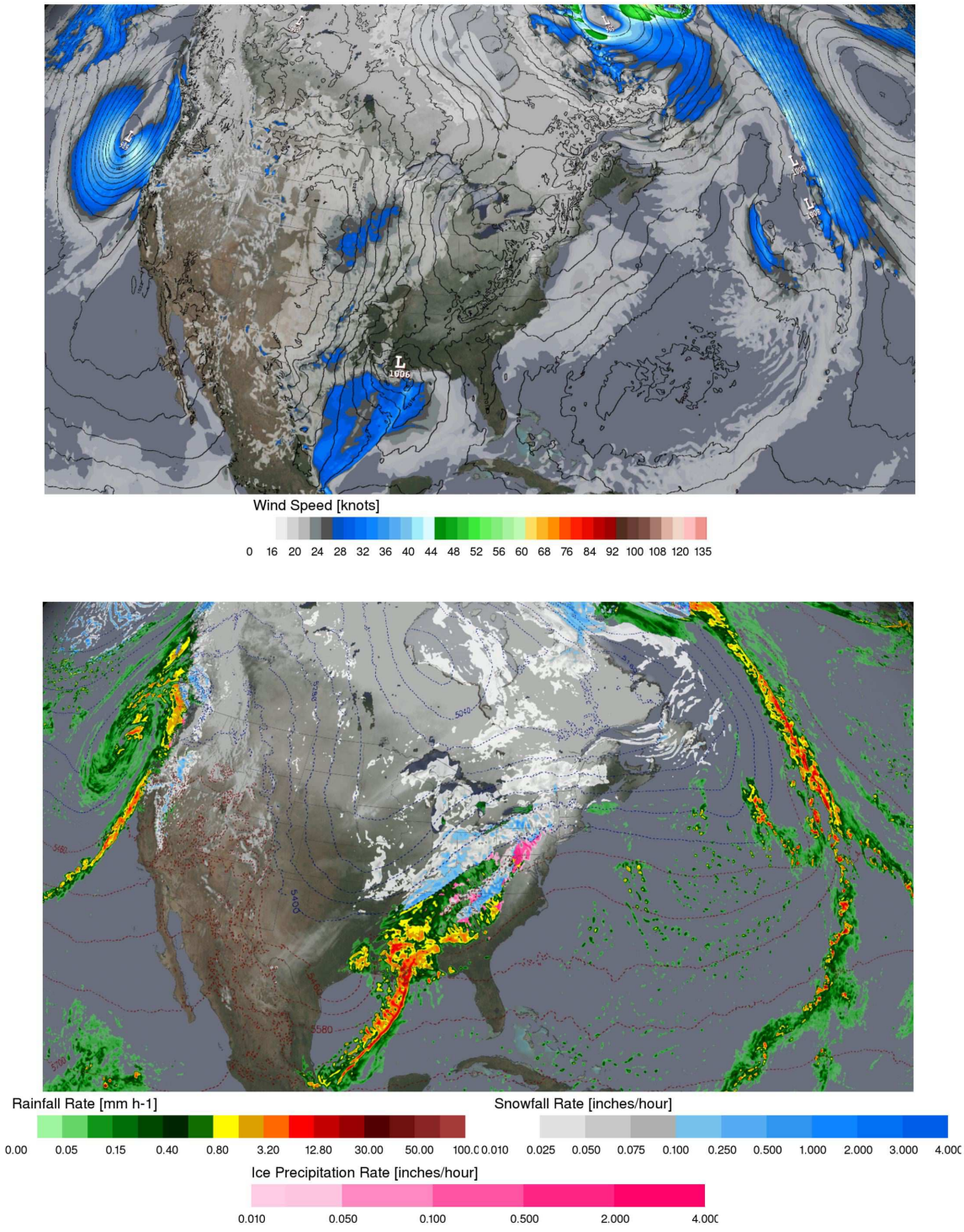

Figure 1.8: 50m-wind speeds and SLP (hPa, top), snow/ice/rain rates and 1000-500 hPa thickness contours (labeled as meters, blue $\leq$5400 m, red >5400 m, bottom) in the 7-km G5NR at 12Z January 18, 2007.

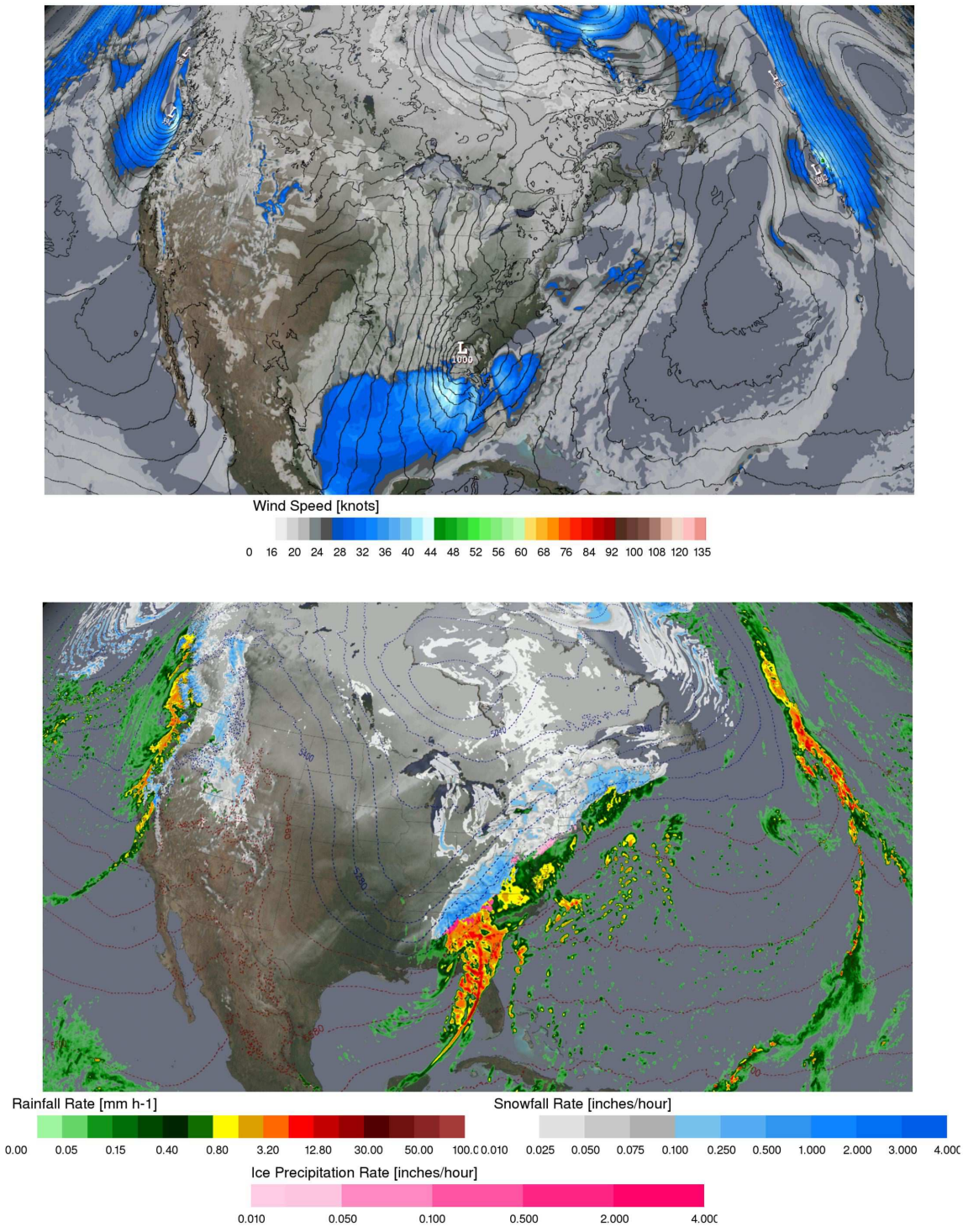

Figure 1.9: As in Figure 1.8 at 00Z January 19, 2007.

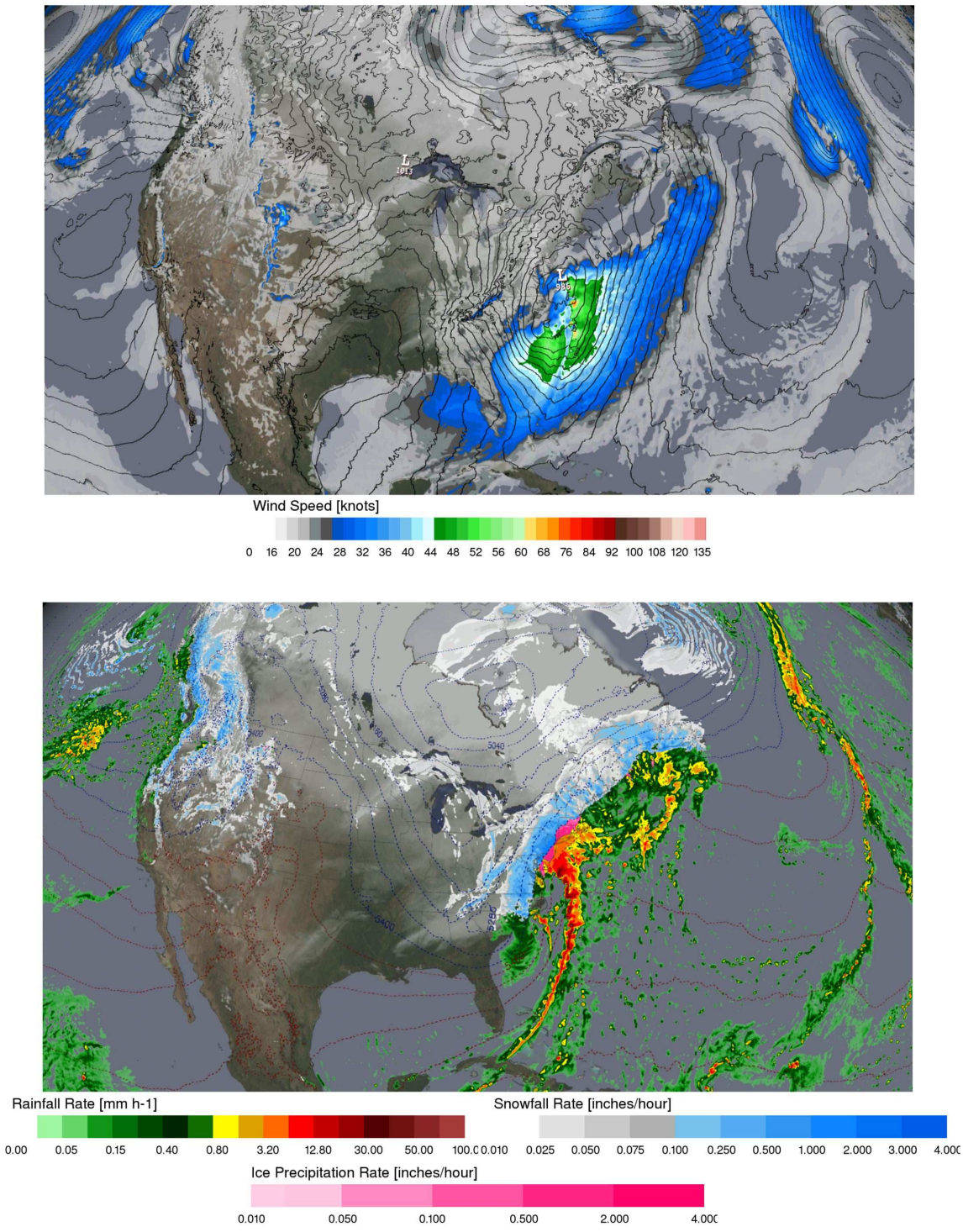

Figure 1.10: As in Figure 1.8 at 012Z January 19, 2007.

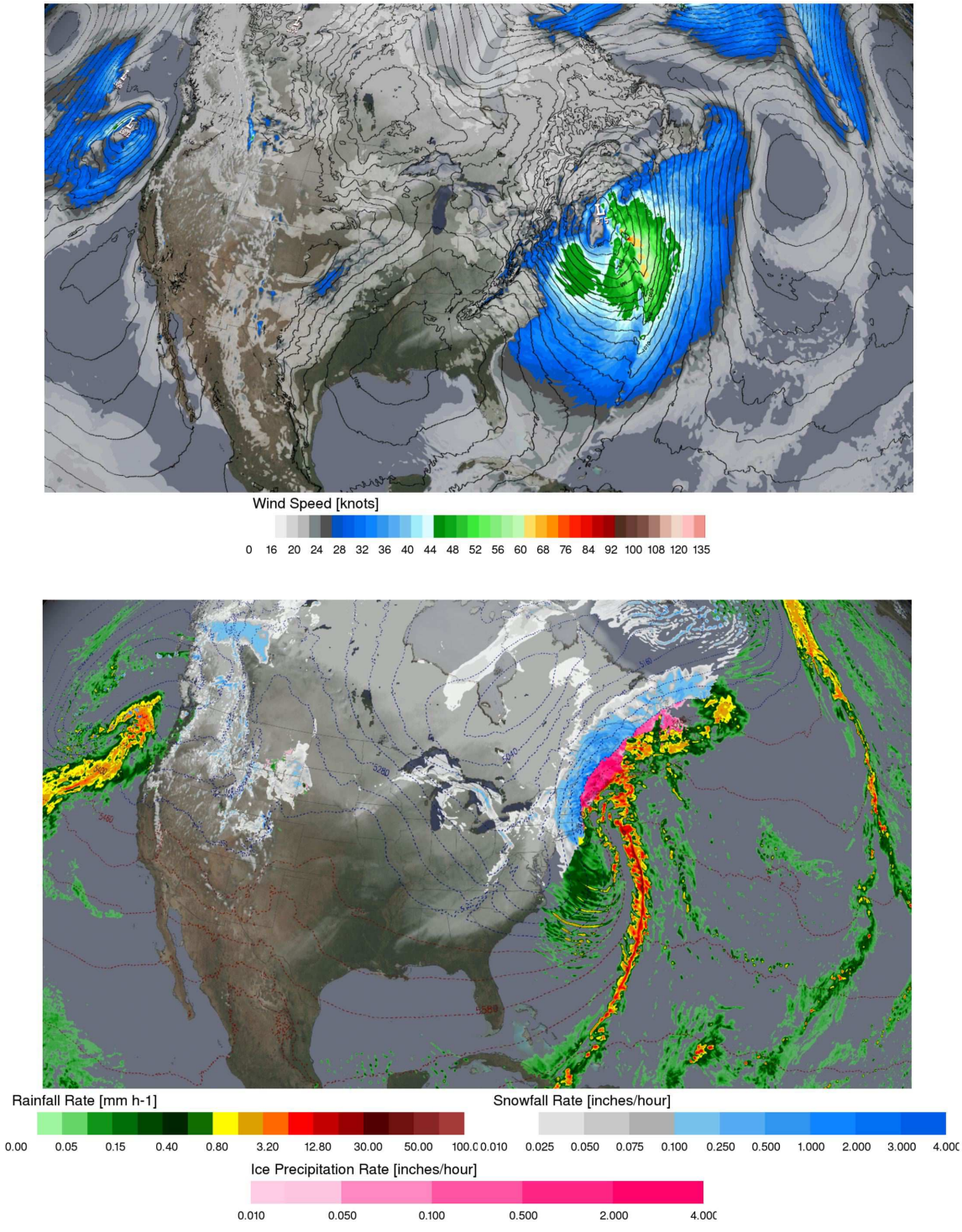

Figure 1.11: As in Figure 1.8 at 00Z January 20, 2007.

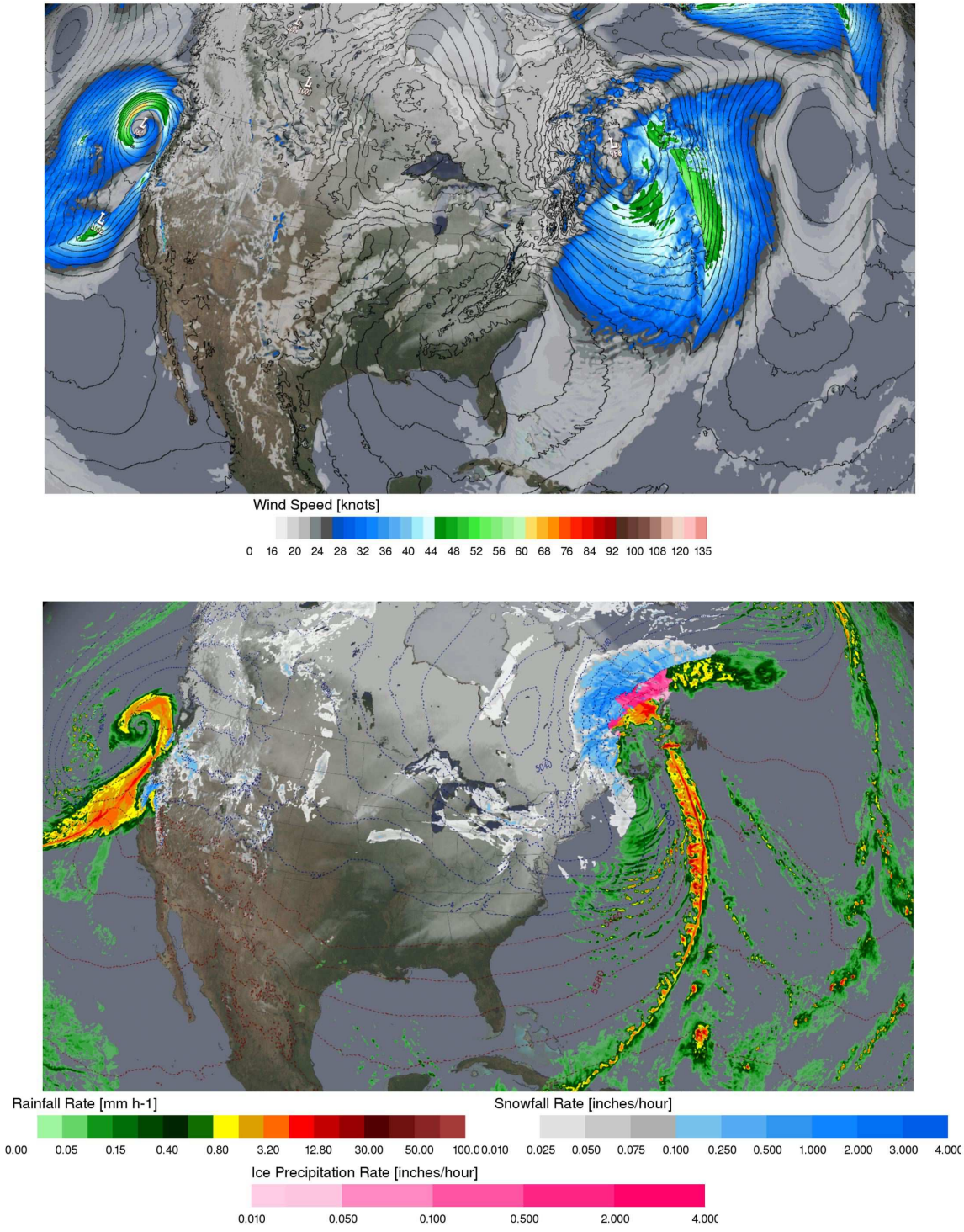

Figure 1.12: As in Figure 1.8 at 18Z January 20, 2007.

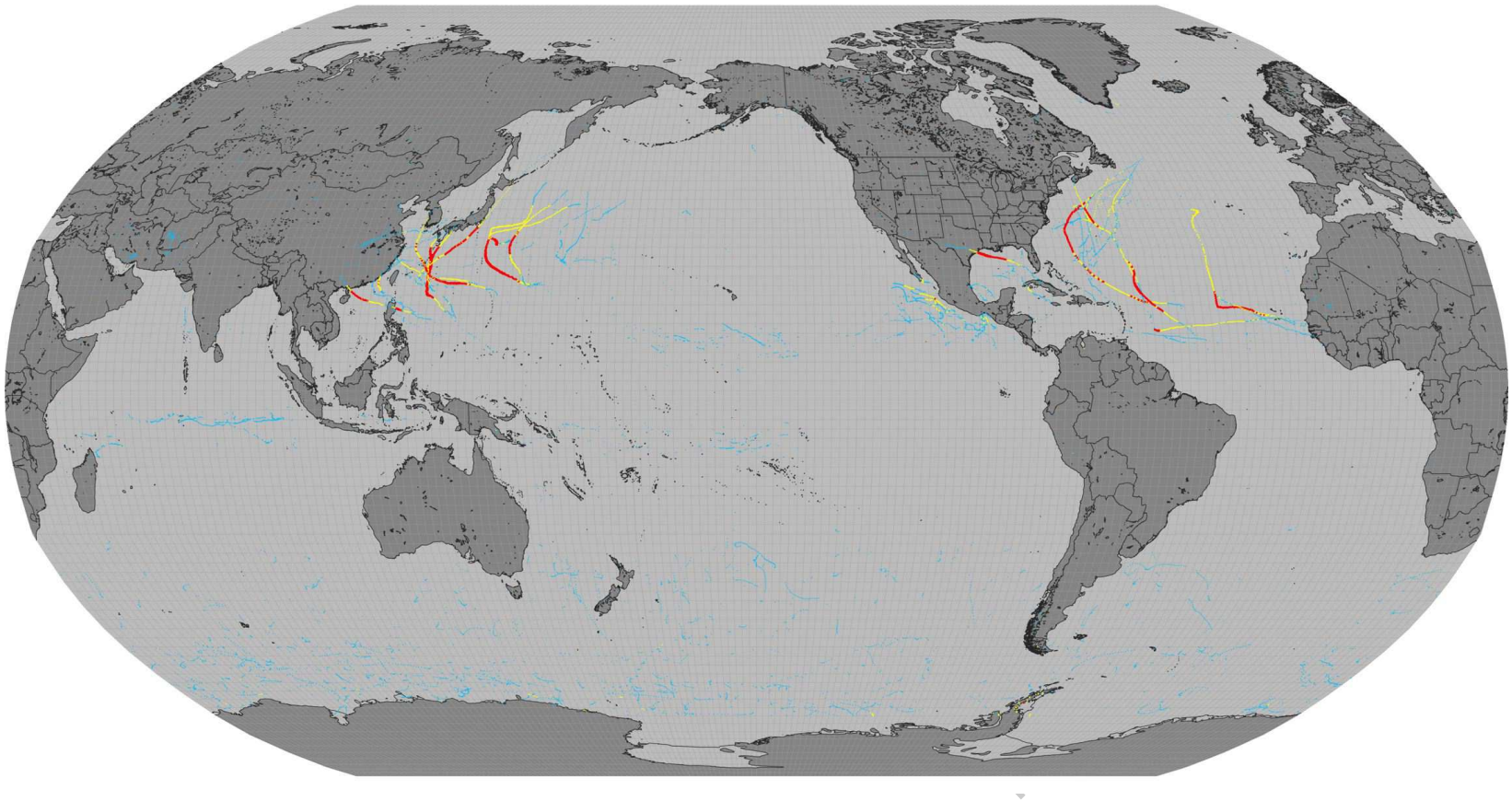

Figure 1.13: Global distributions of tropical cyclone tracks detected in the 7-km G5NR for the annual period from June 2005 to May 2006. Weak surface circulations, tropical depressions and tropical storms are denoted in light blue, tropical cyclones with distinct warm cores and surface winds in excess of 74 miles per hour (mph) are colored yellow, major tropical cyclones with winds in excess of 112 mph are colored in red.

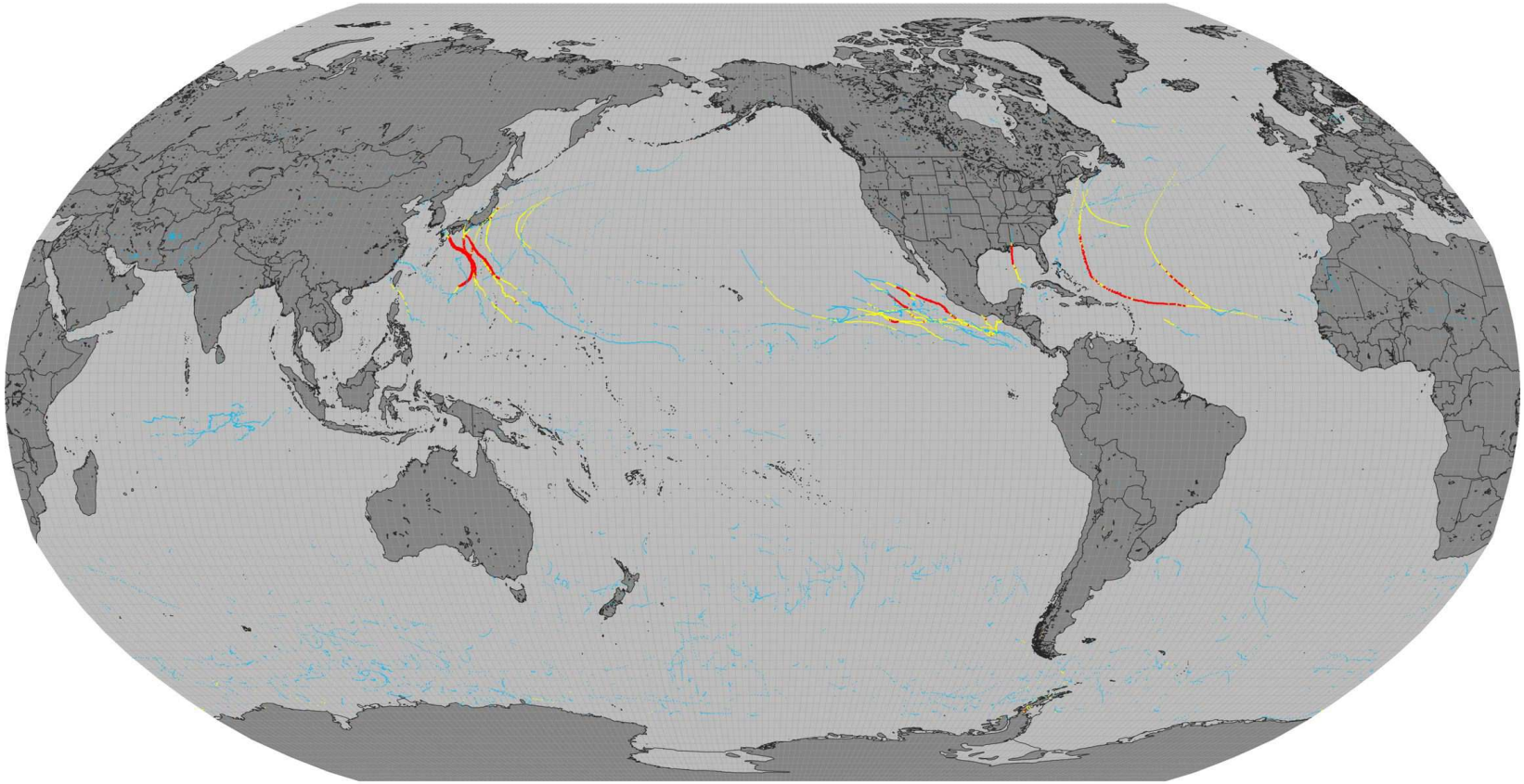

Figure 1.14: As in Figure 1.13 for June 2006 to May 2007.

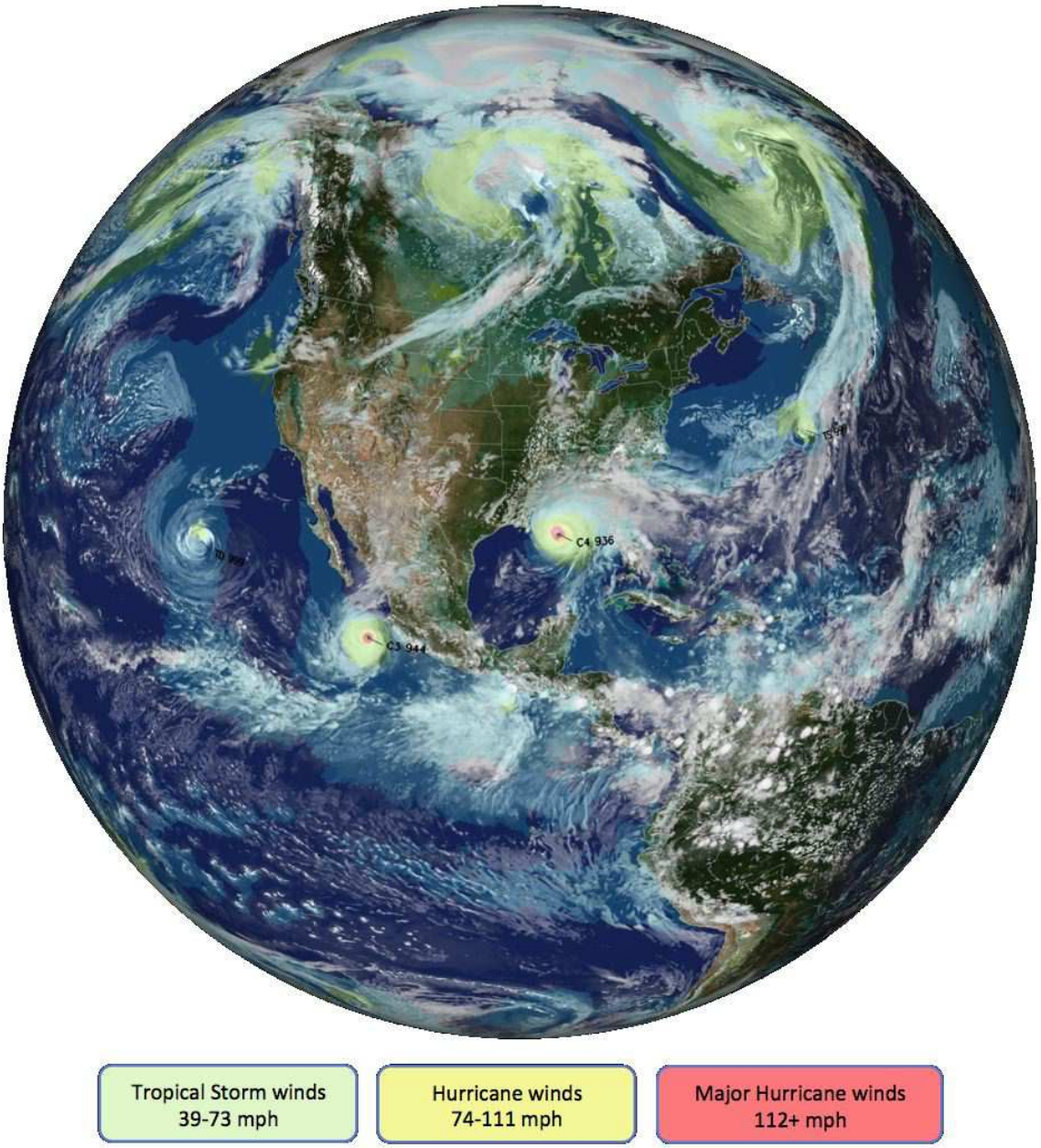

Figure 1.15: Clouds and surface winds speeds showing tropical cyclone activity in the east Pacific and north Atlantic at 2130Z on September 10, 2006 during the 7-km G5NR.

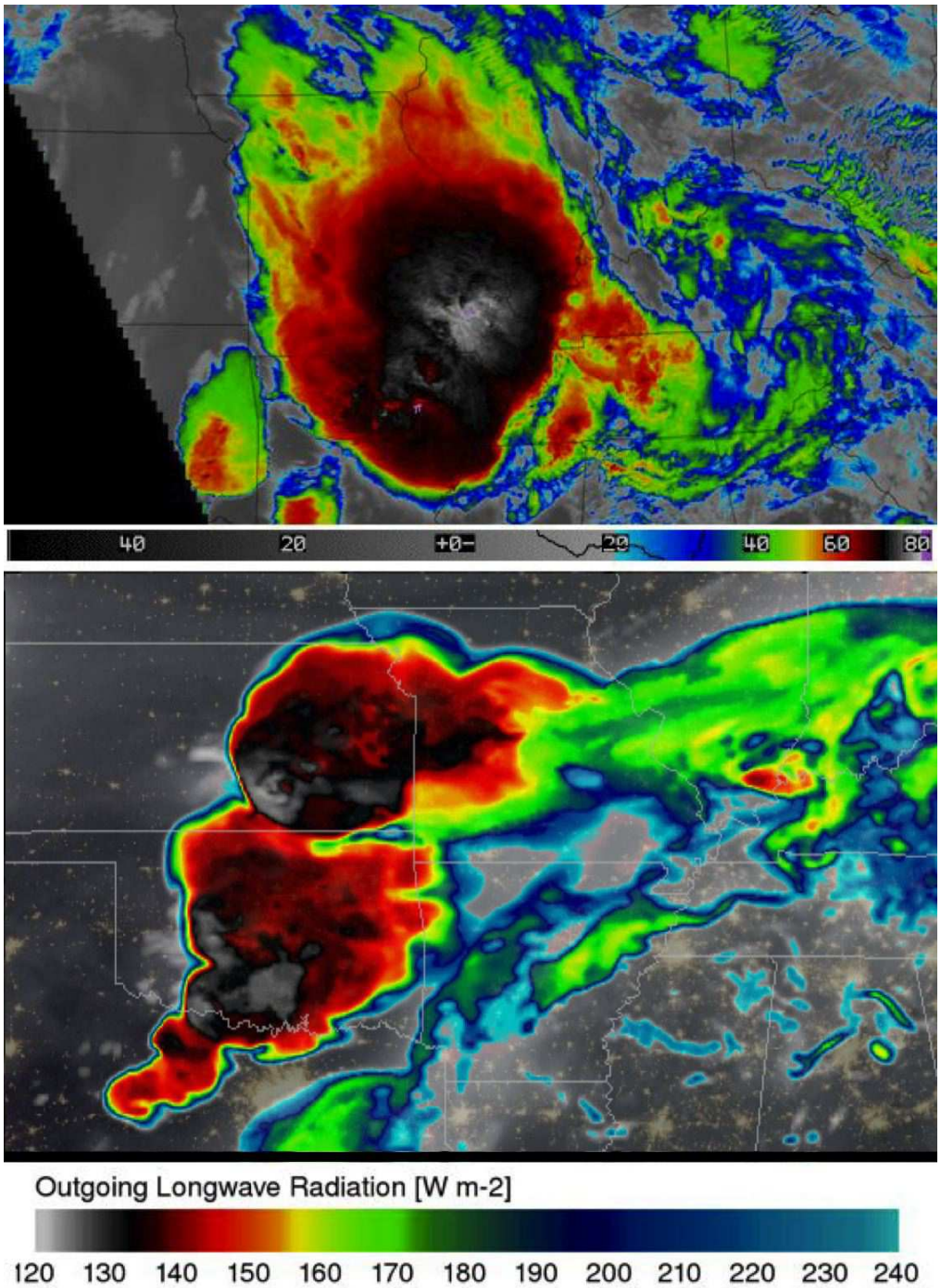

Figure 1.16: A large MCC is observed from AVHRR 15-micron IR brightness temperatures (degrees C) over the central US on April 28, 2014 at 02Z (top). A similar MCC is observed from OLR (Wm^{-2}) in the 7-km G5NR on May 19, 2006 at 04Z (bottom).

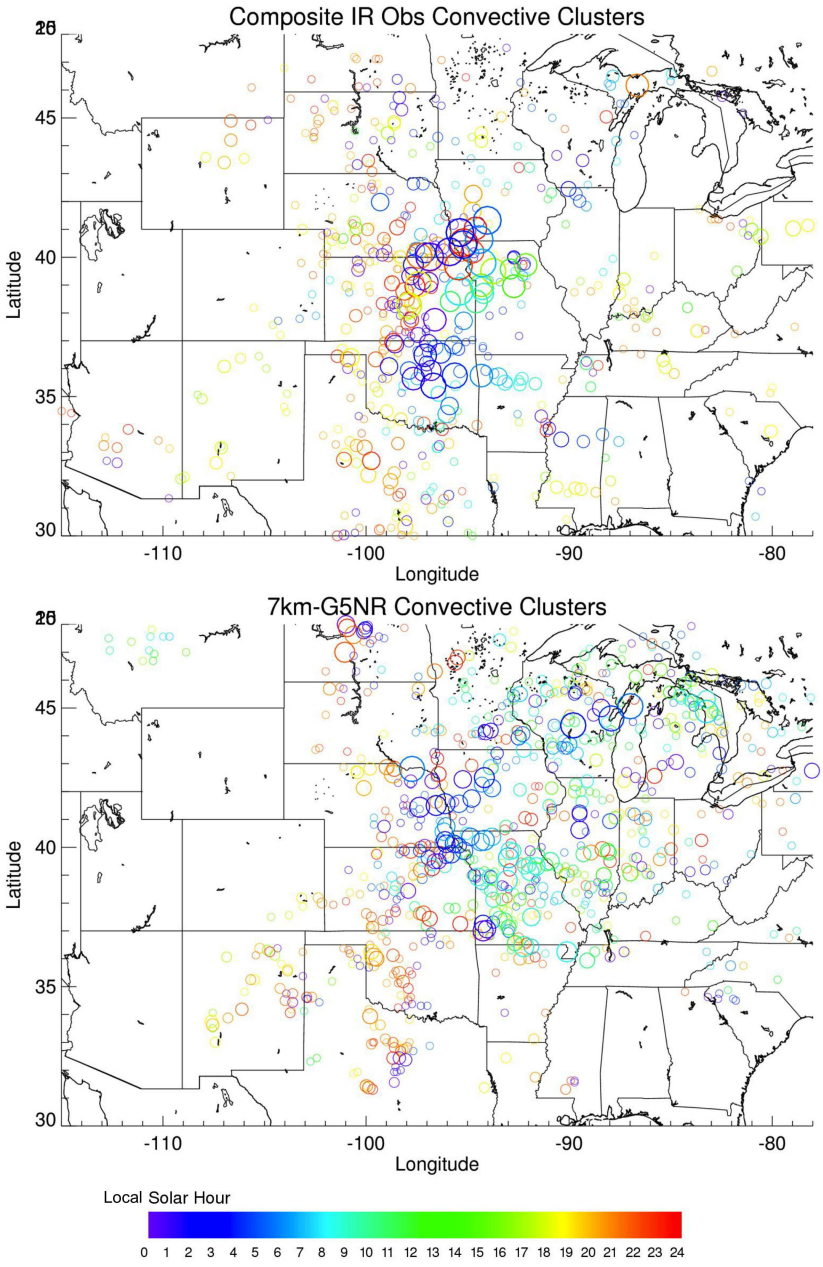

Figure 1.17: Distribution of MCCs from May–June of 2005 and 2006 as detected from composite geostationary IR observations (top) and in the 7-km G5NR (bottom). The size of the circles indicates the relative size of the detected MCC ranging from 100,000 km^2 to >500,000 km^2 . The color of the circles indicates the local solar hour at which the MCC was detected; shades of blue represent overnight hours (00–08), shades of green represent morning to midday hours (09–16), and shades of orange to red represent later afternoon to evening hours (17–23).

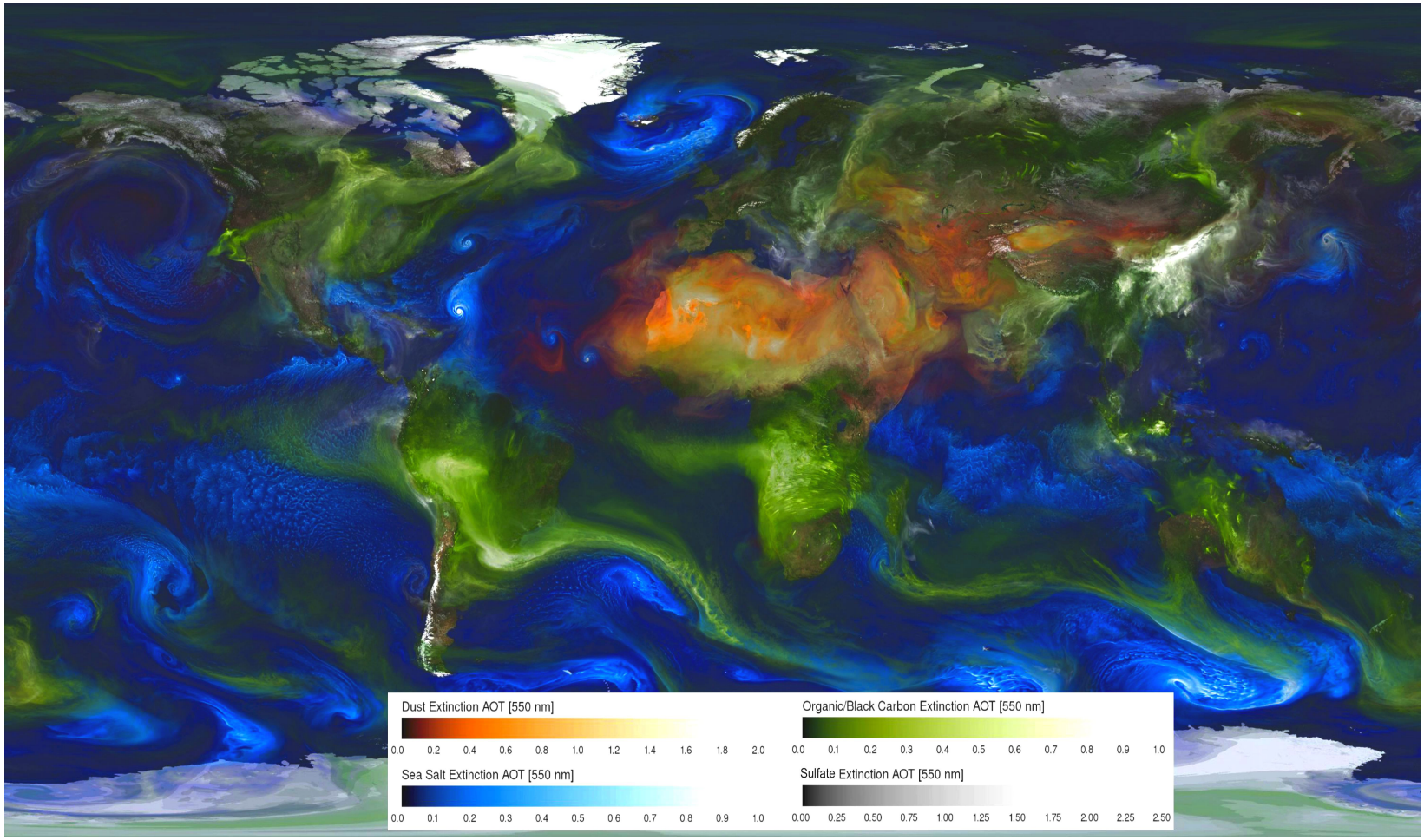

Figure 1.18: Global distribution of aerosols in the 7-km G5NR at 12Z on September 23, 2006.

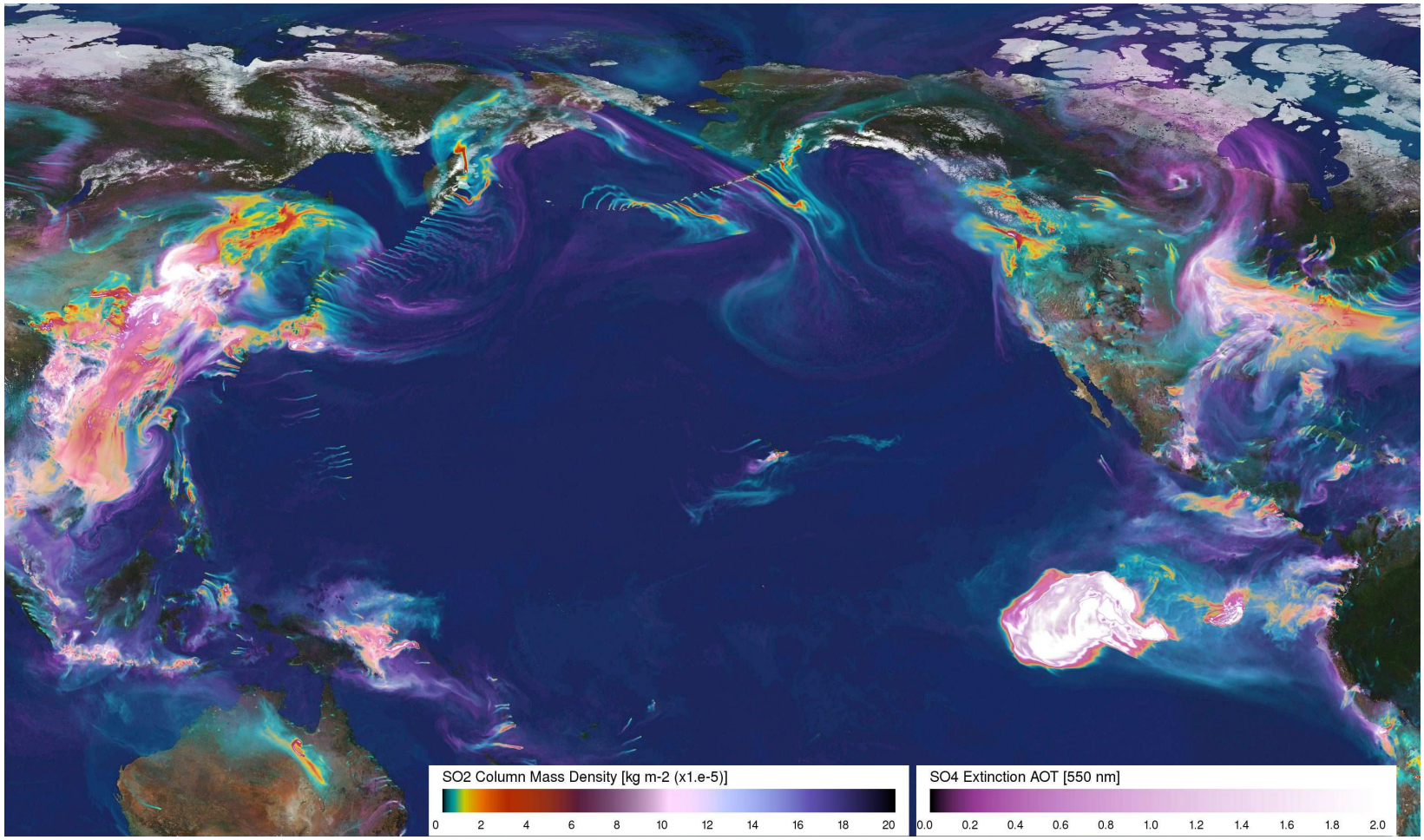

Figure 1.19: Concentrations of SO_2 and SO_4 in the 7-km G5NR at 02Z on October 27, 2005.

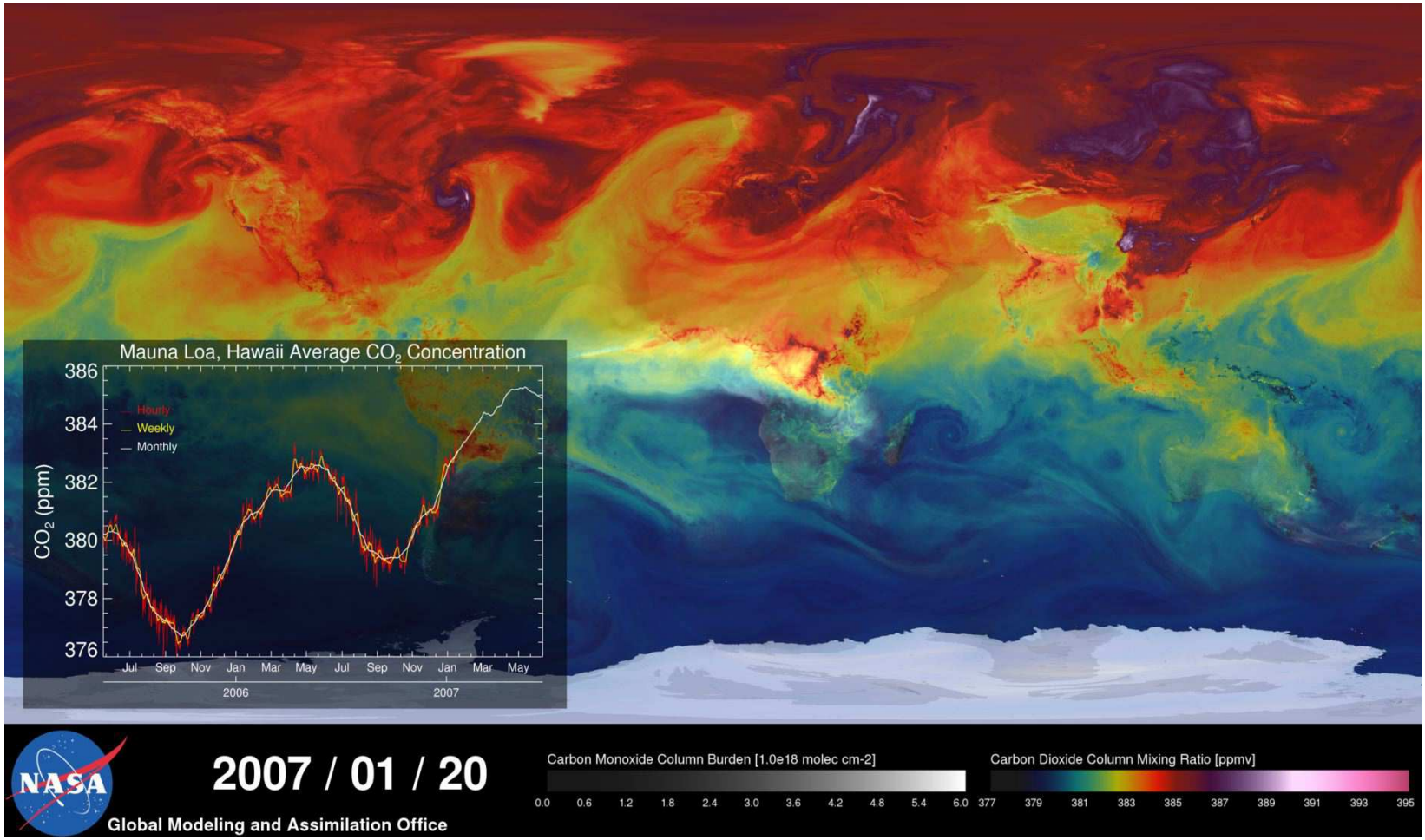

Figure 1.20: Concentrations of CO_2 and CO in the 7-km G5NR at 07Z on January 20, 2007

Chapter 2

Wind and Temperature

Nikki Privé, Ronald M. Errico and Lawrence Coy

In this chapter, the wind and temperature fields of the G5NR are described. The general circulation and time mean fields are discussed in Section 2.1, energy spectra are featured in Section 2.2, synoptic extratropical waves are reviewed in Section 2.3, and dynamics of the stratosphere and mesosphere are addressed in Section 2.4.

2.1 Zonal and Time Means

The general circulation of the G5NR is observed in the zonal and time mean fields of wind and temperature. Time mean fields are examined on a monthly or seasonal mean basis to reveal the annual cycle of the atmospheric state.

Seasonal mean zonal mean tropospheric zonal wind and streamfunction are shown in Figure 2.1 for the combined two years of the G5NR. Overall, the strength and position of the tropospheric zonal jets are realistic, with the strongest westerly jet in the winter hemisphere midlatitudes, a weaker westerly jet in the summer hemisphere midlatitudes, and upper level easterlies in the deep tropics. In the winter hemisphere, a secondary westerly maximum is seen closer to the pole, this being the lower edge of the stratospheric polar jet.

Ideally a month or season selected from the G5NR would not be distinguishable from a similar time period selected at random from the real world. The westerly tropospheric jet strength and

locations for individual months from the G5NR are compared to monthly means from the ERA-Interim (ERA-I) and CFSR reanalyses in Figure 2.2. The G5NR jet maxima amplitudes generally fall within the envelope of the reanalysis amplitudes. One exception is the April to June weakening Northern Hemisphere jet, which is consistently weaker in the G5NR than in the reanalyses. The location of the jet maxima also shows over good agreement between the G5NR and reanalysis, although the JJA Northern Hemisphere jet tends to move further poleward than seen in reanalysis. In the Southern Hemisphere, the strong stratospheric polar jet sometimes results in a more poleward westerly maximum than the tropospheric midlatitude jet, a result seen in both reanalyses and the G5NR.

In Figure 2.1, the zonal mean streamfunction displays the expected Hadley cells, with the strong 'winter' Hadley cell dominant in the June-July-August (JJA) and December-January-February (DJF) seasons, with transitional weaker cells in the September-October-November (SON) and March-April-May (MAM) seasons. Ferrel cells are observed in the midlatitudes.

The shape and strength of the Hadley cells differ somewhat from the circulation found in reanalyses. Figures 2.3 and 2.4 show the strength of the maximum streamfunction of the Hadley cells in each hemisphere along with the locations of the streamfunction maximum, compared with reanalyses as in Figure 2.2. Compared with reanalysis, the G5NR circulation tends to be on the weak side, particularly in the SON and MAM seasons. The CFSR Northern Hemisphere cell (positive streamfunction) is weaker in the boreal summer months than the same circulation cell in the ERA-I reanalysis; the G5NR is in closer agreement with the CFSR.

The streamfunction maximum is displaced further poleward compared to reanalyses, and a pronounced 'jump' occurs in the cross-equatorial Hadley cell where the low-level flow crosses the equator. This type of behavior is commonly found in GCMs, and is often associated with a 'double-ITCZ' feature (Chapter 3). The Northern Hemisphere (positive streamfunction) Hadley cell shows better agreement between the G5NR and reanalyses; as seen in Stachnik and Schumacher (2011), the tendency for low-level cross-equatorial flow to jump at the equator is common across numerous reanalyses for this cell, particularly in DJF. In contrast, the JJA cross-equatorial cell (negative streamfunction) shows minimal low-level equatorial jumping behaviour in the reanalyses, but a strong jump in the G5NR. This results in a weakened cell with poleward shifted streamfunction maximum in the G5NR compared to reanalyses.

Seasonal mean zonal mean meridional wind and temperature are shown in Figures 2.5 and 2.6. The zonal mean meridional wind shows the expected pattern of upper tropospheric tropical maxima in the upper branch of the Hadley cell(s), with return flow at low levels. The equatorial jumping behavior is most visible in the DJF low level flow, where the southward meridional flow reaches a maximum near 10N, and is near zero at low levels at the equator, with weak southward flow near 800 hPa. A weakening of low-level meridional flow is seen at the equator in other seasons as well. The zonal mean temperature fields also show the expected broad tropical maxima in the middle and lower troposphere with sharp poleward-negative gradients in the midlatitudes. There is also a temperature minimum at the tropical tropopause, and the cold upper atmosphere of the polar vortex at the winter pole, which will be discussed further in Section 2.4.

The magnitude of the meridional flow in the upper tropospheric leg of the cross equatorial Hadley cell is compared to reanalysis in Figure 2.7. While there is agreement between the ERA-I and CFSR reanalyses for the northward maximum associated with the Northern Hemisphere (positive streamfunction in Figure 2.1) cell, there is less agreement for the Southern Hemisphere cell, particularly in the boreal summer period when this cell is dominant. The G5NR is in better agreement with the weaker meridional cross-equatorial flow in the ERA-I than the stronger flow in the CFSR.

The temperature minimum at the tropical tropopause is also shown in Figure 2.7, where this minimum is warmer in the G5NR compared to reanalyses for all months. This may impact stratospheric moisture levels, as ascent in this region is the main source of stratospheric moisture, and the cold minimum acts to limit the amount of moisture transported into the stratosphere.

Figure 2.8 shows the jet structure at 300 hPa for both JJA and DJF, comparing long term means from the reanalyses to the two-year mean from the G5NR. The jets in the G5NR show good agreement with the reanalyses. There is more eastward extension of the Northern Hemisphere jet across the Atlantic Ocean and into northern Europe in for DJF in the G5NR compared with reanalyses. In JJA, the weaker jet branch over the south Pacific reconnects to the main jet near South America, a feature not seen in the reanalyses.

The Walker circulation is examined in Figure 2.9, showing the seasonal mean zonal wind averaged within 10° of the equator. For JJA, the strong easterly outflow from the upper level anticyclone over the Asian monsoon region is observed between 0E and 120E. Over the tropical Pacific, the Walker circulation is weak during JJA, with minimal evidence of upper level westerlies. During DJF, the easterly flow over Asia is weaker than in boreal summer, and the two Walker cells over the central/eastern Pacific and Atlantic basins are seen. The Pacific Walker cell is somewhat weaker aloft in the G5NR compared to reanalyses, with a stronger cell observed in 2006-7 compared to 2005-6. The Atlantic Walker cell is weak for DJF in the G5NR in 2006-7, but closer to the reanalysis climatological mean in 2005-6. Upper level easterlies over Africa during DJF are considerably stronger in both years of the G5NR compared to the reanalysis climatologies.

2.2 Energy Spectra

Power spectra P for the wind field at 250 hPa were determined at one time per month during the first year of the G5NR. Results for one such time are presented in Figure 2.10. The spectra are presented separately for rotational and divergent wind as functions of spherical-harmonic, two-dimensional length scale $L = a/n$, where a is the earth's radius and n is the two-dimensional dimensionless wavenumber. Lines indicative of theoretical ranges of 2-dimensional and 3-dimensional turbulence, respectively having $P \propto n^{-3}$ and $P \propto n^{-5/3}$ are also presented. The spectral characteristics noted for this single time are common to all times examined.

Common to almost all atmospheric models and observations (Augier and Lindborg (2013), Burgess

et al. (2013), Blazica et al. (2013), Hamilton et al. (2008), Tulloch and Smith (2006)), and first suggested by Charney (1971), the rotational component of power follows a n^{-3} law for $100 < L < 1000$ km. It strongly dominates the divergent component at the same wavenumbers. For $L < 100$ km the slope of rotational power becomes less steep, but does not approach the $n^{-5/3}$ behavior thought to be indicative of the mesoscale (e.g., Tulloch and Smith, 2006). For $L < 10$ km, it approaches a n^{-8} behavior, steeper than that seen in the previous ECMWF NR (Errico and Privé, 2014) and some other models (Burgess et al., 2013) that has been attributed to unrealistically-strong model damping at the smallest resolved scales.

The ratios of powers of the rotational and divergent winds for $L < 100$ km (the smallest ratio being 4) appear somewhat larger than those seen in the previously mentioned papers at the same elevations and horizontal scales. In fact, the ECMWF model shows the divergent wind spectrum dominating the rotational (Burgess et al. (2013), Errico and Privé (2014)), although this ECMWF result is uncommon. The G5NR result is likely due to the fact that horizontal diffusion is primarily applied to the divergent, rather than rotational wind in the this model.

Qualitatively, the spectra for $L > 100$ km looks like those of other models, theory, and inferences from observations. For smaller scales, model behaviors are more varied, the theory is more uncertain, and the representativeness of observations more suspect. Aside from the weakness of the spectrum of divergent wind compared with that of the rotational wind, the GEOS-5 results fall within the ranges of other reported results. Along with all other reported results, at very small scales the GEOS-5 spectra decrease much more rapidly with decreasing scale than either theory suggests or observations reveal. Thus, the true resolution of the G5NR should be considered as several times lower than its grid spacing of 7 km. Unfortunately, without a better understanding of what the shape of the real atmospheric spectra is and what criteria should be used, it is difficult to define an unambiguous "true" resolution. Also, the significance of the weak spectrum of divergent wind in the G5NR is unclear.

2.3 Extratropical Synoptic Waves

2.3.1 Overall Wave Activity

One measure of wave activity is the variance of metrics of interest. For extratropical synoptic waves, the variance of upper tropospheric meridional wind (v) is commonly chosen. Figure 2.11 shows the standard deviation of 200 hPa v over different seasons, comparing two seasons from the G5NR to multiple seasons from reanalyses.

For JJA, the overall magnitude and pattern of wave activity in the G5NR is similar to that seen in the reanalyses. One notable difference is the area of large standard deviations near 60S from 180W to 60W - these large values are found in both years of the G5NR. The G5NR standard deviations are also somewhat low over the tropical Pacific basin.

In DJF, the G5NR again has similar patterns of wave activity compared with reanalyses, with some differences in the magnitude of activity. There are uniformly higher standard deviations in the G5NR compared to reanalyses from 40S-60S, and also over the North Atlantic. The tropical Pacific again has lower standard deviation in the G5NR compared with reanalyses.

In order to put the two seasons of G5NR wave activity into perspective, individual seasons from the reanalyses are compared to the G5NR in Figure 2.12. The seasonal mean standard deviation of 200 hPa v is calculated for each season in the G5NR, and for the CFSR (1994-2010) and ERA-I (1994-2013) reanalysis, with the areal mean calculated over the region of strongest wave activity for both JJA and DJF in the two hemispheres. Ideally, the G5NR values would fall within the envelope of the reanalysis values, indicating that the G5NR is indistinguishable from the reanalyses.

In JJA, the G5NR standard deviations of v are within the envelope of the reanalysis values, although one year of the G5NR has weak activity over the North American region. However, for DJF the G5NR values are relatively high in both years, particularly in the eastern hemisphere, with localized excursions above the envelope of reanalysis results.

2.3.2 Wave Characterics

Synoptic scale extratropical waves are further evaluated in terms of the spectra of phase speed and wavenumber. This type of cross-spectral analysis is familiar from Wheeler and Kiladis (1999), using the method of Hayashi (1971) to calculate the spectra. For these calculations, the 200 hPa meridional wind is averaged over a latitude range, and used in an unfiltered state as there is relatively little noise in the meridional wind field. Eastward progressing waves are assigned positive wavenumbers, while westward progressing waves are assigned negative wavenumbers. In Figure 2.13, the entire two-year G5NR period is used, in comparison to longer periods for ERA-I (1994-2013) and CFSF (1994-2010). The shorter G5NR period will tend to yield a 'spottier' appearance to the phase-spectra diagrams.

In the Northern Hemisphere, the phase spectra are quite similar for the G5NR and reanalyses, with greatest power at wavenumbers 5-7, and phase speeds up to 10 $\mathrm{m\,s^{-1}}$, with higher speeds for higher wavenumbers. The Southern Hemisphere also shows similar properties of synoptic waves for the G5NR and reanalyses. Wavenumbers 4-6 are dominant, with phase speeds from 3 to 13 $\mathrm{m\,s^{-1}}$, again with faster speeds for higher wavenumbers. These values are in agreement with previous studies (Chang and Yu (1999), Chang (1999), Dell'Aquila et al (2005)).

The technique of phase spectra decomposition can also be used to estimate group velocities. The method of Zimin et al. (2003) allows the wave packet magnitude to be calculated around a latitude band. These wave packets can then be decomposed using the method of Hayashi (1971) to find the group velocity and wave packet size spectra. These calculations are performed for the same regions as the phase speed spectra previously shown, filtering for wavenumbers 1–20 to capture packets of synoptic and planetary waves only, with the results illustrated in Figure 2.14. The "wave packet

wavenumber" is not the wavenumber of the component waves, but instead the "wavenumber" of the entire wave packet.

As expected, the group velocities are faster than the phase speeds, and the wave packet sizes are larger (smaller "wavenumber") than the wavenumber of the component waves. In the Northen Hemisphere, the G5NR group velocities are similar to the group velocities of the CFSR, with group velocities up to 15 $\mathrm{m\,s^{-1}}$. ERA-I has greatest power for somewhat higher group velocities, up to 20 $\mathrm{m\,s^{-1}}$. The group velocities are roughly twice as fast as the phase speeds, which results in the observed downstream development of synoptic waves, and which is consistent with theoretical properties of Rossby waves.

In the Southern Hemisphere, there is relatively good agreement between group velocities for the G5NR and both reanalyses. Again, the group velocities are higher than the phase speeds, with greatest power for group velocities of 15–30 $\mathrm{m\,s^{-1}}$. The G5NR does have some local power maxima at slow group velocity (wavenumbers 4–5, 3–12 $\mathrm{m\,s^{-1}}$) that is not seen in the reanalyses.

2.4 Stratospheric Overview

2.4.1 Quasi-Biennial Oscillation

The current configuration of the GEOS AGCM produces a tropical lower stratospheric Quasi-Biennial Oscillation (QBO) that is generated by a combination of resolved global scale waves and parameterized gravity waves. Figure 2.15 (upper panel) shows the tropical zonal winds with a downward propagating QBO signal dominating in the lower stratosphere. At 10 hPa the easterlies are stronger in magnitude that the westerlies (35 vs 20 $\mathrm{m\,s^{-1}}$) in agreement with observations. With only two years of the G5NR it is difficult to analyze the period precisely, however, the lower panel in Figure 2.15 shows the difference in corresponding months between the two years, a process that removes annual and semi-annual cycles that repeat between the two years, highlighting the QBO signal. If the QBO period in the G5NR was exactly two years then the two halves of the figure would match at the middle time (by definition the left and right halves are the negative of each other). The discontinuity at the middle of the figure (where the contour lines jump up) shows that the G5NR QBO period is slightly less than two years. The observed QBO periods is close to 27 months, so the G5NR descends a bit too quickly.

2.4.2 Annual Cycle

Figure 2.16 compares the two annual cycles of the G5NR mid-stratospheric 90°N temperature with the corresponding monthly averaged temperatures from MERRA. The winter (Dec–Mar) polar temperatures in the G5NR are colder than typical MERRA winters while the spring (May

and June) temperatures are warmer. The G5NR realistically captures the annual cycle of polar temperature change and are generally within the range seen by MERRA.

Figure 2.17 shows that the mid-stratospheric jet generally follows the polar temperatures by being stronger than most of the MERRA years during the winter season (Nov–May). In particular the G5NR 2006 December winds are $\sim$10m s^{-1} stronger than is seen in any of the MERRA Decembers. The relatively strong winds seen in May suggest that the seasonal weakening of the polar jet is somewhat delayed in the G5NR. Note that the January 2006 winds (blue diamonds) are much stronger in the G5NR than in MERRA, as MERRA reflects the decrease in winds experienced during the major Stratospheric Sudden Warming (SSW) of January 2006 while no warming occurred in the G5NR.

More detail of the zonal wind at 10 hPa and 60°N is seen in Figure 2.18, where the NH winter G5NR winds are persistently near the maximum values seen by MERRA. There are no mid-winter stratospheric warming events in the G5NR since the G5NR zonal wind at this location remains positive until the final spring warming in April.

The winter (May–Oct) Southern Hemisphere in the G5NR (Figures. 2.19 and 2.20) also shows somewhat cold polar temperatures and strong polar jet winds when compared to MERRA. As in the Northern Hemisphere, the relatively cold temperatures and strong winds seen in the G5NR in October indicate a delayed end to winter when compared to MERRA. Despite the wintertime cold pole and strong winds the overall seasonal cycle is well captured in the G5NR winds and temperatures.

2.4.3 Planetary Waves

The relatively strong NH wintertime jet and cold polar temperatures in the G5NR are associated with relatively weak stationary planetary wave activity propagating upward from the troposphere. Figure 2.21 shows the meridional heat flux at 200 hPa due to stationary waves (calculation based on monthly averaged meridional wind and temperature fields), near the tropopause. The meridional heat flux is proportional to the vertical component of the Eliassen-Palm (EP) flux, a useful measure of the vertical flux of wave activity (Andrews et al. 1987, page 128). For the G5NR the vertical flux of stationary wave is particularly weak in January and February. Since the stratospheric winds remain westerly throughout the winter (no warming events) the planetary waves are not blocked by the presence of easterlies in the stratosphere as often happens after major stratospheric sudden warming events. Instead the reduction in vertical stationary wave propagation is likely due to the stratospheric winds being too strong westerly, a configuration that can also reduce vertical planetary wave propagation.

The corresponding Southern Hemisphere (SH) meridional heat flux at 200 hPa due to stationary waves is shown in Figure 2.22. Note that in the SH negative values are associated with upward propagating planetary waves. In agreement with MERRA, the G5NR stationary planetary waves

are weaker in the SH than in the NH. The G5NR wave fluxes tend to be strong compared to MERRA in July during both years and somewhat strong during June as well, but most of the SH winter/fall season (Aug-Oct) shows G5NR planetary wave forcing to vary somewhat between the two years in good agreement with MERRA.

Figure 2.23 shows typical G5NR mid-stratospheric EPV (Ertel Poltential Vorticity) fields vertically interpolated to the 850 K potential temperature surface. The SH has a more zonal pattern than the NH and even though the stationary planetary waves are weak compared to MERRA, the G5NR shows a high, anti-cyclonic, region over the North Pacific, in agreement with the climatological location. Note the fine horizontal filaments that are resolved in the G5NR.

2.4.4 Resolved Gravity Waves

The high horizontal resolution* of the G5NR enables the detailed examination of resolved gravity waves (GW). The largest amplitude GW's in the mid-stratosphere G5NR are directly associated with orography and these waves are often seen to affect the EPV far downstream of the GW origin. An example of a large amplitude GW over Greenland that generated large downstream EPV perturbations can be seen in the 850 K EPV on 26 January 2007 (Figure 2.24). The downstream EPV developed a strongly perturbed pattern in response to the large amplitude GW over Greenland. The vertical GW structure in the potential temperature, vertical velocity, and zonal wind are shown in Figure 2.25. The waves are seen to originate from the east coast of Greenland (the white area adjacent to the bottom of the panels) and grow in amplitude into the middle stratosphere. There is evidence of wave breaking in the mid-stratosphere ($\sim$10 hPa) as the potential temperature surfaces over turn at those altitudes.

The ability of breaking orographic waves to produce downstream changes in EPV can be seen in a second example (Figure 2.26) where the flow over the Andes on the west coast of South America generates high and low EPV streaks. In this example the EPV changes near the orography appear to be advected downstream over hundreds of kilometers. The resolution of the G5NR allows the development of this vorticity perturbation to be directly associated with the orographically produced GW divergence field (Figure 2.27). Seen at 3 hourly intervals the mid-stratospheric divergence first grows over the orography. Later (at 8 Sep 00 and 03 UTC) when the GWs break, the vorticity perturbations begin to grow. That the GW's begin to break at that time can be seen in the local reversal of the potential temperature gradients and an increase in eddy (K_{zz}) mixing (not shown). The horizontal resolution of the G5NR is essential for a realistic representation of these processes.

In the mesosphere rings and half circles (rings partly filtered as they propagate vertically through changing background winds), characteristic of small scale convective forcing, dominate the vertical velocity field. To examine the influence on the momentum budget of these smallest scale waves, the vertical momentum flux has been calculated from the full horizontal resolution G5NR (0.0625°)

*See Section 2.2 for a discussion of the effective resolution of the G5NR.

and the derived reduced grid (0.5°) u and w fields and plotted at 0.128 hPa (Figure 2.28). Results show that the largest momentum fluxes found at this time (60°N, Figure 2.28, top panel) are well resolved at the reduced grid scale and are associated with the underlying orography, so that little is gained by the high horizontal resolution of the G5NR. In contrast, in the tropics and subtropics the smaller scales can be seen to contribute substantially to the momentum fluxes, however the overall magnitude of these fluxes are small compared to the northern winter momentum fluxes. The relatively minor contribution of the smallest scale GWs to the momentum budget in the G5NR may be a reflection of the reduced effective resolution discussed in Section 2.2.

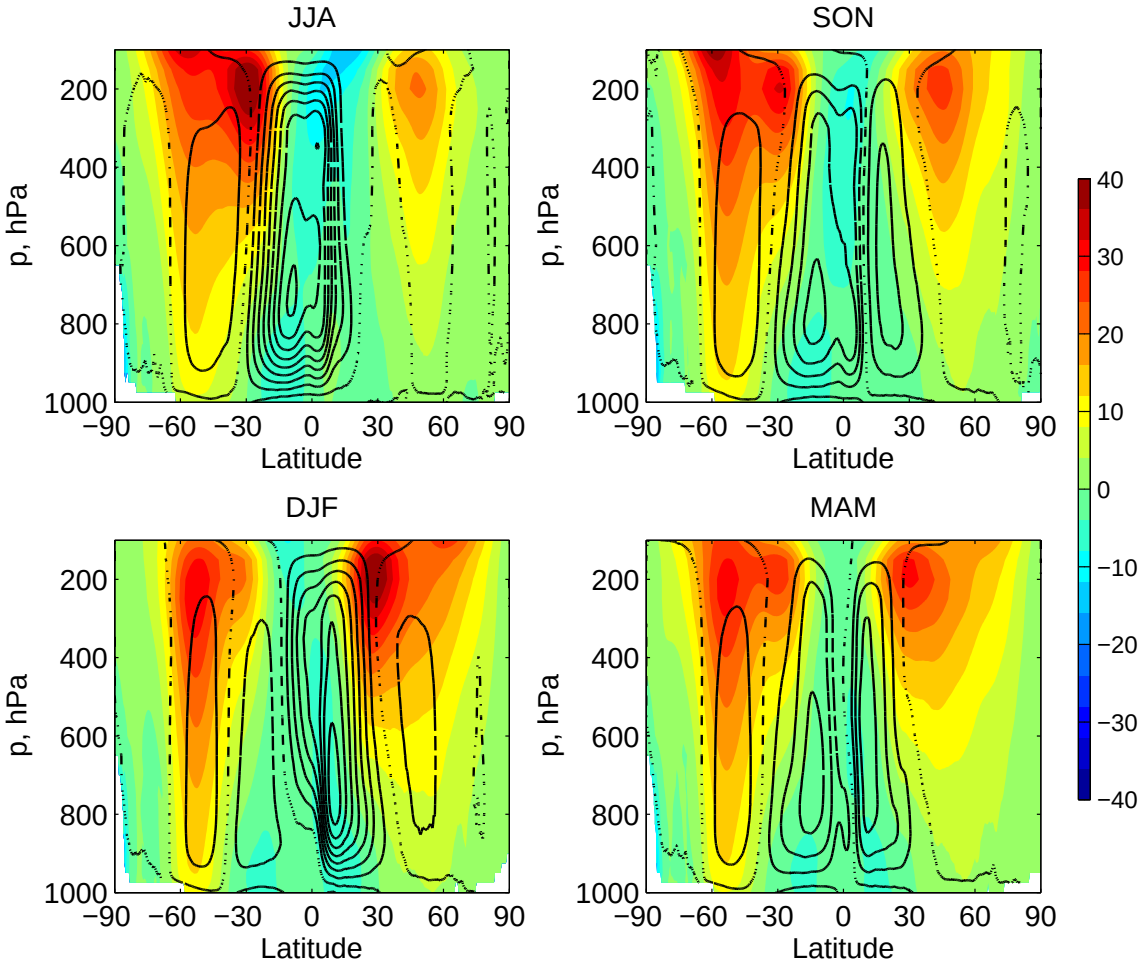

Figure 2.1: Time mean zonal mean of the G5NR zonal wind (color contours, $\mathrm{m\,s^{-1}}$) and streamfunction (black contours, kg $\mathrm{s^{-1}}$). Dashed lines indicate negative (counter clockwise) streamfunction; dot-dash line indicates zero streamfunction line. Seasonal means include both years of the G5NR.

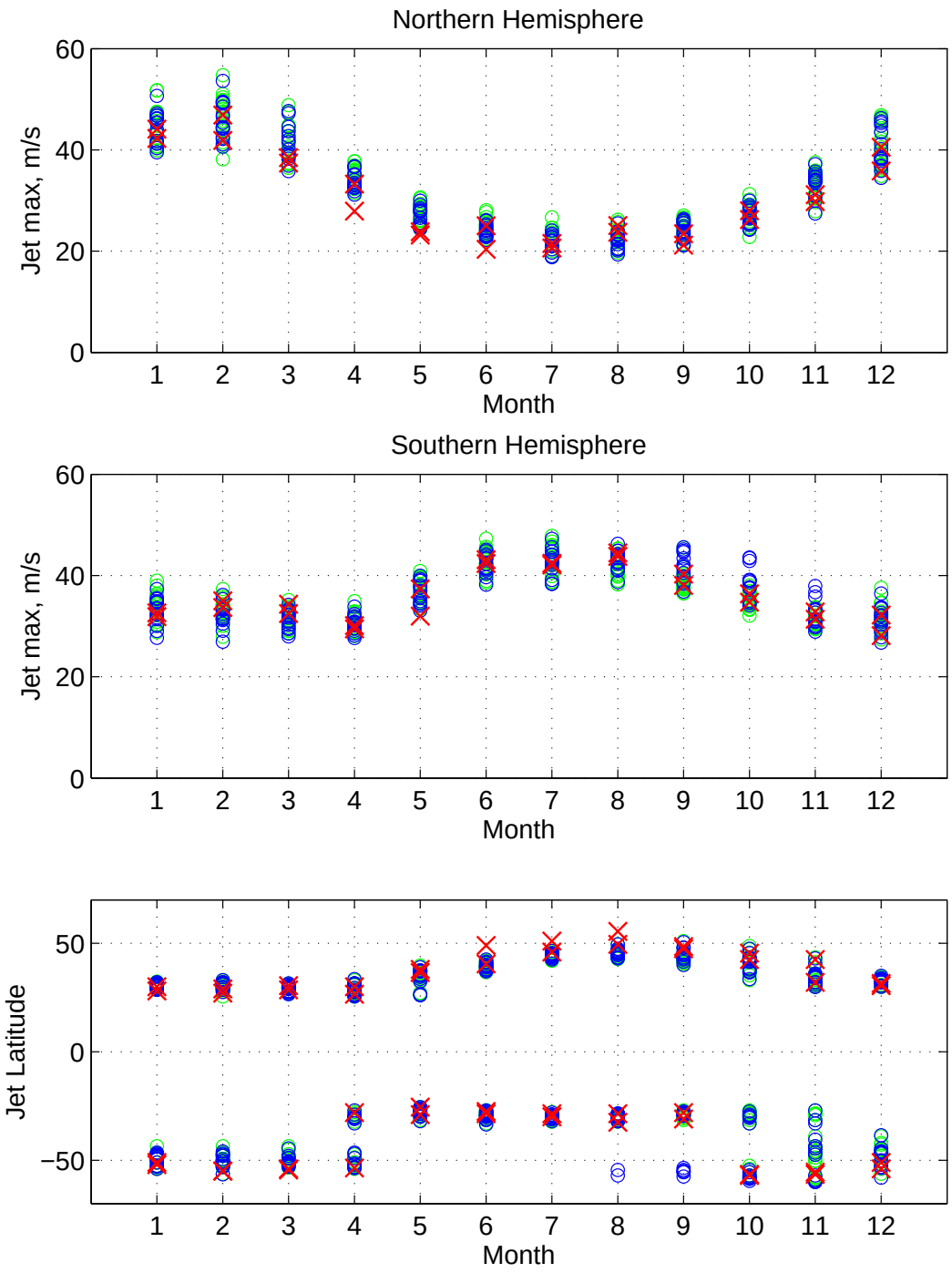

Figure 2.2: Monthly time mean zonal mean maximum strength of the tropospheric zonal wind in each hemisphere (top two panels), and the location of the maximum (lower panel). Blue circles, CFSR 1994-2010; green circles, ERA-I, 1994-2013; red crosses, G5NR. Each symbol indicates one month of one year.

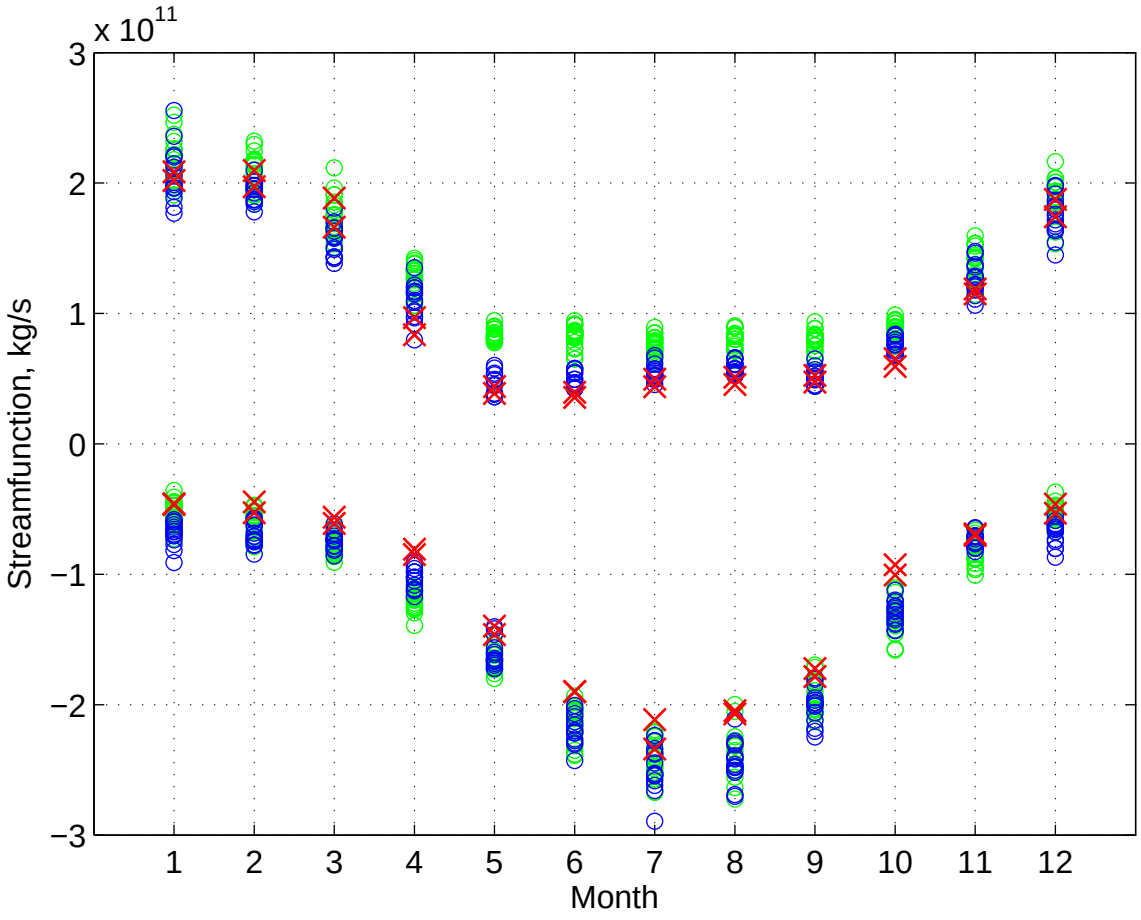

Figure 2.3: As for Figure 2.2, but for the maximum streamfunction of both Hadley cells. Northern hemisphere cell has positive streamfunction, Southern hemisphere cell has negative streamfunction.

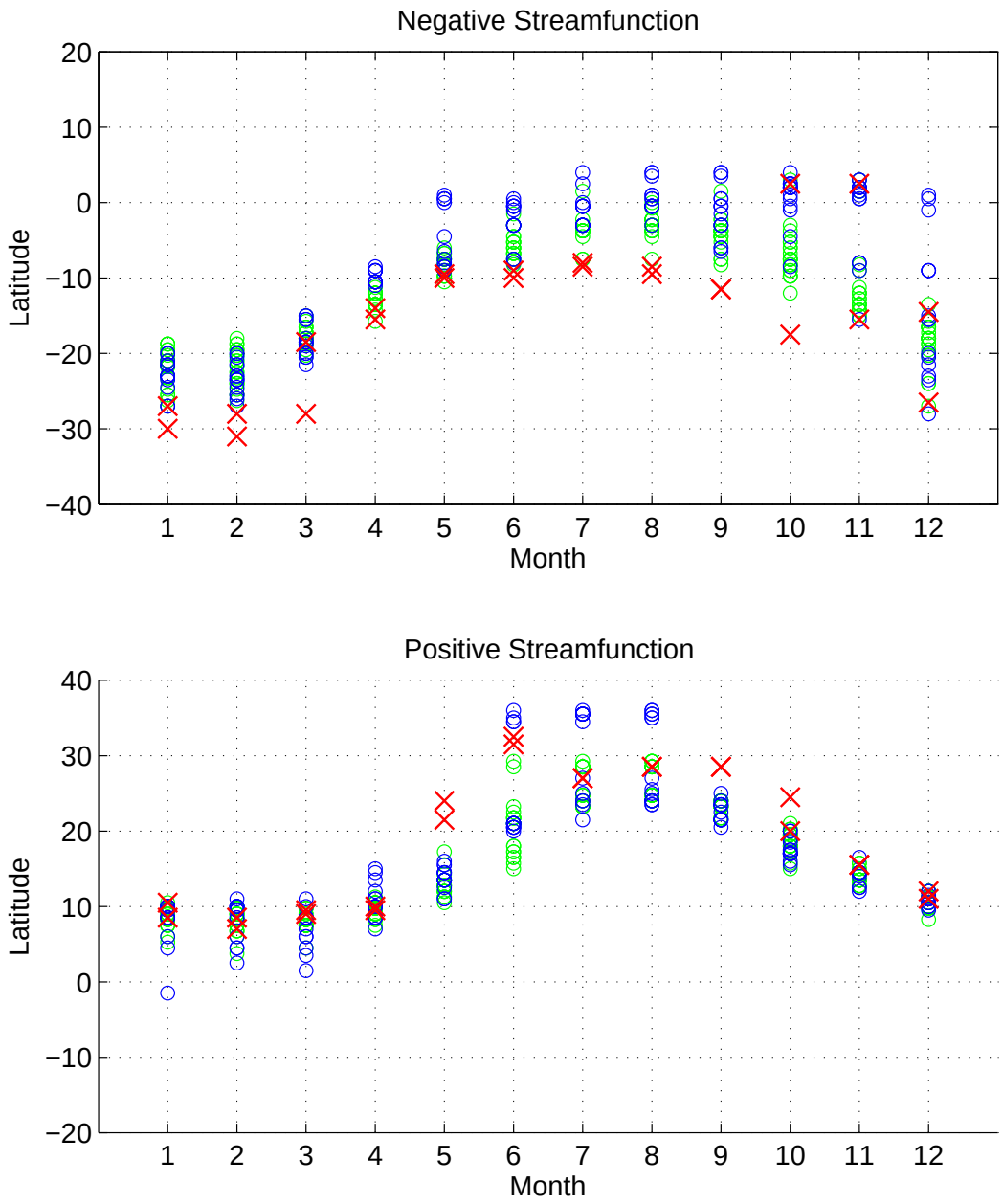

Figure 2.4: As for Figure 2.2, but for the location of the maximum streamfunction of the two Hadley cells.

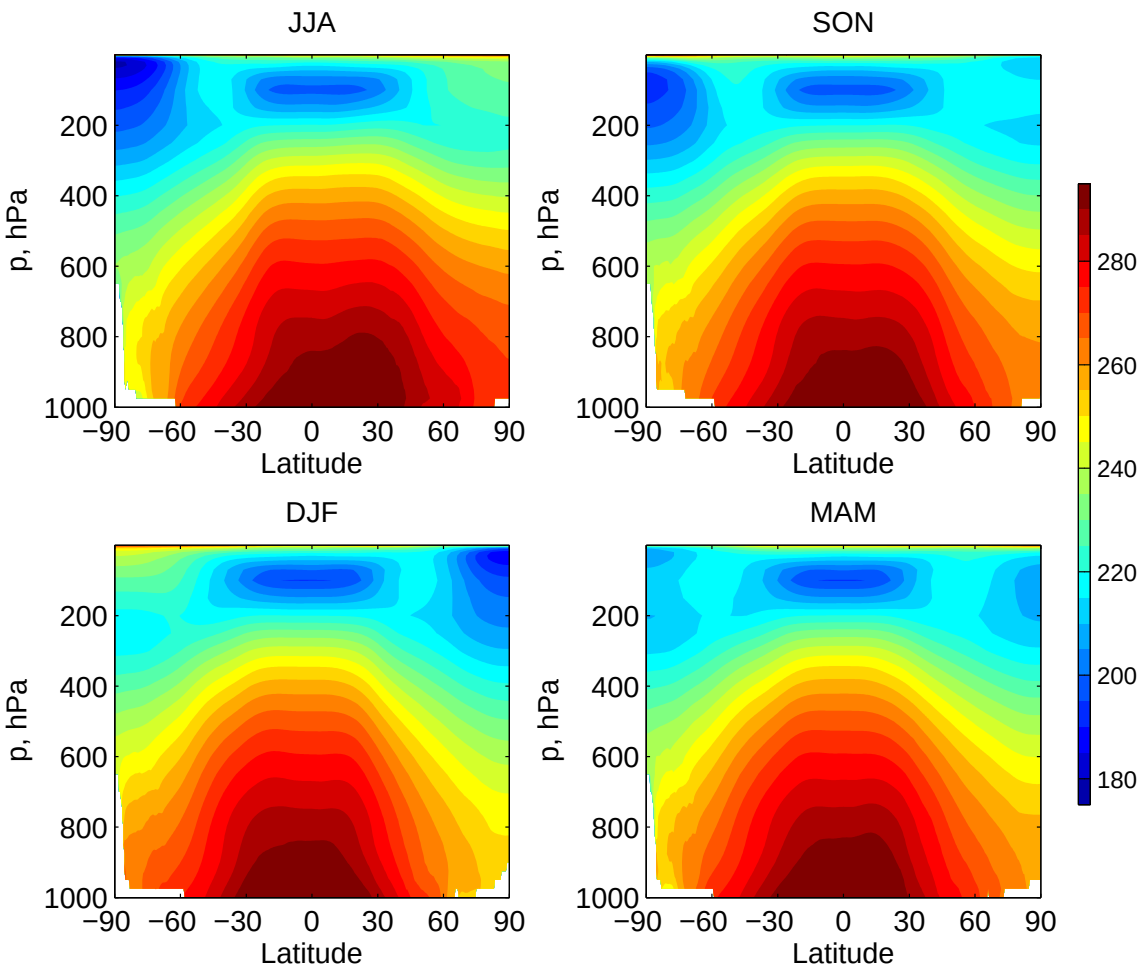

Figure 2.5: Time mean zonal mean of the G5NR for temperature (K). Seasonal means include both years of the G5NR.

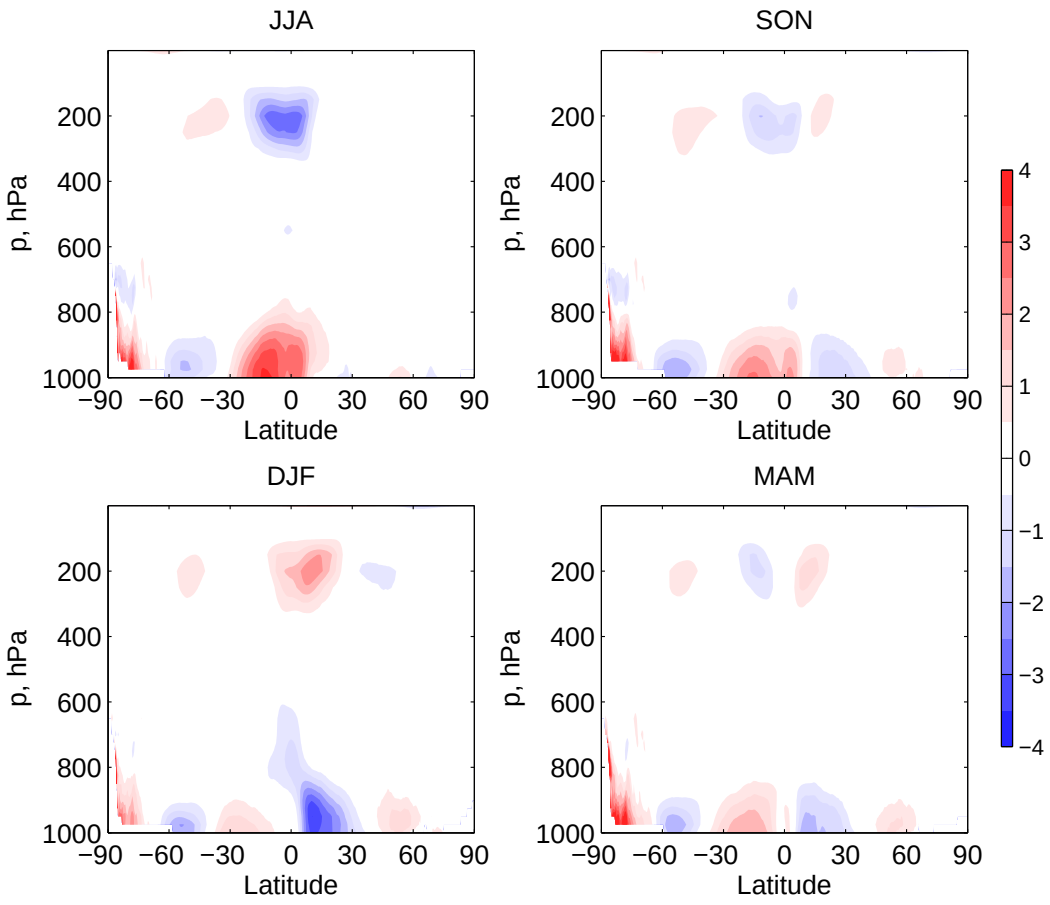

Figure 2.6: As for Figure 2.5, but for the zonal mean meridional wind, v (m s^{-1}).

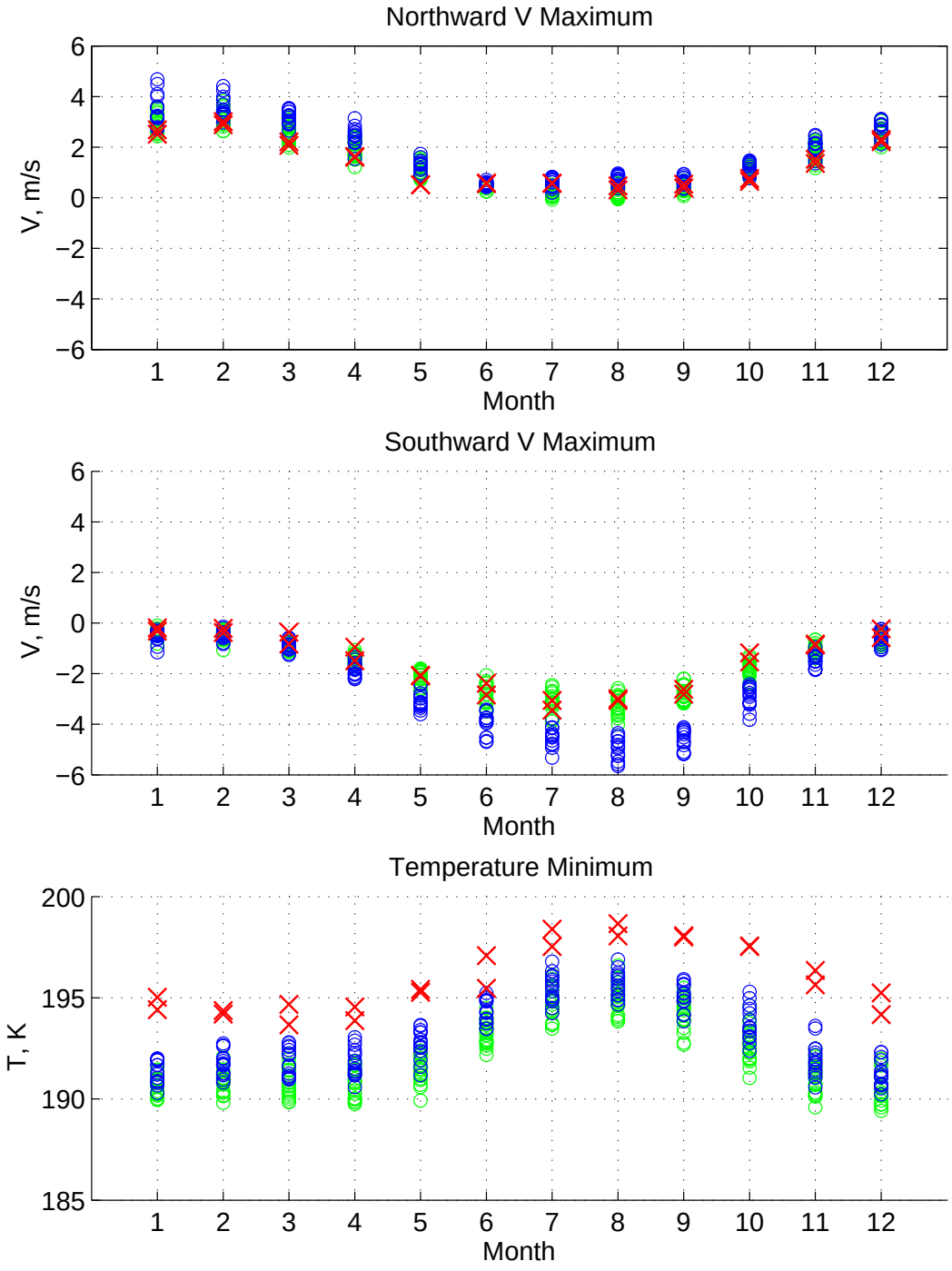

Figure 2.7: As for Figure 2.2, but for the tropical upper tropospheric zonal mean meridional wind maximum, v (m s^{-1}), top and center panels. Lower panel, temperature of tropical tropopause temperature minimum (K).

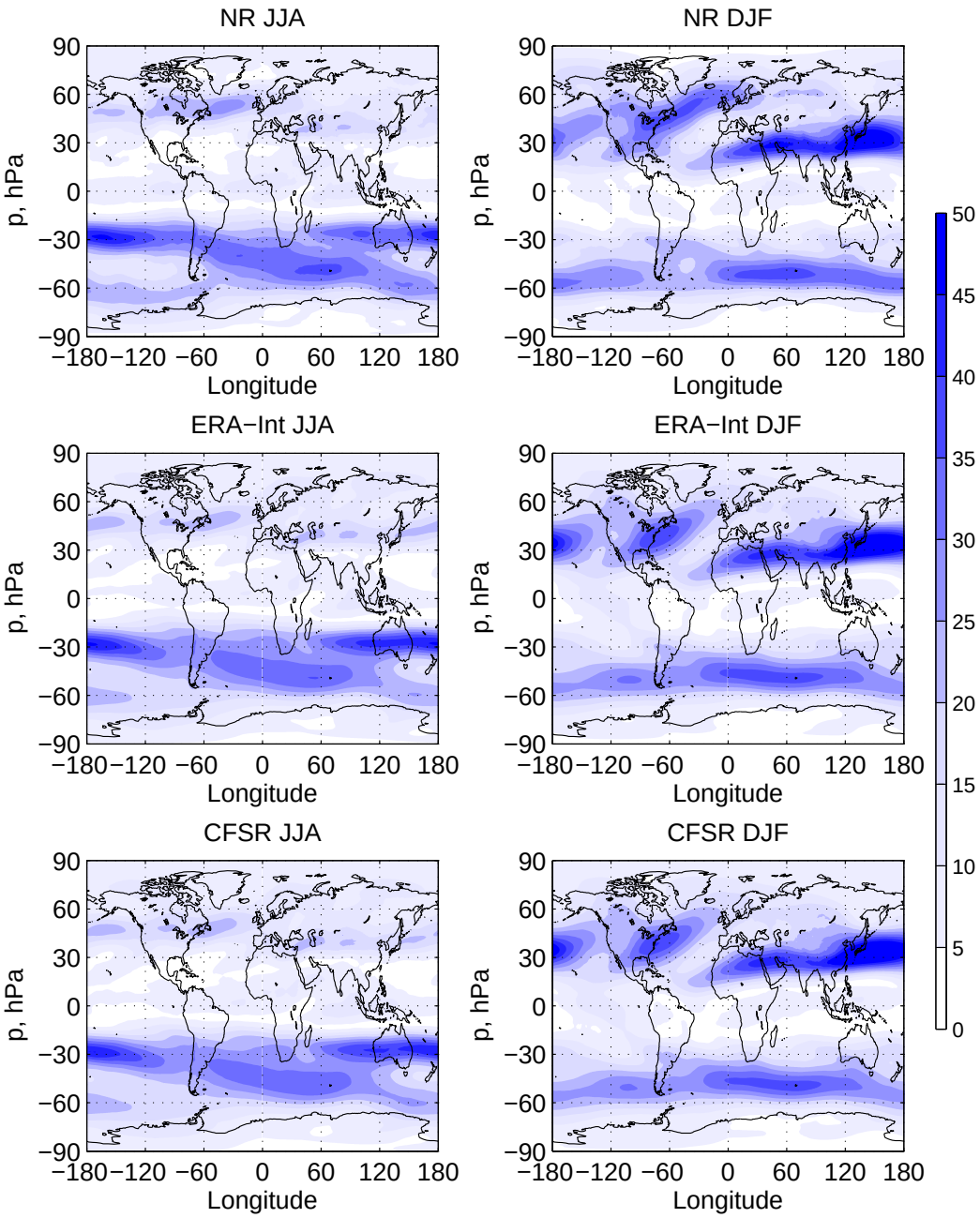

Figure 2.8: Multi-year seasonal mean horizontal wind speed at 300 hPa, $\mathrm{m\,s^{-1}}$.

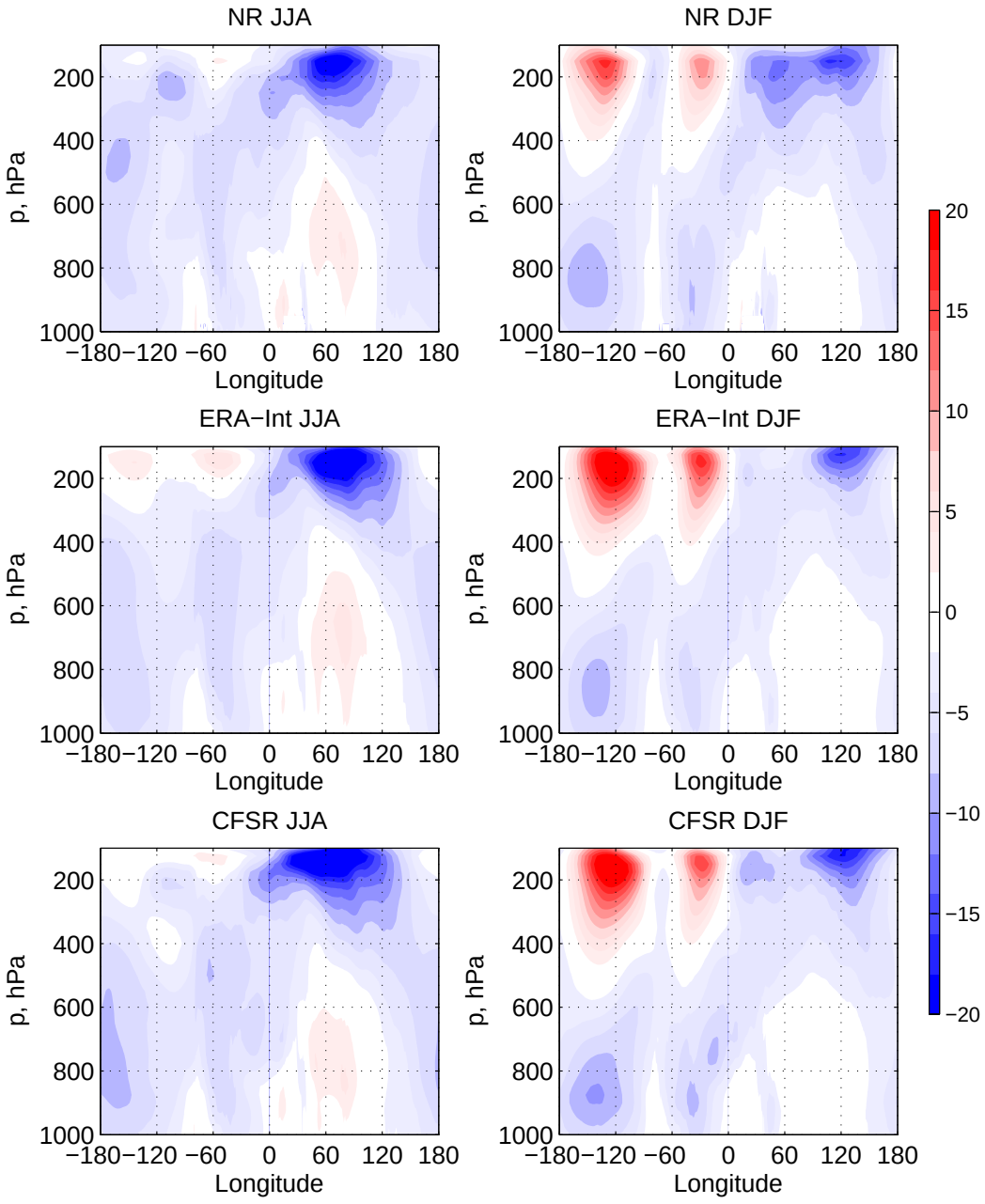

Figure 2.9: Multi-year seasonal mean zonal wind averaged between 10N and 10S, $\mathrm{m\,s^{-1}}$.

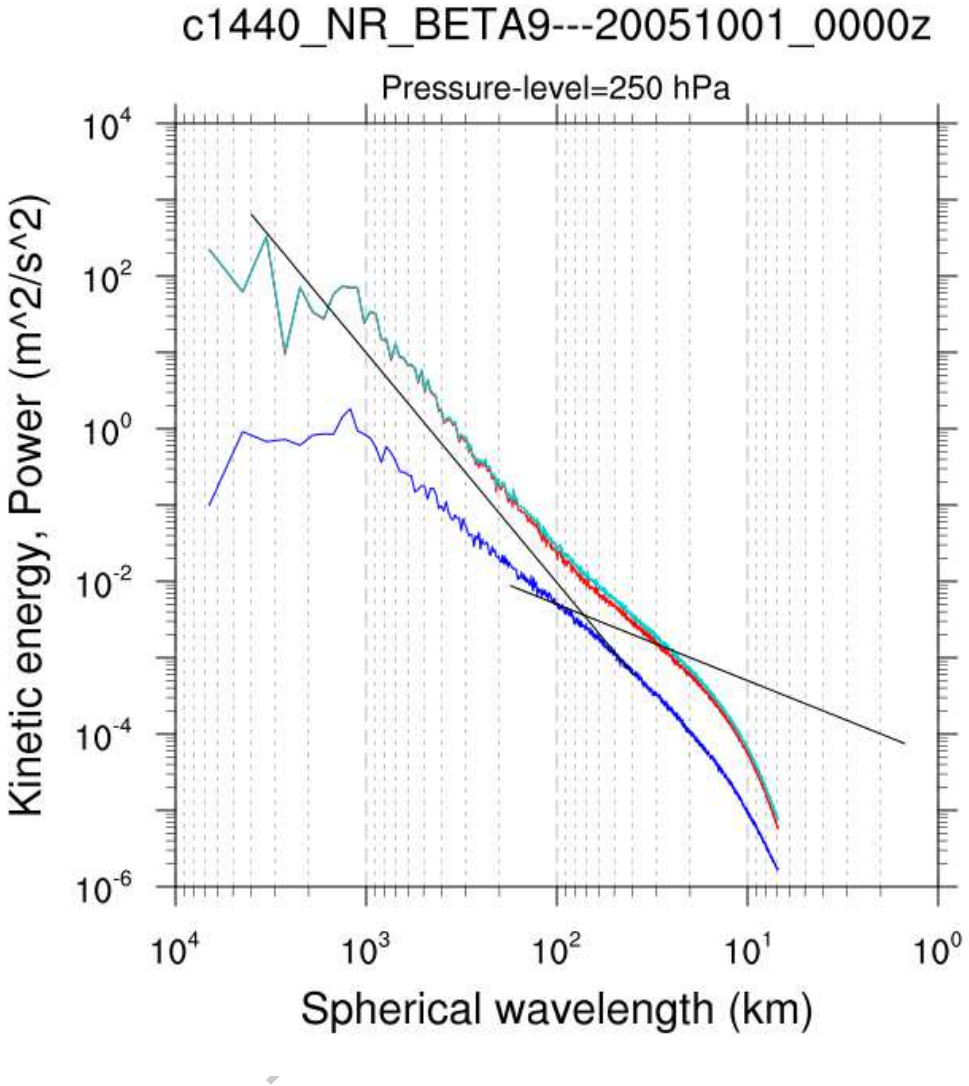

Figure 2.10: Power spectra of kinetic energy on the 250 hPa level. Rotational energy, red line; divergent energy, blue line; total energy, green line. Black lines indicate -3 and -5/3 slope lines.

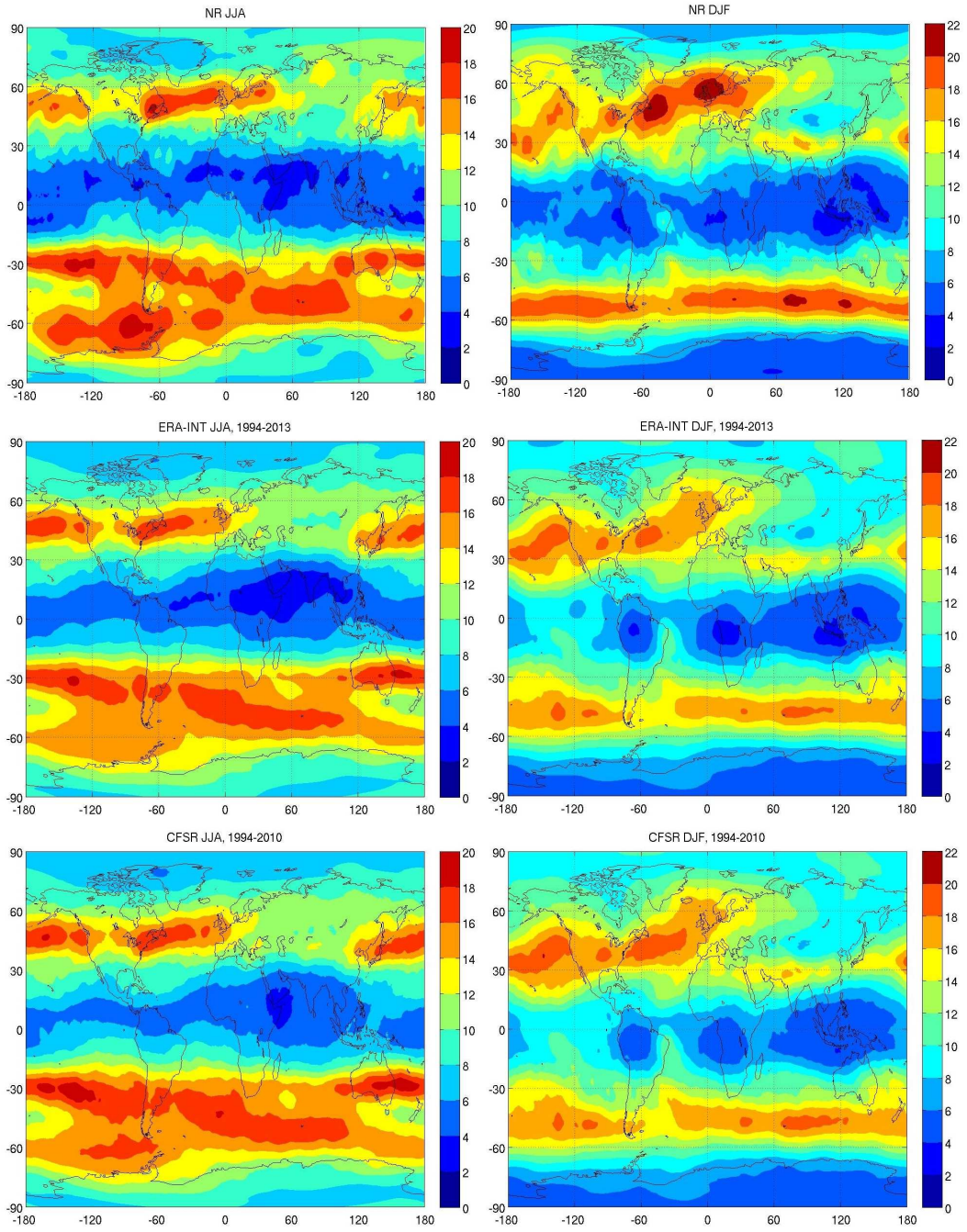

Figure 2.11: Multi-year seasonal standard deviation of 200 hPa meridional wind, $\mathrm{m\,s^{-1}}$.

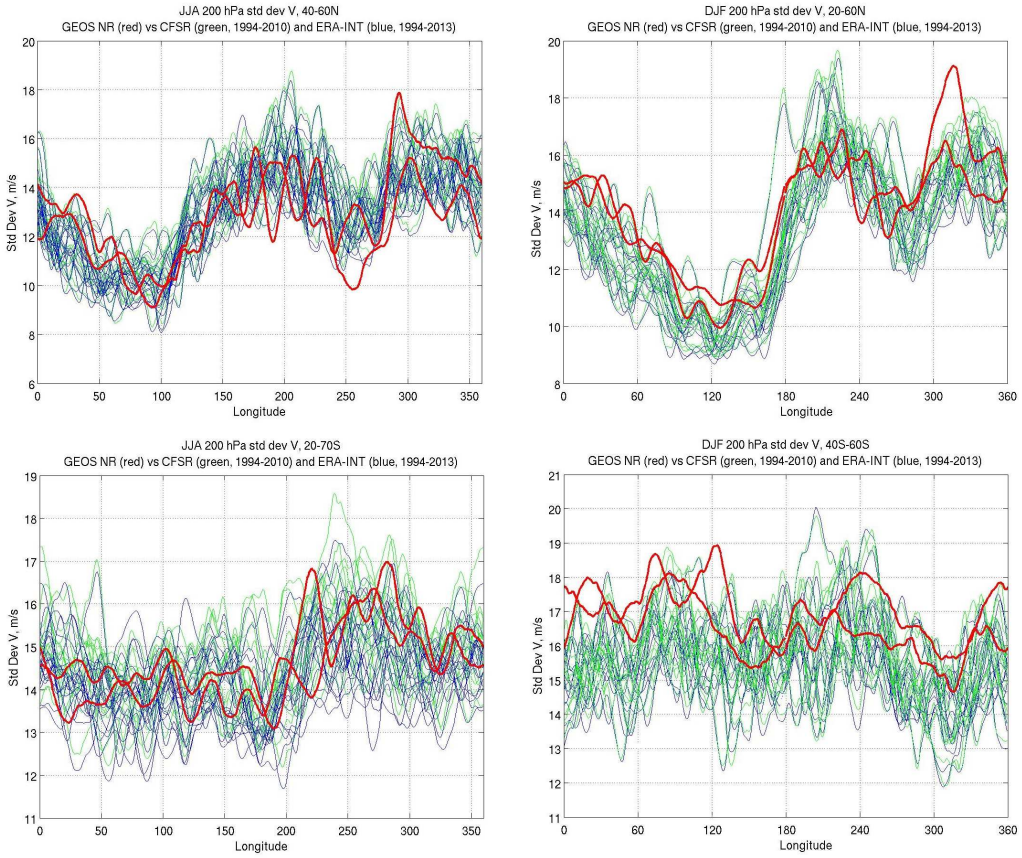

Figure 2.12: Individual seasonal standard deviation of 200 hPa meridional wind along latitudinal bands, $\mathrm{m\,s^{-1}}$. Blue lines, ERA-I (1994-2013); green lines, CFSR (1994-2010); red lines, G5NR. Top left, JJA from 40N-60N; top right, DJF from 20N-60N; bottom left, JJA from 20S-70S; bottom right, 40S-60S.

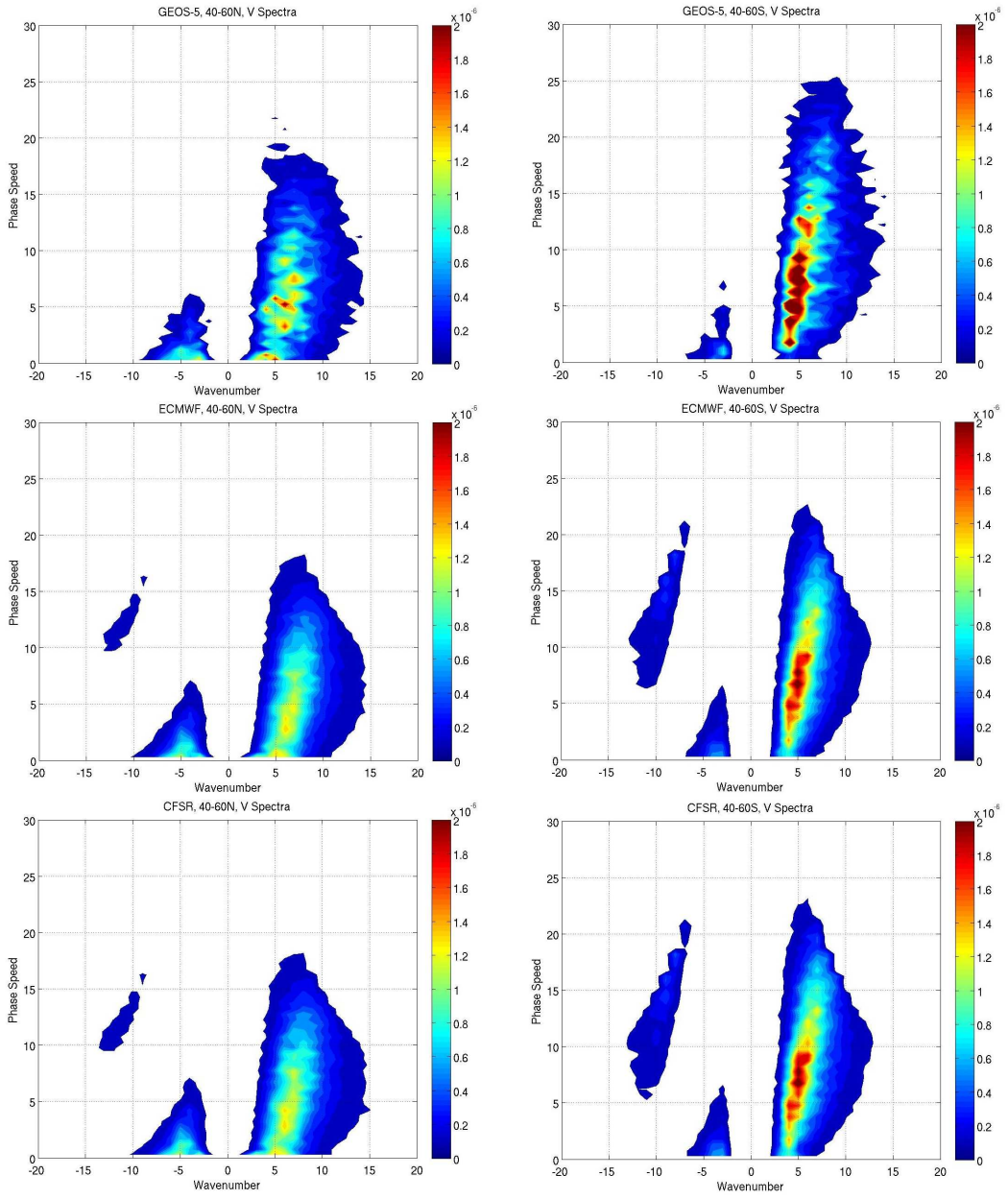

Figure 2.13: Phase-spectra decomposition of 200 hPa meridional wind, phase speed in $\mathrm{m\,s^{-1}}$, contours of power ($\mathrm{m^2 s^{-2}}$). Positive wavenumbers indicate eastward progression, negative wavenumbers indicate westward progression. Left panels, 40N-60N; right panels 40S-60S. Top panels, G5NR; center panels, ERA-I (1994-2013); lower panels, CFSR (1994-2010).

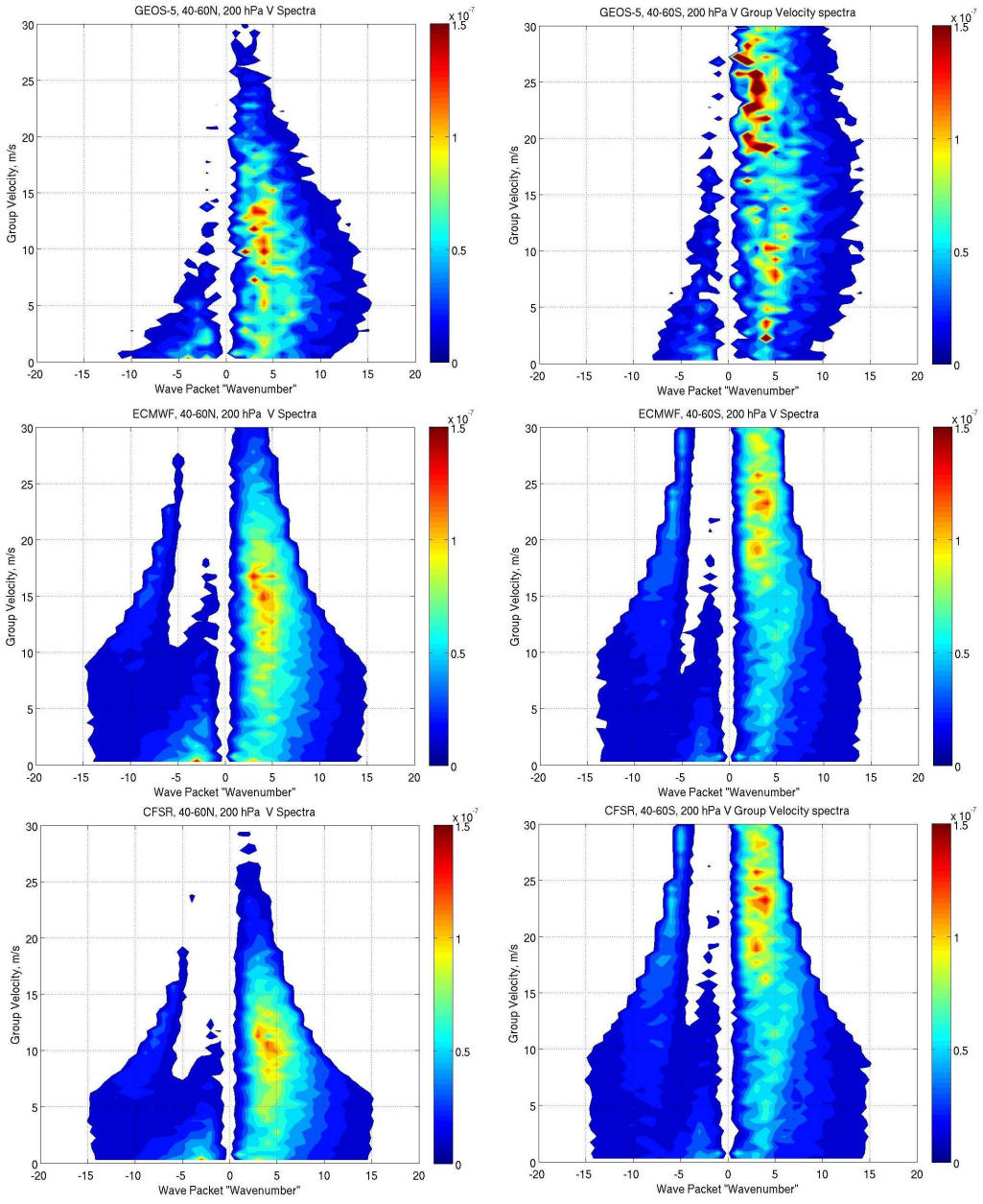

Figure 2.14: Phase-spectra decomposition of wave packets of 200 hPa meridional wind, contours of power (m^2s^{-2}). Wavenumbers indicate 'wavenumber' of wave packet, not wavenumbers of component waves. Positive wavenumbers indicate eastward progression, negative wavenumbers indicate westward progression. Left panels, 40N-60N; right panels 40S-60S. Top panels, G5NR; center panels, ERA-I (1994-2013); lower panels, CFSR (1994-2010).

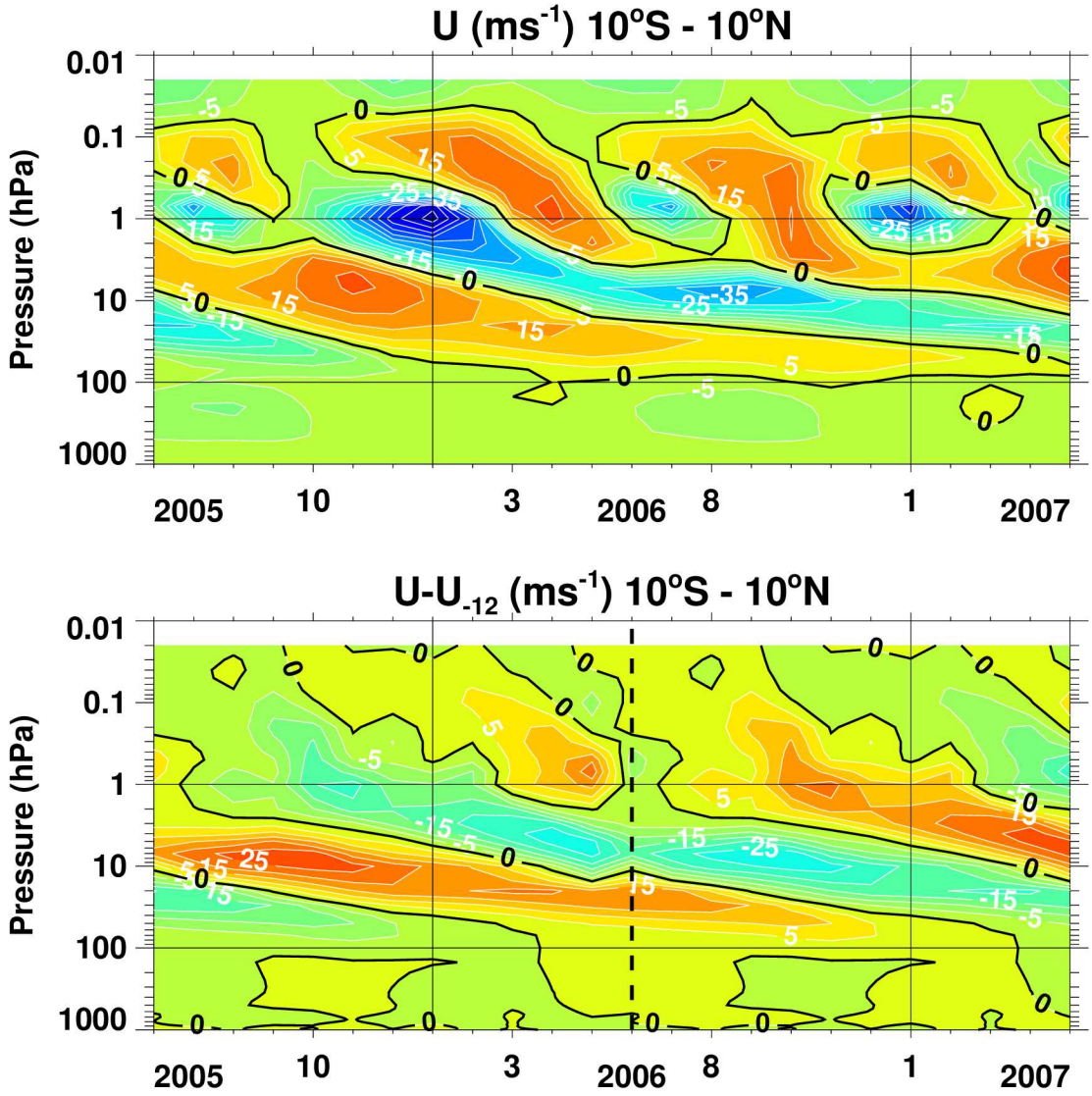

Figure 2.15: Top panel: G5NR monthly averaged zonal wind component ($\mathrm{m\,s^{-1}}$, contour interval: 5 $\mathrm{m\,s^{-1}}$), averaged zonally and between 10°S and 10°N. Bottom panel: Same field as top panel but filtered by differencing the each month of the second year from the first year, and each month of the first year from the second year to remove annual and semi-annual signals.

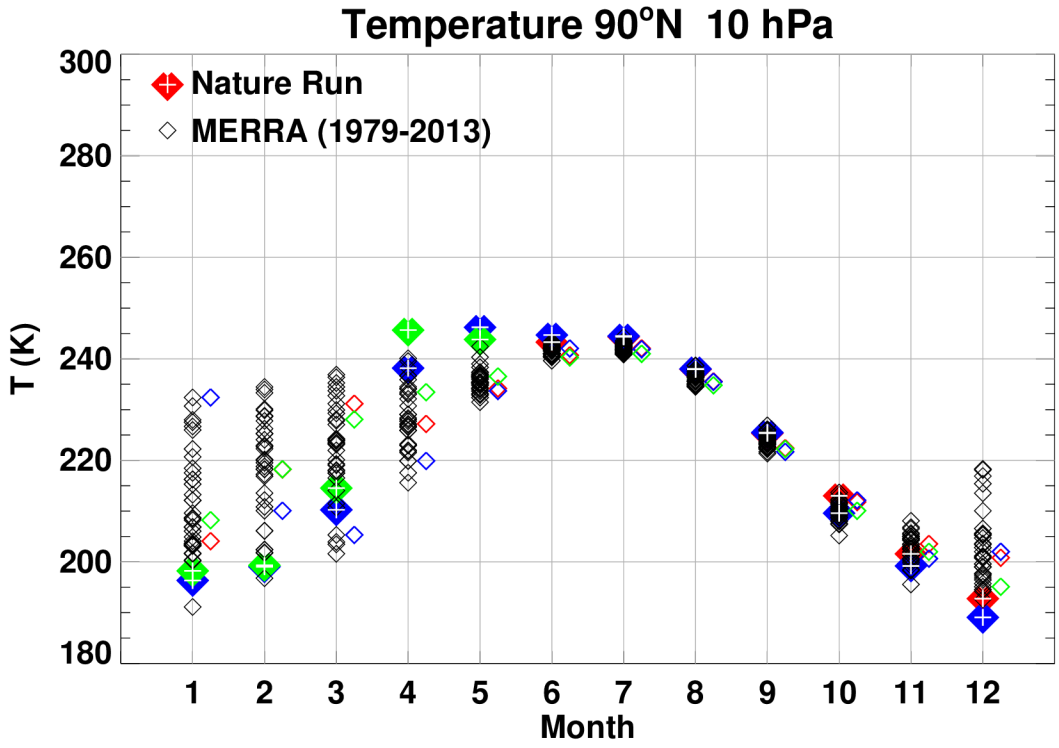

Figure 2.16: Monthly average 10 hPa temperatures at 90°N for the G5NR (filled diamond symbols) and MERRA (unfilled diamond symbols). The colors denote the years 2005 (red), 2006 (blue), and 2007 (green). Note that the symbols for the MERRA 2005–2007 years have been slightly offset in time, colored, and repeated for clarity.

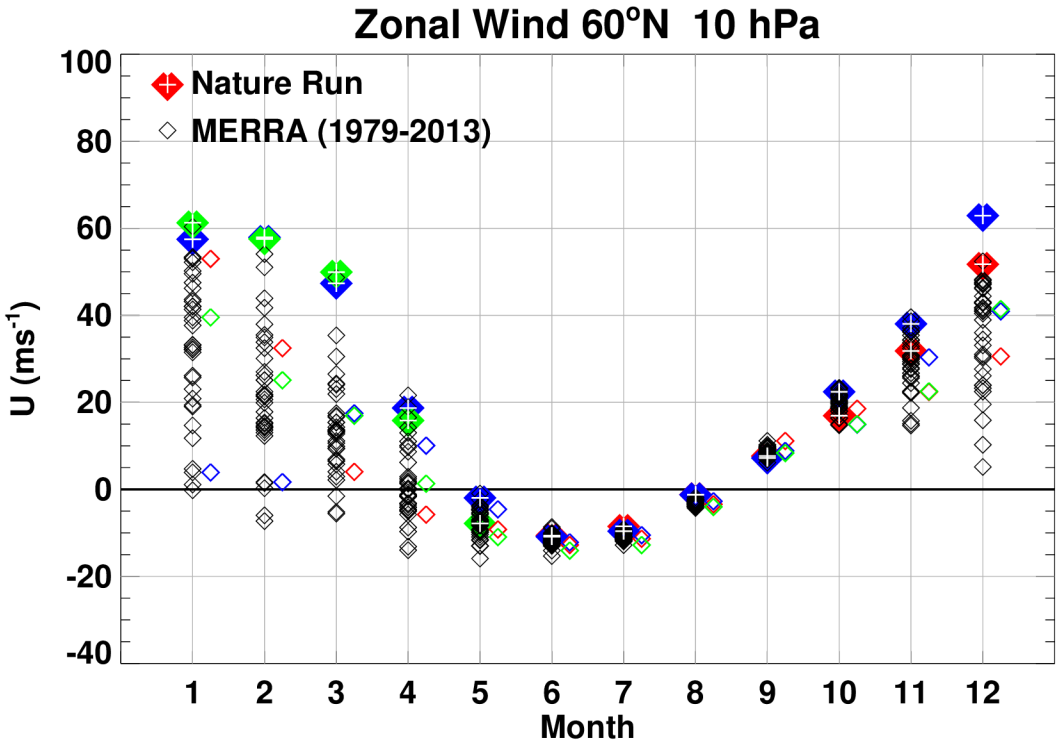

Figure 2.17: Monthly average 10 hPa zonally averaged zonal wind component at 60°N for the G5NR (filled diamond symbols) and MERRA (unfilled diamond symbols). The colors denote the years 2005 (red), 2006 (blue), and 2007 (green). Note that the symbols for the MERRA 2005–2007 years have been slightly offset in time, colored, and repeated for clarity.

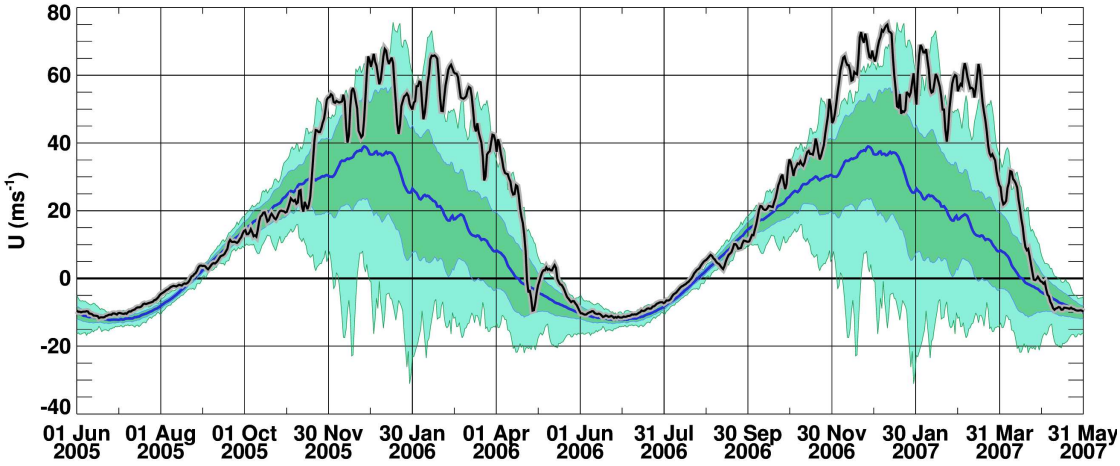

Figure 2.18: Daily (12 UTC) zonally averaged zonal wind at 10 hPa and 60°N for the G5NR (black curve) and the multi-year (1979–2014) averaged MERRA (blue curve). The green filled area denotes plus or minus one standard deviation from the mean, and the boundary of the light blue filled area denotes the extreme values seen by MERRA

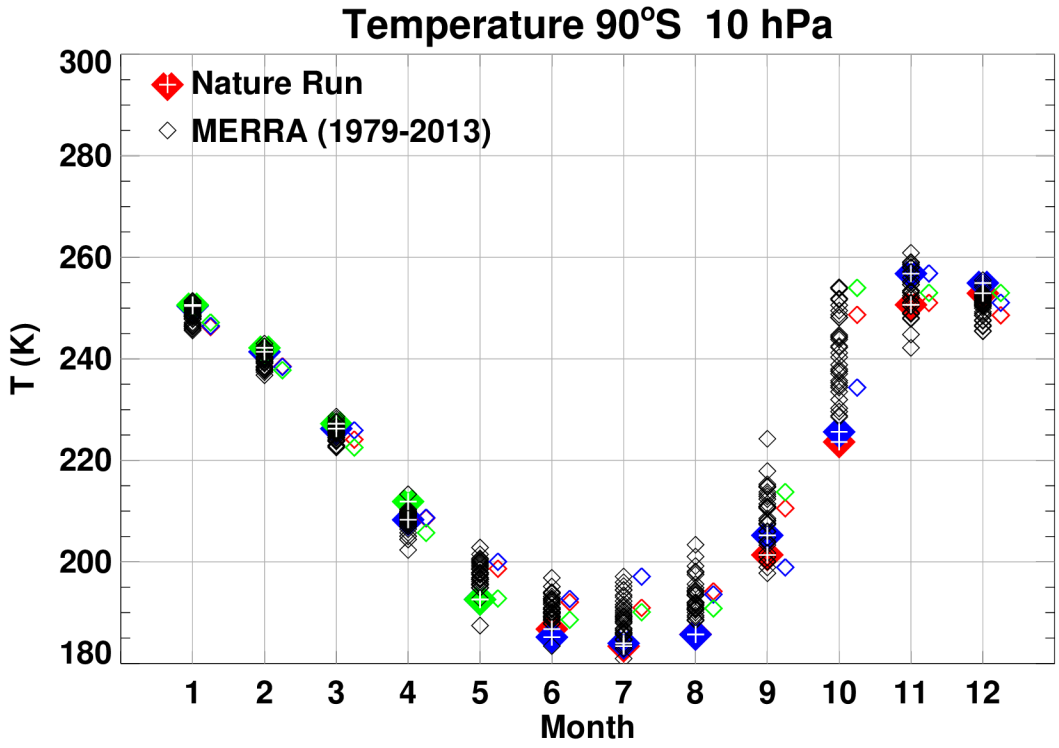

Figure 2.19: As in Figure 2.16 but for 90°S.

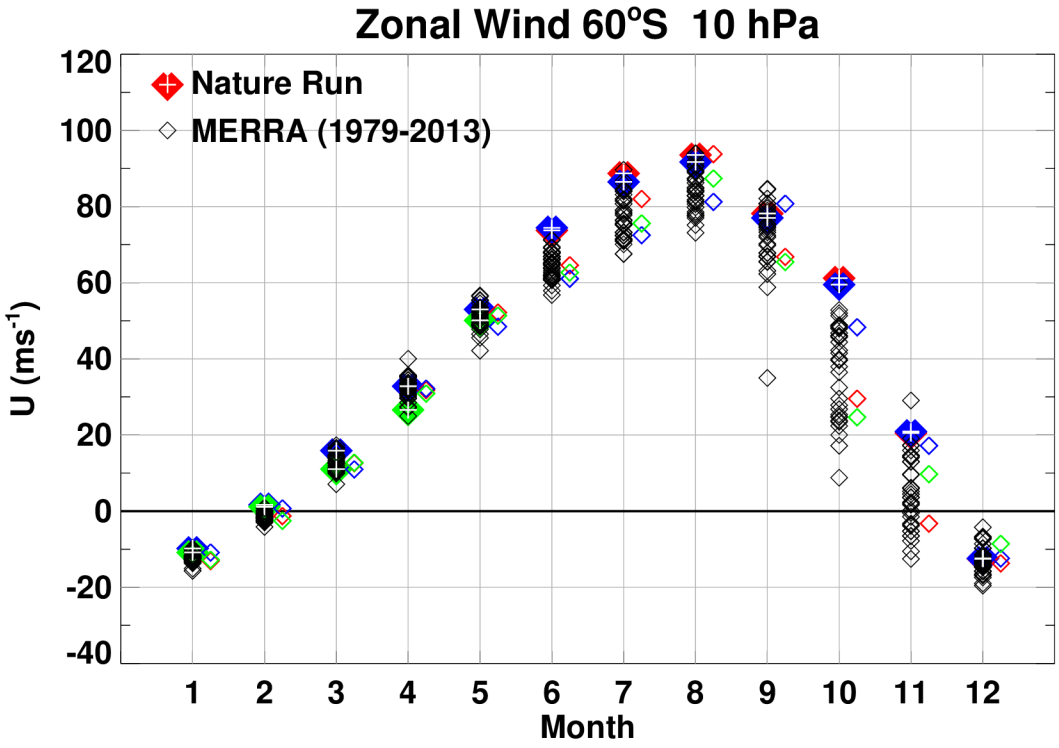

Figure 2.20: As in Figure 2.17 but for 60°S.

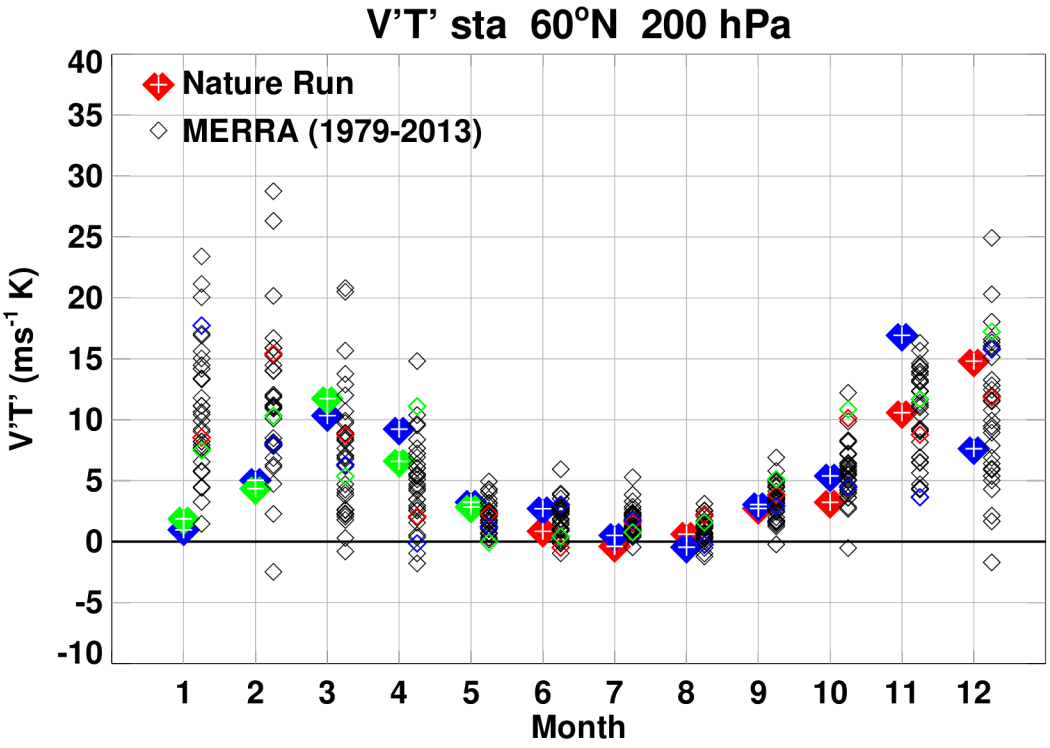

Figure 2.21: Meridional heat flux ($\mathrm{m\,s^{-1}K}$) due to stationary waves at 200 hPa and 60°N. Symbols for G5NR and MERRA as in Figure 2.16.

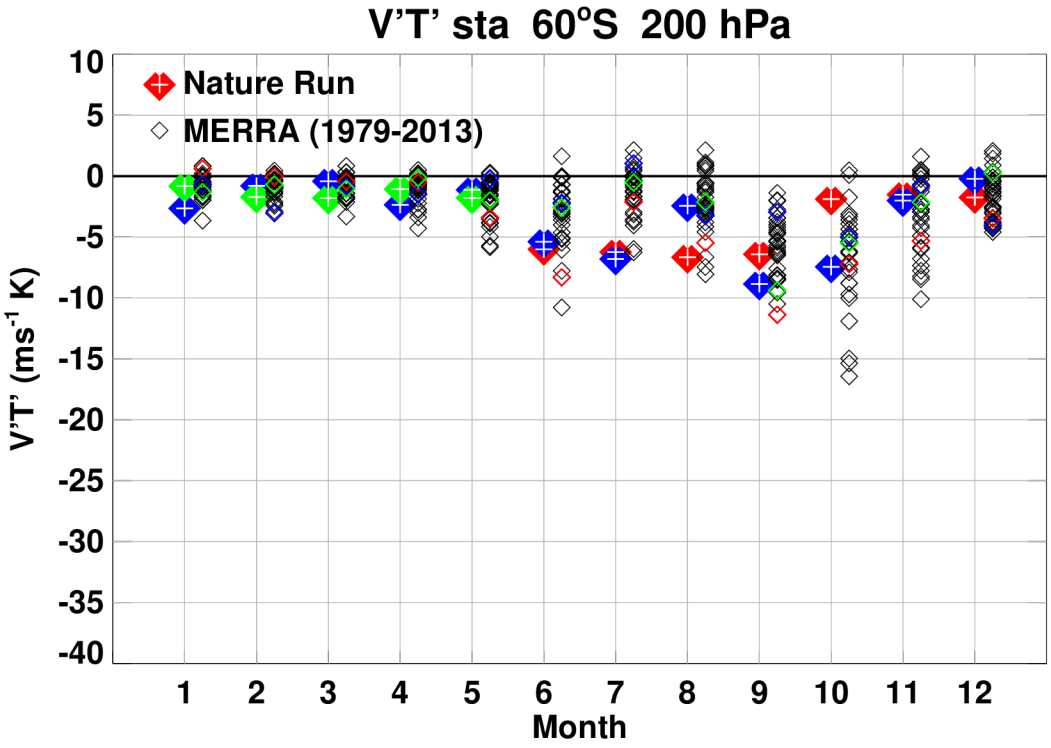

Figure 2.22: Meridional heat flux ($\mathrm{m\,s^{-1}K}$) due to stationary waves at 200 hPa and 60°S. Symbols for G5NR and MERRA as in Figure 2.16.

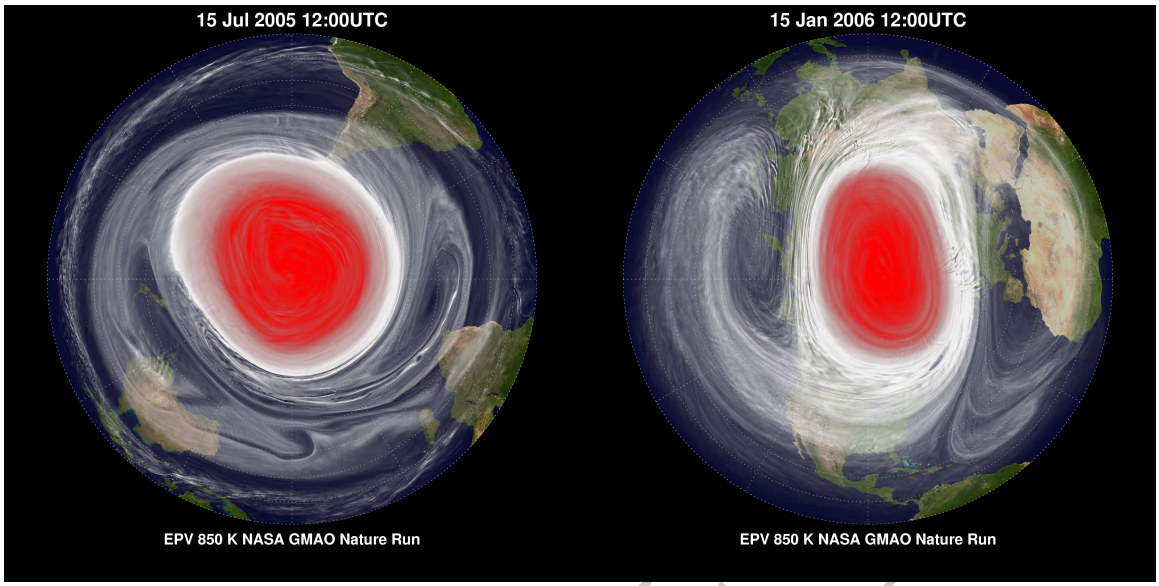

Figure 2.23: G5NR absolute value of EPV for the SH on 15 July 2005, 12 UTC (left) and the NH for 15 January 2006, 12 UTC (right). The EPV has been vertically interpolated to the 850 K potential temperature surface (∼10 hPa) with high values colored red, middle values colored white, and low values transparent.

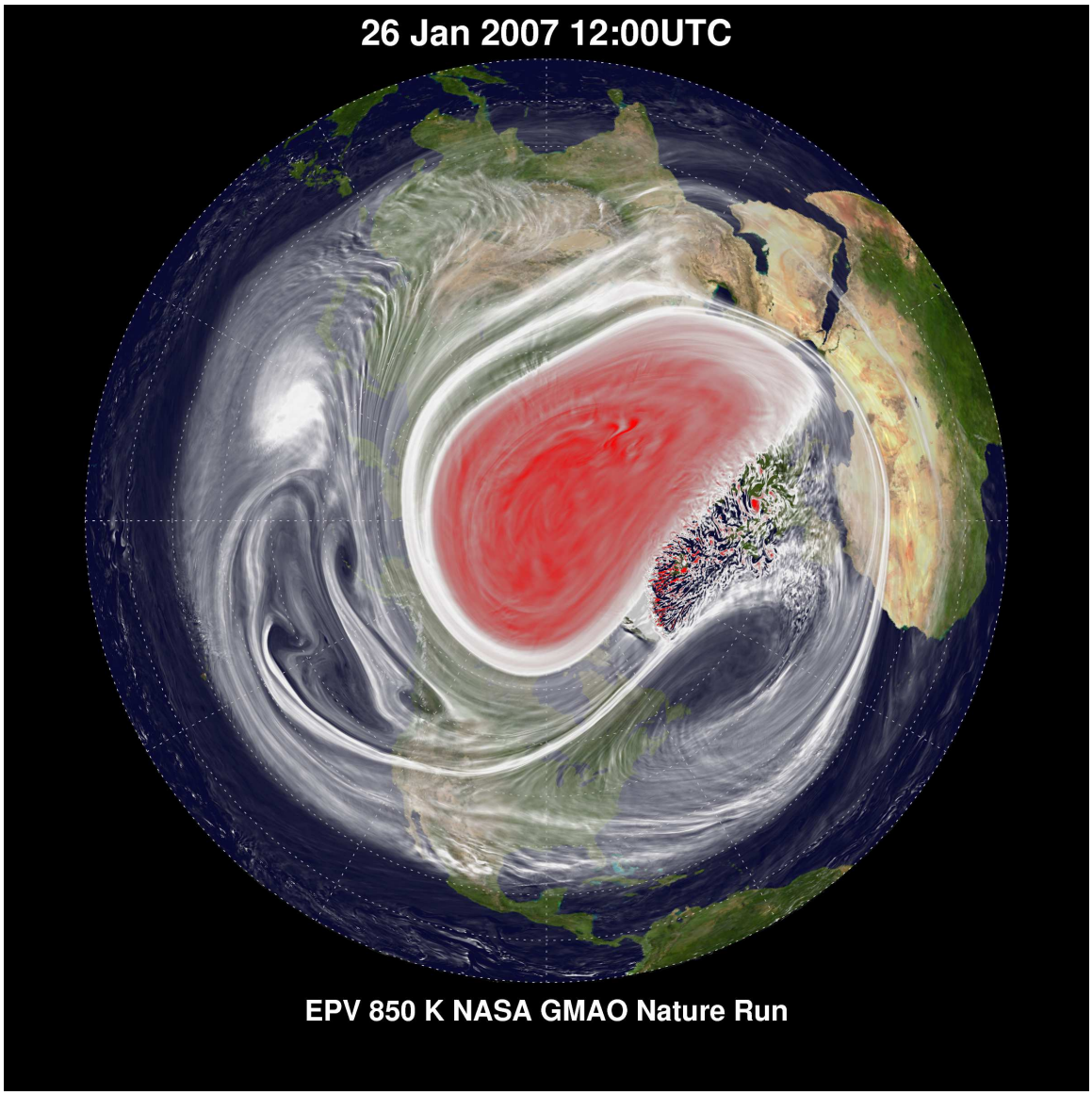

Figure 2.24: G5NR absolute value of EPV for 16 January 2007, 12 UTC. Same scaling as in Figure 2.23

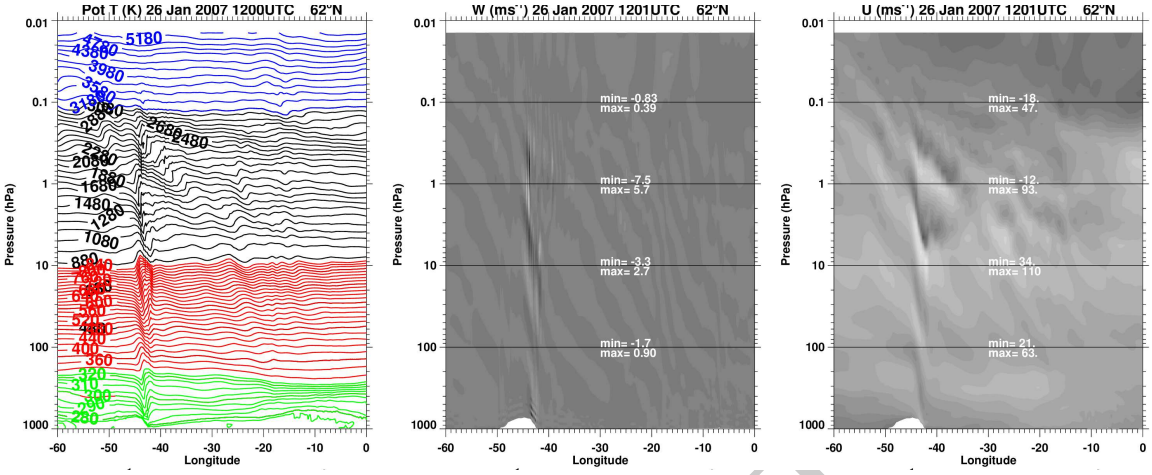

Figure 2.25: Longitude-height cross section over Greenland showing potential temperature (left), vertical velocity (center), and zonal wind component (right) on 26 Jan 2007, 12 UTC. All fields are taken from the G5NR.

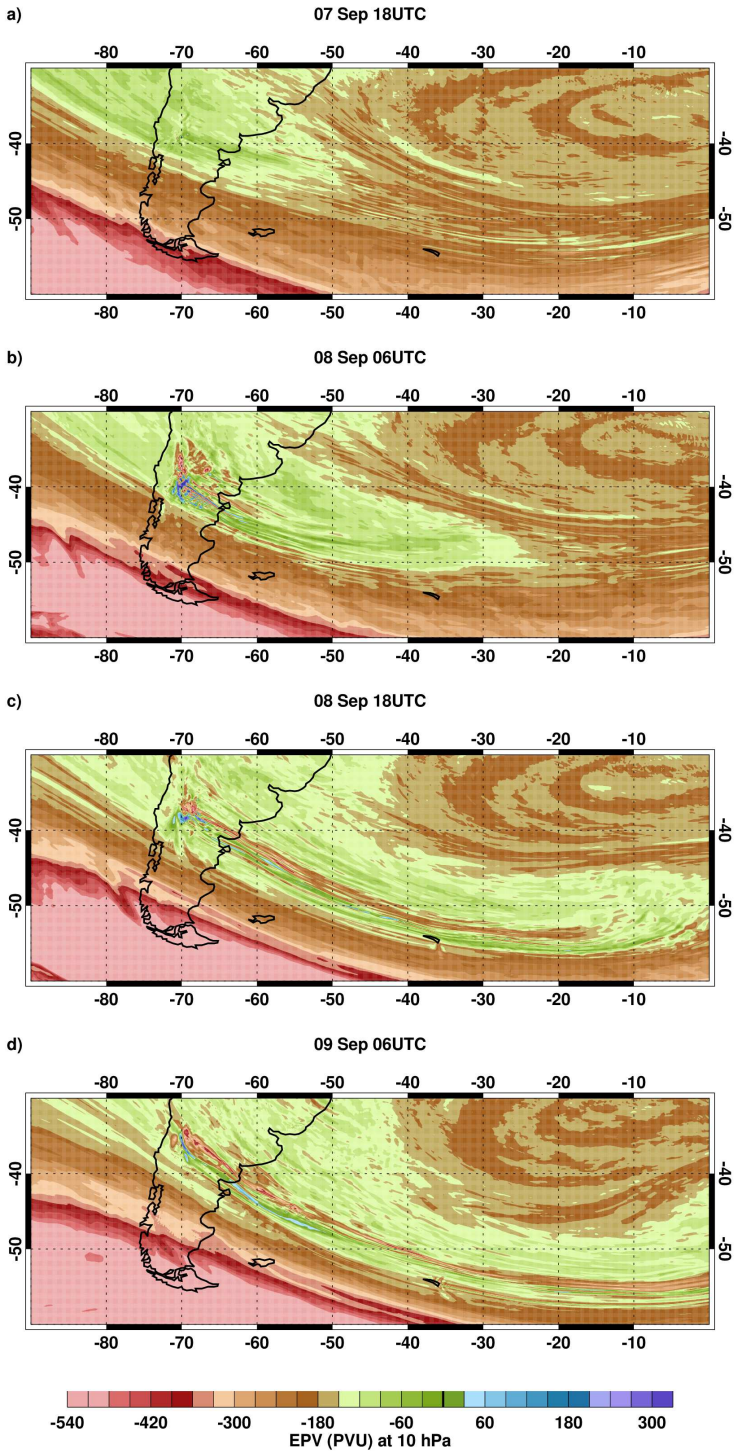

Figure 2.26: G5NR 10 hPa EPV fields during 2005 at 12 hr intervals: a) 7 Sep 18 UTC, b) 8 Sep 06 UTC, c) 8 Sep 18 UTC, and d) 9 Sep 06 UTC.

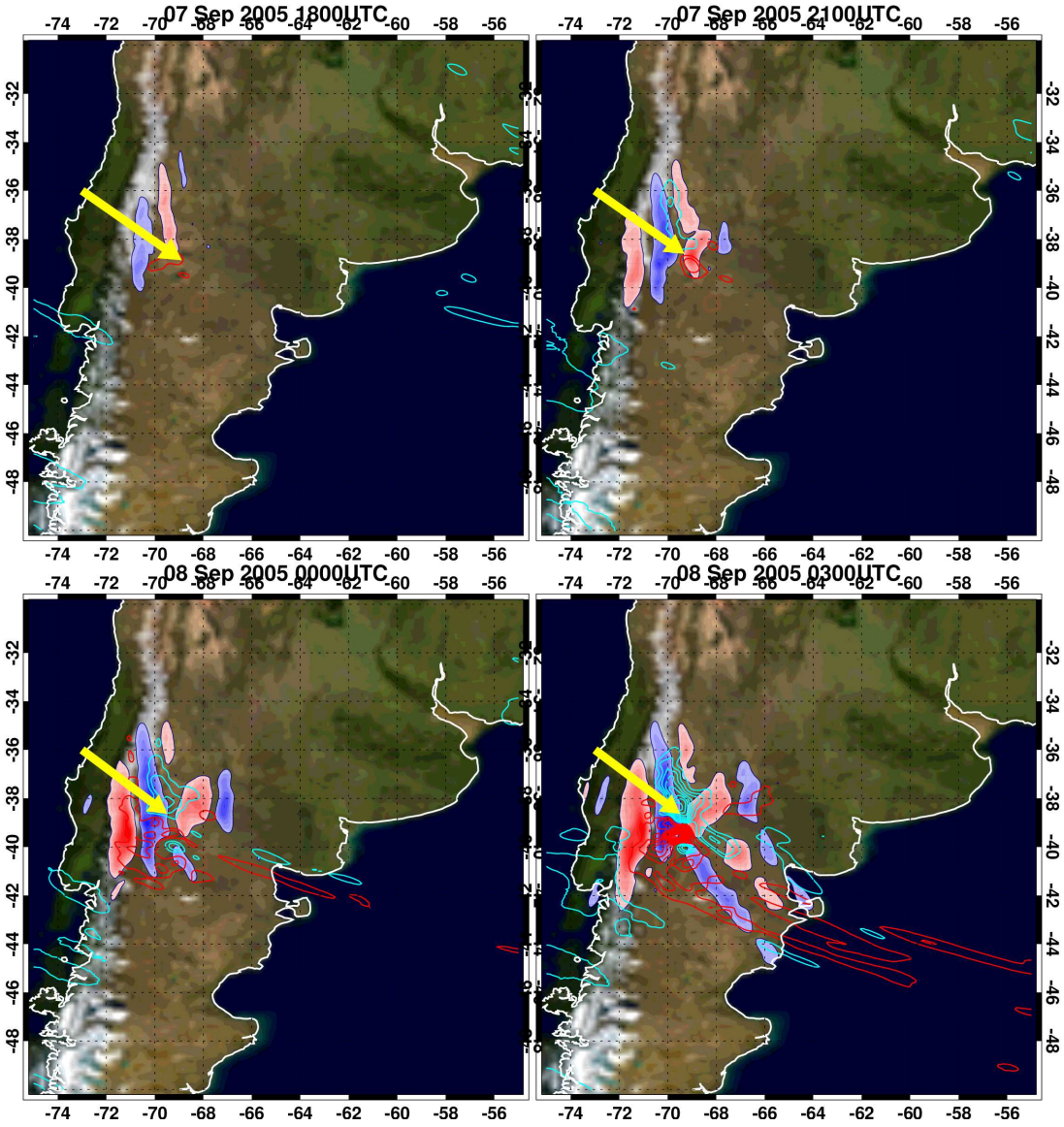

Figure 2.27: G5NR horizontal divergence field (blue and red filled contours) and vorticity field (blue and red unfilled contours) at 10 hPa during 2005 on a) 7 Sep 18 UTC, b) 7 Sep 21 UTC, c) 8 Sep 00 UTC, and d) 8 Sep 03 UTC. The yellow arrow denotes the direction of the prevailing wind throughout the troposphere and lower stratosphere.

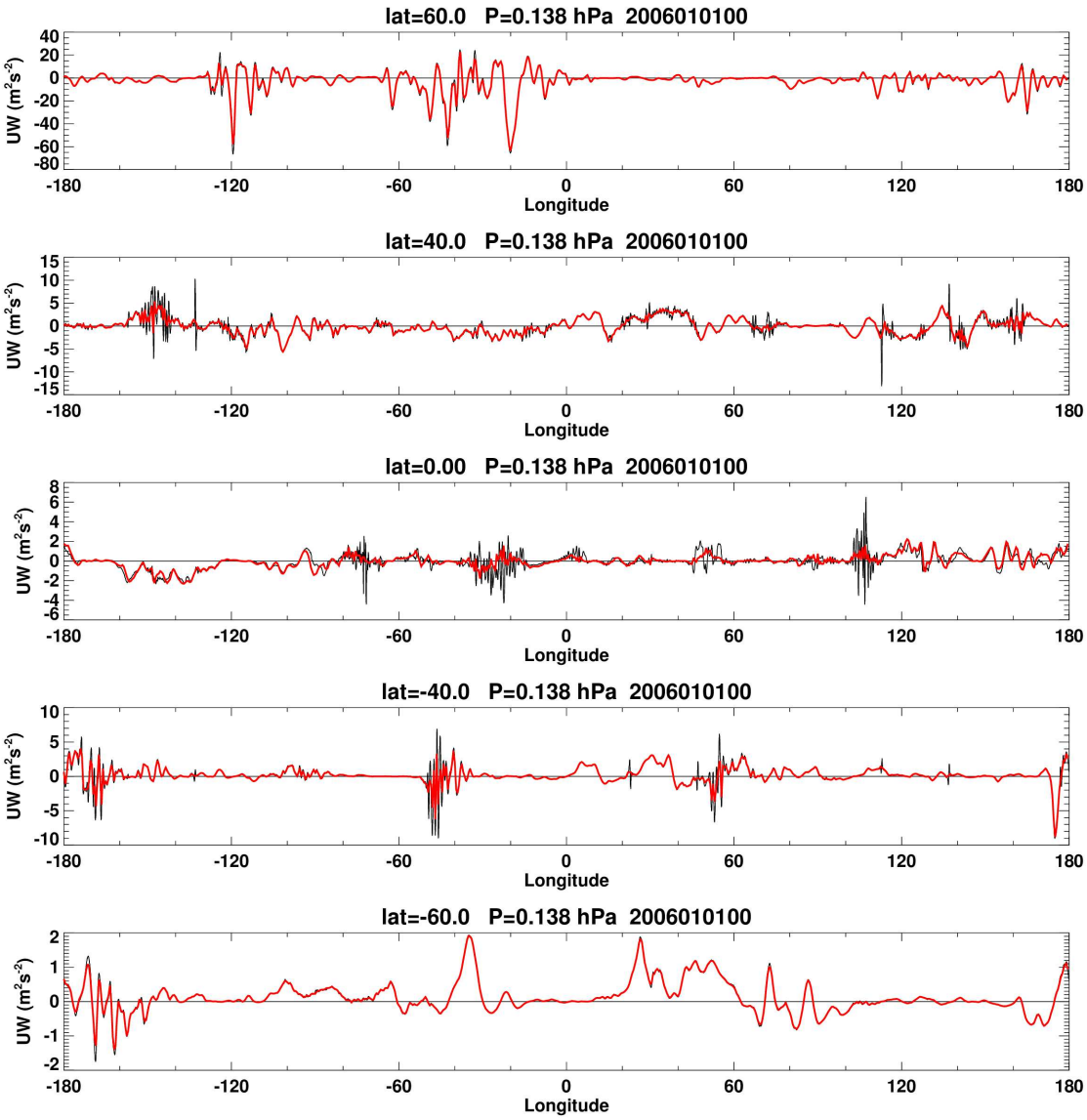

Figure 2.28: Mesospheric (0.138 hPa) GW vertical momentum flux ($\mathrm{m\,s^{-1}}$) on 1 Jan 2006 00 UTC for calculations using the full horizontal resolution fields (0.0625°, black curves) and reduced grid saved fields (0.5°, red curves). Note the different vertical scales on each panel.

Chapter 3

Humidity and Precipitation

Andrea Molod, Min-Jeong Kim, Jyothi Nattala, Michael Bosilovich, Siegfried Schubert and Winston Chao

Atmospheric components of the G5NR hydrological cycle are examined here in comparison with various observationally based estimates. The analysis includes an assessment of monthly mean vapor, cloud condensate and precipitation, mean surface moisture exchange, and moisture variability at time scales from the diurnal to the seasonal. The G5NR simulation spans 2 years only, and is forced with observed sea surface temperatures, and so the majority of the comparisons to follow will assess the climate of the G5NR against observations from the same June 2005–August 2007 time period as the G5NR simulation.

3.1 Verification Data Sources

Verification for the mean state variables, particularly temperature, zonal wind and related fields is provided by the climatology of the Modern-Era Retrospective Analysis for Research and Applications (MERRA, Rienecker et al., 2011). MERRA has two primary objectives: to place observations from NASA's Earth Observing System satellites into a climate context and to improve upon the hydrologic cycle represented in earlier generations of reanalyses. It covers 1979-present with ongoing reanalyses at 0.5° resolution with 72 vertical levels.

ERA-Interim (ERA-I, Dee et al., 2011) is used for a second estimate of model-dependent fields, including humidity, meridional wind and related fields at a resolution of approximately 0.7° and

61 levels. It is a reanalysis by ECMWF currently produced from 1979 onwards using the ECMWF forecast model and is intended to bridge from the earlier ERA-40 reanalysis to a future project that will cover the 20th century.

One of observational estimates for total precipitation is from the Global Precipitation Climatology Project (GPCP) satellite-gauge precipitation product of Huffman et al. (1995). The precipitation estimate is a combination of microwave satellite data, infrared satellite data, rain gauge analyses, and numerical weather prediction models. The first step of the technique used to combine the various data sources is the development of a multi-satellite product using microwave and infrared at low latitudes, and microwave data alone at higher latitudes. The second step is the inclusion of the rain gauge analysis, weighting each field by its inverse relative error variance. Finally, ECMWF numerical model results are used to fill data voids in the combined satellite-gauge estimate. The bias estimated from this technique is 3.7 mm month^{-1}.

The other observational estimate for total precipitation is from the Climate Prediction Center (CPC) Merged Analysis of Precipitation (CMAP) product of Xie and Arkin (1996, 1997). The merging method starts with the creation of a base period (July 1987June 1995) by combining IR, SSM/I, and Microwave Sounding Unit (MSU) satellite data using a maximum likelihood approach. Next, the possible biases are removed by combining the results of the first step with gauge analyses via a blending technique. Over land it is assumed that the combined satellite estimates can represent the structure of the precipitation distribution and that there is no bias in gauge estimates. Over the ocean, the bias remaining after the first step is removed by comparison with the atoll gauge data over the Tropics and by subjective assumption regarding the bias structure over the extratropics.

3.2 Mean Atmospheric Humidity

The specific (QV) and relative humidity (RH) fields from the G5NR and the comparison with MERRA and ERA-I reanalyses are shown in Figures 3.1 and 3.2. The differences in specific humidity between the two reanalyses, particularly in the tropics near the surface, are comparable in magnitude to the differences between the G5NR and either reanalysis, and so the comparison against both is provided here. The general trend is for high G5NR specific humidities as compared to either reanalysis above 700 mb in both JJA and DJF, by up to 1 g kg^{-1}. High specific humidities relative to both reanalyses are also found near 850 mb in the southern hemisphere near 25-30S in both seasons by up to 1 g kg^{-1} relative to MERRA and up to 1.8 g kg^{-1} relative to ERA-I. In these regions these differences are on the order of 15-20% of the total specific humidity. The wet bias is these two regions is also reflected in the comparison between the relative humidity in G5NR and either reanalysis shown in Figure 3.2. In in the tropics near 900 mb, the G5NR is dry with respect to MERRA and wet with respect to ERA-I, and at the surface is dry with respect to both reanalyses, more so with respect to ERA-I. The difference between the two reanalyses here makes it difficult to attribute these differences to a bias in the G5NR humidity. The relative humidity field additionally shows a wet bias near 200 mb of up to 30% RH in both seasons and a dry bias near 300-400 mb of up to 10% RH, accentuated at higher latitudes.

The comparison between the G5NR total precipitable water (TPW) and the estimate from SRB is presented in Figure 3.3 for DJF (panels a, c, e) and JJA (panels b, d, f). This comparison provides an assessment of model low level moisture bias in the region where the reanalyses provide different estimates and cannot be used for this purpose. The G5NR TPW is biased high by up to 0.5 mm (out of approximately 6 mm) in DJF in the region of the south pacific convergence zone, and high by up to 0.5 mm throughout the northern hemisphere tropics and extratropics in JJA.

3.3 Cloud Condensate

Zonal means of the annual mean G5NR cloud ice and cloud water are shown in Figures 3.4 and 3.5 in comparison with the climatology of the CloudSat based estimates of Li et al. (2012) and Li et al. (2013), respectively. Figure 3.4 shows general agreement between the G5NR and the CloudSat non precipitating cloud ice in terms of altitude and latitudinal distribution, but shows that the G5NR cloud ice is substantially overestimated (by up to 10 mg kg^{-1}, a factor of 2) near 300 mb in the tropics. The CloudSat cloud water estimate is considered less accurate than the cloud ice estimate (Li et al., 2013), so the differences may not all be G5NR bias, but the G5NR cloud water estimate shows substantial disagreement with the CloudSat non precipitating cloud water. G5NR cloud water shows the same general altitude and latitude distribution, but is higher than CloudSat almost everywhere by almost a factor of 2.

3.4 Second Moments of Total Water

As part of the standard output of the G5NR (da Silva et al., 2014), a suite of second moments were computed at native resolution and aggregated to approximately 0.5^o resolution. These fields, along with the 0.5^o resolution first moments, can be used to compute 0.5^o subgrid scale (SGS) variances resolved by the G5NR. For example, the SGS variance of total water (Q_T, the sum of vapor, cloud ice and cloud liquid) is written: ${\sigma_{Q_T}}^2 = (\ < {Q_T}^2 > - < Q_T > * < Q_T >\ )$, where <> refers to an 0.5^o average. The zonal mean ${\sigma_{Q_T}}^2$ as a function of pressure is shown in Figure 3.6a for JJA. The maximum variance is found near boundary layer cloud tops in the tropics, decreases below perhaps due to smoothing by turbulent motions, and decreases aloft due to the decrease in mean total water. The 0.5^o SGS variance of total water is related to the "critical relative humidity" specified as part of the AGCM moist processes, and for the shape of the probability distribution function used in the GEOS-5 AGCM, can be written as: $RH_c = 1 - \frac{\sigma_{Q_T}}{q^*}$, where q^* is the saturation specific humidity. RH_c is shown in Figure 3.6b, is largest (near 1.0) near the surface in the tropics, and decreases to values of 0.9 towards higher latitudes and towards higher altitudes. RH_c computed in this manner can be used as a validation for the values that are specified in the GEOS-5 AGCM when run at 0.5^o resolution (in MERRA, for example), and can be used to develop a state dependant parameterization. Inset as part of Figure 3.6b is the vertical profile of RH_c used in the GEOS-5 AGCM over the oceans when run at 0.5^o resolution. The profile is characterized by a tanh function, which has a value near 1. at the surface, decreases to a value of 0.93 at approximately 850 mb, and

remains at that value aloft. Although this profile is a simple depiction of the variations in the RH_c computed from the G5NR SGS variance, the basic character and magnitude are well captured by the 0.5^o AGCM.

3.5 Precipitation

General comparisons between the G5NR and observations of large scale features, trends and seasonal variations in precipitation provide a reasonable sense of the ability to simulate convection and atmospheric supersaturation-related rainfall. The observational precipitation datasets chosen for this comparison are from the Global Precipitation Climatology Project (GPCP) estimates of Huffman, due to the extensive raw data coverage over land (section 3.1) and the blending of several different types of data over oceans, and from the Climate Prediction Center (CPC) Merged Analysis of Precipitation (CMAP), which is also a merged gauge-satellite product but which has a different mix of input satellite data (Yin et al., 2004).

Figure 3.7 shows the G5NR precipitation as compared to both GPCP and CMAP in DJF and JJA. Northern winter G5NR precipitation in the tropics is underestimated in the region of the South Pacific Convergence Zone (SPCZ), a region which has been shown (Hurwitz, et al., 2011) to be important for poleward transport of energy in the stratosphere. In addition, the Pacific Intratropical Convergence Zone (ITCZ) precipitation is overestimated by up to 5 mm day^{-1} relative to both GPCP and CMAP estimates. The central feature of the oceanic precipitation in the G5NR in JJA is the "double ITCZ" structure, common to many high resolution AGCM simulations (REFS), and the apparant shift eastward of the region of maximum precipitation in the warm pool, common to many AGCMs at any resolution (REFS).

Land-only precipitation is shown in Figure 3.8 using a different color shading to accentuate the behavior over land. There is generally good pattern agreement between the G5NR and both the GPCP and CMAP precipitation in DJF, although the G5NR precipitation is low over central South America by up to 4 mm day^{-1} relative to both observational estimates. The G5NR precipitation is low relative to GPCP but in good agreement with CMAP over Europe. In addition, the DJF precipitation is overestimated over the Andes. In JJA, the magnitude of the precipitation in the G5NR is in generally good agreement with both observational estimates, but there are shifts in pattern in several locations. The Asian monsoon precipitation is shifted to the north in the G5NR, resulting in an overestimate in the northern monsoon regions and an underestimate in the southern monsoon region. This is tied to an overestimate of precipitation over the slopes of the Tibetan Plateau. In North America in JJA there is a general trend towards overestimating precipitation in the north and west, and underestimating precipitation in the south and east.

3.6 NEWS Global and Regional Water Budgets

The NASA Energy and Water Cycle (NEWS) Program has produced a climatology of the water and energy budget data derived from EOS satellite data, retrieved level 4 data products and reanalyses (limited usage to variables and places where observed systems are weak) (Rodell et al. 2014, L'Cuyer et al. 2014). The data providers also included uncertainty estimates. Using an optimization routine and the uncertainty estimates, the water and energy cycle data were balanced constrained by known physical conditions and relationships. We present both versions for completeness and a better assessment of uncertainty. The observed data are generally available from 2001-2010, to approximate the early 21st century climate. The constrained balance of the observations can allow some reasoning of long term global and regional bias in the G5NR.

Figure 3.9 shows the water cycle of the G5NR compared to the NEWS assessment of observations. Over the ocean, too strong water cycling occurs with excessive precipitation and evaporation, in the G5NR. In addition, too much water is transported from ocean to land leading to increased continental precipitation and runoff. Clear biases in the G5NR water cycle are apparent. Yet, land evaporation is very close to the NEWS estimate, despite the overestimate of precipitation. One consideration would be that the evaporation may have regional biases that cancel in the global average.

NEWS processed regions concurrently with the global data. The regions consist of major continents and ocean basins, though some smaller regions have also been considered, producing mean annual cycles of all water budget terms in each (Figure 3.10). In North America, cold season precipitation in the G5NR matches closely the NEWS merged data. In warm seasons, the excessive precipitation is generally matched by surface runoff. Evaporation is close to the merged data in magnitude; however, there may be a subtle phase shift of the surface evaporation. Eurasia generally follows the seasonal cycle of North America, though the water storage amplitude is somewhat damped. In Africa, evaporation is underestimated in the early part of the year, and precipitation is overestimated later in the year, leading to runoff overestimates all year. The comparison of South American precipitation is reasonable when integrated for the continent. However, sub-continental biases do seem to be canceling out (see Figure 3.7). Mainland Australia experiences an overestimate of their wet season precipitation, and also noticeable phase shift of the G5NR's annual cycle of the water budget. The Oceana continent (or Australasian and Indonesian Islands of the tropical west Pacific) systematically both receives and produces too much precipitation. When taken as a whole, the global land evaporation compares well with NEWS estimates, while precipitation and runoff are biased high (the global land annual cycle tracks closely with North America and Eurasia).

3.7 NEWS Global Energy Budget

In the global sense, there are many flux terms that are simulated within reasonable range to the NEWS energy budget results (Figure 3.11). There seems to be too much shortwave radiation

reflected at the top of the atmosphere (though the G5NR OLR is close to the NEWS OLR). This deficit in the energy seems to be compensated for in net surface imbalance. The G5NR has 9.4 W m^{-2} net energy leaving the ocean surface to the atmosphere (this term is 6.4 W m^{-2} in the global average). The global estimate from balancing observations is 1W/m2 directed into the surface. The main areas of bias in decreasing importance are the North Atlantic, Indian and South Pacific oceans. While such errors can occur in models, here we document the bias for the G5NR users. Spatial considerations are also very important, for example, the OLR has regional bias that may be important for any individual use of the data (see sections **??** and **??** for specific examples).

3.8 Selected Results on Monsoonal and Diurnal Precipitation Variability

Here we examine the verisimilitude of the precipitation associated with selected tropical wave, monsoonal, and diurnal variability produced in the G5NR for the period June 2005 - July 2006. The results include Hovmöller diagrams of daily means to highlight subseasonal propagation, maps of monthly means to highlight the basic patterns and the seasonal development of the various monsoons and related low-level winds, as well as maps of the mean diurnal cycle of precipitation over North America

Comparisons are made with the high-resolution CMORPH (Joyce et al. 2004) precipitation estimates. The CMORPH or CPC MORPHing technique produces global precipitation analyses at very high spatial and temporal resolution. The technique uses precipitation estimates derived from the passive microwaves aboard the DMSP 13, 14 and 15 (SSMI), the NOAA-15, 16, 17 and 18 (AMSU-B), and AMSR-E and TMI aboard NASA's Aqua and TRMM spacecraft, respectively. We use here fields from the years 2005 and 2006 from an updated CMORPH dataset that has recently been reprocessed and bias corrected by NOAA (Pingping Xie, personal communication) to produce an hourly, 16-year record at a horizontal resolution of 8 km and covering the globe from 60S-60N.

3.8.1 Tropical waves

Figure 3.12 provides an overall view of the tropical wave activity as it is reflected in the daily mean precipitation field averaged between 10S and 10N. Overall the G5NR appears to do a good job of simulating the basic eastward and westward propagating tropical systems (e.g., easterly waves). Several things stand out as being somewhat unrealistic. The very regular and strong eastward propagation simulated over the Pacific appears to be associated with overly active Kelvin waves propagating eastward from the Pacific warm pool. On the other hand, there is insufficient eastward propagation from the Indian Ocean into the warm pool, with the latter deficiency appearing to contribute to an underestimate of the warm pool precipitation and northward propagation (linked to the eastward propagation) of precipitation associated with Indian monsoon breaks and resurgences. Some evidence for the latter is shown in Figure 3.13, which highlights the northward propagation

that often occurs over the Indian monsoon region at subseasonal time scales but is absent in the G5NR.

3.8.2 South and East Asia

Figure 3.14 shows the monthly (April - July 2006) evolution of the precipitation and 850mb winds with the focus on the south and east Asian monsoon regions. The model reproduces the basic evolution quite well, including the monsoon onset over India. Other key features include the northward movement of the precipitation over Australasia, and the persistent (but slowly northward moving) east-west rain band known as the Meiyu front over eastern China, Taiwan, Korea (Changma front) and Japan (Baiu front). The latter northward movement is highlighted in Figure 3.15, which shows the observed and simulated northward propagation of the precipitation during June and early July that is quite prominent in the simulation though it is less regular in the observations during that year. A key component of the monsoon development over southern Asia is the seasonal evolution of the Somali jet. Figure 3.16 shows that the model does a very credible job in reproducing the observed timing of the initial development, magnitude and overall horizontal structure of the jet, keeping in mind (as discussed above) that there is likely some unforced (by SST) interannual variability in the jet development.

3.8.3 Africa and South America

The development of the west African monsoon rains are tied to seasonal northward progression of the Atlantic ITCZ and the associated southwesterly winds that bring moisture into western Africa in late June and move back south by October. Figure 3.17 shows that the model captures that development quite well, including the abundant precipitation that falls over much of central Africa from July into September. The observations show a much stronger land-sea contrast than the simulation with an abrupt drop in precipitation in going from ocean to land in western Africa that is not apparent in the simulation. Whether this in part reflects a problem with the CMORPH data is unclear and requires further investigation. Figure 3.18 shows the evolution of the low level winds, highlighting the development of the southwesterlies during June and July. The development in the model is much stronger than the observed (MERRA) with the southwesterlies near 10N already well developed and extending into Africa by July. This contrasts with the rather weak southwesterlies over the tropical Atlantic during that time from MERRA and these do not extend into Africa.

The evolution of the South American summer monsoon is characterized by an onset during October, followed by a 3-month mature phase, and demise in April. During the peak of the monsoon, convection over the southern part of the Amazon Basin contributes to the establishment of the Bolivian high: an anticyclone that is responsible for the near-surface easterly moisture flux into the tropical and subtropical Andes over northern Brazil, as well as the southward extension of the moisture fluxes into Bolivia and regions further south. Figure 3.19 shows that the model does quite well in reproducing the basic evolution of the monsoonal precipitation, including the onset

of strong precipitation over the Amazon basin in December, and the southward movement of the Atlantic ITCZ precipitation as it impinges on the continent in December and January, though the model appears to rain too much over the Andes. The model also does a remarkably good job of simulating the basic seasonal evolution of the low level winds over the South American continent (Figure 3.20).

3.8.4 North America

Figure 3.21 shows the development of the North American monsoon from June through August of 2005. The observations show the typical seasonal development and northward progression of monsoonal precipitation over the Sierra Madre Occidental along the west coast of Mexico. The simulation shows a realistic placement of the maximum precipitation in that region though perhaps starting somewhat earlier than observed (but again keeping in mind that there is likely substantial year to year variability in that development). Both the model and observations show the signature of an active hurricane season especially in the August precipitation field. The major deficiency in the simulation in this region is the large summer precipitation bias over the eastern Pacific Ocean, Mexico and Central America south of 20N. The simulation of the low-level wind field (Figure 3.22) is overall quite good with a realistic low level jet over the Great Plains seen here as a westward extension of the easterlies associated with the Bermuda High. The model does produce excessive westerlies in the eastern tropical Pacific and this is likely linked to the excessive precipitation in the region (cf. Figure 3.21)

The diurnal cycle is a key component of the mean climatology over a number of regions of North America, reflecting important regional circulations and weather systems phasing to the diurnal solar forcing. As shown in Figures 3.23 and 3.24 model does a credible job of capturing key diurnal variations over Mexico, Central America and the Caribbean: these appear to be associated in part with land-sea breeze circulations. The model also captures some aspects of the diurnal cycle over the United States including the afternoon maximum over the southeast (though somewhat too weak), and the late afternoon maximum over the Rockies, with some propagation to the east into early evening. The model, however, fails to capture the nocturnal maximum over the northern Great Plains. Further analysis (not shown), suggests that the model is capturing some of the initial eastward propagation into the western parts of the Great Plains associated with late afternoon eastward propagating weather systems but, despite having what appears to be a very realistic low level jet, does not generate the distinctive nocturnal maximum over the Great Plains which in the observations is tightly coupled to the evolution of the low level jet.

3.8.5 Summary

The G5NR generates a wide range of tropical wave, monsoonal, and diurnal variability that is in many ways quite similar to the observed. This includes a range of eastward and westward moving tropical weather systems, the northward propagation of the east Asian monsoon, the onset of the

south Asian (Indian) monsoon, the basic seasonal development of the African, South American and North American monsoons and related low level circulations. The analysis of the diurnal cycle was limited to North America, but here too the model reproduces many of the basic regional and other small scale features of the diurnal cycle that appear to be linked to land-sea breeze circulations.

There are a number of aspects of the simulation that are unrealistic but it should be noted that these are for the most part similar to those found in coarser resolution simulations with earlier versions of this and other state-of-the-art climate models including, the lack of slow eastward moving Madden-Julian (MJO)-type convectively coupled wave propagation especially over the Indian Ocean and Pacific warm pool (presumably impacting the ability to simulate subseasonal variability of the Indian monsoon), and the lack of a nocturnal precipitation maximum over the northern US Great Plains in summer, despite producing a rather realistic low level jet. Other deficiencies include excessive precipitation over high topography (especially the Andes) and excessive summer precipitation over the eastern Pacific, Mexico and Central America south of 20N.

3.9 Specific Humidity (QV) and Total Surface Precipitation Flux (PrFLX):

In this section, we compare the vertical structure of QV ($\mathrm{kg \cdot kg^{-1}}$) and PrFLX ($\mathrm{kg \cdot m^{-2} \cdot s^{-1}}$) simulated by the G5NR against that obtained from reanalysis (NCEP CFSR (Saha et al. 2010) & MERRA (Rienecker et al. 2011)) for the months of June to September (JJAS). Daily anomalies of QV and PrFLX (for JJAS 2005 and 2006) for G5NR and analysis are computed at a specific time (1330 hrs) by removing the monthly mean diurnal cycle. It is known (Neale et al. 2008) that model simulated PrFLX in the vicinity of the tropical central and eastern Pacific Intertropical Convergence Zone (ITCZ) region ($30^{o}\mathrm{S} - 30^{o}\mathrm{N}$, $120^{o}\mathrm{E} - 80^{o}\mathrm{W}$) tends to be in disagreement with observations/analysis. We therefore focus on the simulated PrFLX and QV in this region. Firstly, convective regimes of deep and shallow convection are identified using daily large-scale (LS) mid-tropospheric vertical velocity (OMEGA500 ($\mathrm{hPa \cdot day^{-1}}$)), following Bony et al., 2004. Using OMEGA500 as a proxy for convective and subsidence regimes (i.e. OMEGA500 $< \backslash > 0$ respectively), QV and PrFLX are then analyzed in specific regimes by compositing the anomalies into equal bins of width 10 hPa $\mathrm{day^{-1}}$.

3.9.1 PDF of OMEGA500 and Composite PrFLX Anomaly

Figure 3.25 shows the probability distribution function (PDF) of OMEGA500 and the composite PrFLX anomaly in the various circulation regimes. The PDFs peak at about 25 $\mathrm{hPa \cdot day^{-1}}$, consistent with widespread subsidence associated with clear-sky radiative cooling in the tropics (Bony et al. 2004). The normalized peak grid point average is about 0.08 in the analysis while the area of LS descent is relatively larger in the G5NR (peak value of 0.1). As a consequence, the area of LS ascent is higher in the analysis relative to G5NR across the convective regimes. The

composite PrFLX anomaly in the analysis peaks at above 0.025 $kg \cdot m^{-2} \cdot s^{-1}$ in the deep convective regime (OMEGA500 < -80 $hPa \cdot day^{-1}$), while the value actually lies below the diurnal monthly mean value in the G5NR in this regime. A general reduced contrast is seen across the regimes in the composite G5NR PrFLX anomaly relative to analysis.

3.9.2 Composite QV Anomaly

The composite QV is shown in Figure 3.26, along with the difference values between the analysis and G5NR. While the range of composite vertical QV across the regimes is similar in CFSR and G5NR, the vertical structure in the convective regime (OMEGA500 < -60 $hPa \cdot day^{-1}$) is rather different. In particular, there are two distinct peak composite QV values in the G5NR (centered near the surface and at about 800 $hPa \cdot day^{-1}$) across the deep convective regime, in contrast to analysis which shows a single peak value centered at this pressure level. The general drying of the atmosphere in the strong subsidence regime (OMEGA500 > 60 $hPa \cdot day^{-1}$) is also absent in the G5NR, unlike that in the analysis.

3.9.3 Covarying Anomaly Patterns of QV and PrFLX

In order to examine covarying patterns of QV and PrFLX anomalies, the canonical correlation analysis (CCA) is performed on these fields. The CCA finds linear combinations (LCs) of two variables in independent data sets that have maximum correlation in time (Delsole et al. 2003). The EOF analysis method is used to compress the co-varying fields and apply the CCA in a lower-dimensional subspace such that the dominant modes of variability in time are captured (Delsole and Tippett). In this study, following the method of Delsole and Tippett, the reduction of space is obtained by projecting the original time series (TS) onto the leading principal components (PCs).

Figure 3.27 shows the leading physical patterns (also called canonical loading vectors) corresponding to a maximally correlated set of distinct TS (called canonical variates) of QV and PrFLX that are LCs of elements of QV and PrFLX such that the two LCs have maximum correlation. The PCs and canonical variates are normalized to unit variance, and hence the loading vector absorbs the actual units of the field. The panels on the left and center show zonal and meridional cross-sections of the leading QV pattern, while that on the right shows the leading PrFLX pattern. The analysis PrFLX exhibits increased positive anomalies across the Pacific and west of the dateline, extending in a diagonally-oriented manner across the South Pacific Convergence Zone (SPCZ). This pattern is maximally correlated with positive anomalies of vertical QV west of 130^oW across 20^oS - 20^oN in the vicinity of the warm pool region. In contrast, two longitudinally distinct centers of positive G5NR PrFLX anomalies are seen to extend across the Pacific at about 10^o latitude. This structure is maximally correlated with vertical positive anomalies of QV in regions on either side of the dateline (also over the cold tongue region, unlike that in analysis), with a distinct vertical center of negative QV anomaly centered at 5^oN to the immediate east of the dateline. It can be speculated that spurious drying north of 5^oN and to the immediate east of the dateline is partly responsible for

the spurious vertical peaks of stratified positive QV anomaly noted earlier in the deep convective regime.

In summary, the general trend of the simulated QV and PrFLX in the G5NR is to exhibit increased areas of subsiding motion in the G5NR across the equatorial Pacific and spurious vertical drying centers across the dateline presumably in the deep convective regimes. This is correlated with reduced PrFLX anomalies to the west of the dateline and in the SPCZ, unlike that in the analysis, resulting in the classic double-ITCZ precipitation error.

3.10 Precipitation Flux and Condensate

This section focuses on the validation of precipitation fields in the G5NR. By comparing with TRMM Precipitation Radar (PR) Level 2 product (2A25), we examine several aspects of the GEOS-5 nature run's precipitation fields in terms of precipitating area fraction, average surface precipitation rate, probability distribution of preciptation rate, convective and stratiform precipitation area fraction and precipitation rate, and vertical distribution of precipitation. For the purpose of this study, the 2005 June - August (JJA) months of the G5NR and TRMM PR data are considered.

3.10.1 Verification Data

The level-2 precipitation profiles from TRMM PR, 2A25 Version 6 (Kozu et al, 2001, Iguchi et al. 2000) are the verification data used in this study. The TRMM PR can estimate quantitative rainfall estimation over land as well as ocean. The TRMM satellite has an orbital domain extending from 35°N-35°S and has a precessing orbit so that it samples the full diurnal cycle. The algorithm 2A25 retrieves profiles of the radar reflectivity factor, Z, with rain attenuation correction and rain rate for each radar beam by the combination of Hitschfeld-Bordan and surface reference method [Iguchi 2000]. Owing to power constraints, the TRMM PR has a relatively low sensitivity of 17 dBZ (which corresponds to a precipitation rate of approximately 0.5 mm/hr). Therefore, this study uses only data $\geq$ 17 dBZ to avoid the ambiguity of sampling at lower reflectivities. To collocate the data, the G5NR precipitation is projected from the model domain to the observation scale considering similar spatial resolution both for the G5NR and TRMM PR. The PR data are nearly continuous in time while the G5NR data are only available every 30 min. Therefore, a nearest-neighbor-in-time sampling of the G5NR data is performed to collocate the data rather than linearly interpolating (Figure 3.28). More than 200,000 collocated data were used in this study.

3.10.2 Rainy Area Fraction

Fractions for rainy area and non-rainy area are compared between TRMM PR and the G5NR. As mentioned in the previous section, PR is not sensitive to the reflectivity below 17 dBZ which is approximately corresponding to 0.5 mm/hr rain rate. Therefore, data points with precipitation rate > 0.5mm/hr (≤ 0.5 mm/hr) were considered rainy (non-rainy) in the comparisons. Results are summarized in Table 3.2. About 2.8% of collocated TRMM PR data were rainy and 3.5% of collocated G5NR data were rainy so that the latter has 0.7% larger rainy area. Maximum surface precipitation rate occurred during the period considered in this study was 265.3 mm/hr for PR and 298.4 mm/hr for the G5NR. Mean and standard deviation of PR surface precipitation rate were 2.34 mm/hr and 25.47 mm/hr, respectively. Mean and standard deviation of the G5NR surface precipitation rates were 2.64 mm/hr and 36.9 mm/hr. That is, the G5NR presents about 10% larger averaged precipitation rate than the TRMM PR observations.

3.10.3 Probability Distribution of Surface Precipitation

To evaluate the G5NR surface precipitation for different precipitation intensity, probability distributions of surface precipitation rates in TRMM PR observations and the G5NR data were calculated for each 0.5 mm/hr precipitation rate bin and upto the precipitation rate of 200 mm/hr (Figure 3.29). Comparisons show that G5NR exhibits larger frequency than TRMM PR observations for light precipitation rates (< 1 mm/hr) and for heavy precipitation rates (> 20mm/hr) while it has smaller frequency for precipiation rates ranging 1 mm/hr and 20 mm/hr compared to the TRMM PR observations.

3.10.4 Convective Precipitation vs. Stratiform Precipitation

Precipitation is generally considered to be of two clearly distinguishable types: stratiform and convective. Houze (1982, 1989) demonstrated that the relative proportions of convective and stratiform rain amounts can be used to infer the vertical structure of latent heating in a tropical precipitating system. Higher fractions of stratiform rainfall are associated with an upward shift in the level of maximum heating and an increase in the vertical heating gradient in the upper troposphere. Horizontal variations in the vertical heating profile associated with tropical precipitating systems can affect the large-scale dynamical response because the generation of potential vorticity in the tropics is directly proportional to the local vertical gradient in the heating profile (Hartmann et al. 1984, Haynes and McIntyre 1987, Mapes and Houze 1995).

In the PR 2A25 products, all observation points are classified as convective, stratiform or "other" based on the vertical profile of reflectivity and the horizontal variability of the radar echo. Data in the other category are considered unreliable and are ignored here. The GEOS-5 moist physics schemes allow for the simultaneous presence of stratiform and convective precipitation, and the

ratio of one to the other is highly dependent on model configuration and resolution (Molod et al., 2014). For the present comparison, the total precipitation from the G5NR is categorized as "convective" if the convective source precipitation generated by the model is greater than 0.5 mm/hr, and "stratiform" otherwise. The total precipitation must exceed 0.5 mm/hr to exceed the trace limit of TRMM.

Table 2 summarizes the comparisons of convective and stratiform precipitation fractions from TRMM PR and the G5NR data. Results show that convective and stratiform rainy area fractions for the nature are remarkably consistent with the PR observations: In the nature run, convective and stratiform rainy area fractions are 22.9% and 77.1%, respectively while convective and stratiform rainy area fractions for TRMM PR are 23.3% and 76.7%, respectively. Mean (standard deviation) surface precipitation rate for convective precipitation is 153.0 (347.2) mm/hr which is slightly smaller (larger) than TRMM PR average rain rate of 164.2 (205.5) mm/hr for convective precipitation. Average surface precipitation rate for stratiform precipitation is 50.9 (82.8) mm/hr for the G5NR which was slight smaller than 58.7 (81.5) mm/hr for TRMM PR observations.

3.10.5 Vertical Distribution of Precipitation

The benefit of active instrument like radar to measure precipitation is that observations can provide the vertical structure of precipitation. It should be noted that the units for precipitation fields in the G5NR are generated in kg/kg to be easily converted to the input units for radiative transfer models while precipitations in TRMM PR 2A25 products have unit of mm/hr. Therefore, it is not possible to make quantitative comparisons for the vertical distribution of rainrates directly but still qualitative comparisons of the vertical structures of TRMM PR and the nature precipitation can provide useful information for the validations. As shown in Figure 3.30, the vertical extension of precipitations is consistent between TRMM PR and the G5NR over the tropical and subtropical regions where TRMM PR observations cover. In addition, the latitudinal location of Intertropical Convergence Zone (ITCZ) characterized by the intense precipitation rates in TRMM PR is very clost to the location where the main ITCZ in the G5NR exists. It should be noted that another weak ITCZs existed in the G5NR between the equator and 5°S which were not present in the TRMM PR observations.

3.10.6 Summary

The G5NR presents about 10% larger averaged surface precipitation rate than the TRMM PR observations. Especially the G5NR shows larger frequency for light precipitation rates (< 1 mm/hr) and for heavy precipitation rates (> 20 mm/hr) compared to the TRMM PR observations. In contrast, the G5NR shows smaller frequency for precipiation rates ranging 1 mm/hr and 20 mm/hr compared to the TRMM PR observations. The convective and stratiform rainy area fractions for the nature are remarkably consistent with the PR observations. Mean precipitation rates for both

precipitation types were similar but the standard deviation of precipitation rates in G5NR for convective precipitation type was about 70% larger than the TRMM PR observations.

Table 3.1: Using EOS observations, merged data products and reanalyses, NEWS has developed an energy budget for the globe and continental basins. This table shows the global energy budget for the combined original data, and a constrained budget. The constrained budget was developed with physical realism, a simple error model and rigorous error estimates of the contributing data. NEWS data include the EOS period from 2001-2010, while the G5NR data are for Jun 2005 - May 2007. Units are W m^{-2}

Budget Term		Original	Constrained	G5NR
Incoming Solar	F	340 0.5	340 0.5	340
Outgoing Shortwave	OSR	100 5	98 2	106
Outgoing Longwave	OLR	238 2	239 2	240
Downwelling LW at SFC	LW↓sfc	344 7	339 4	334
Downwelling SW at SFC	SW↓sfc	190 6	187 3	184
Surface Emitted	LW↑sfc	398 6	400 4	394
Surface Reflected	SW↑sfc	22 2	22 1	23
Sensible Heating	SH	21 5	23 3	21
Precipitation LH	LvP	77 7	80 4	87
Evaporation LH	LvE	75 7	80 4	87
Surface Heat Storage	Net Abs.	0.6 0.4	0.91	-6.44

.

	TRMM PR	G5NR
Rainy	**2.8 %**	**3.5 %**
Non-rainy	**97.2 %**	**96.5 %**
Rainrate Avg.	**2.33 mm/day**	**2.62 mm/day**
Rainrate STD	**25.5 mm/day**	**37.0 mm/day**
Maximum rainrate	**265.3 mm/hr**	**298.4 mm/hr**

Table 3.2: Comparisons of rainy area fraction and mean surface rainrate between TRMM Precipitation Radar data and the G5NR.

	TRMM PR	G5NR
Convective precip area	**23.3 %**	**22.9 %**
Stratiform precip area	**76.7 %**	**77.1 %**
Convective rainrate Avg	**164.2 mm/day**	**153.0 mm/day**
Stratiform ainrate Avg	**58.7 mm/day**	**50.9 mm/day**
Convective rainrate STD	**205.5 mm/day**	**347.2 mm/day**
Stratiform ainrate STD	**81.5 mm/day**	**82.8 mm/day**

Table 3.3: Comparison of convective and stratiform precipitation fractions between TRMM Precipitation Radar data and the G5NR.

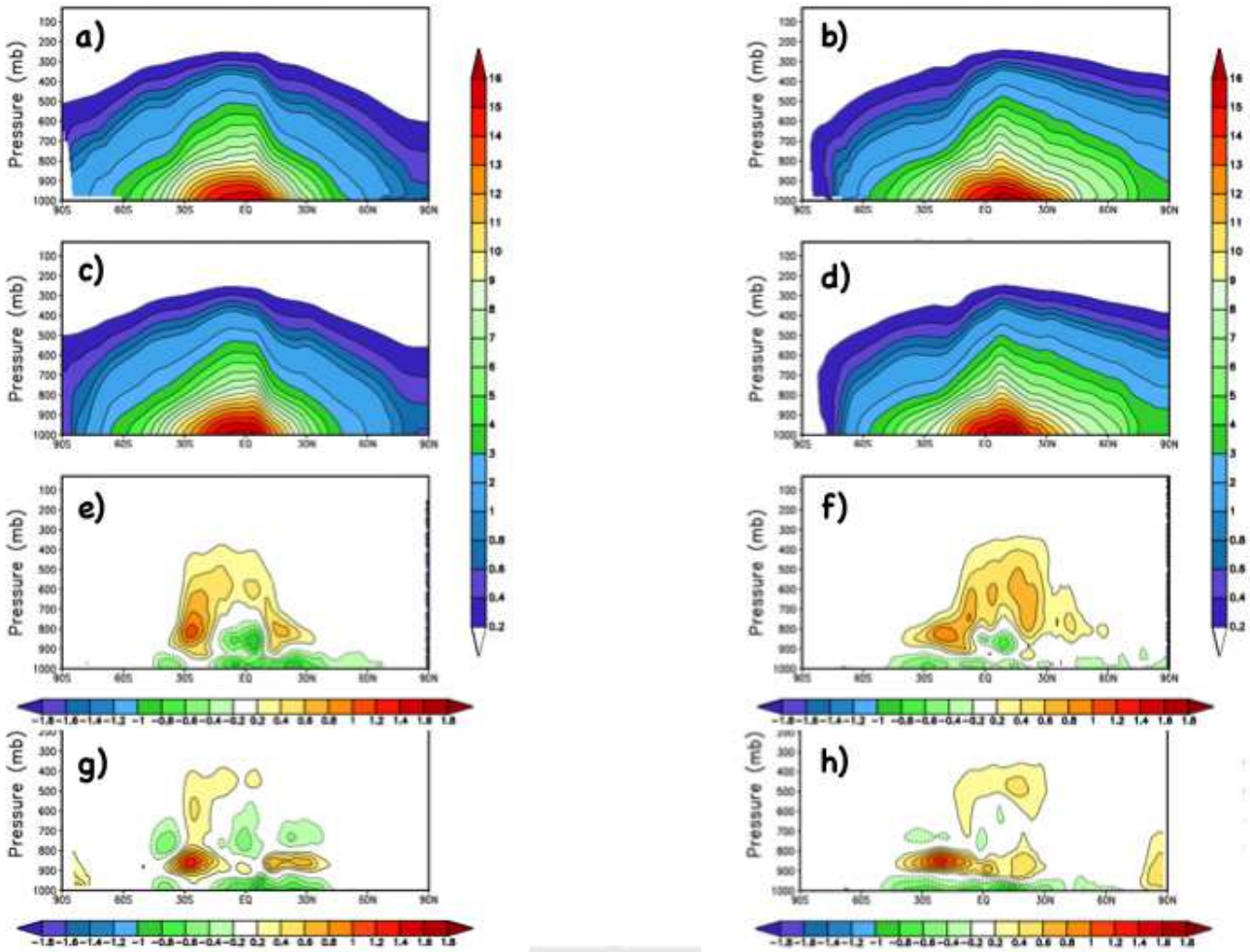

Figure 3.1: Seasonal mean specific humidity in g kg^{-1} from a) the G5NR in DJF, b) the G5NR in JJA, c) MERRA in DJF, d) MERRA in JJA, e) the difference G5NR - MERRA in DJF, f) the difference G5NR - MERRA in JJA, g) the difference G5NR - ERA-I in DJF, h) the difference G5NR - ERA-I in JJA.

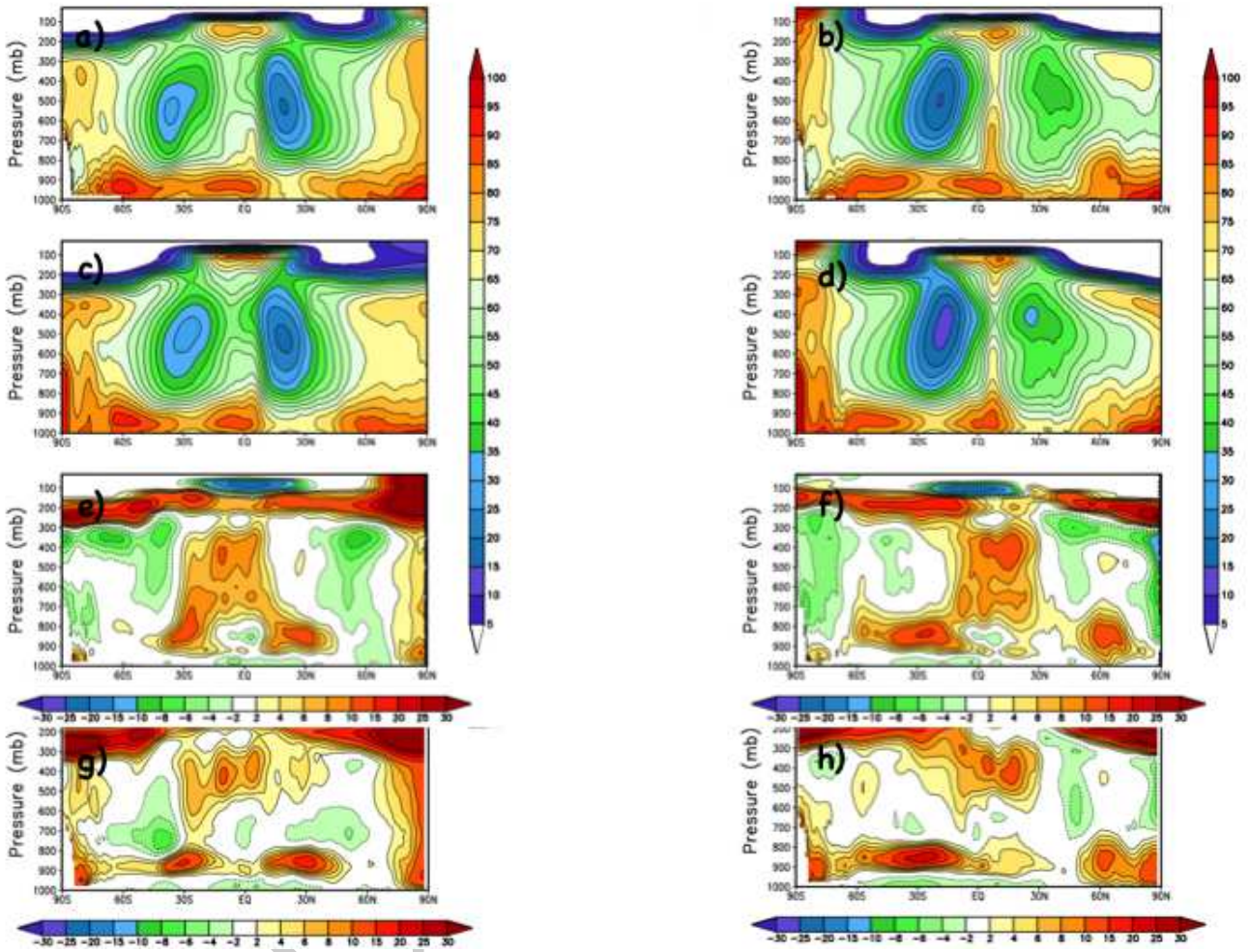

Figure 3.2: Seasonal mean relative humidity in % from a) the G5NR in DJF, b) the G5NR in JJA, c) MERRA in DJF, d) MERRA in JJA, e) the difference G5NR - MERRA in DJF, f) the difference G5NR - MERRA in JJA, g) the difference G5NR - ERA-I in DJF, h) the difference G5NR - ERA-I in JJA.

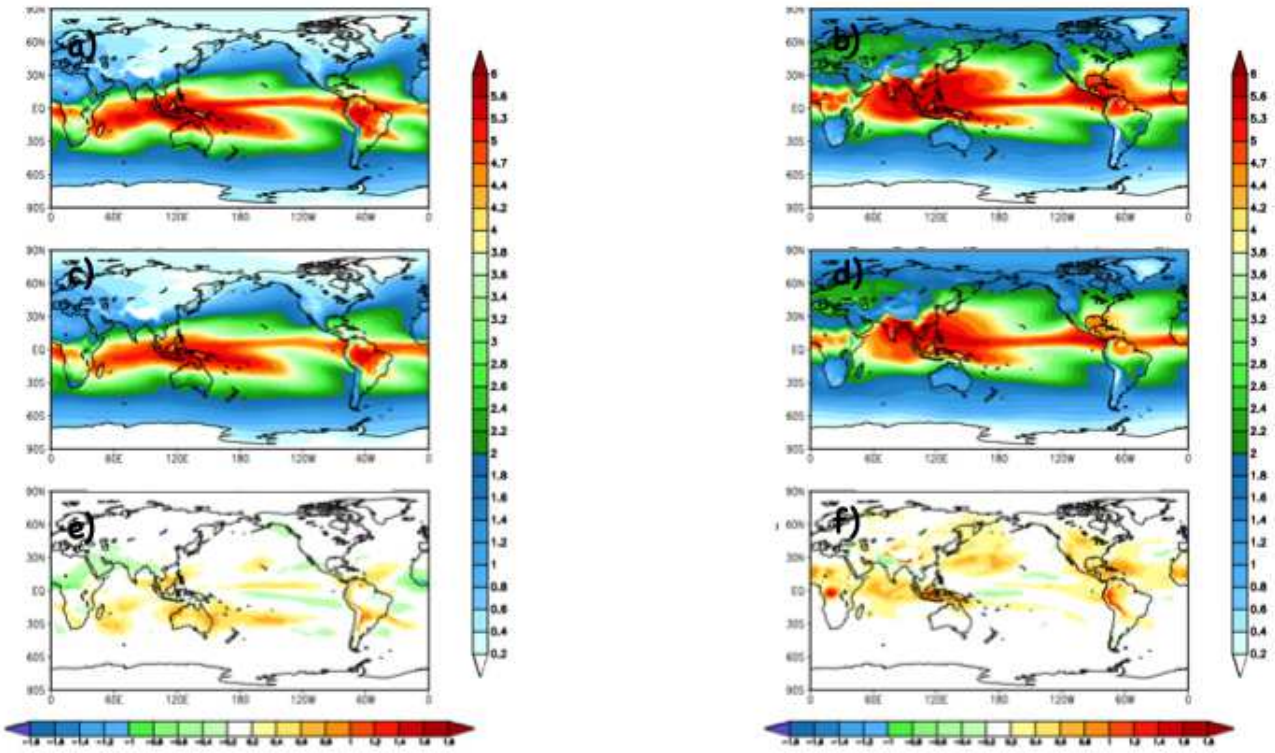

Figure 3.3: Seasonal mean total precipitable water mm from a) the G5NR in DJF, b) the G5NR in JJA, c) SRB in DJF, d) SRB in JJA, e) the difference G5NR - SRB in DJF, f) the difference G5NR - SRB in JJA.

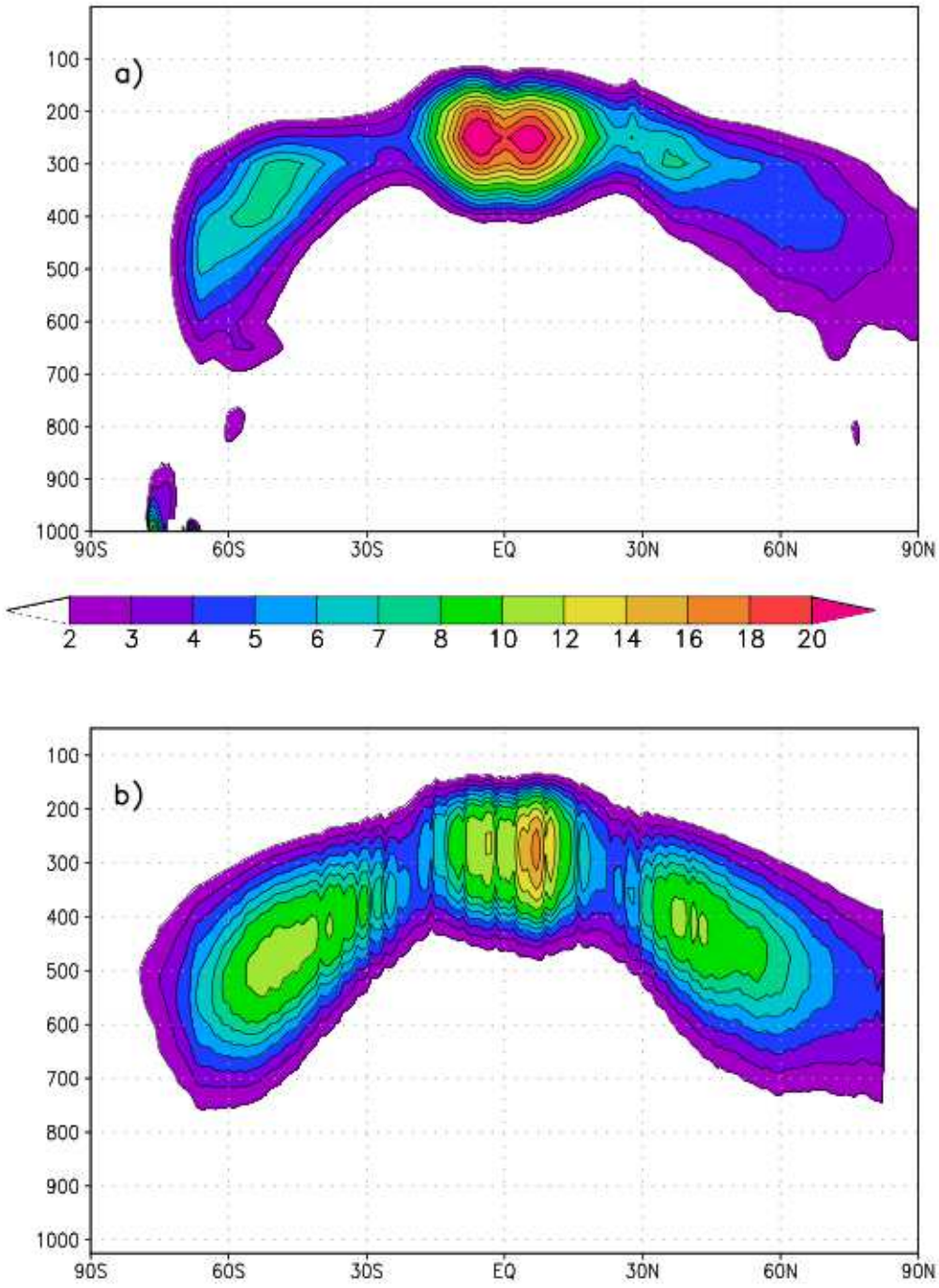

Figure 3.4: Annual mean cloud ice content in mg kg^{-1} from a) the G5NR, b) CloudSat non-precipitating cloud ice.

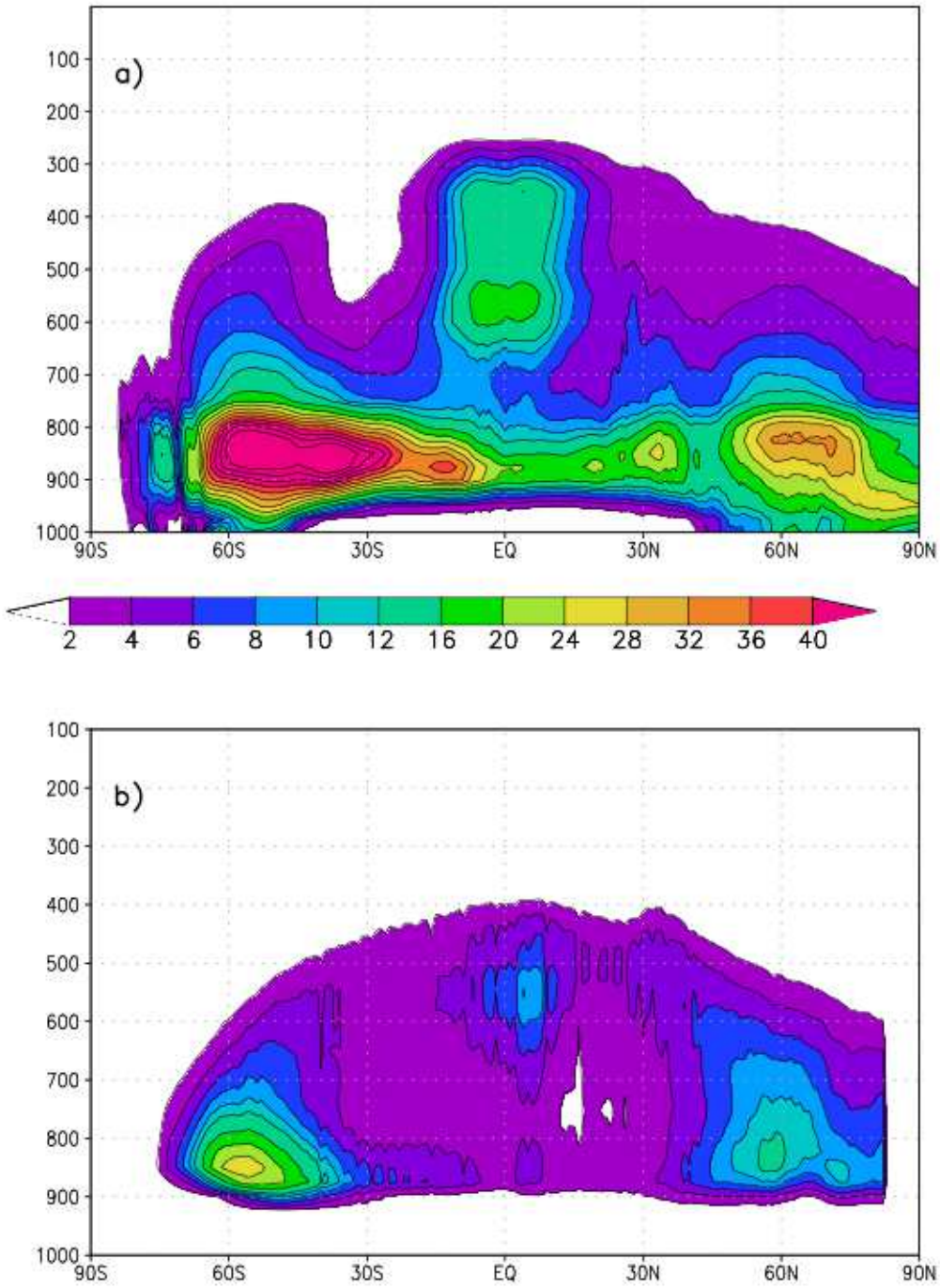

Figure 3.5: Annual mean cloud liquid water content in mg kg^{-1} from a) the G5NR, b) CloudSat non-precipitating cloud liquid water.

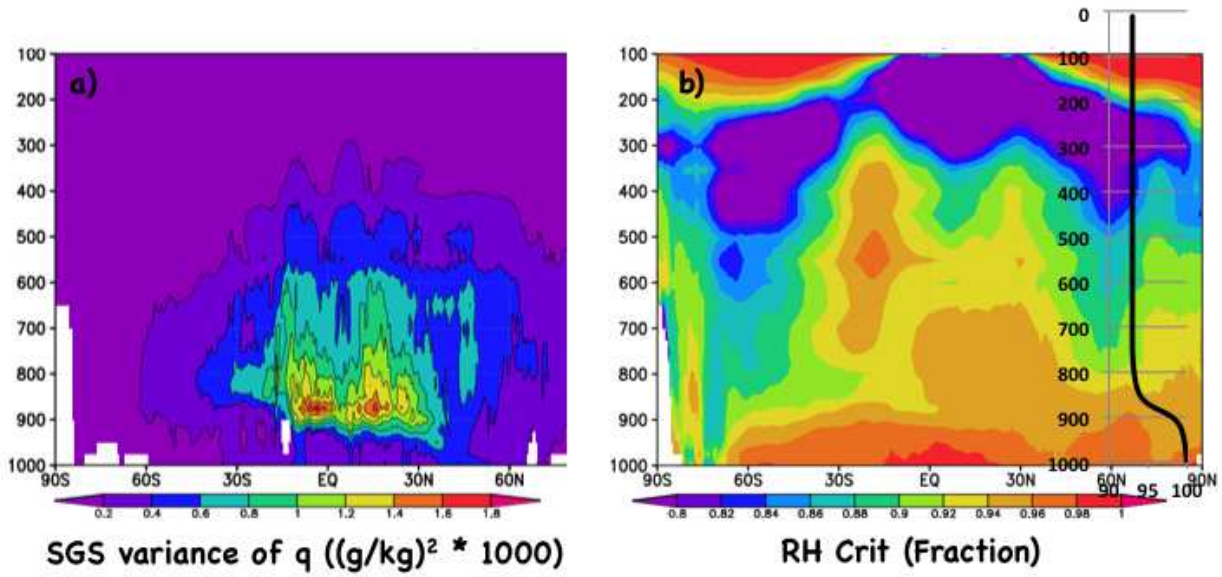

Figure 3.6: a) 0.5^o subgrid scale variance of total water in $(\mathrm{g\,kg^{-1}})^2 * 1000$, b) Critical relative humidity (RH_c) in fraction computed from G5NR, inset RH_c profile used in 0.5^o GEOS-5 AGCM.

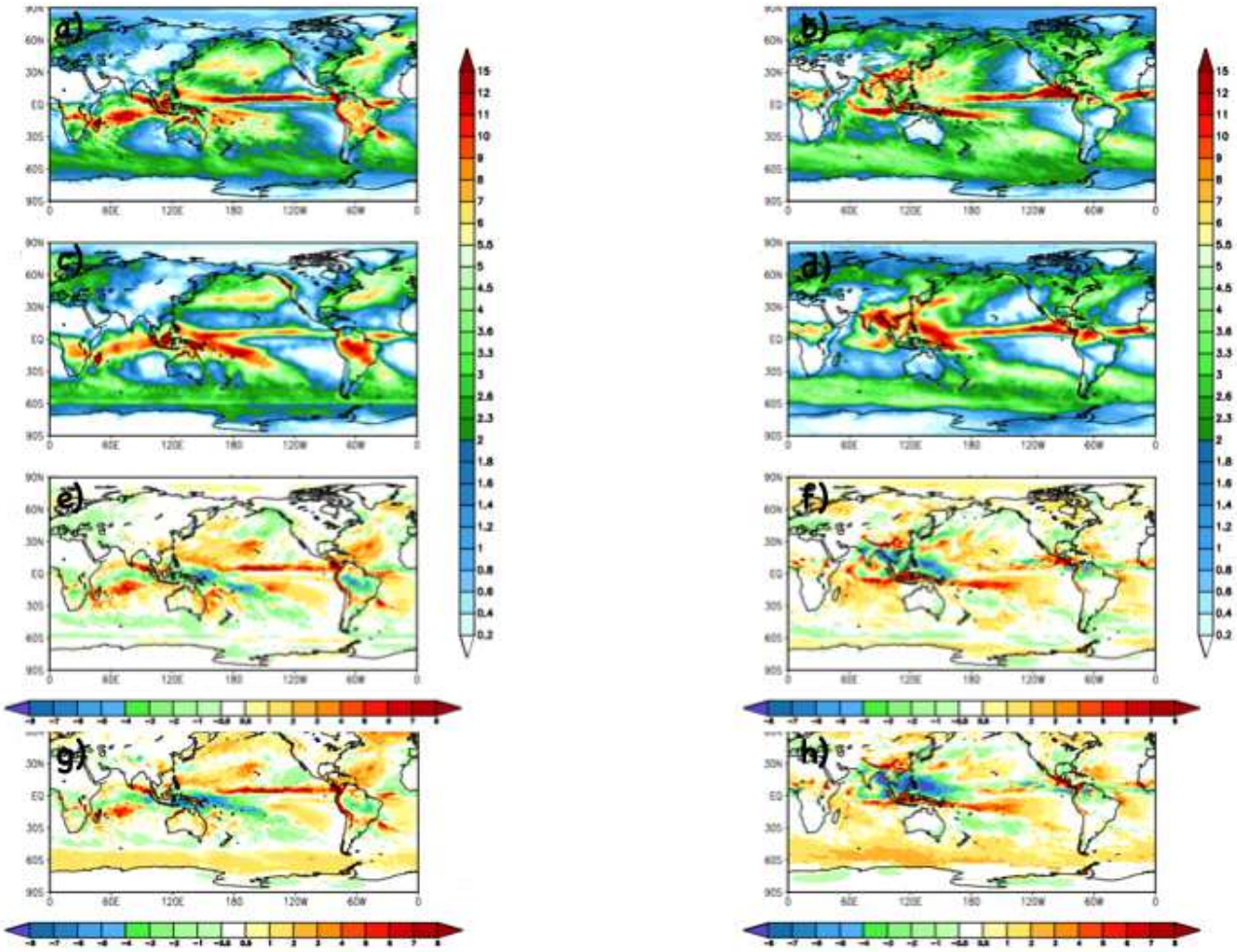

Figure 3.7: Seasonal mean total precipitation in mm day^{-1} from a) the G5NR in DJF, b) the G5NR in JJA, c) MERRA in DJF, d) MERRA in JJA, e) the difference G5NR - MERRA in DJF, f) the difference G5NR - MERRA in JJA, g) the difference G5NR - ERA-I in DJF, h) the difference G5NR - ERA-I in JJA.

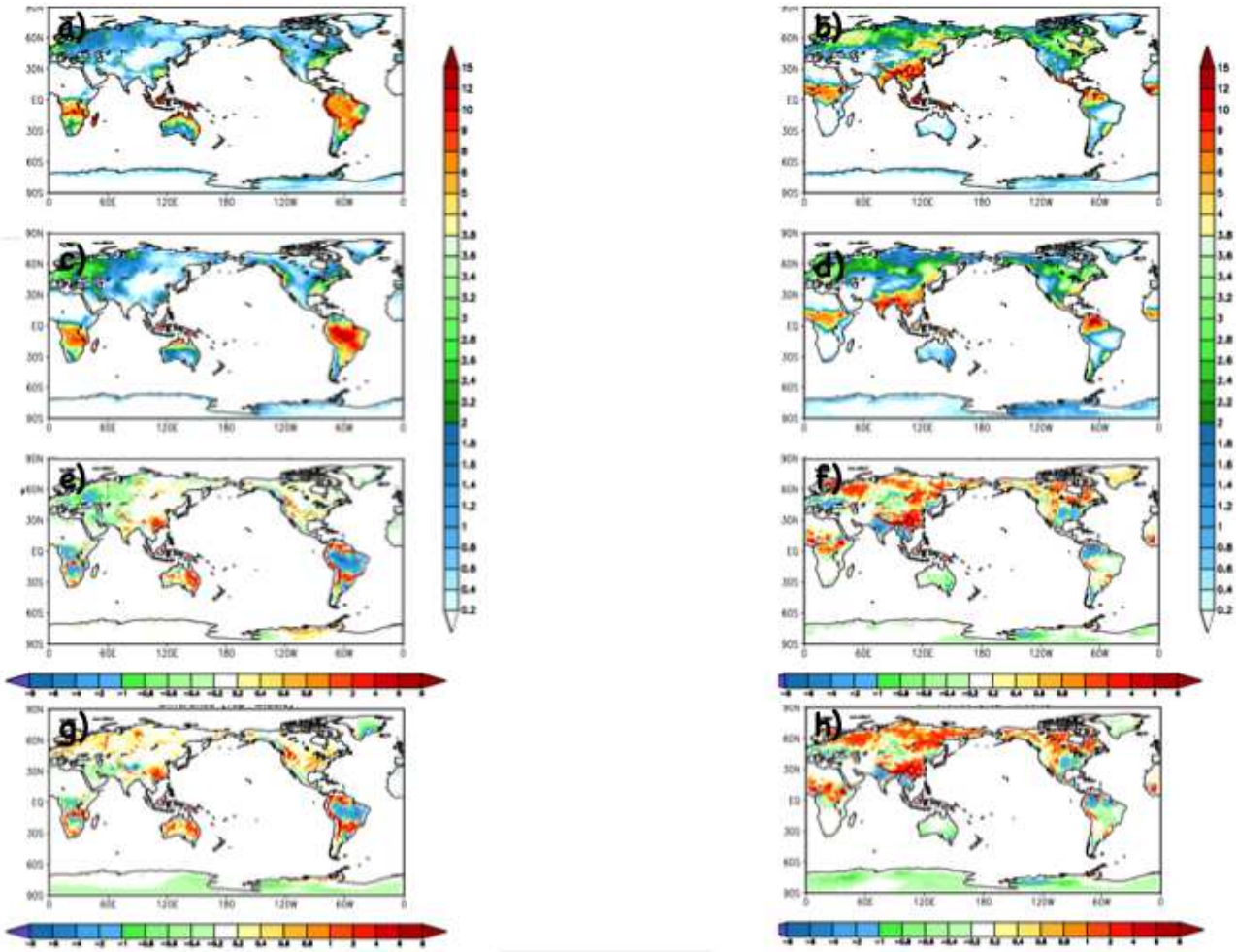

Figure 3.8: Seasonal mean total precipitation over land only in mm day^{-1} from a) the G5NR in DJF, b) the G5NR in JJA, c) MERRA in DJF, d) MERRA in JJA, e) the difference G5NR - MERRA in DJF, f) the difference G5NR - MERRA in JJA, g) the difference G5NR - ERA-I in DJF, h) the difference G5NR - ERA-I in JJA.

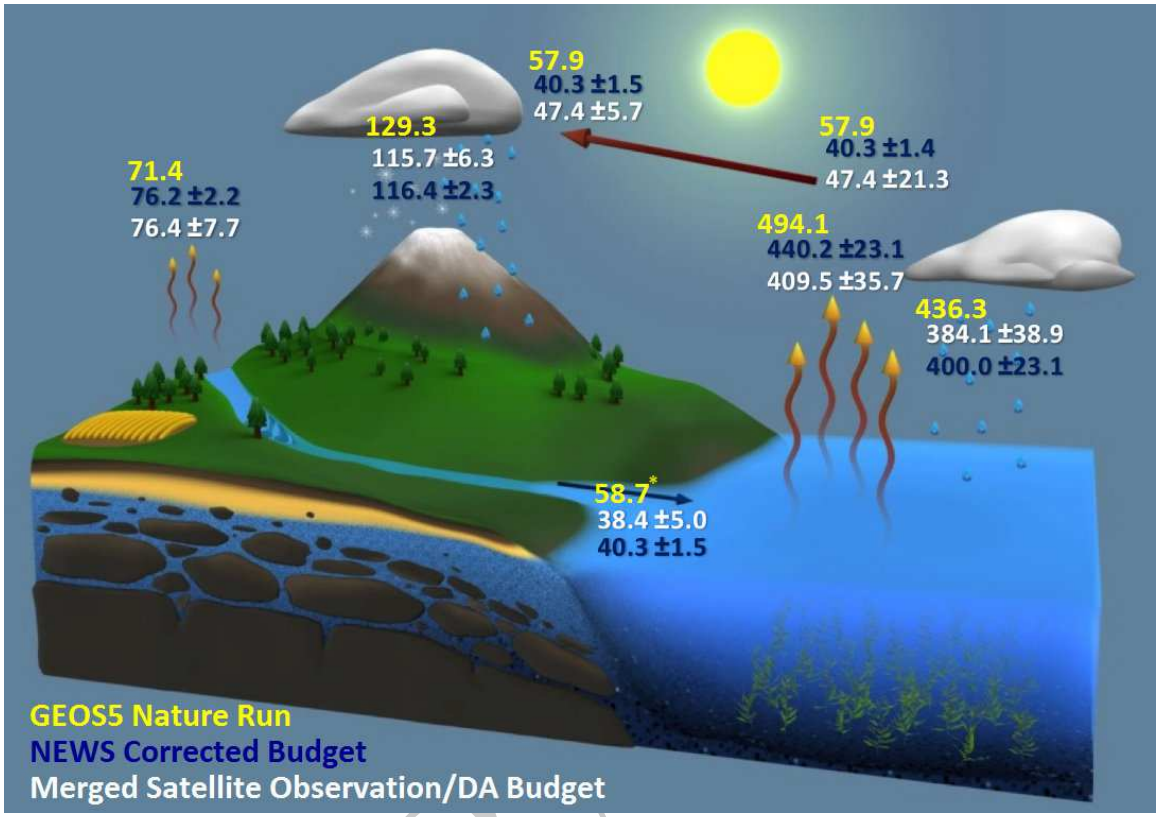

Figure 3.9: Graphical depiction of the G5NR Global Water Cycle terms in units of $km^3\ yr^{-1}$ compared to that of the NEWS water cycle terms before and after constraint. Note that the G5NR balance also considers a small total tendency term, -0.12 $km^3\ yr^{-1}$ globally. Runoff as considered here does not include glacier runoff and other approximations, leading to an imbalance between runoff and the terrestrial data. In addition, terrestrial water storage has also not been included.

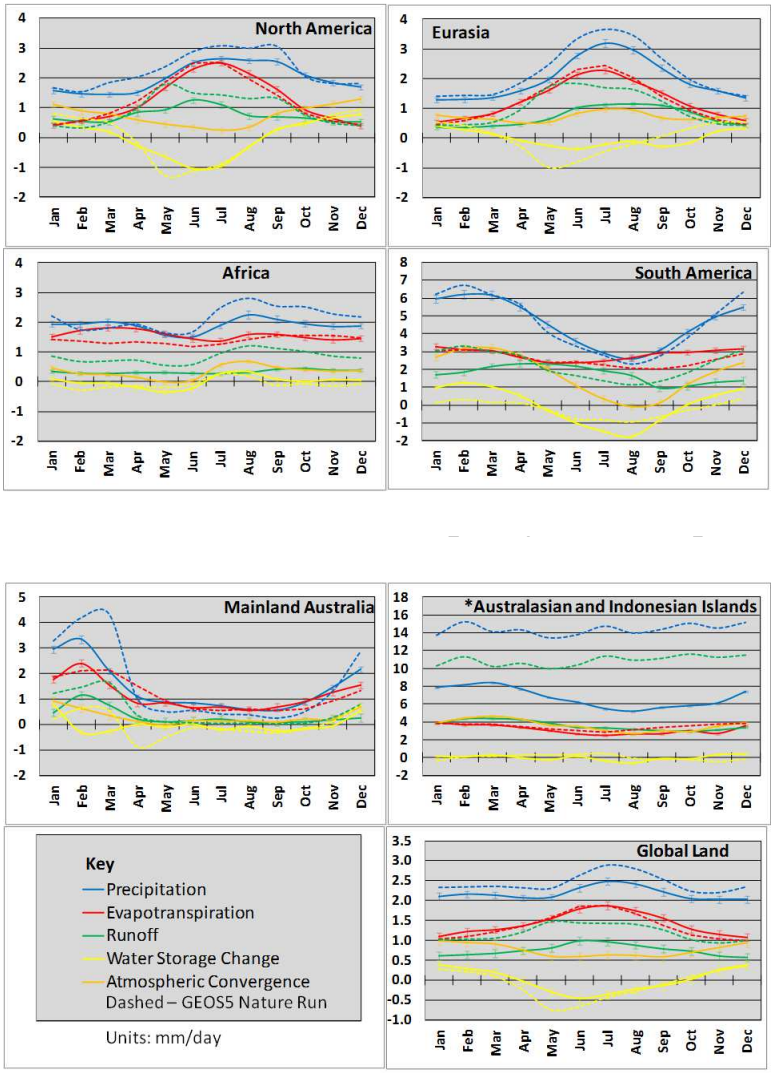

Figure 3.10: Monthly hydrological quantities in G5NR and NEWS. Dashed lines indicate the G5NR, solid lines with error bars represent the NEWS Climatology. The full nature run, Jun2005-May2007 were used.

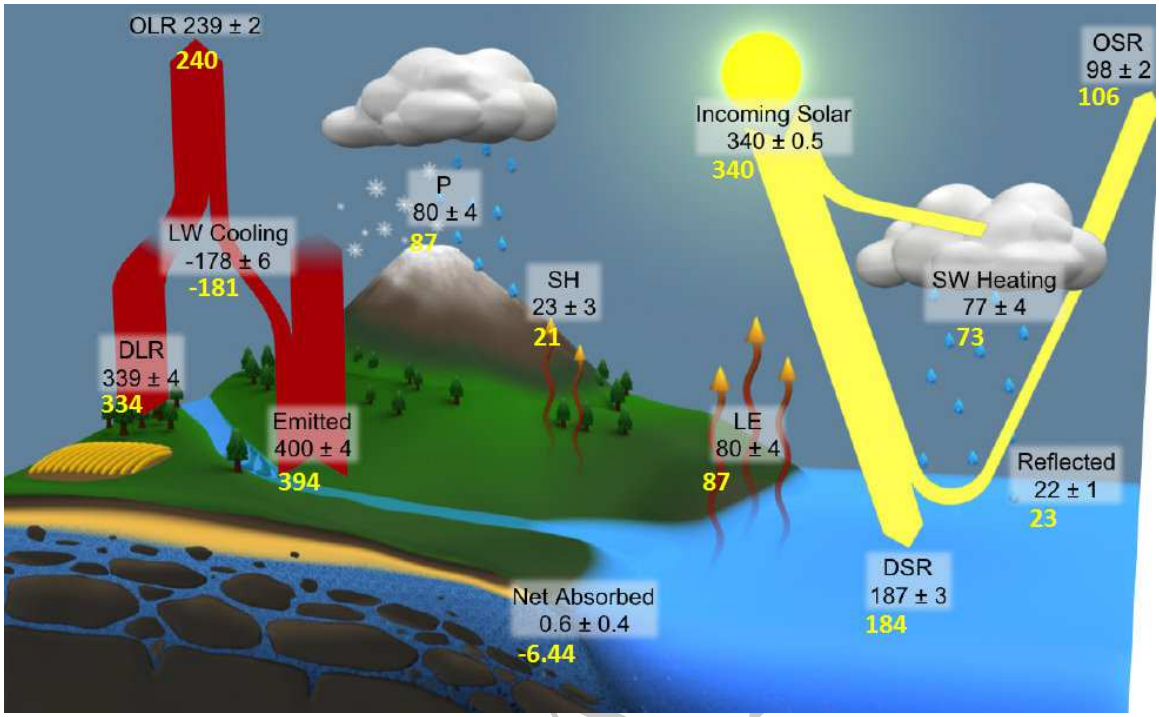

Figure 3.11: Graphical depiction of the NEWS constrained merged satellite energy balance (black) and G5NR energy components (Yellow). Units are W m^{-2}

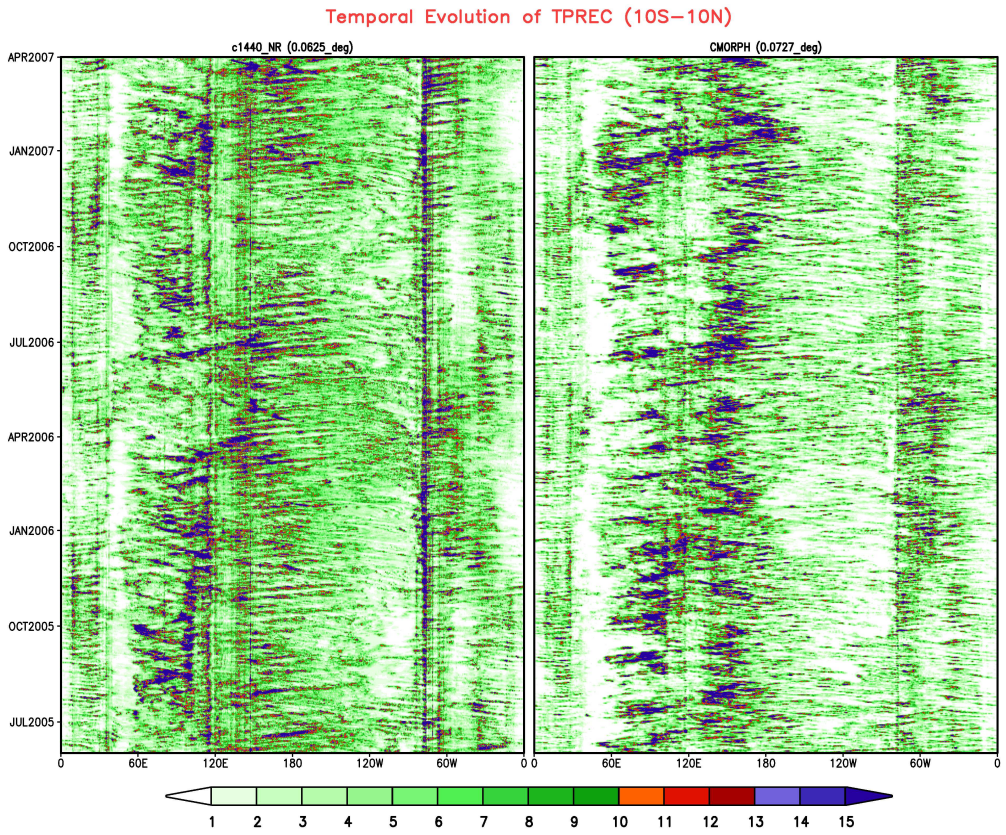

Figure 3.12: Hovmöller diagrams of daily mean precipitation averaged between 10S- 10N and 0-60E. Left panel is for the G5NR. Right panel is for the CMORPH observations. Units: mm day^{-1}.

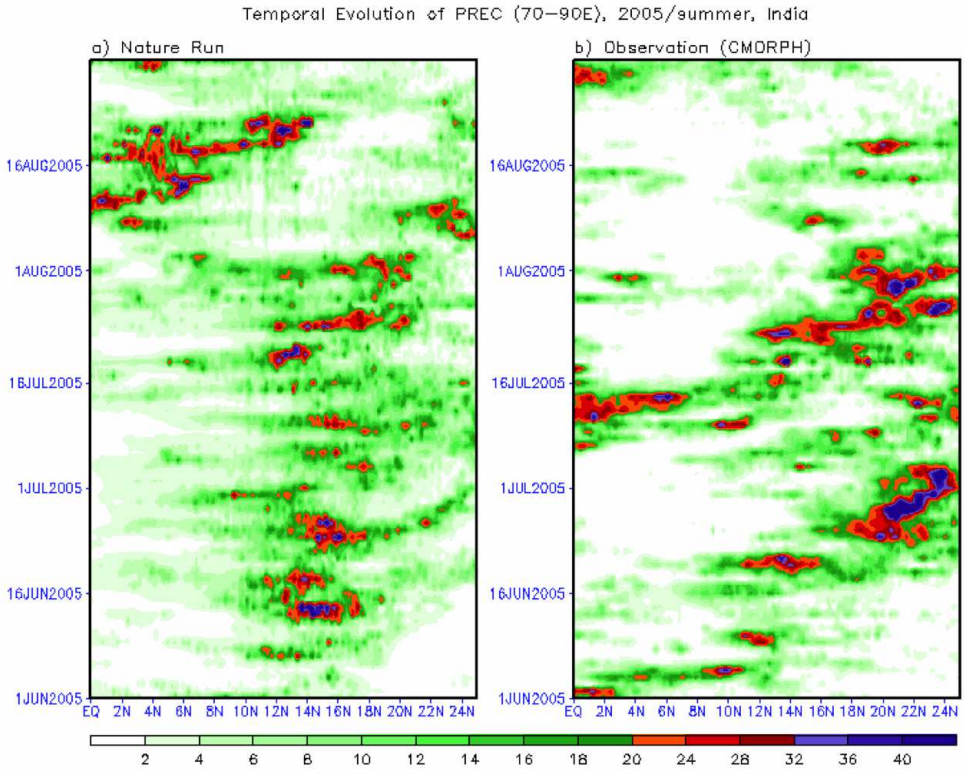

Figure 3.13: Northward progression of the Indian monsoon precipitation during June through August 2005. Left is for the G5NR, and right panel is for the CMORPH observations. Units: mm day^{-1}.

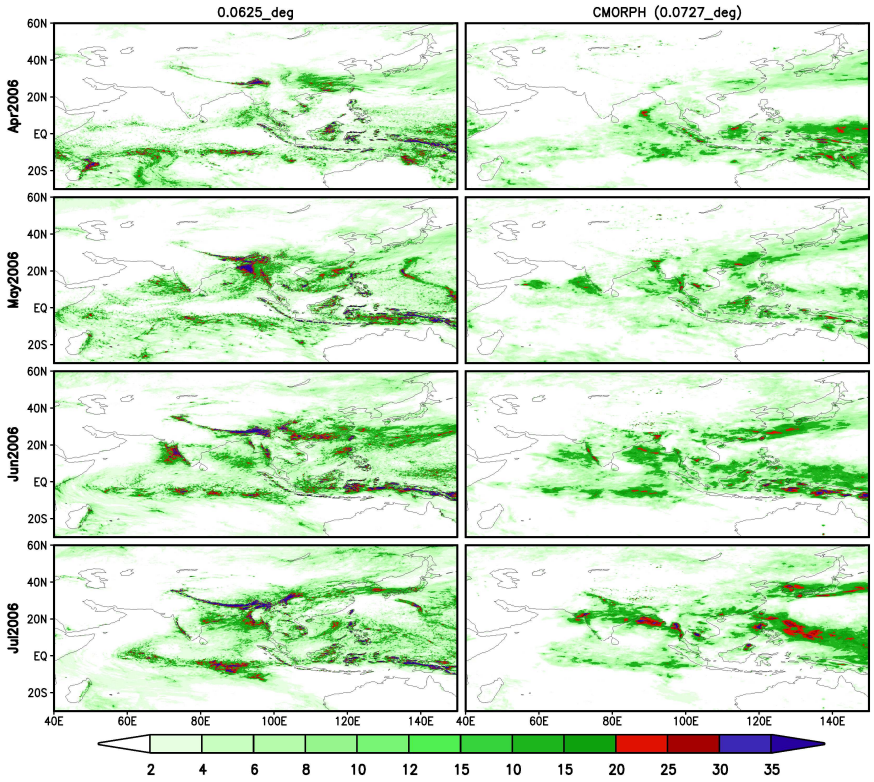

Figure 3.14: April - July 2006 monthly mean precipitation maps focusing on the Indian Ocean and western Pacific warm pool regions. Left panels are for the G5NR. Right panels are for the CMORPH observations. Units: mm day^{-1}.

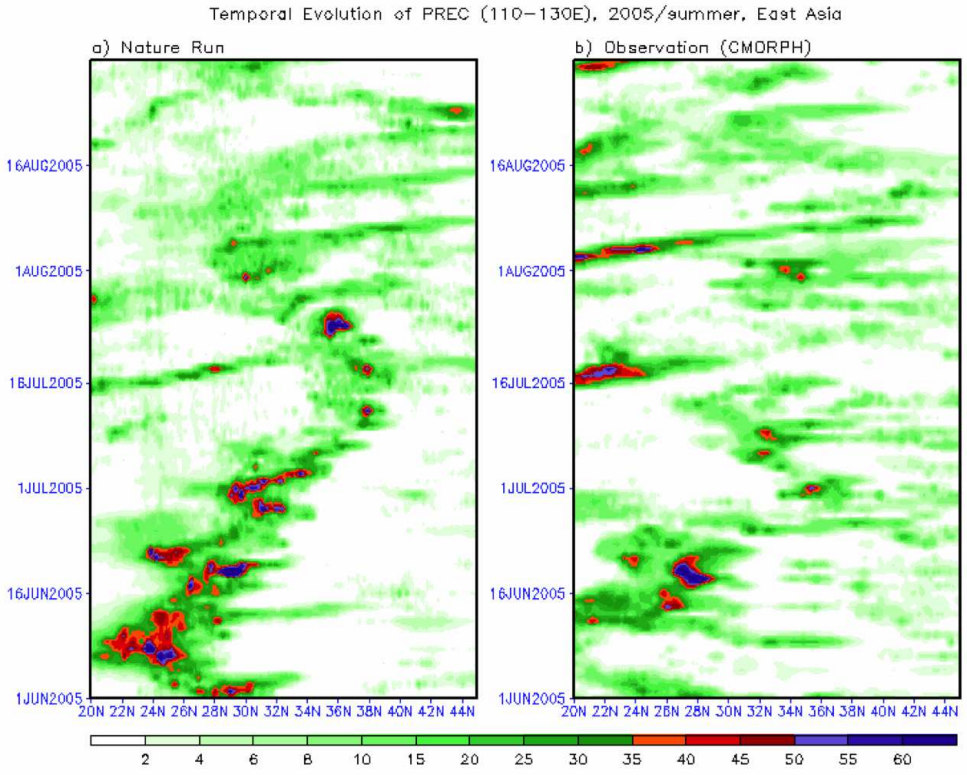

Figure 3.15: Northward progression of the East Asian monsoon precipitation during June through August 2005. Left is for the G5NR, and right panel is for the CMORPH observations. Units: mm day^{-1}.

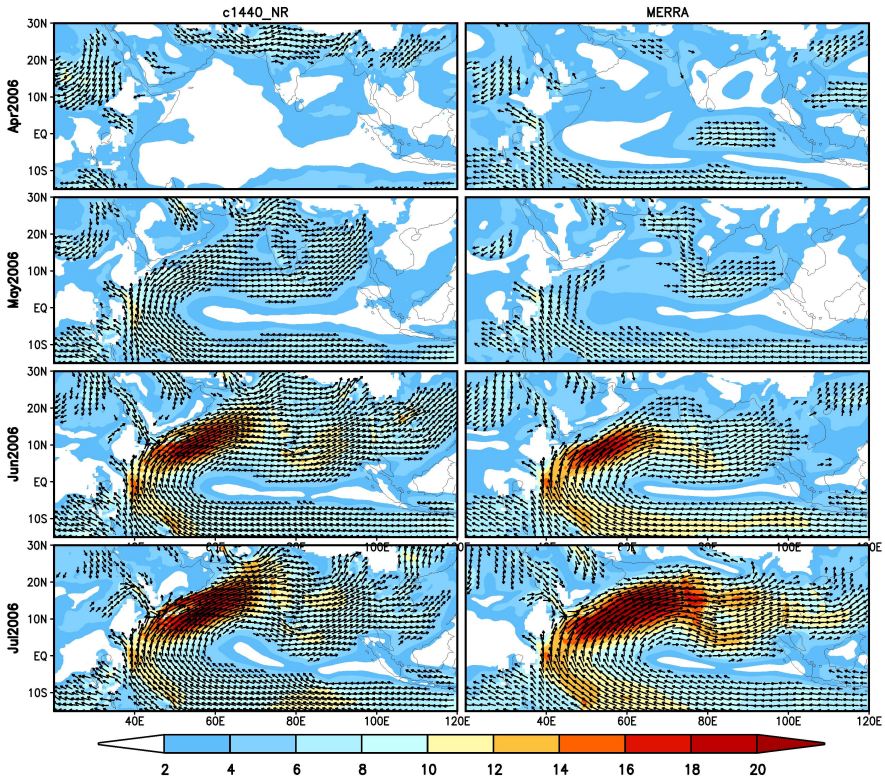

Figure 3.16: April through July 2006 wind vectors and speed at 850mb. Left is for G5NR, and right panel is for the CMORPH observations over southern Asia. Units: m s^{-1}

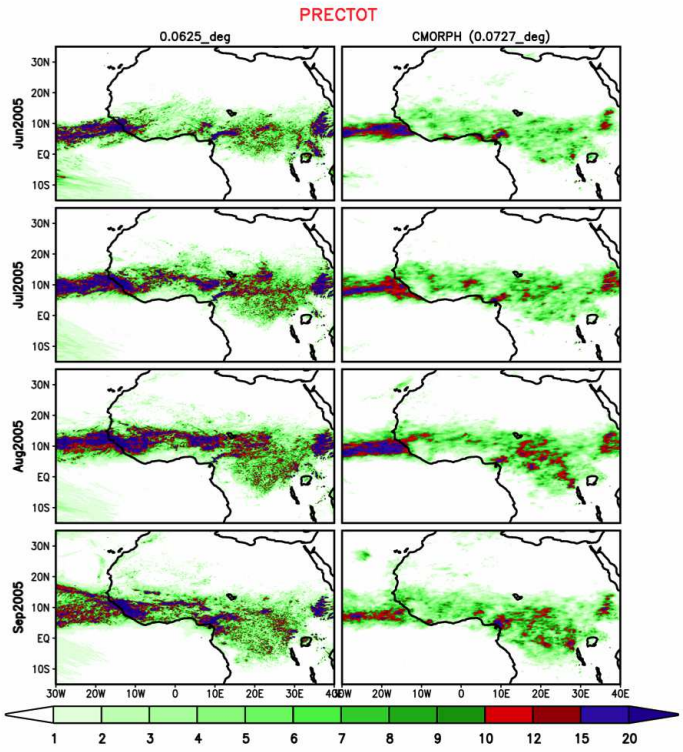

Figure 3.17: June through September 2005 precipitation over Africa. Left is for the G5NR, and right panel is for the CMORPH observations. Units: mm day^{-1}.

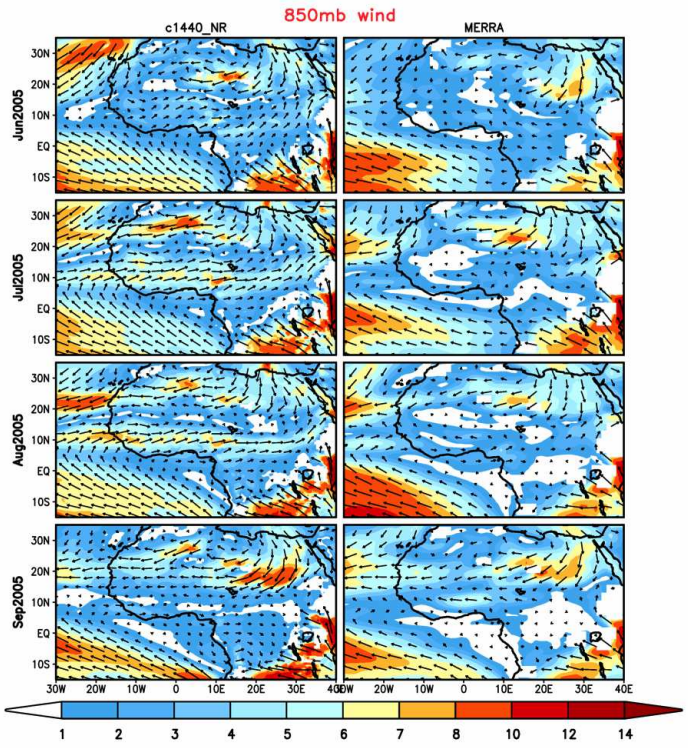

Figure 3.18: June through September 2005 wind vectors and speed over Africa. Left is for the G5NR, and right panel is for MERRA. Units: m $\sec^{-1}$.

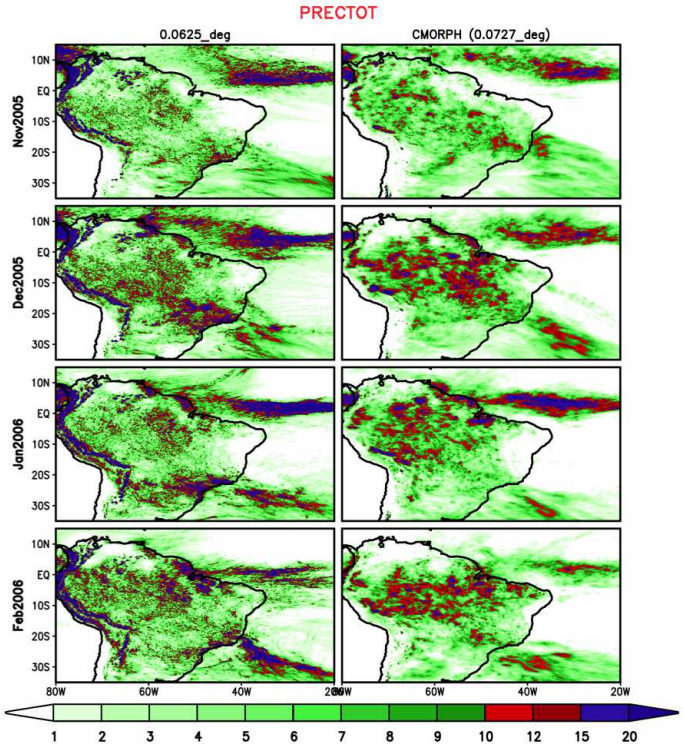

Figure 3.19: November 2005 through February 2006 precipitation over South America. Left is for the G5NR, and right panel is for the CMORPH observations. Units: mm day^{-1}

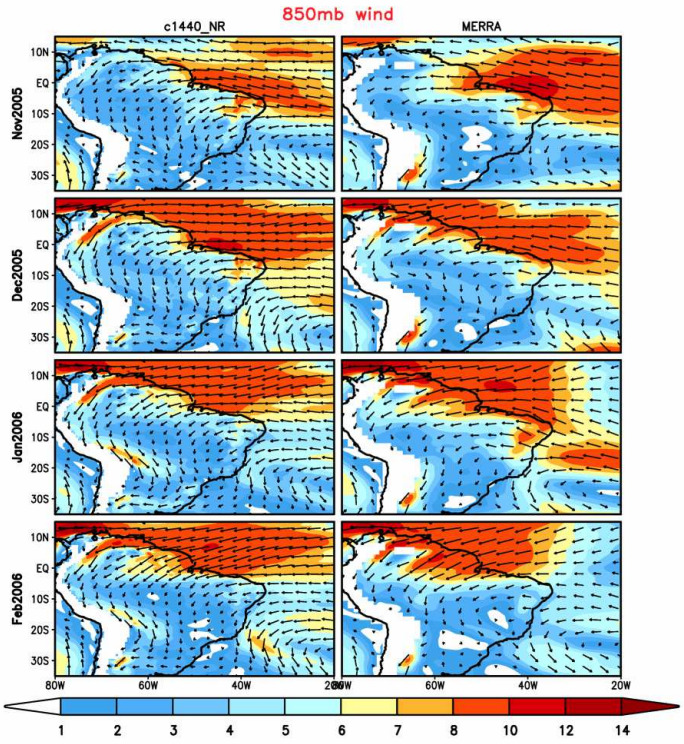

6

Figure 3.20: November 2005 through February 2006 wind vectors and speed over South America. Left is for the G5NR, and right panel is for MERRA. Units: m sec^{-1}.

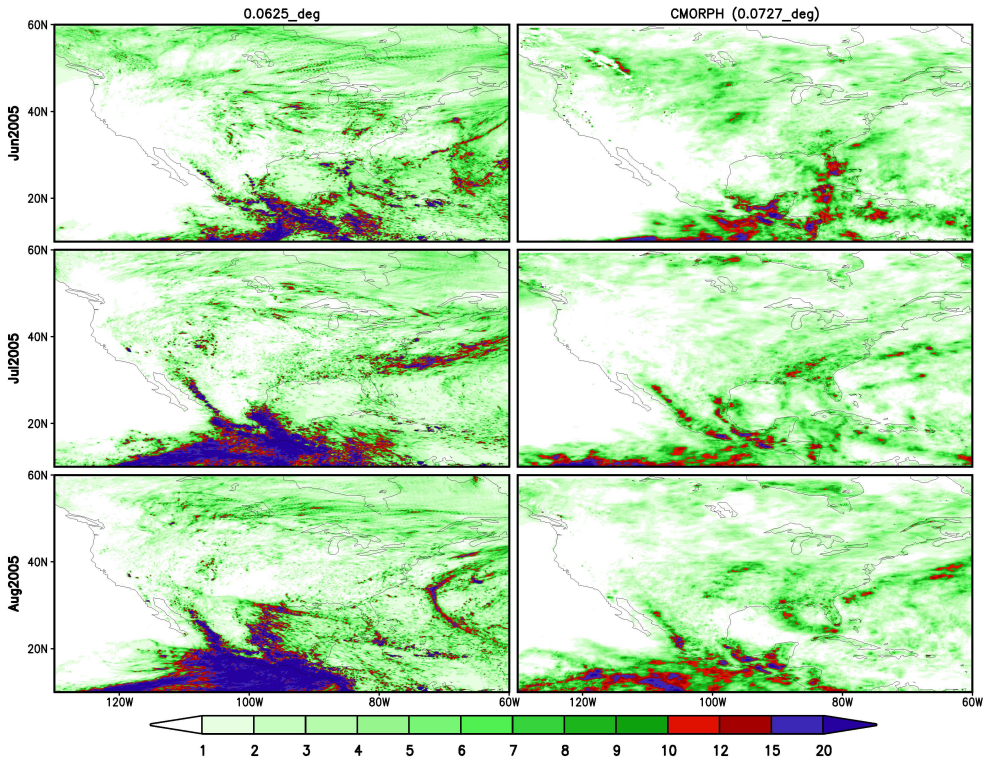

Figure 3.21: Simulated and observed monthly mean precipitation (June-August 2005). Units: mm day^{-1}.

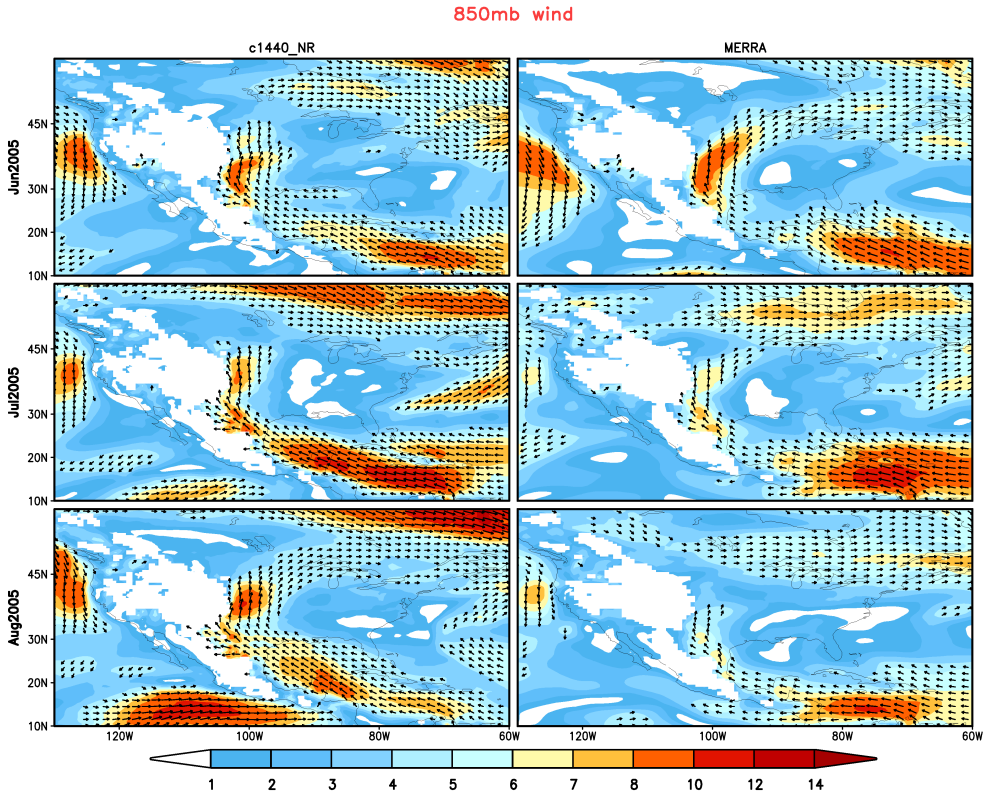

Figure 3.22: Simulated and observed 850mb winds (June-August 2005). Units: m $\sec^{-1}$.

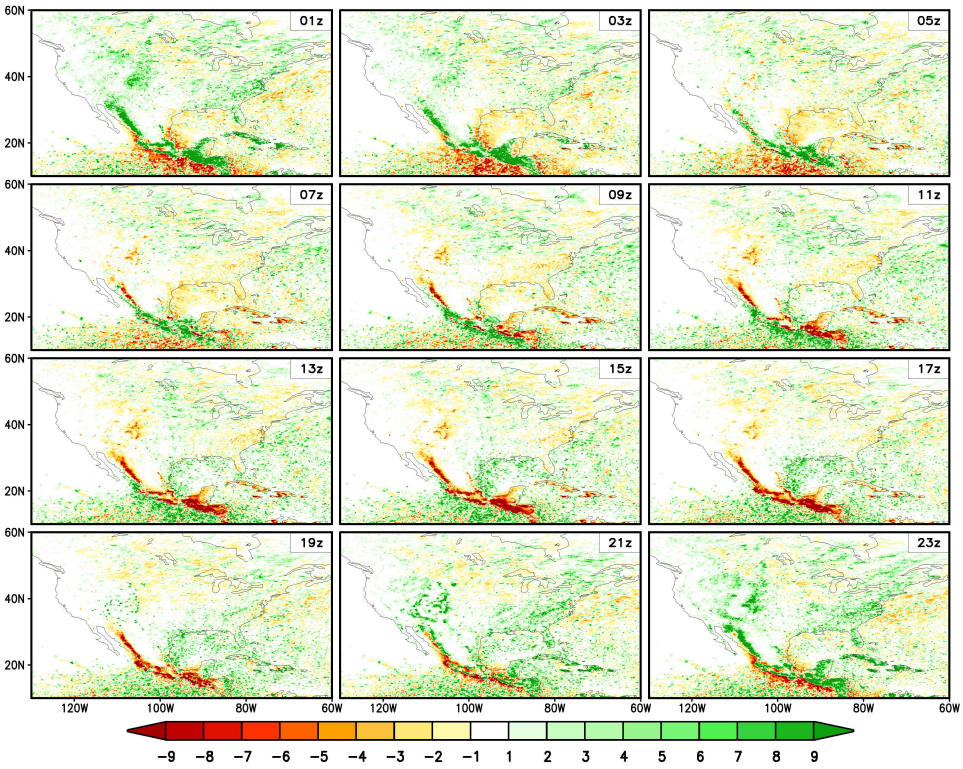

Figure 3.23: Time mean (JJA 2005 and 2006) simulated diurnal cycle of precipitation over North America. Units: mm day^{-1}.

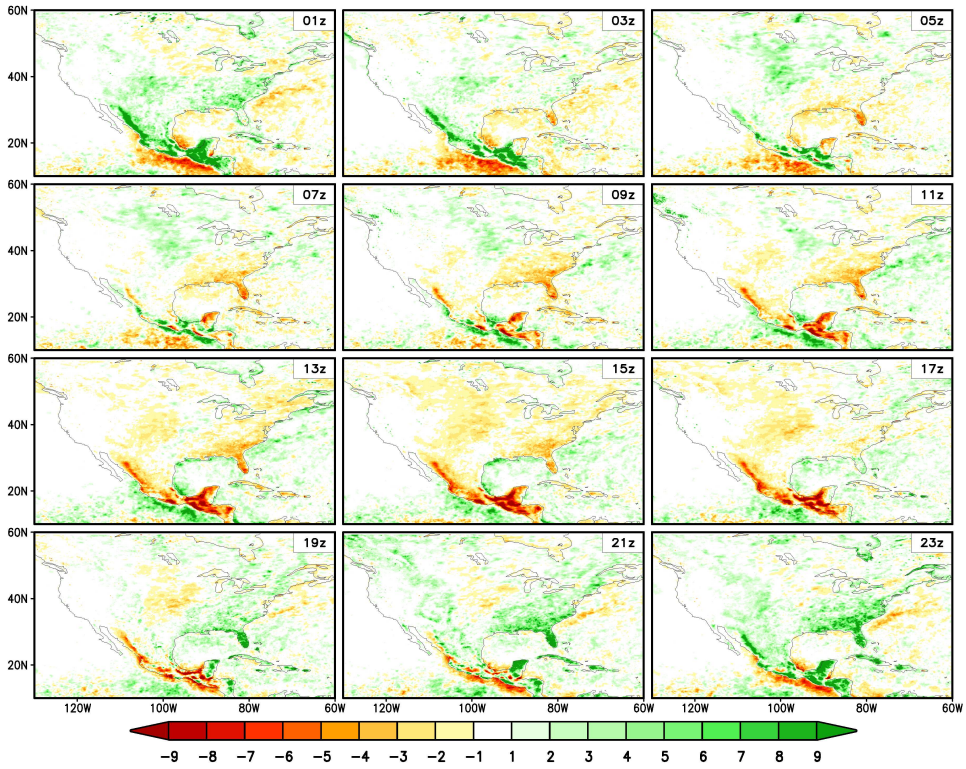

Figure 3.24: Time mean (JJA 2005 and 2006) observed (CMORPH) diurnal cycle of precipitation over North America. Units: mm day^{-1}.

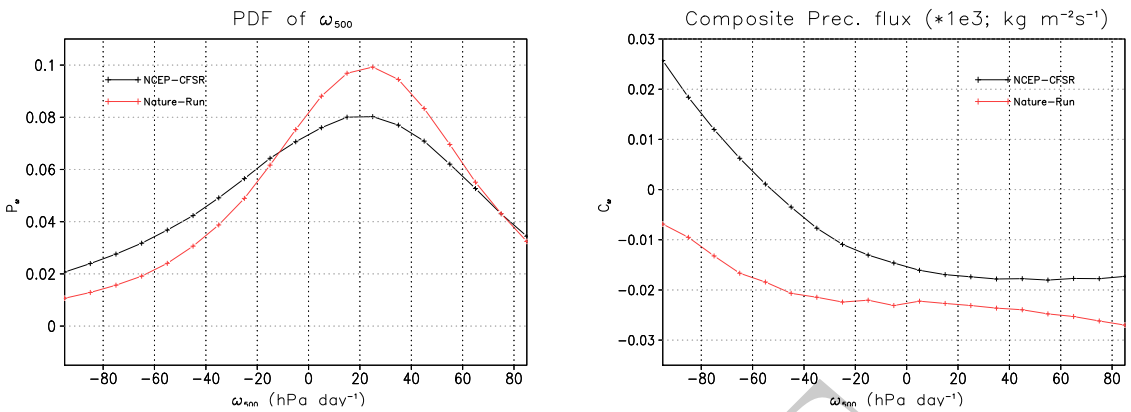

Figure 3.25: Probability distribution function (PDF) of diurnal mid-tropospheric vertical velocity (OMEGA500) hPa $\cdot$ day^{-1} and composite precipitation flux anomaly kg $\cdot$ m^{-2} $\cdot$ s^{-1} from CFSR & the G5NR in JJAS.

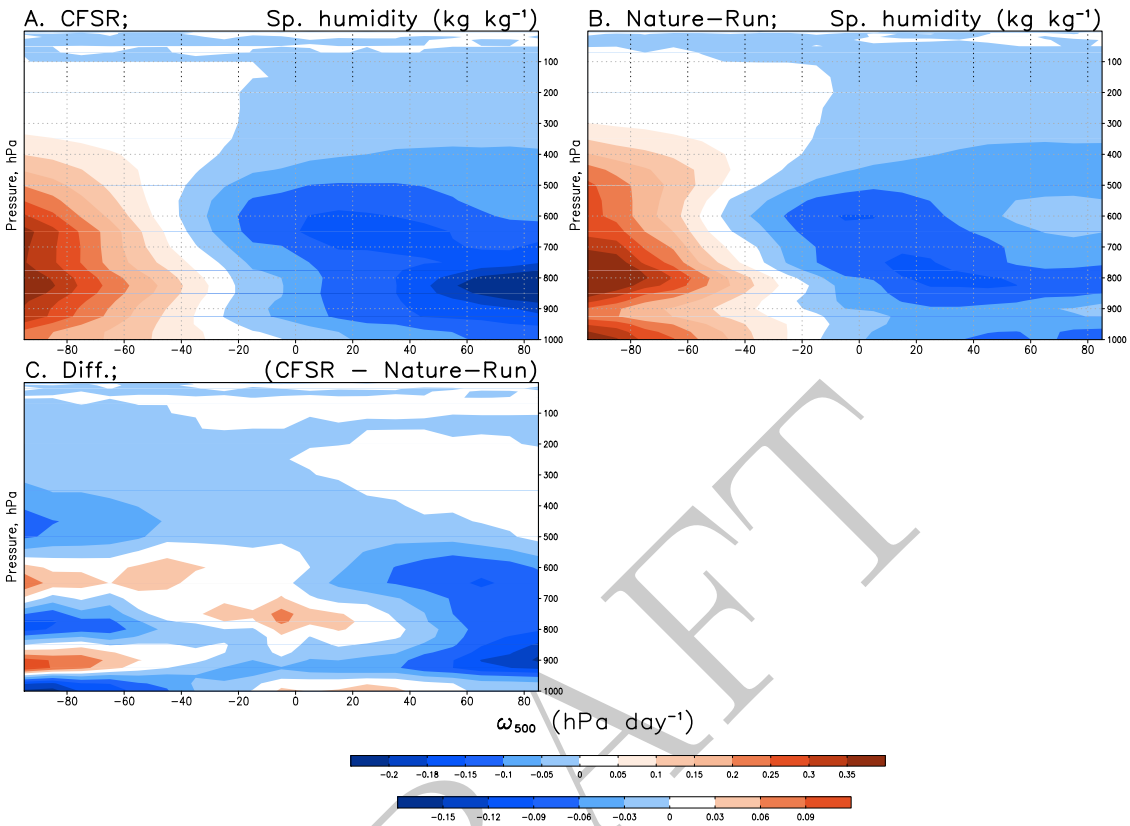

Figure 3.26: Composite specific humidity anomaly $\mathrm{kg} \cdot \mathrm{kg}^{-1}$ from A) the CFSR in JJAS B) the G5NR in JJAS C) the difference CFSR - G5NR in JJAS

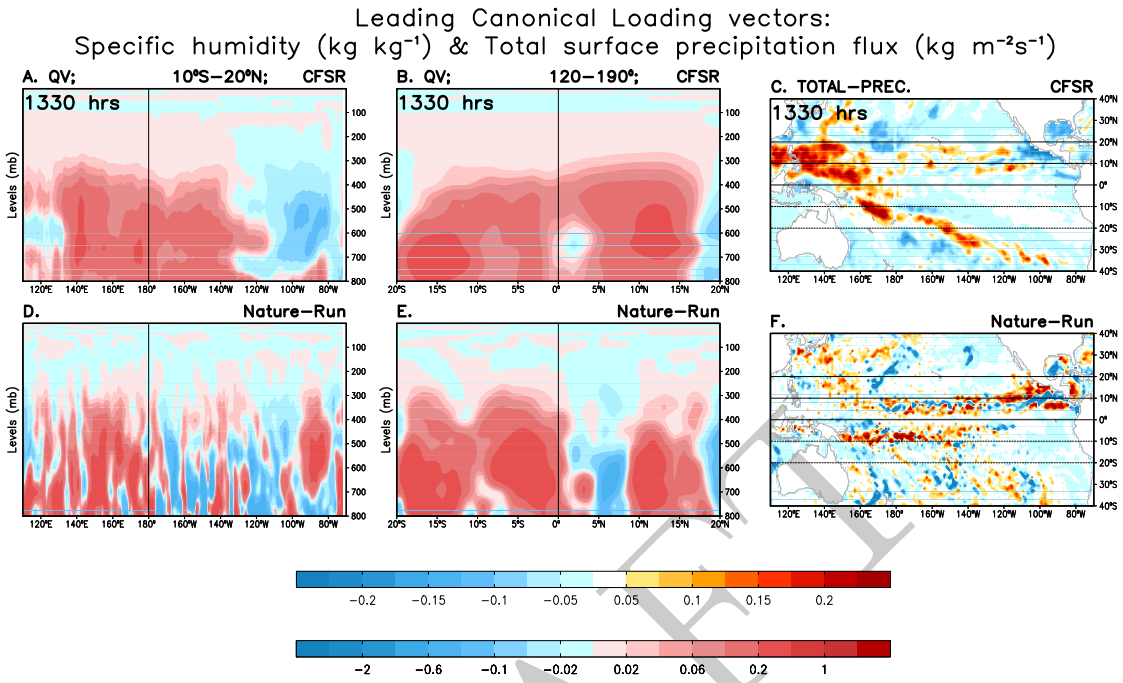

Figure 3.27: Leading CCA patterns of specific humidity $\mathrm{kg} \cdot \mathrm{kg}^{-1}$ and precipitation flux anomaly $\mathrm{kg} \cdot \mathrm{m}^{-2} \cdot \mathrm{s}^{-1}$ from A) the CFSR averaged between 10^oS - 20^oN B) the CFSR averaged between 120^o - 190^o C) the CFSR D) the G5NR averaged between 10^oS - 20^oN E) the G5NR averaged between 120^0 - 190^o F) the G5NR

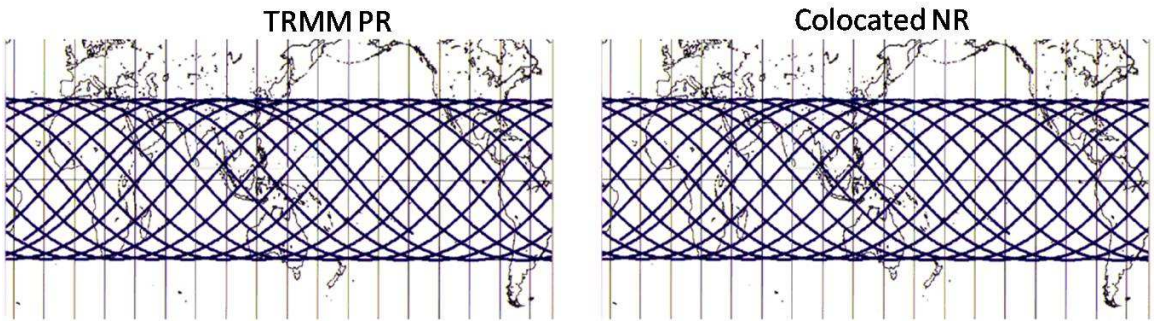

Figure 3.28: For comparisons with TRMM Precipitation Radar (PR) data, the G5NR precipitation is projected from the model domain to the PR observation points. Nearest-neighbor-in-time sampling of G5NR precipitation fields was performed to collocate data.

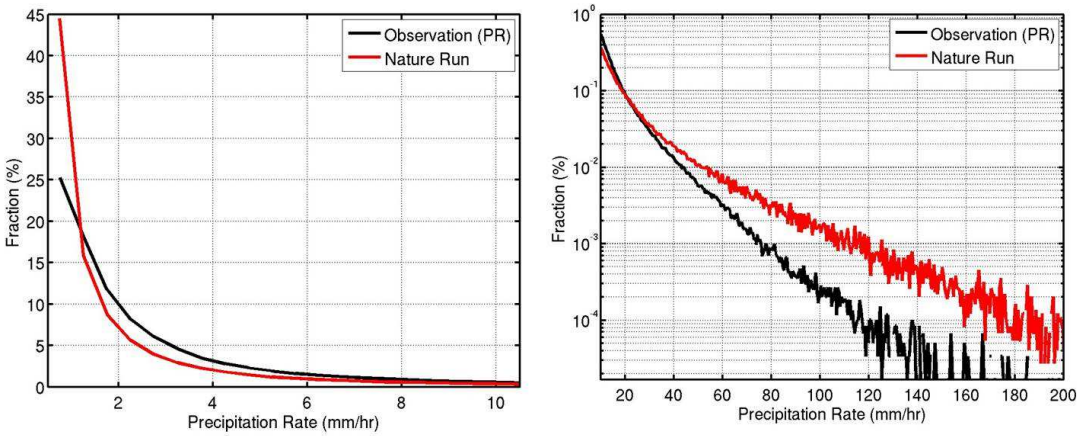

Figure 3.29: Comparisons of probability distribution of surface rain rates between the G5NR and TRMM PR data.

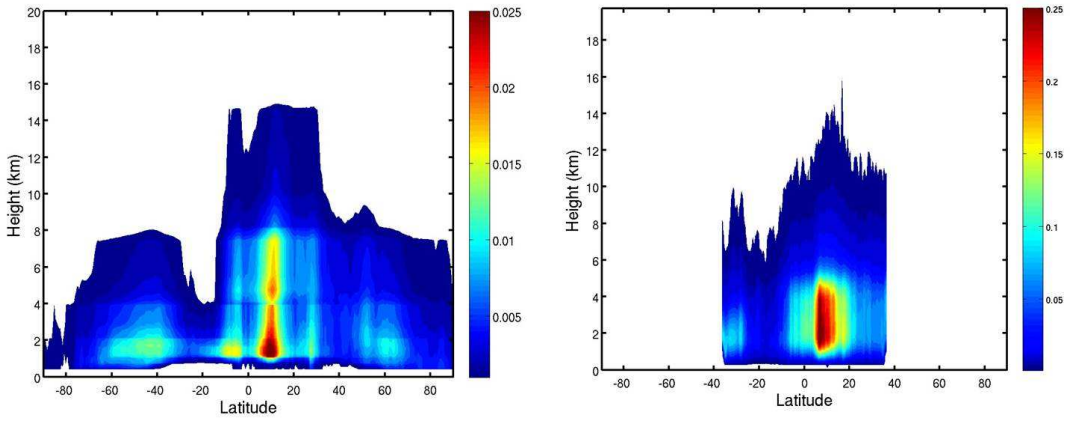

Figure 3.30: Comparison of vertical distribution of precipitation between the G5NR and TRMM Precipitation Radar data.

Chapter 4

Tropical Cyclones and Related Phenomena

Oreste Reale, Deepthi Achuthavarier, Gary Partyka and Marangelly Fuentes

Among the requirements of a nature run for use in OSSEs is "a realistic climatology consisting of *realistic weather patterns*" (McCarty et al. 2012). Different Instrument Science Teams may have different requirements for features that can be considered realistic. For example, the Science Team for Cyclone Global Navigation Satellite System (CYGNSS) could benefit from realistic OSSEs, as long as the nature run adopted can resolve wind fields on the scale of 10 km or less, particularly around high-impact weather features such as tropical cyclones (TCs) and intense extratropical disturbances. This chapter focuses TC activity in the G5NR over various basins (Atlantic, Eastern Pacific, North Indian and South Indian Oceans), as compared with observations. Elements of the circulation that are important in the formation of TCs, or in controlling their evolution, are also discussed. Finally, an example of an extra tropical transition is provided and future work is discussed.

4.1 Tropical Cyclone Activity and Structure in Previous Nature Runs

A previous nature run that has served the OSSE community for several years was produced by the European Centre for Medium-Range Weather Forecasts in 2006 (hereafter referred to as the ECMWF NR), and is documented, among other places, in Reale et al. (2007), Masutani et al.

(2010) and McCarty et al. (2012). It was produced at a T511 wave truncation, corresponding to a horizontal resolution of about 40 km at the equator. The ECMWF NR was considered one of the first free-running simulations, forced only by prescribed 2005 SSTs and sea-ice, which produced a realistic depiction of tropical cyclone activity. The activity was considered realistic because: 1) the average climatological factors that are conducive to cyclogenesis were present, and 2) the frequency, distribution, life cycle, and track of TCs were within observed climatological ranges. The evaluation of the ECMWF NR demonstrated not only that TCs were present, but that they originated out of realistic and very specific weather patterns and underwent realistic evolution and decay, including dissipation, landfall or extra tropical transition. Moreover, individual TCs displayed an overall realistic structure in terms of vertical alignment, presence of a warm-core, winds in excess of 50 $\mathrm{m\,s^{-1}}$ and an eye-like feature (i.e., a virtually windless column), as shown in Figure 4.1. While the eye-like feature was broader and more diluted than a real TC eye because of the relatively coarse resolution of the simulation, the ECMWF NR nevertheless has been an invaluable tool for the OSSE community for several years.

4.2 Tropical Cyclone Activity and Structure in the G5NR

4.2.1 Tropical Cyclones in the Atlantic

It is important to demonstrate that TCs occur in the G5NR not as sporadic or localized events, but as a realistic consequence of realistic large-scale forcings. The preliminary step is to verify that the climatology of the main dynamical players over the African Monsoon region and the tropical Atlantic is well represented. Figure 4.2 shows a meridional vertical cross-section of zonal wind at 0°, comparing the G5NR in the July, August, and September (JAS) months of two different years with the corresponding MERRA years. It is worth stressing that a comparison of monthly means cannot be interpreted as an actual seasonal forecasting validation. Since the G5NR is a free-running simulation constrained only by SSTs, and in which the memory of initial conditions is removed by the sufficiently long spin-up, a strict correspondence with observed means should not be expected. It can only be noted that the G5NR represents the basic features of the African Monsoon circulation, namely: a) the Tropical Easterly Jet (TEJ), an upper-tropospheric jet located at about 100–200 hPa, b) the African Easterly Jet (AEJ) at about 600 hPa and peaking at about 12°N–16°N, c) the low-level westerly monsoonal flow confined below 800 hPa, and finally d) the low-level easterly flow (also known as Harmatthan flow) at about 27°N. The overall depiction of the AEJ in the G5NR is about 20% weaker than in MERRA, but it should be remembered that the AEJ depiction is affected by very large uncertainties, with differences of 20% in speed even among *state-of-the-art reanalyses* such as ERA-40, NCEP-R2, JRA-25 and MERRA, as discussed in detail in Wu et al. (2009) and in Wu et al. (2012).

Aside from the intensity, the position of AEJ, TEJ and low-level monsoonal flow is very important because the cyclonically-sheared southward side of the AEJ (in which horizontal shear dominates) is conducive to barotropic instability at about the jet level, while the lower levels below the AEJ

(in which vertical shear dominates) are conducive to baroclinic instability. African Easterly Waves (AEWs) arise out of a combination of mechanisms: the presence of localized triggers, which can be convective in nature and may alter the vorticity and thermal profile of the atmosphere, and the favorable large-scale environment in which barotropic-baroclinic instability of the Charney-Stern type can occur (e.g., Kiladis et al. 2006; Hall et al. 2006; Thorncroft et al. 2008; Wu et al. 2012). Moreover, the presence of the TEJ, which is responsible of strong easterly shear and is generally unfavorable for development of vertically aligned structures, is an important player that confines the potential development of TCs to a narrow latitude range (just few degrees south of the AEJ and north of the Inter Tropical Convergence Zone). The presence of all the fundamental elements of the African Monsoon region atmospheric circulation is a good preliminary assurance that the model may be capable of producing realistic weather patterns.

The next logical step is to verify whether the G5NR is able to produce realistic AEW activity. This is a complex issue because at least three types of AEWs are currently known: the 2.5–6 day waves developing to the south of the AEJ at about the jet level, the low-level baroclinic wave developing below the AEJ, and less known 6–9 day waves developing at the AEJ level to the north of it. For a comprehensive discussion of various types of AEWs, see Wu et al. (2013). The AEWs that are more relevant to TC development are the 2.5–6 day waves developing to the south of the AEJ at about the jet level. In addition, the tracking or definition of AEWs may involve sophisticated objective methodologies (i.e., Berry et al. 2006) or the use of spectral techniques such as the Hilbert-Huang transform (Wu et al. 2013). However, a very simple way of detecting them is to plot a latitude-time Hovmøller diagram of the meridional component of the wind at or slightly below the jet level, and at a latitude south of the jet.

In Figure 4.3 the 700 hPa Hovmøller obtained from the G5NR for the months of August 2005 and 2006 is plotted for the latitude of 15°N and for a longitude range spanning from 40°W to 40°E and can be compared with Figure 4.4 where the same quantities are computed from MERRA data. The comparison reveals that in both the G5NR and reanalyses, the amplitude, frequency and propagation speed of the AEWs are the same. In particular, waves occur at a given longitude approximately every 3–6 days, they propagate westward at a speed of about $5°–8°\,d^{-1}$. Other features of the AEWs as produced by the G5NR and present also in MERRA include a discontinuity at about 15°W in correspondence to the African coastline, where the transition of disturbances from land to ocean is observed and a pronounced diurnal cycle (evident by the horizontal lines on the easternmost side of the panels). Other realistic features that can be noted in the AEWs as produced by the G5NR, are: a) occasional higher wind speeds, indicating the tendency of some AEWs to develop as TCs, b) upward curvatures (indicating acceleration) and c) disappearance (indicating either dissipation or disturbances which move to the north of the affected latitude). Aside from the higher detail present in the G5NR due to the much higher resolution, the similarity between the AEW activity as produced by the G5NR and the reanalyses is remarkable. Comparison with other months (e.g., July and September) reveal a similar correspondence between G5NR and MERRA (not shown).

The next step is to investigate TC number, tracks, distribution and life cycles. Figure 4.5 shows the tracks of TCs in the G5NR for 2005 and their center pressures. Only 'pure' TCs are plotted,

and their extra-tropical transitions are not followed. A caveat should be inserted. The storm detection algorithm involves parameters such as center pressure and presence of warm core. The use of 'thresholds' can modify the number of detected storms. In particular, it was found that less stringent thresholds in terms of warm-core intensity allow many more (weaker) depressions to be detected as TCs, especially over the Indian Ocean. For clarity, it was decided to concentrate on stronger storms, and use the same more stringent criteria throughout all basins, which led to a slightly lower total number of TCs. Individual researchers can alter these criteria according to their needs, and may be able to detect a slightly higher number of TCs than the 17 TCs shown in Figure 4.5 by including some weak systems at a tropical depression intensity level. The choice of thresholds in the TC-detecting algorithm also affects a hurricane's life span: a system undergoing transition can be categorized as extra tropical (or still tropical) with a more (or less) stringent threshold. Since we have consistently used a stringent definition of TC, it should be noted that some TC tracks could be prolonged if less restrictive tracking choices were to be adopted.

Figure 4.6 shows the observed 2005 TC tracks and center pressures for the Atlantic, obtained from the National Hurricane Center HURDATA2 best track database available at

`http://www.nhc.noaa.gov/data/#hurdat`

which contains 6-hourly center pressure, winds, and location (Sampson and Schrader 2000). Retrospectively classified storms and non-developing depressions are not included in this plot. While the TCs produced by the G5NR are less than observed (17 versus 27, with the latter being an all-time record), the track distribution in the G5NR is very realistic. The majority of the TCs are of the Cape Verde type, tracking across the Atlantic and recurving north. Two TCs originate in the Gulf of Mexico, leading to an overall very realistic partition between Gulf and Atlantic systems (e.g., Asnani 2005). One system (TC 17) originates in the westerlies, as typical for late-season hurricanes. It is particularly noteworthy that four TCs reach central pressures of less than 945 hPa, in good agreement with the observations for that year.

The comparison with the 2006 season, which was much less active (Figures 4.7 and 4.8), shows that the G5NR produces only 10 TCs in 2006 (against 9 observed). It should not be expected that a free-running model forced only by SST produces the same number of cyclones as in observations, since there are many factors controlling TC frequency other than SST. Moreover, as previously said, the choice of the detection algorithm affects the TC number. However, the fact that the model-generated natural variability compares well with the observed variability, is remarkable. For reference, it should be noted that the ECMWF NR produced only 12 TCs with 2005 SSTs (Reale et al. 2007).

While, as noted before, a rigorous correspondence between observed and modeled storms cannot be expected, the fact that the interannual variability in the G5NR has the same sign as the observed one suggests that SST alone, as is reasonable to expect, exerts some control on TC number. As noted for 2005, the distribution of tracks is realistic, with a majority of Cape Verde systems, and four storms forming in the Caribbean or in the Gulf.

In both years the TCs produced by the G5NR display a life time spanning from a few days to less than two weeks. Individual tracks reveal singularities (i.e., sharp curvature changes) as well as binary interaction (i.e., two cyclones rotating around a common center with the stronger one moving at a lower speed, not shown), all features that are well known to forecasters and that frequently occur in nature.

The final step in the investigation consists of examining the individual structure of the most intense storms taken at representative times.

Figure 4.9 shows a zonal cross-section of wind and temperature across TC 2 (from map in Figure 4.5) taken at 1800 UTC 17 September 2005. The expected features of a mature hurricane can be noted: a perfectly aligned structure, with wind speeds in excess of 65 $\mathrm{m\,s^{-1}}$, a strong warm core (greater than 12°C), a spatial scale on the order of few hundreds of km, a radius of maximum wind on the order of about 40–50 km, and and a distinct eye-like feature with a very clear windless column. The overall structure is very realistic and represents an improvement with respect to the hurricane seen in Figure 4.1, which was the best produced by the ECMWF NR.

The very realistic representation of TC 2 is not an isolated occurrence in the G5NR. The subsequent Figures 4.10 and 4.11 display two different snapshots of 2005 hurricanes in the G5NR: TC n. 9 and TC n. 12, taken at an early development stage, and at a mature stage, respectively. Both display the same realistic features: perfectly calm central column, vertical alignment, scale on the order of hundreds of km, radius of maximum wind on the order of tens of km, and pronounced warm core. Interestingly, the snapshot depicting the strongest and most mature hurricane (Figure 4.11), whose warm core temperature anomaly exceeds 14°C, is also the one characterized by the tightest and most narrow eye-like feature, in agreement with the well-known fact that TCs reduce their scale during intensification, with the strongest systems displaying the most narrow and confined eyes (e.g., Asnani 2005).

4.2.2 Tropical Cyclones in the Eastern Pacific

The seasonal activity and presence or interannual variability of TCs have been investigated in the G5NR for other basins where global models typically have more difficulties, even in assimilation mode. Figures 4.12 and 4.13 compare the Eastern Pacific TC activity for 2005, while Figures 4.14 and 4.15 depict the corresponding activity for 2006. Given the same caveats about the TC detecting and tracking algorithm previously noted, and the fact that by choosing a less restrictive definition of TC, more weaker TCs and longer tracks could be detected, the results suggest that interannual variability is reasonably reproduced by the G5NR, with more TCs in 2006. In fact, the number of observed TCs in 2005 and 2006 were 14 and 18, respectively, as compared with 8 and 19 in the G5NR. As for TC genesis, the region between 90°W and 120°W, and between 10°N and 15°N, is the favorable location in both the G5NR and observations, with a predominant TC motion towards the west-north-west. However, the presence of outliers and TCs displaying erratic or retrograde motion with respect to the easterly flow (known to forecasters), is not captured very

well by the G5NR, with TCs displaying less track variability than observed.

While the investigation of the Western Pacific tracks is ongoing, an overall assessment of the dynamics over the Pacific seems to suggest that this basin is more penalized than others by prescribed SSTs and the resulting inability of surface fluxes to respond and adapt to the atmospheric forcing. However, in spite of the absence of air-sea interaction which could be represented only by a coupled model, it should be noted that some important atmospheric circulation elements which were missing in previous nature runs (see Reale et al. 2007) are represented in the current one. Notable among these are features resembling westerly bursts. Figure 4.16 compares the equatorial zonal wind at approximately 950 hPa in the G5NR and MERRA for August 2006. Ideally, a time-longitude plot of unfiltered equatorial wind across the Pacific reveals, in the midst of predominantly easterly flow, two sets of lines, representing propagating anomalies: peaks of increased easterly speed which travel within the easterly flow, moving from east to west, and regions of decreased easterlies (or westerlies) which travel against the easterly flow, moving from west to east. When these anomalies are stronger than the mean flow they appear as eastward-propagating westerly anomalies and are aptly named 'westerly bursts'. Westerly bursts are associated with the Madden-Julian oscillation (MJO, Madden and Julian 1971, 1972) but are strongly controlled by other factors, first and foremost the phase of the ENSO. Transitioning ENSO can affect the clarity of an MJO unfiltered signal. The 2005 and 2006 summers were not particularly representative in terms of the MJO signal, with the ENSO phase transitioning from positive to negative (2005) and then from negative to positive (2006). However, evidence of westerly bursts (i.e., eastward moving areas of westerly wind) is nevertheless clear in Figure 4.16 particularly to the west of the date line. While the G5NR underestimates the intensity of the westerlies, it is important to note that these bursts have not been detected by this team in other non-coupled global simulations.

4.2.3 Tropical Cyclones in the Northern Indian Ocean

The Northern Indian Ocean is arguably the most difficult basin for TC forecasting. Even objective analyses can provide poor representations of existing TCs in this region, as in the 2008 case of Nargis discussed by Reale et al. (2009). Free-running models examined by this team, including but not limited to the ECMWF NR, have produced results ranging seasons without a single storm in the Northern Indian Ocean, to seasons in which up to 40 TCs were simulated. The latter, unrealistically large number of TCs is probably due to extreme model sensitivity to small changes in the circulation. In fact, the SSTs over the Indian Ocean are extremely warm (often more than 30°C) but the environment is not generally conducive to TC development because of the very strong shear. Moreover, during the summer, the low-level circulation is controlled by the Somali Jet (SJ), with southwesterly flow peaking at about 900 hPa in connection with the Indian Monsoon (e.g., Krishnamurti et al. 1976, Halpern and Woiceshyn, 2001), while the upper level circulation is controlled by the TEJ, with easterly flow peaking at about 150 hPa (e.g., Chen and van Loon 1987, Nicholson et al. 2007) creating zonal shear values of up to -40 $\mathrm{m\,s^{-1}}$ or more. In spite of the huge fluxes consequent to the very warm marine temperature, and the environment being extremely conducive to convection, cyclonic circulations cannot generally overcome the vertical shear except in very rare situations when the shear relaxes and very sudden development can occur. Other cases

show TCs which cannot fully overcome the shear and present shallow structures which keep being eroded above 300 hPa by the upper-level easterly flow. In this environment, which essentially has surplus energy available but hostile dynamical forcing, small errors in the representation of the shear can lead to large errors in the depiction of TC activity.

With this in mind, it is easier to appreciate the representation of TC activity in the G5NR over the northern Indian Ocean. Figures 4.17 and 4.18 compare the representation of the Somali Jet in 2006 (2005 does not offer a significantly different situation, and is not shown). It can be noted that the predominantly easterly flow over the southern hemisphere is deflected northward and then northeastward by the combining effect of the Indian monsoon low and the orography of eastern Africa, in agreement with observations and other modeling studies (e.g., Chakraborty et al. 2009). It also is worth noting that the higher resolution of the G5NR allows a sharper depiction of the SJ than MERRA, including the well-known bifurcation caused by the 'Horn of Africa'. Most interesting is the SJ vertical structure. From aircraft measurements acquired during campaigns such as Monsoon Experiment (MONEX 79; e.g., Holt and Sethuraman 1985) it is known that the SJ is a very shallow feature, peaking at about 10°N–15°N and about 875 hPa and disappearing at about 600 hPa. These features are clearly represented in Figure 4.19 and are confirmed by the reanalyses (Figure 4.20).

Probably because of the overall realistic rendering of the *mean* SJ in the G5NR, the representation of the Northern Indian TC activity has improved with respect to previous long simulations. Figures. 4.21, 4.22, 4.23 and 4.24) show a total of 4 TCs in 2005 in the G5NR versus 7 that were observed, and 6 in 2006. However, given the fundamentally erratic nature of TCs over that basin, the spatial distribution of TCs and their tracks vary significantly. As noted previously, very small lapses in the shear can very quickly trigger a TC genesis process, making it extremely difficult overall to predict TCs in the northern Indian Ocean. In terms of vertical structure, the G5NR displays a significant number of non-fully developed systems, or systems fighting against shear, in agreement with climatology (not shown).

4.2.4 Tropical Cyclones in the Southern Indian Ocean

Over the Southern Indian Ocean, the G5NR produces very realistic activity (Figures 4.25, 4.26, 4.27 and 4.28) not just in terms of overall number, but in terms of track distribution. TCs generally form between 5°S and 15°S (except for a few originating to the west of Madagascar) and track southward or westward, gradually recurving eastward under the westerly flow influence, but displaying frequent singularities in their tracks, such as loops, sharp recurvatures and binary interactions. The G5NR exhibits a very convincing spectrum of TC tracks over this basin. Finally, a zonal vertical cross section of wind and temperature across a mature TC reveals the high degree of consistency between TC structures produced by the G5NR over *all* basins (Figure 4.29): the system is very symmetric, with a pronounced warm core, winds in excess of 65 $\mathrm{m\,s^{-1}}$, a very well-defined eye, and a radius of maximum wind on the order of 45 km.

4.3 Other Significant Weather Phenomena

4.3.1 Example of Tropical-Extratropical Transition

Important weather phenomena that may be of interest to scientists developing OSSEs for future instruments are TCs that undergo extra-tropical transitions (ETs). During ET, a warm-cored cyclone evolves into a larger scale baroclinic system undergoing a number of transformations that involve, among others, a change in its primary energy source from latent heat to baroclinic energy conversion processes (e.g, Sinclair 1993; Kyle and Bosart 2014). This evolution typically takes on the order of two to three days and is marked by an expansion of the low-level wind field, the development of frontal structures (particularly a warm frontal-like band poleward and downstream of the vortex), and a more asymmetric distribution of precipitation about the cyclone.

A representative case of a deep warm-core tropical cyclone that undergoes ET in the G5NR is highlighted in Figure 4.30. This figure illustrates the four primary stages of such an event from incipient tropical genesis, maximum warm-core peak intensity, early ET, and finally mature ET. In Figure 4.31 we see the tropical cyclone just east of 150°E on the northern fringe of supportive SSTs. Upstream of the cyclone, a deep mid-latitude trough is found in a favorable position to induce the cyclone to undergo ET. The upstream trough is neither too close to the tropical cyclone to quickly absorb it, nor too far upstream to have limited baroclinic effects on the cyclone prior to its reaching colder SST's (and thereby leading to rapid decay). Figure 4.31b provides further evidence of a fully mature ET, with a classic frontal "T-bone" structure in the precipitation and wind fields, especially sharp and concentrated about the warm-frontal feature along 52°N. Also noteworthy is the asymmetric distribution of rainfall near the southwest quadrant of the vortex.

4.3.2 Ongoing Validation of Other Mesoscale Features

While a realistic representation of large-scale baroclinic cyclones and their statistics is certainly not a novelty in long simulations, even at much lower resolutions, (and is not discussed in this chapter) there are other atmospheric features that, even if not fully tropical, are seldom captured in global models and are therefore worthy of mentioning as being of interests for OSSE work.

One such feature is the Mei-Yu front, which is a baroclinic area strongly convective in nature, resulting from the interaction of the Asian monsoon with mid latitude circulation, and stretching from west-south-west to east-north-east along from the Chinese coast into the Pacific. Generally studies of the Mei-Yu front have been performed with mesoscale models, but our analysis provides evidence that the G5NR can provide a representation of the Mei-Yu (not shown).

Other interesting features typically absent or misrepresented in lower-resolution GCMs are polar and arctic lows. These sub-synoptic scale vortices display strong similarities with hurricanes, even

if developed at high latitudes. Similarities include some level of vertical alignment, the presence of an eye-like feature, a prominent role played by convection, and latent and sensible total heat fluxes that can reach values comparable to hurricanes, even if with larger a contribution from the latter (e.g., Rasmussen and Turner 2003). A somewhat intermediate category between fully tropical cyclones and polar lows is represented by Mediterranean tropical cyclone-like vortices (e.g., Reale and Atlas 2001). All these types of events have been observed in the G5NR and will be the subject of future detailed investigations.

4.4 Summary

The G5NR has been evaluated with respect to tropical cyclone activity and other tropical weather phenomena. It was noted that a viable nature run must be able to produce TCs which arise out of very precise large-scale forcings. The presence in the G5NR of the important dynamical features over the African Monsoon region and the tropical Atlantic has been confirmed. The production of African Easterly Waves in the G5NR compares well to reanalyses. The investigation reveals that the G5NR captures the fundamental aspects of TC activity in all relevant basins (Atlantic, Eastern Pacific, North Indian Ocean and South Indian Ocean), producing realistic numbers of TCs with realistic tracks and life spans. The Atlantic TC seasons as depicted in the G5NR for 2005 and 2006 show interannual variability consistent with observations, with more storms in 2005. Over the Pacific, the presence of westerly bursts in the G5NR is confirmed. Over the Indian Ocean it is found that the G5NR contains a realistic depiction of the Somali Jet in both years. An example of a TC undergoing realistic extratropical transition was also presented. Our results confirm that the G5NR is well suited for OSSEs targeting (but not limited to) tropical cyclones and represents a vast improvement with respect to previous long simulations that have served the OSSE community for several years.

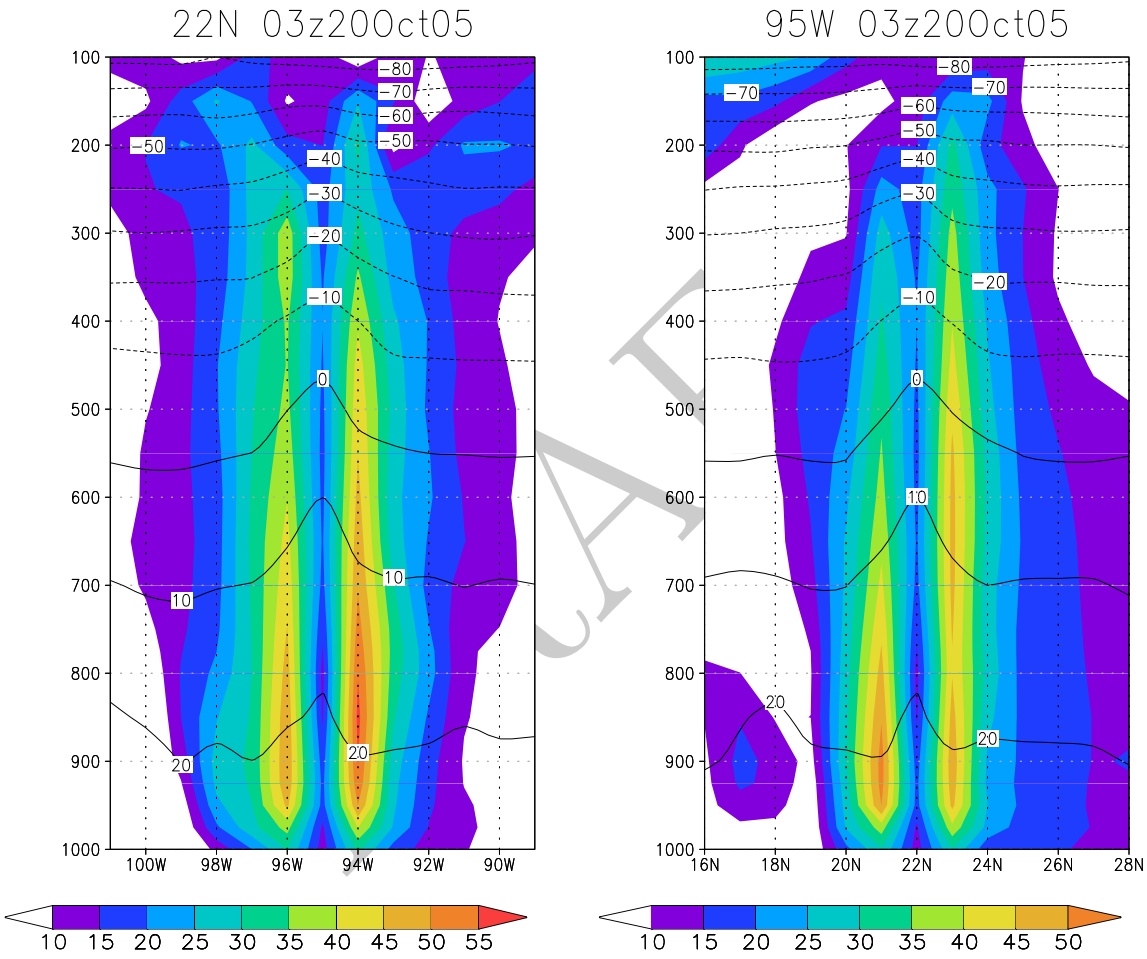

Figure 4.1: Zonal and meridional vertical cross-sections of winds (shaded, $\mathrm{m\,s^{-1}}$) and temperature (black contours, °C) for the strongest Atlantic tropical cyclone in the ECMWF NR. The ability to produce features closely resembling TCs without "bogusing" or insertion of any data was considered remarkable for a free-running model (e.g., Reale et al. 2007), and has represented the reference for next-generation NRs.

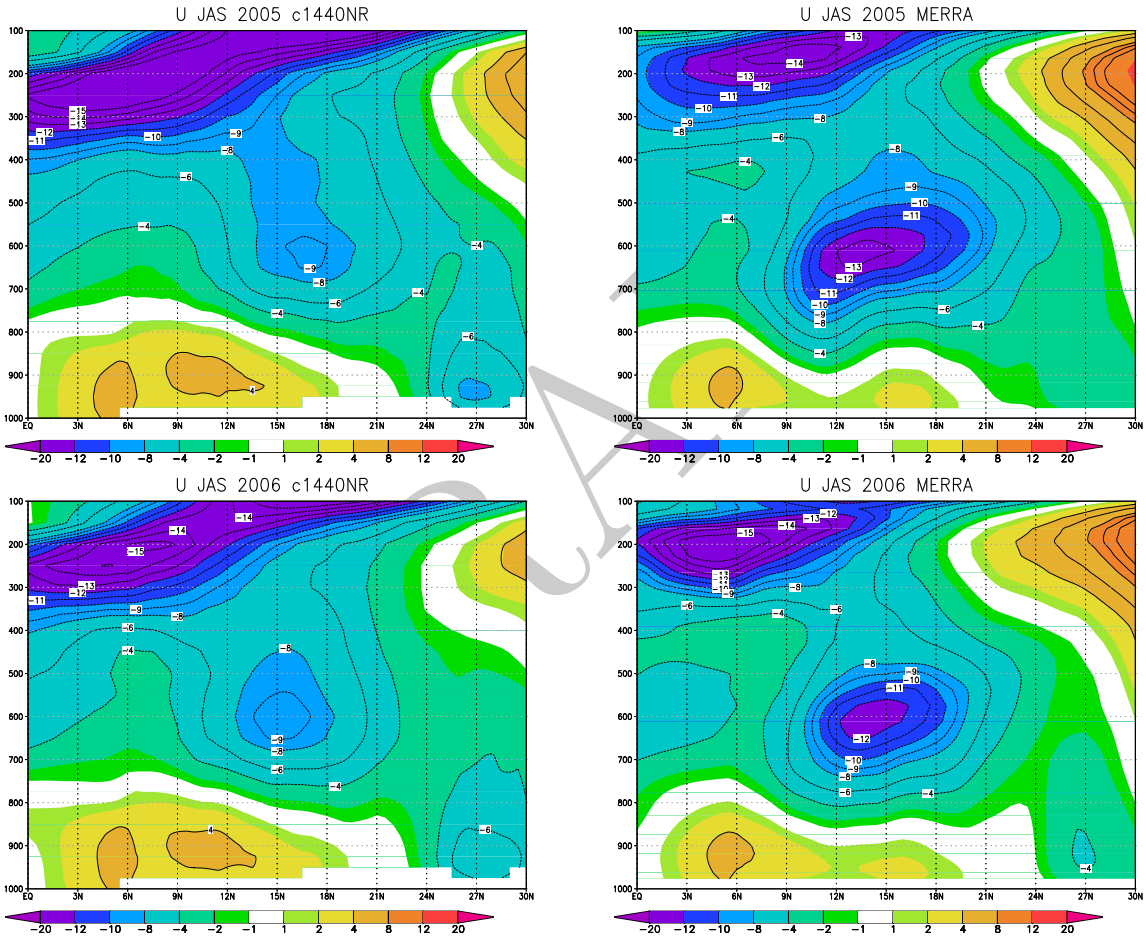

Figure 4.2: Vertical meridional cross section of zonal wind at 0° longitude ($\mathrm{m\,s^{-1}}$) in the G5NR (left) and MERRA (right), for 2005 (above) and 2006 (below).

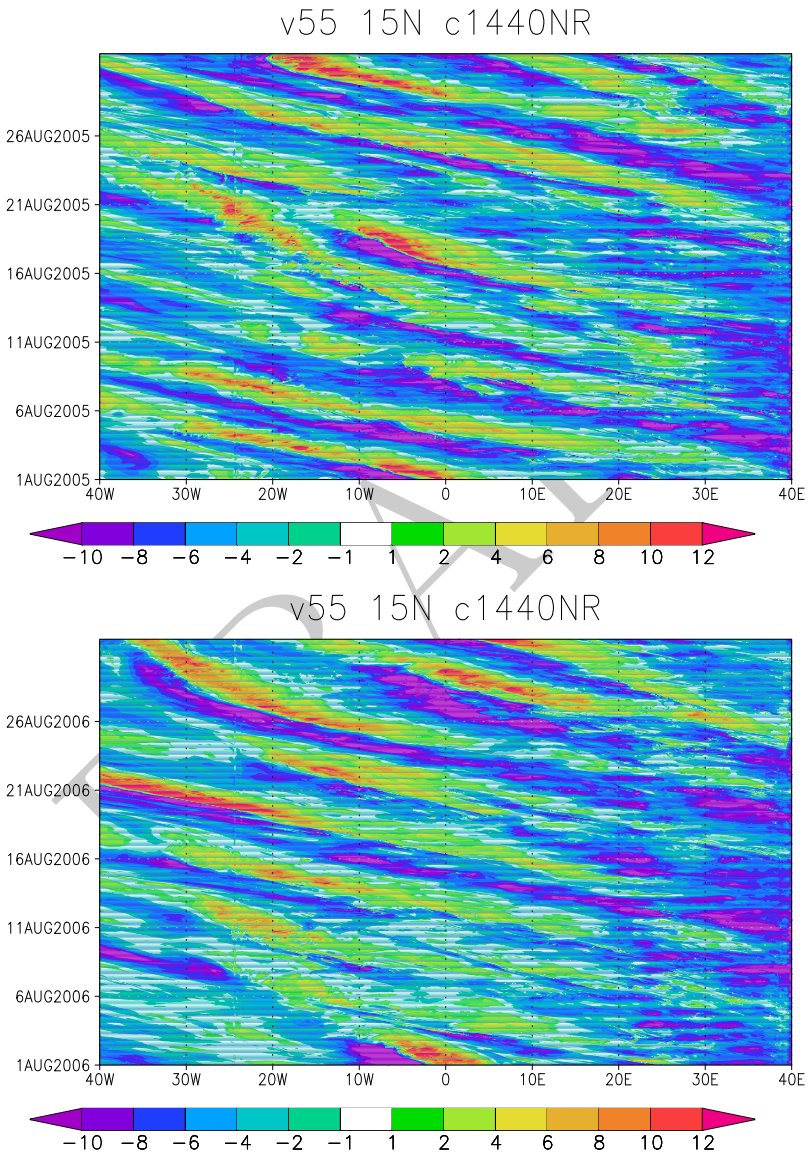

Figure 4.3: African easterly wave activity in the G5NR: Hovmöller plots of meridional winds at about 700 hPa (level 55), August 2005 and 2006. Time upward.

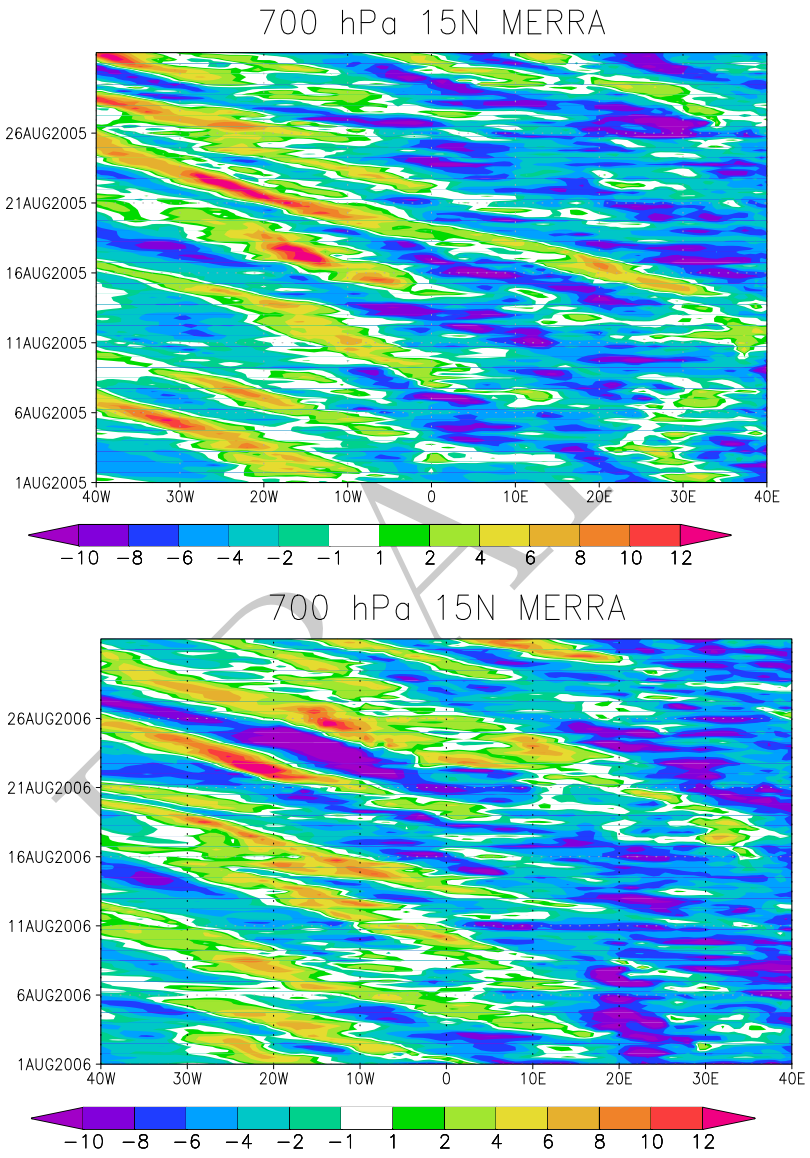

Figure 4.4: African easterly wave activity in MERRA: Hovmöller plots of $700hPa$ meridional winds, August 2005 and 2006.

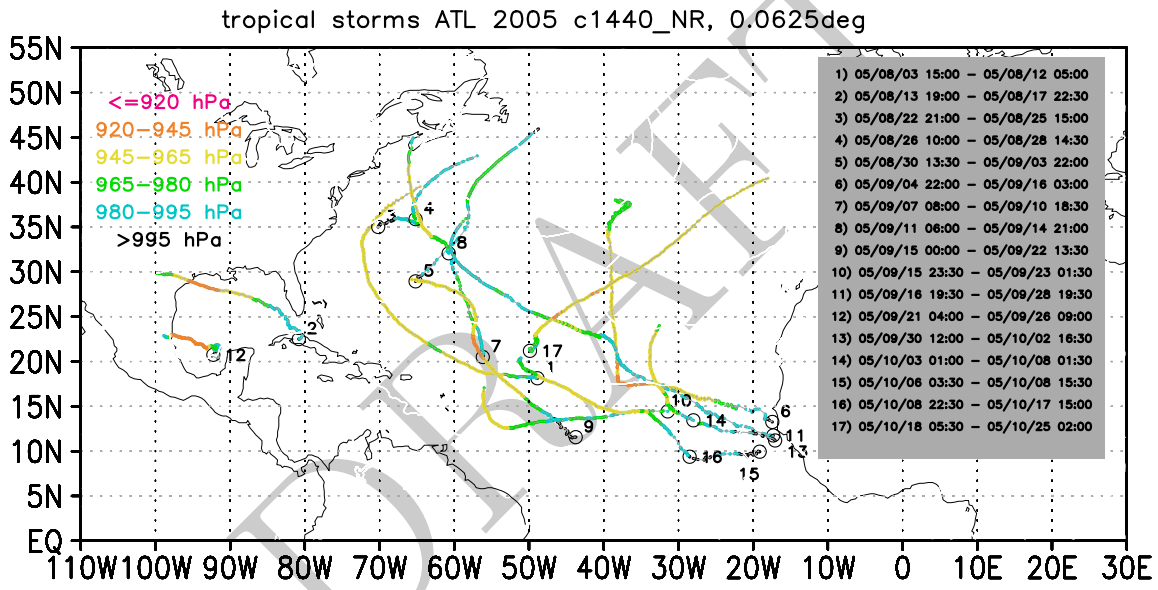

Figure 4.5: Tropical cyclone activity over the Atlantic in 2005 in the G5NR. Individual cyclone track colors indicate center pressure from the 7-km output. Open circles are drawn at the beginning of tracks and start and end dates are listed in yy/mm/dd hh:mm format.

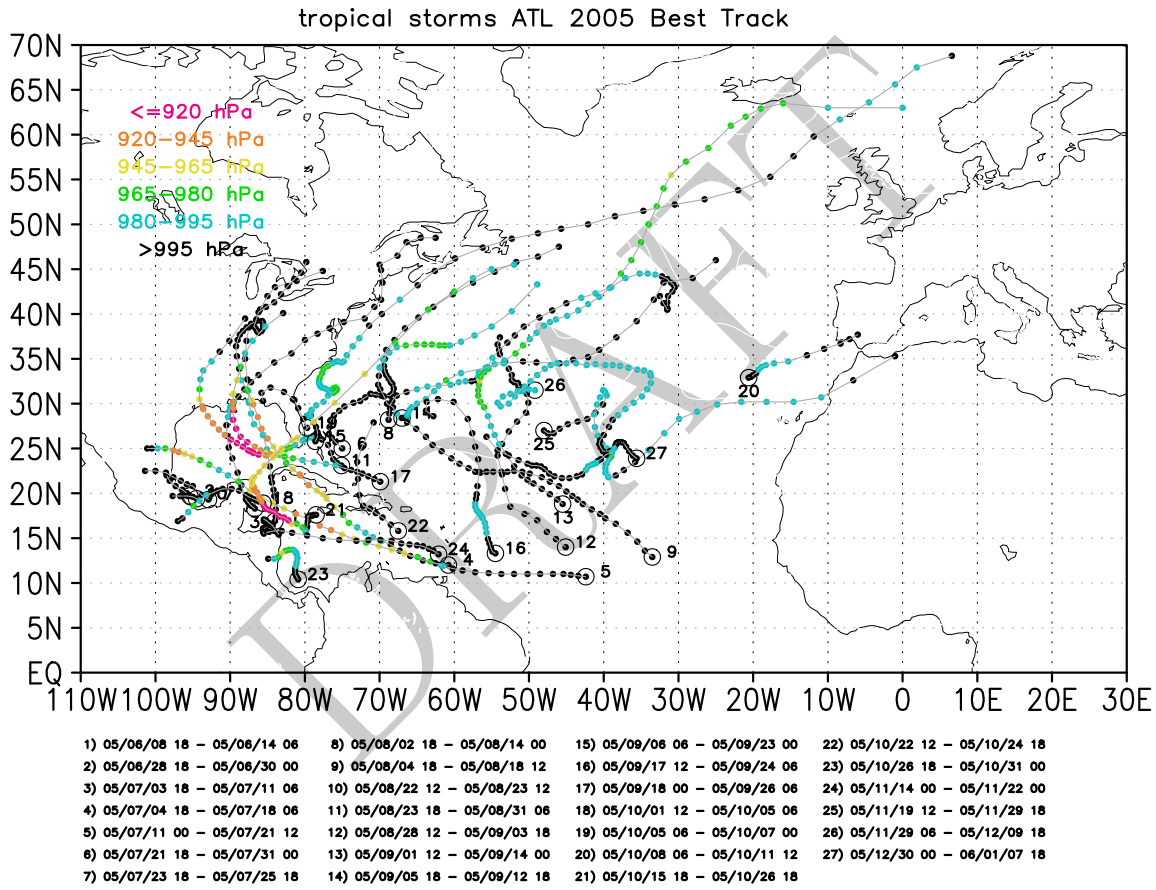

Figure 4.6: Same as in Figure 4.5, but from the NHC, 2005 season (observed best tracks).

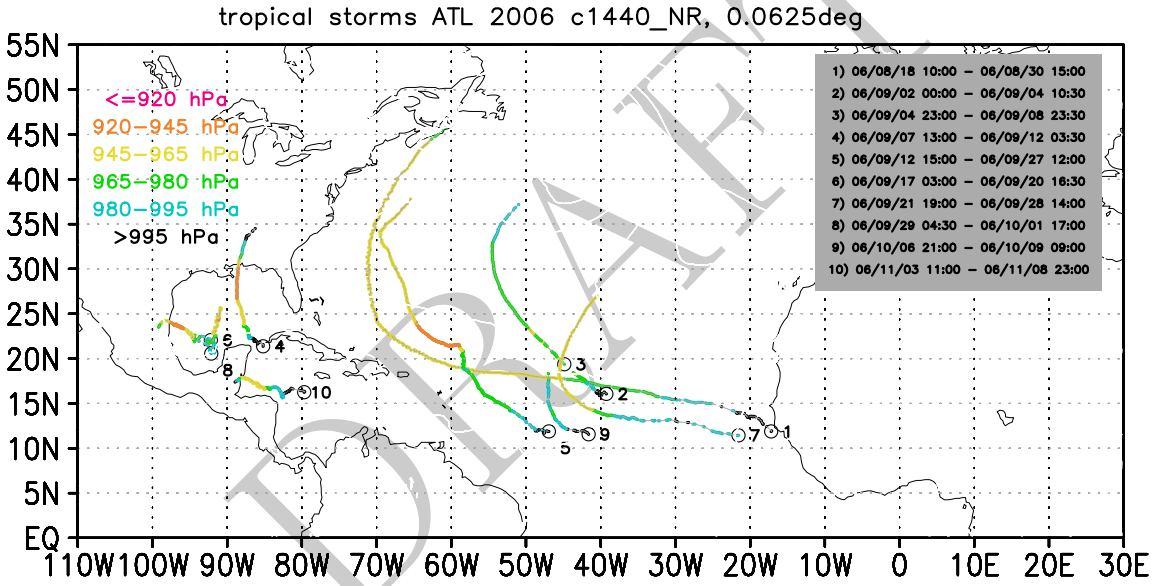

Figure 4.7: Same as Figure 4.5, but for 2006.

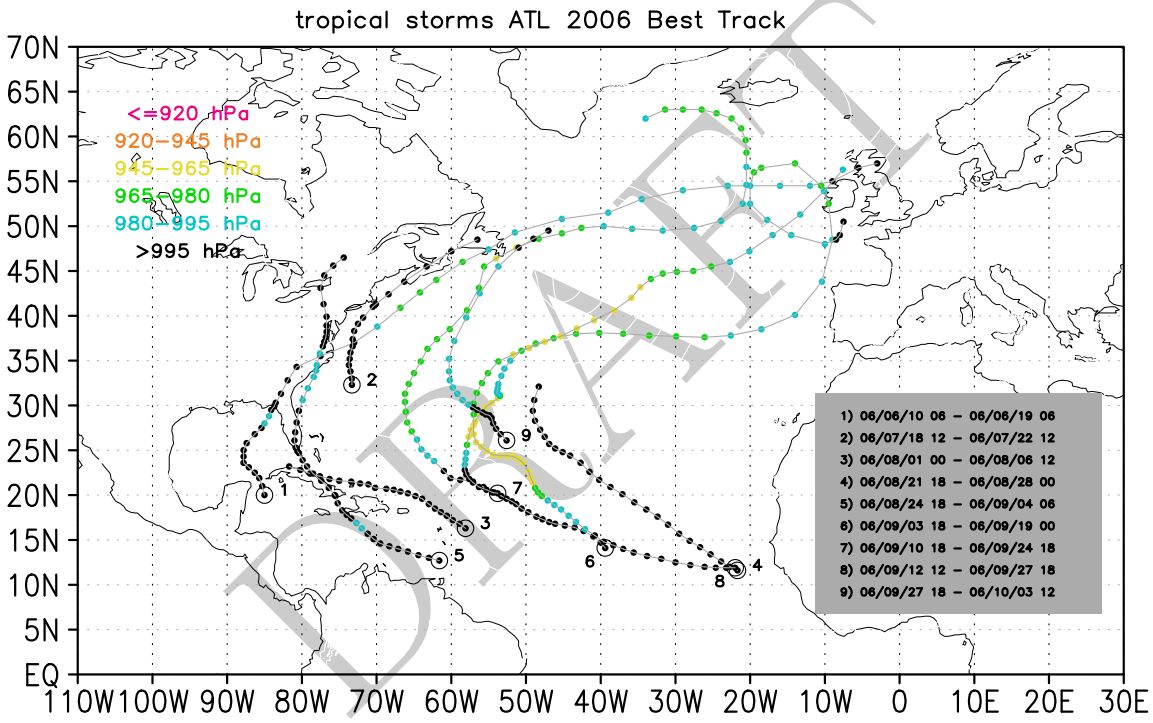

Figure 4.8: Same as Figure 4.5, but from the NHC, 2006 season (observed best tracks).

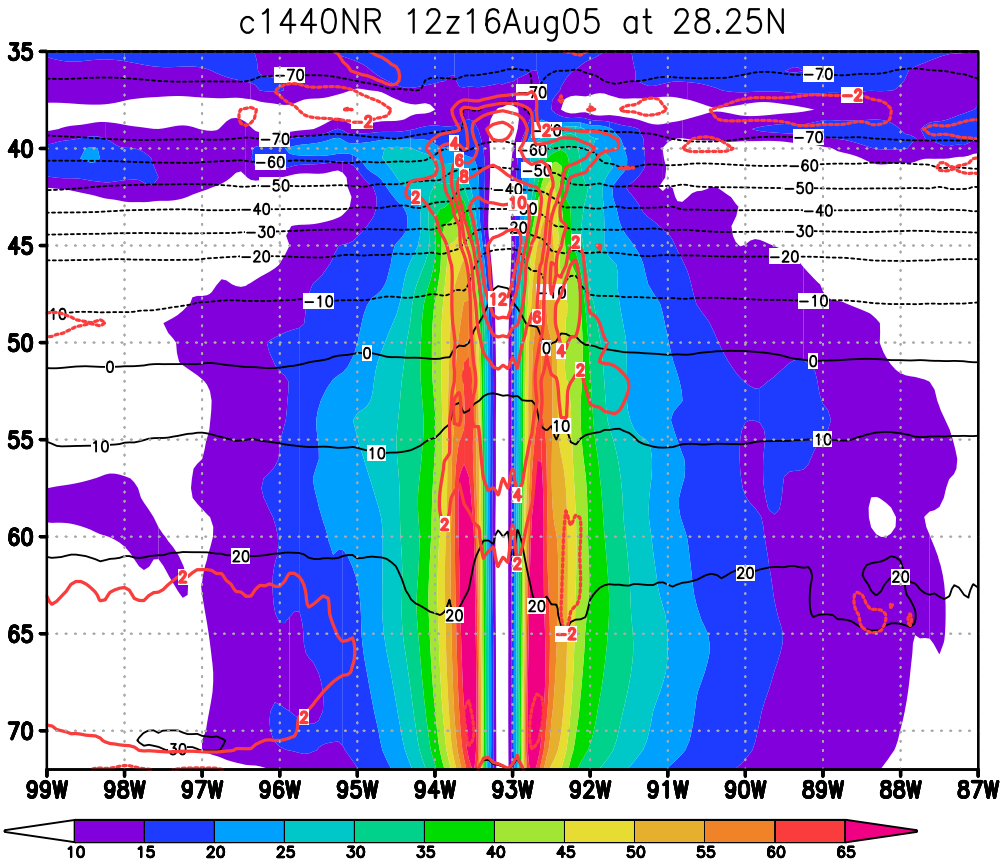

Figure 4.9: Zonal vertical cross-sections of winds (shaded, $\mathrm{m\,s^{-1}}$) and temperature (black contours, °C) for an Atlantic hurricane (TC 2, from Figure 4.5 reference map) in the G5NR. Temperature anomalies (°C, red contours) are computed by subtracting a zonal mean temperature for that latitude, spanning across 20° in longitude.

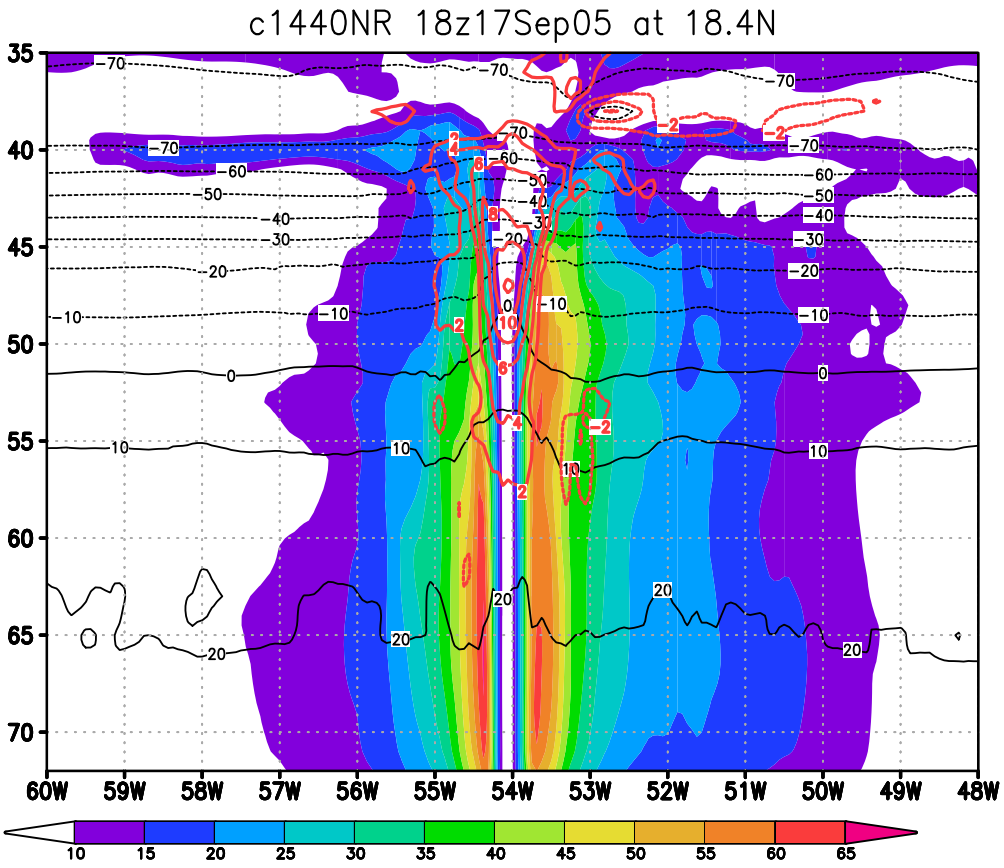

Figure 4.10: Same as in Figure 4.9, but for an Atlantic hurricane (TC 9) at an early development stage.

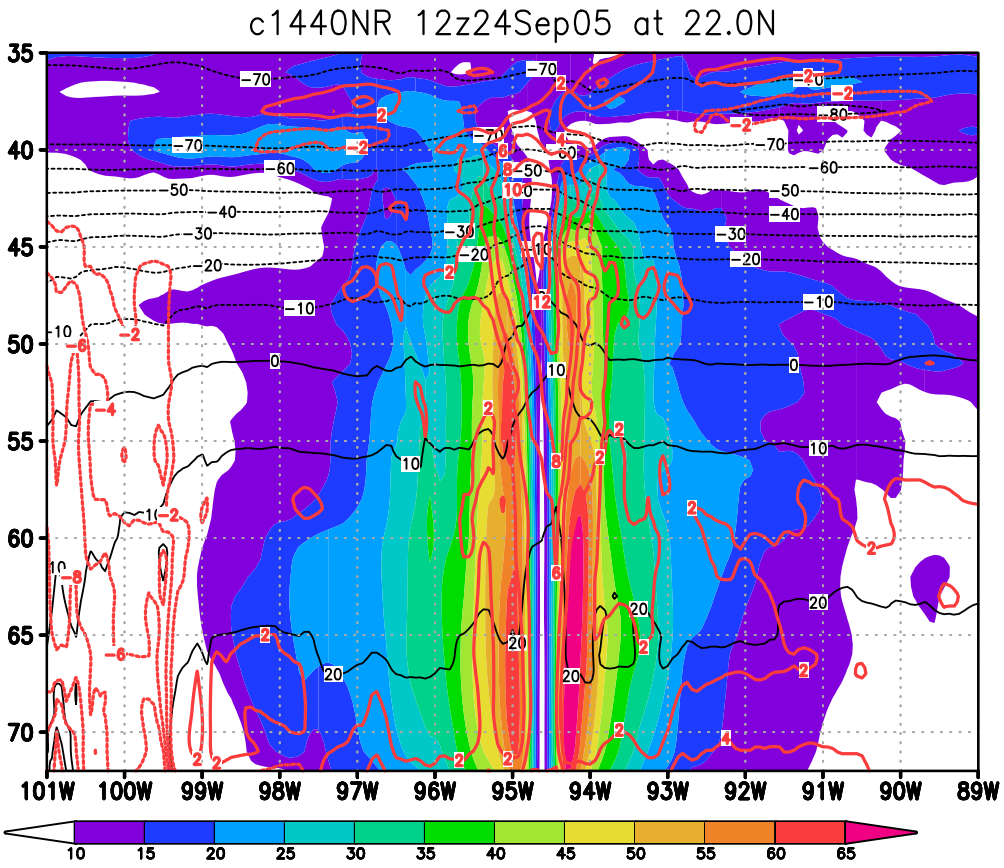

Figure 4.11: Same as Figure 4.9, but for an Atlantic hurricane (TC 12) at a mature development stage.

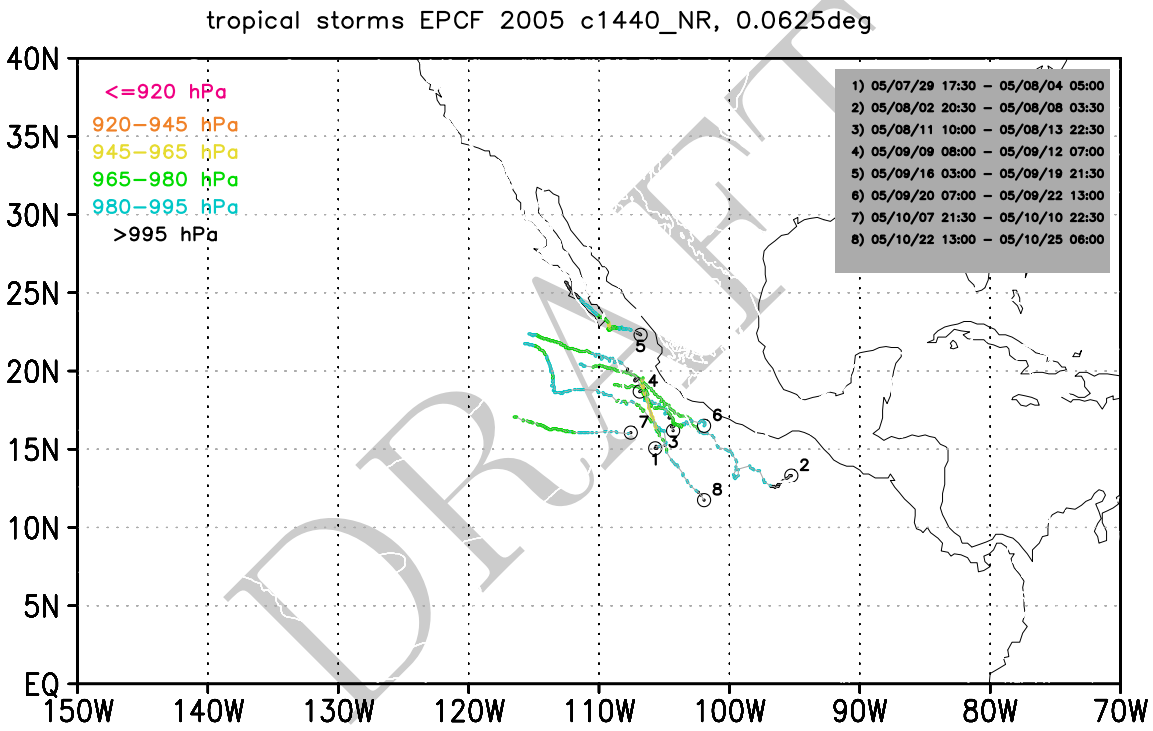

Figure 4.12: Tropical cyclone activity over the Eastern Pacific in 2005 in the G5NR. Individual cyclone track colors indicate center pressure from the 7-km output. Open circles are drawn at the beginning of tracks and start and end dates are listed in yy/mm/dd hh:mm format.

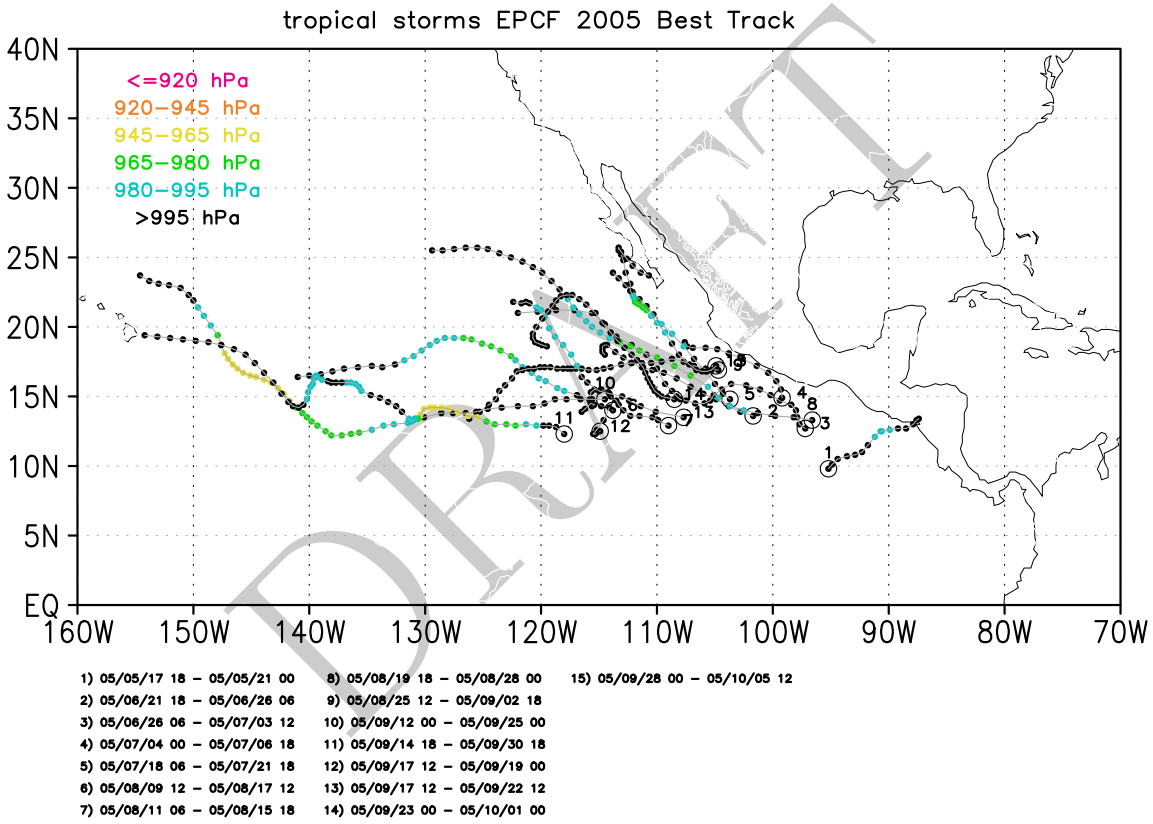

Figure 4.13: Same as Figure 4.12, but from the NHC, 2005 season (observed best tracks).

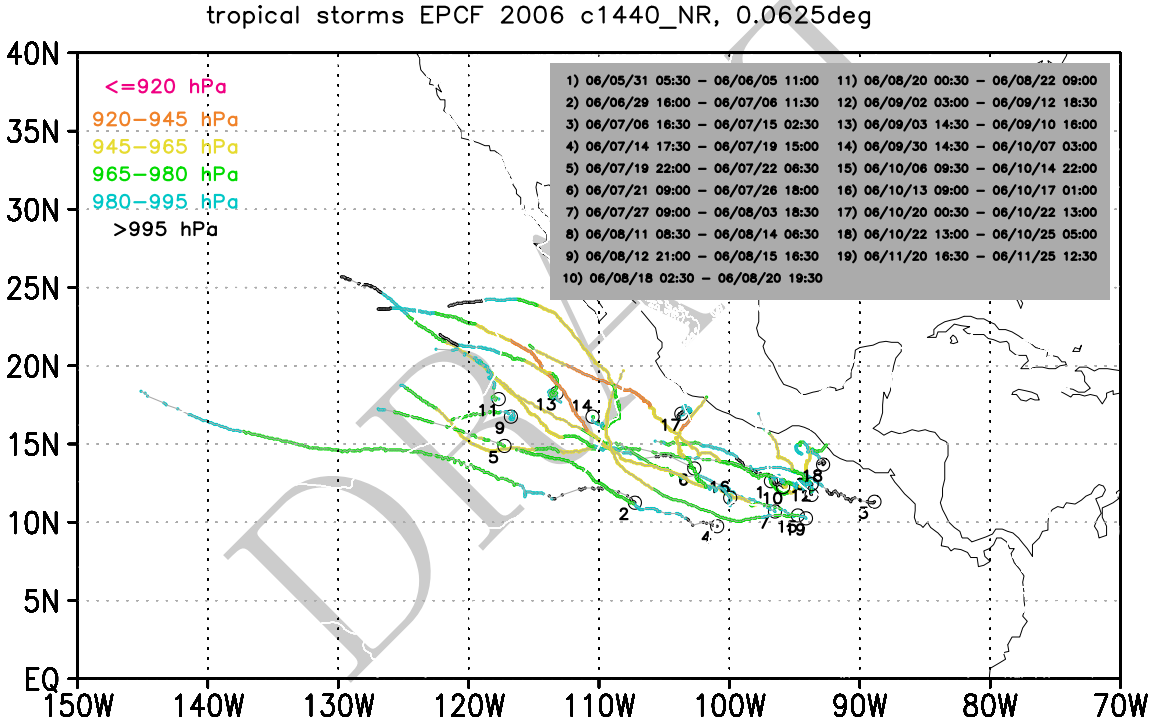

Figure 4.14: Same as Figure 4.12, but for 2006.

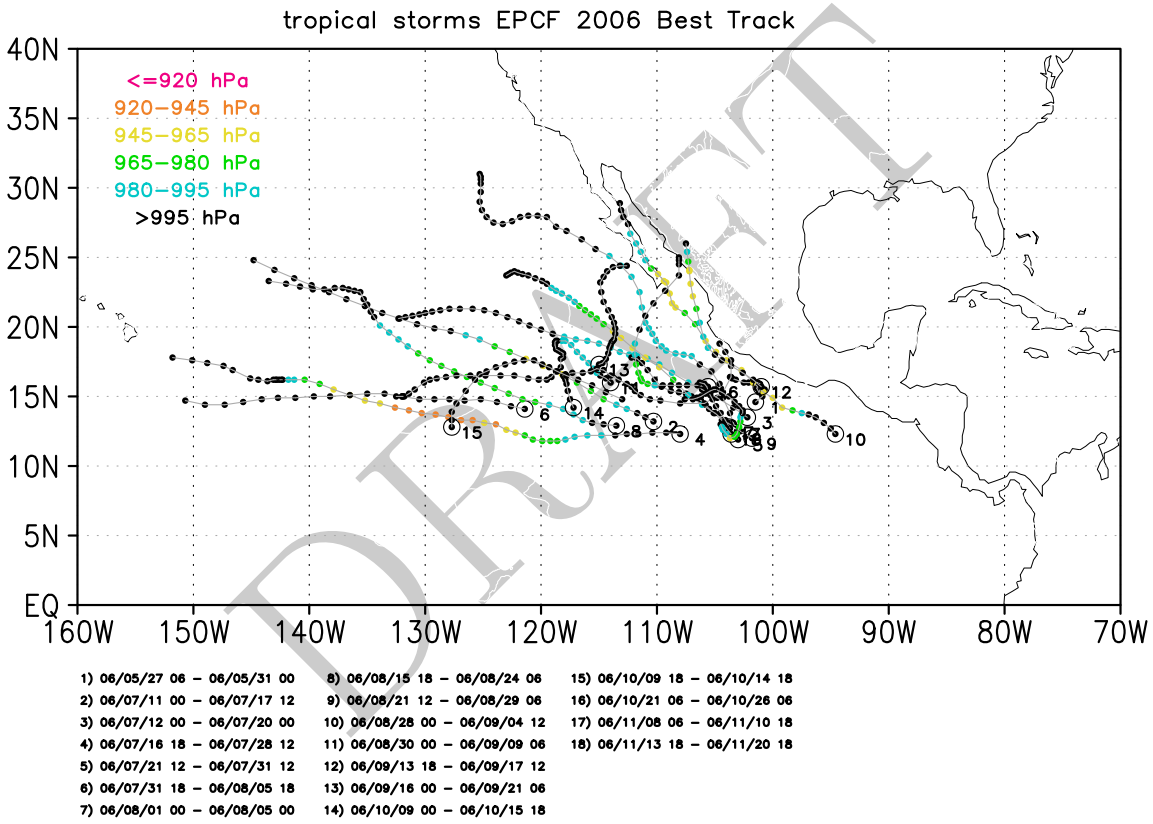

Figure 4.15: Same as Figure 4.12, but from the NHC, 2006 season (observed best tracks).

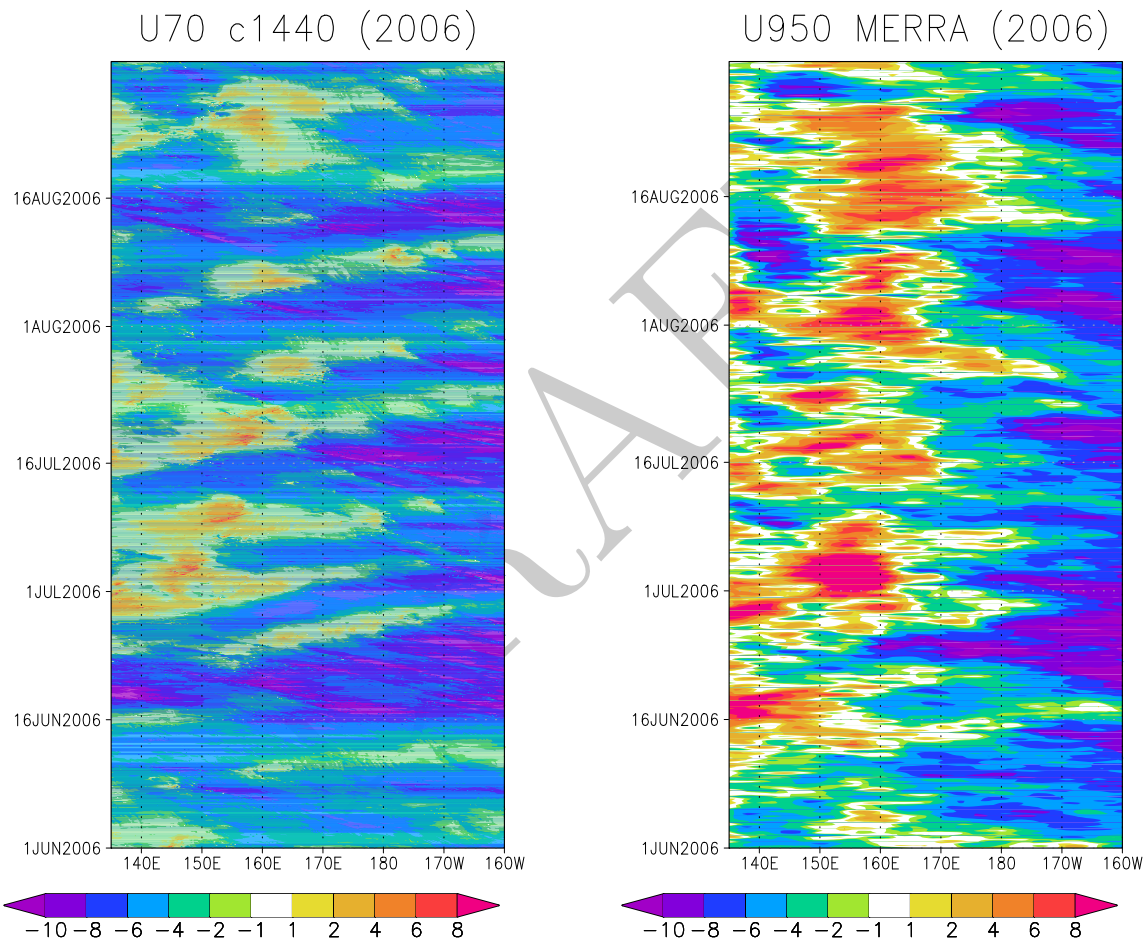

Figure 4.16: Hovmöller diagram of equatorial low-level zonal wind (model level 70) in JJA 2006 across the central Pacific in the G5NR (left) and 950 hPa wind from MERRA (right).

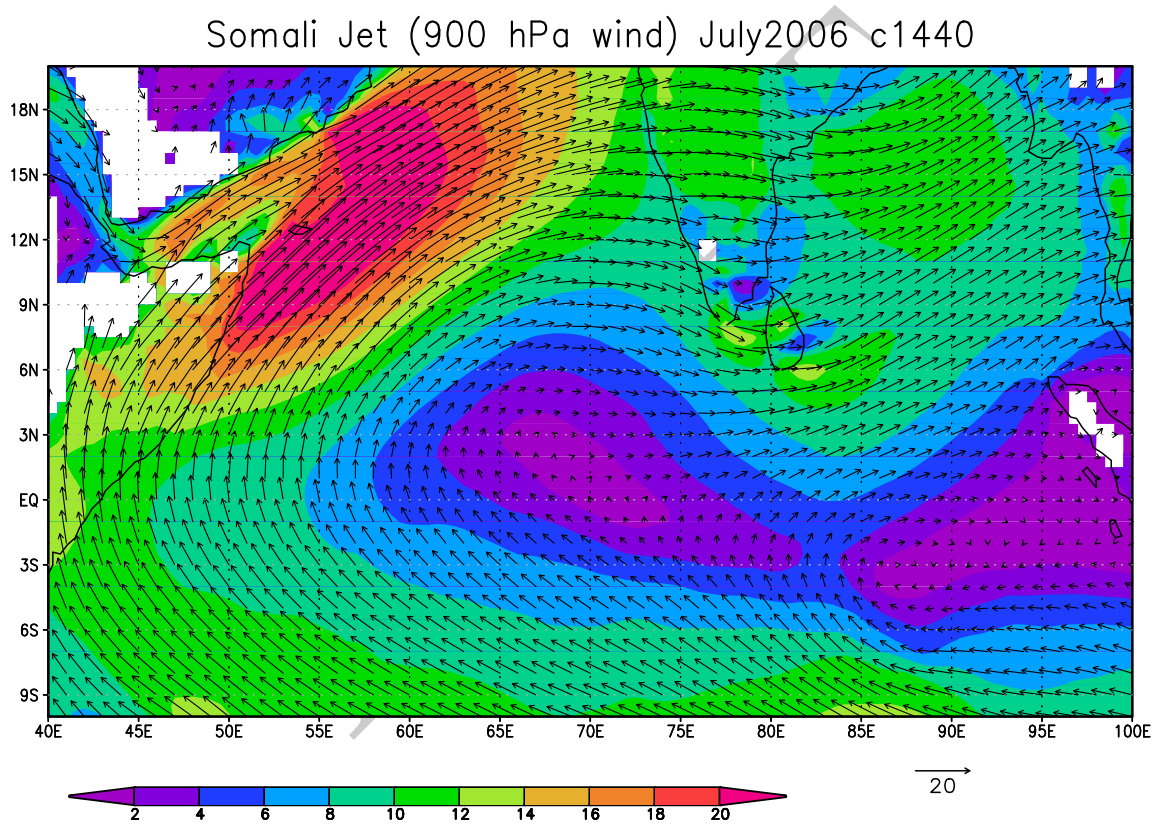

Figure 4.17: 900 hPa wind in July 2006 across the Indian Ocean in the G5NR.

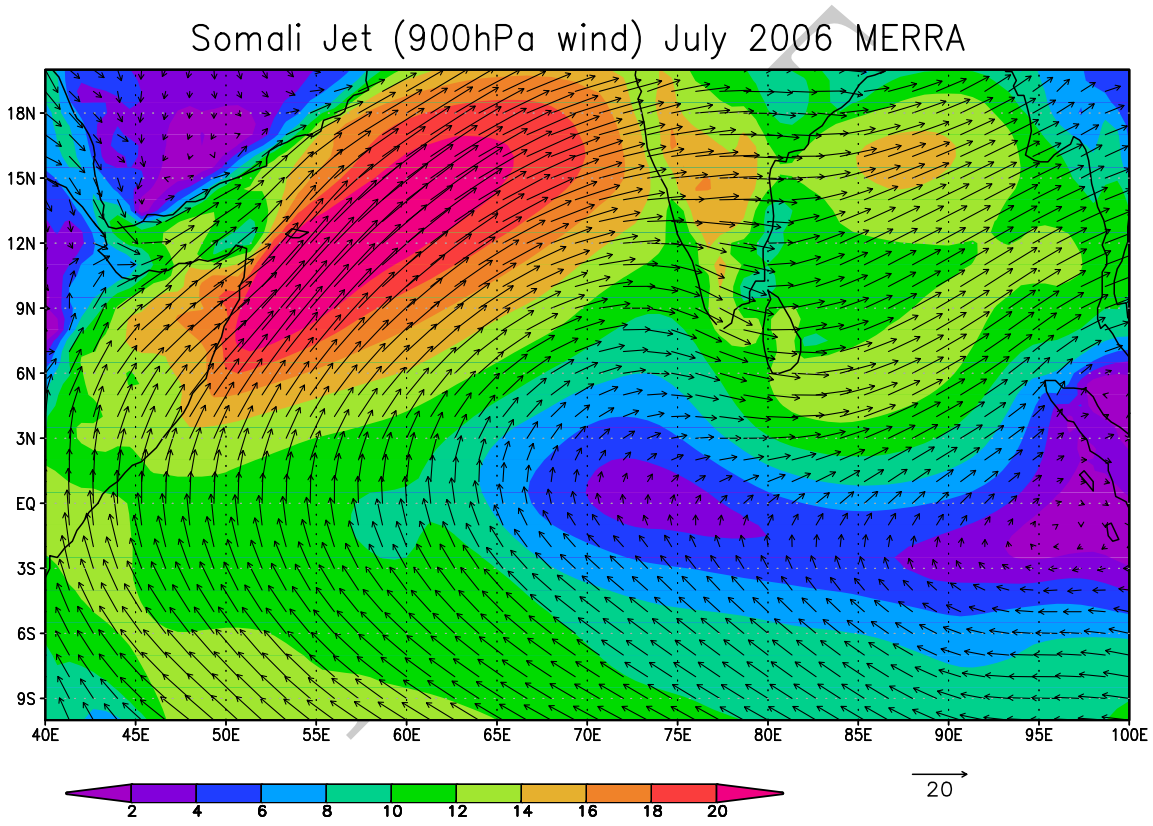

Figure 4.18: Same as Figure 4.17, but for MERRA.

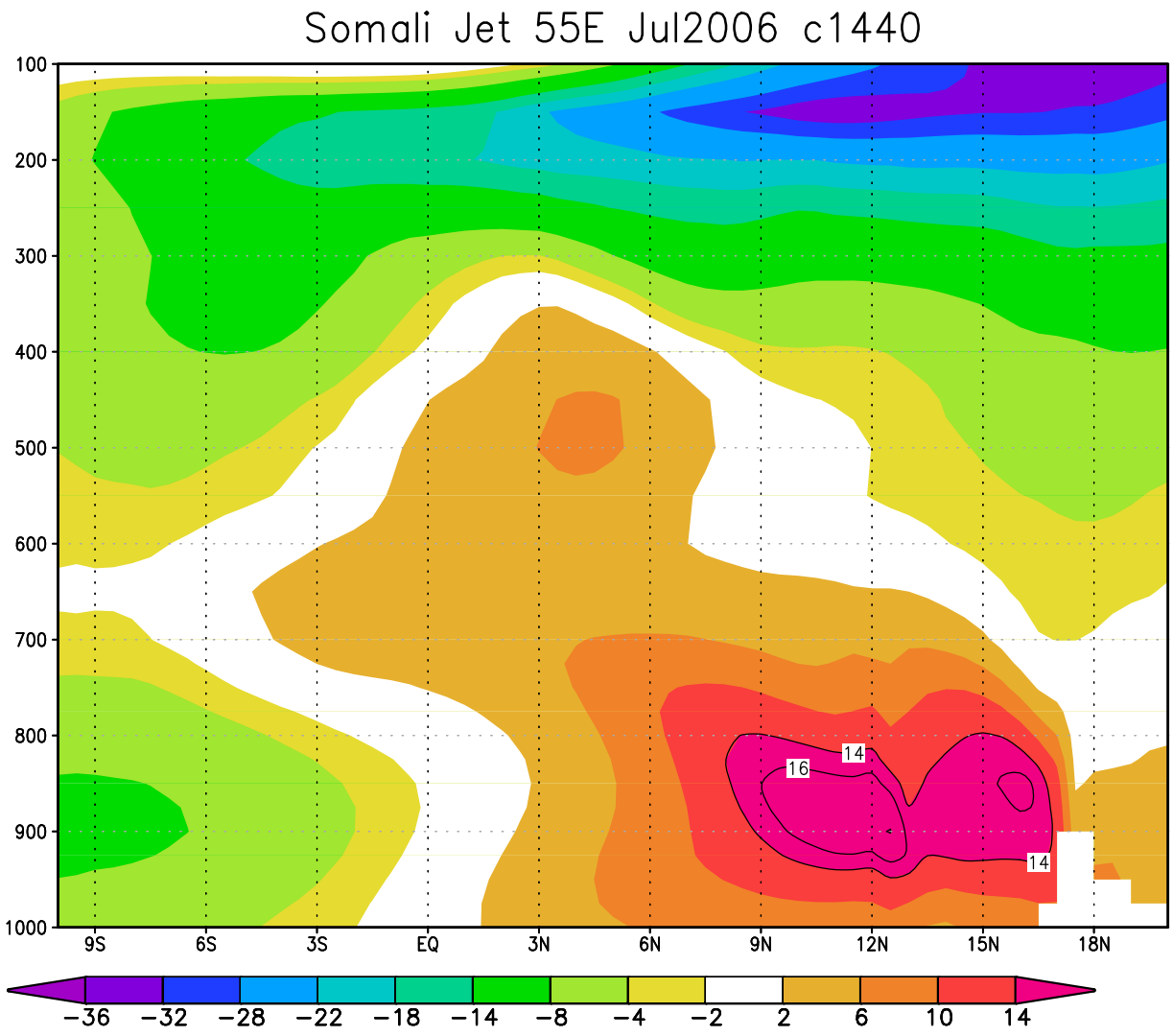

Figure 4.19: Vertical meridional cross section of the Somali Jet in July 2006 in the G5NR.

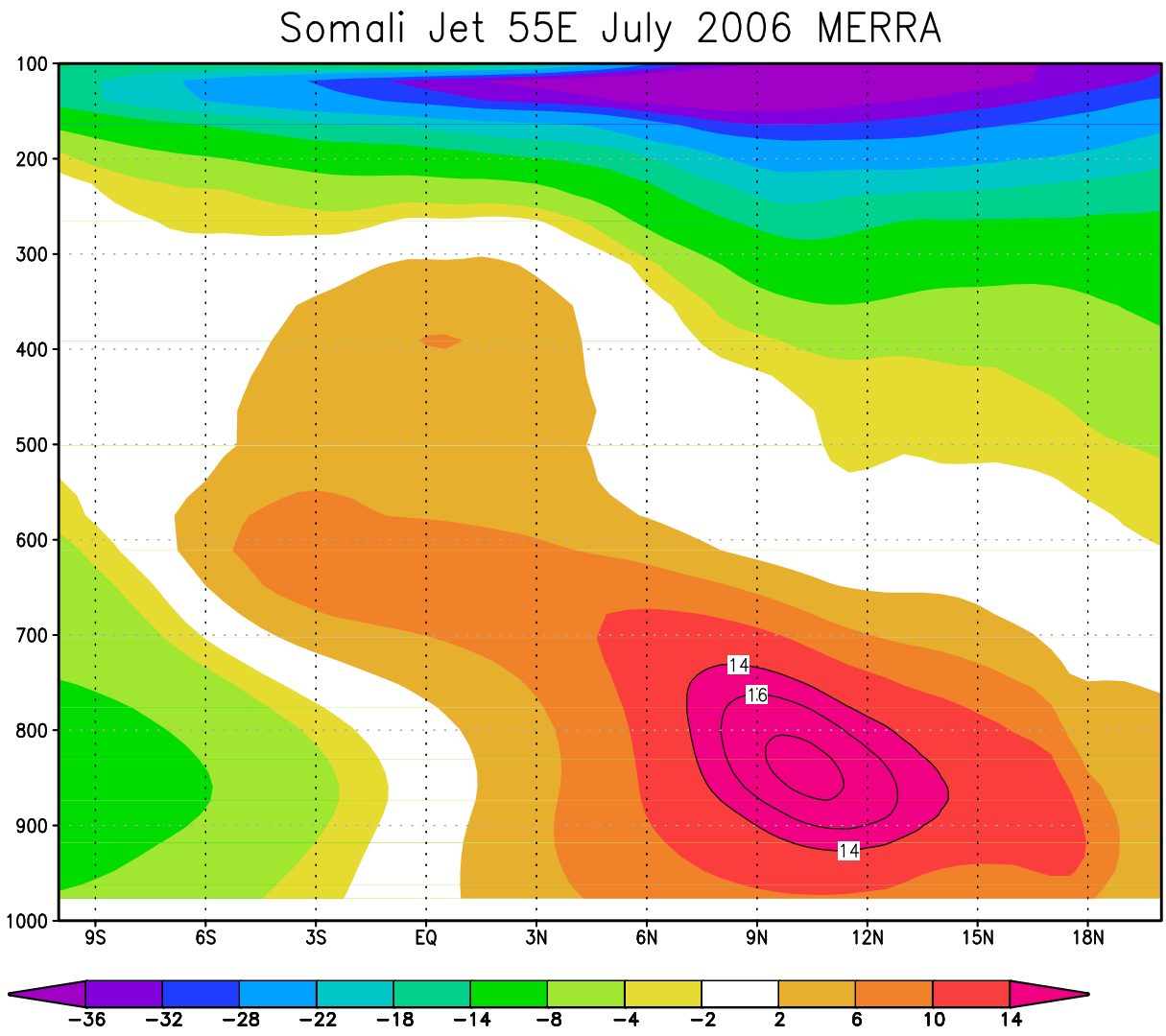

Figure 4.20: Same as Figure 4.19, but for MERRA.

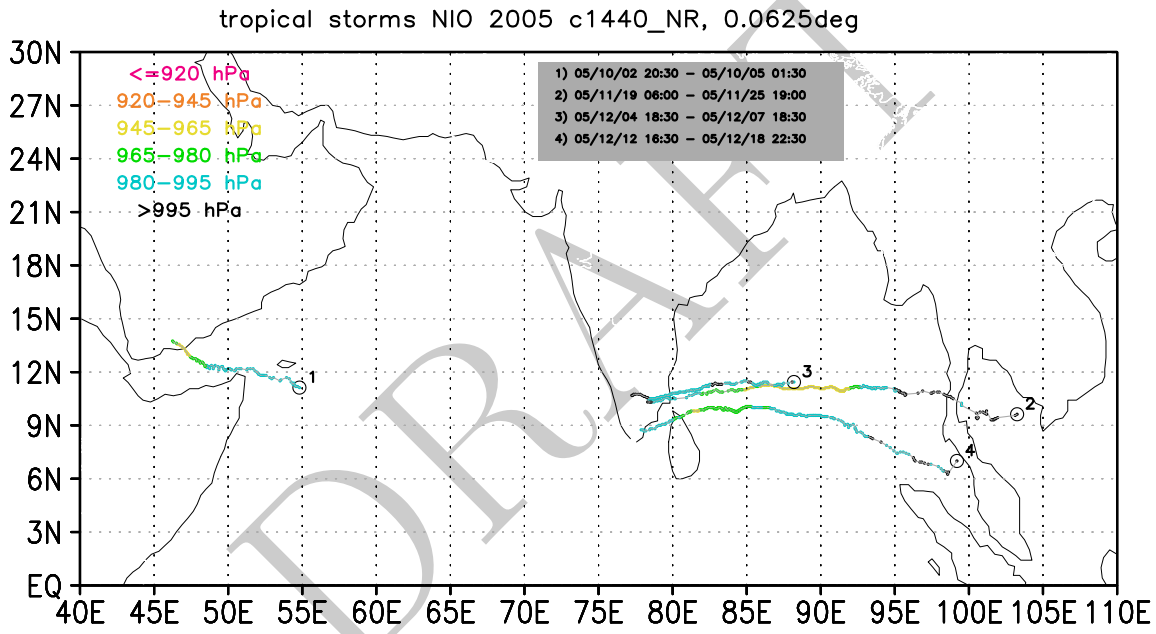

Figure 4.21: Tropical cyclone activity over the Northern Indian Ocean in 2005 in the G5NR. Individual cyclone track colors indicate center pressure from the 7-km output. Open circles are drawn at the beginning of tracks and start and end dates are listed in yy/mm/dd hh:mm format.

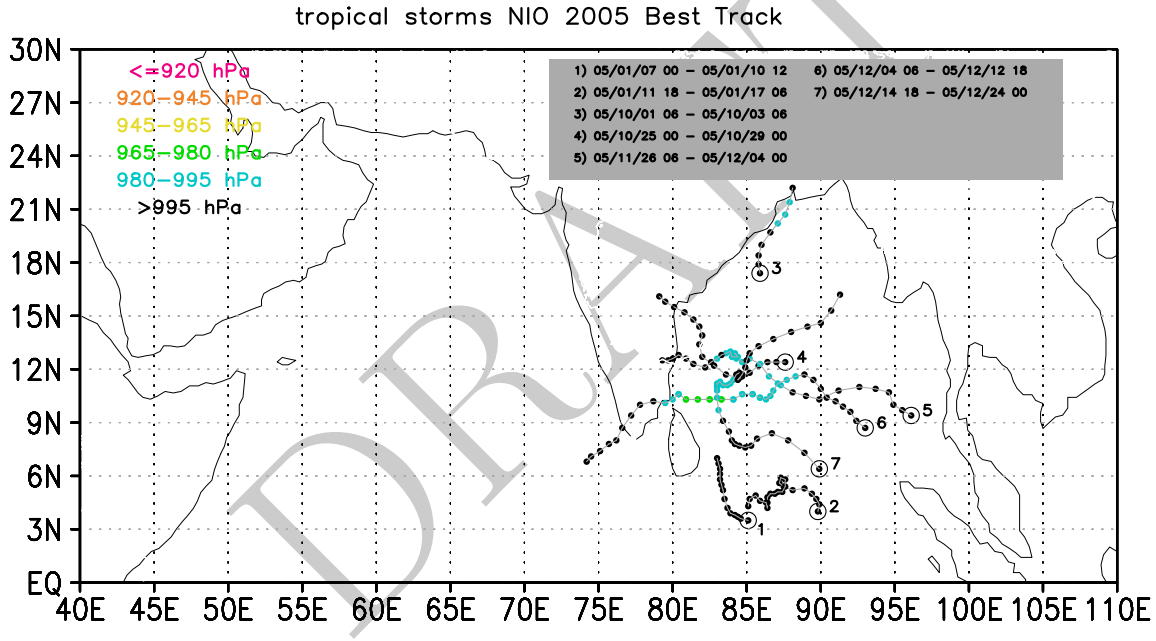

Figure 4.22: Same as Figure 4.17, but from the JTWC, 2005 season (observed best tracks).

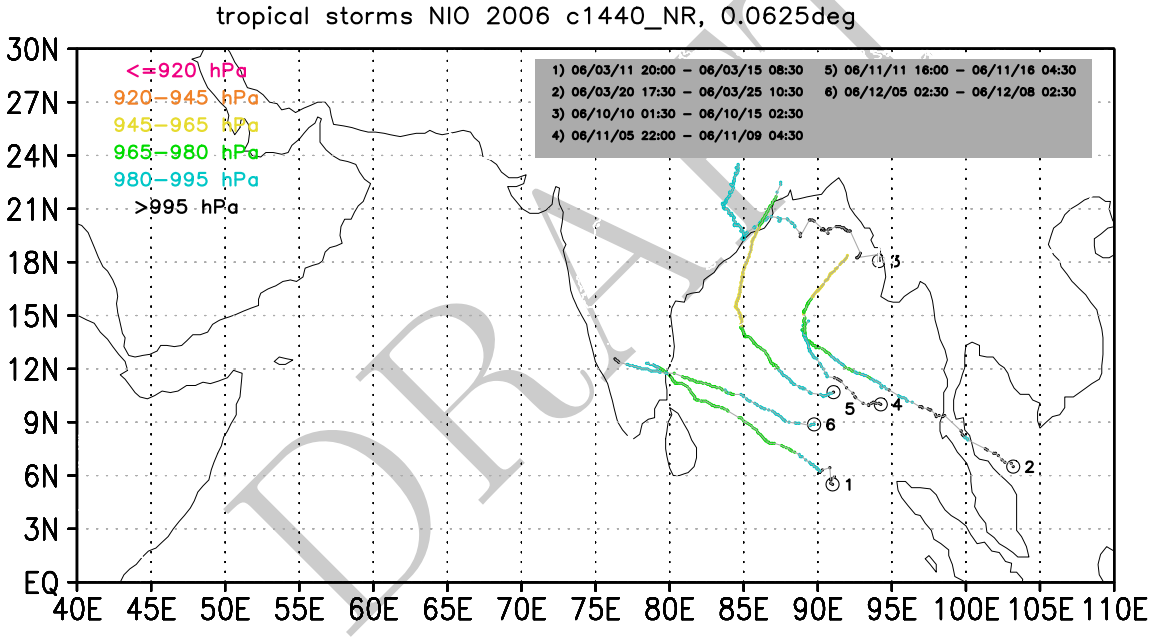

Figure 4.23: Same as Figure 4.17, but for 2006.

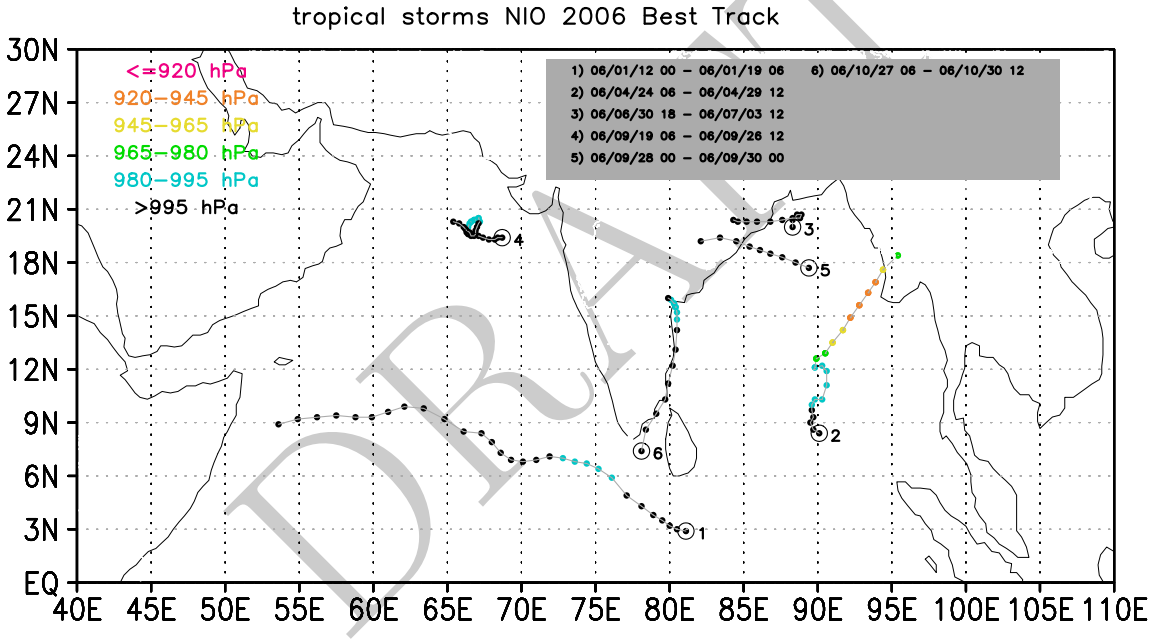

Figure 4.24: Same as Figure 4.17, but from the JTWC, 2006 season (observed best tracks).

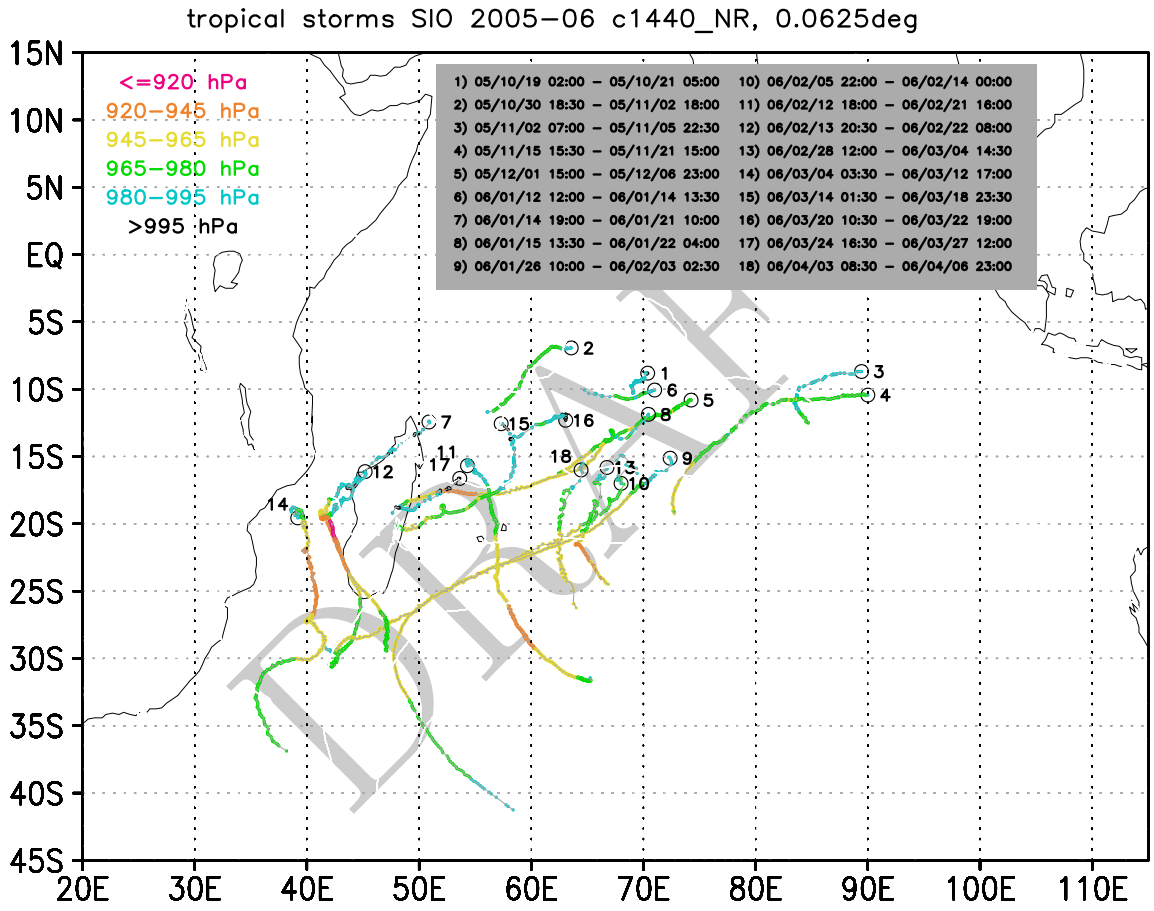

Figure 4.25: Tropical cyclone activity over the Southern Indian Ocean in 2005-2006 in the G5NR. Individual cyclone track colors indicate center pressure from the 7-km output. Open circles are drawn at the beginning of tracks and start and end dates are listed in yy/mm/dd hh:mm format.

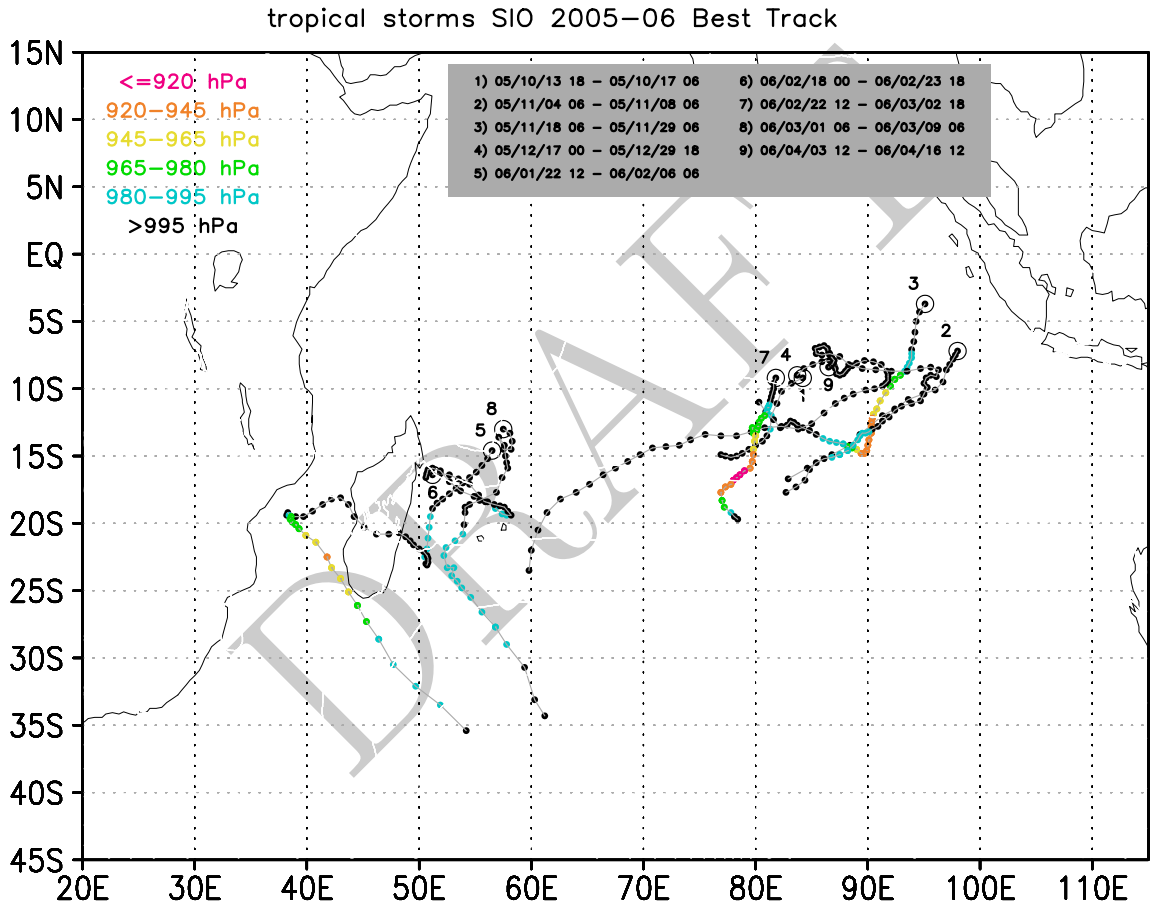

Figure 4.26: Same as Figure 4.25, but from the JTWC, 2005-2006 season (observed best tracks).

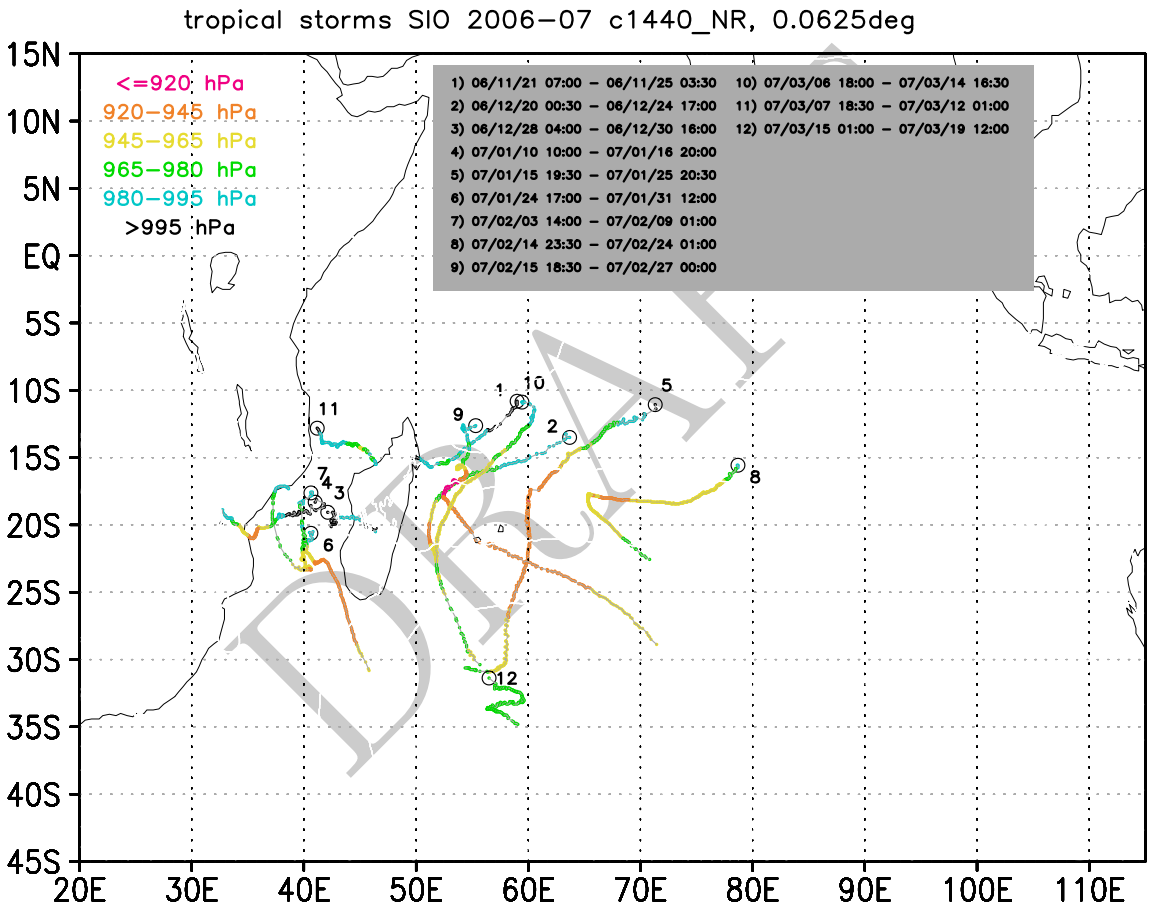

Figure 4.27: Same as Figure 4.25, but for 2006.

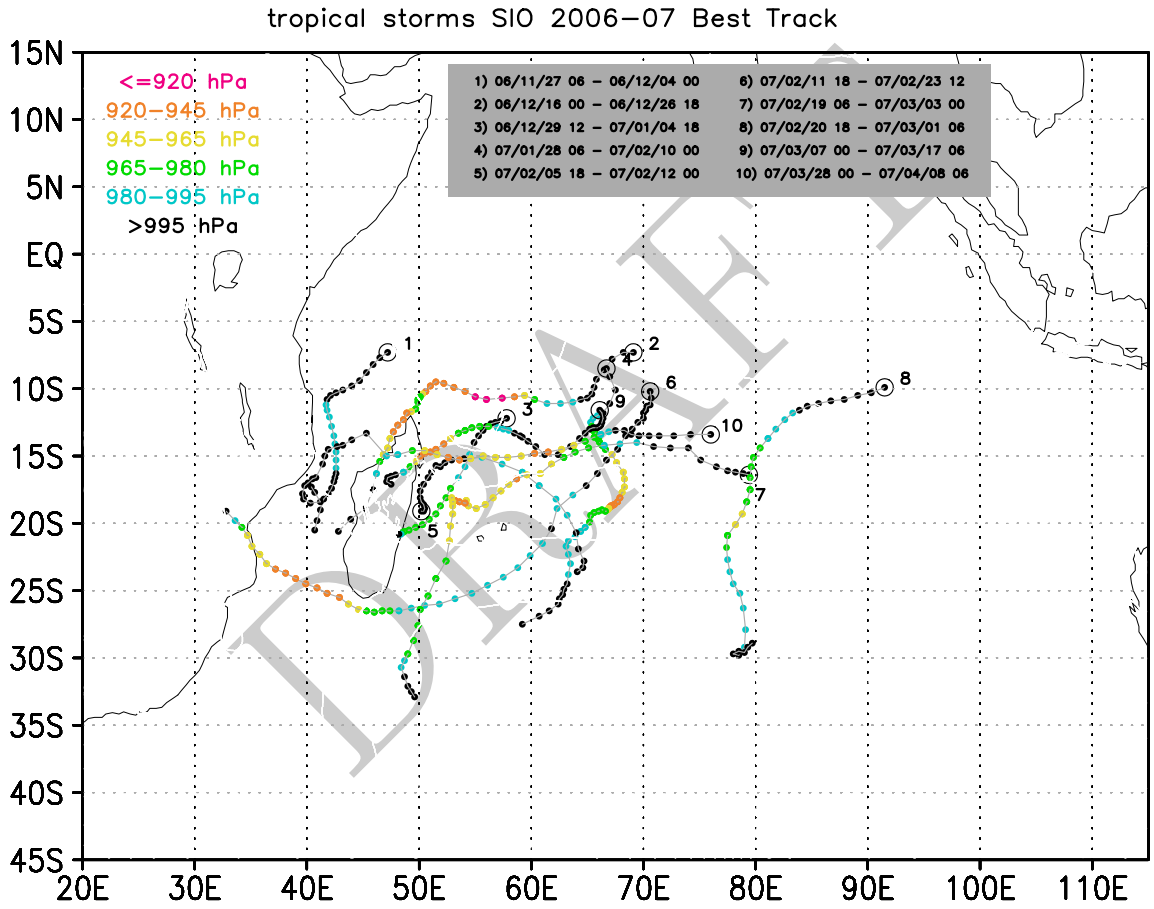

Figure 4.28: Same as Figure 4.25, but from the JTWC, 2006-2007 season (observed best tracks).

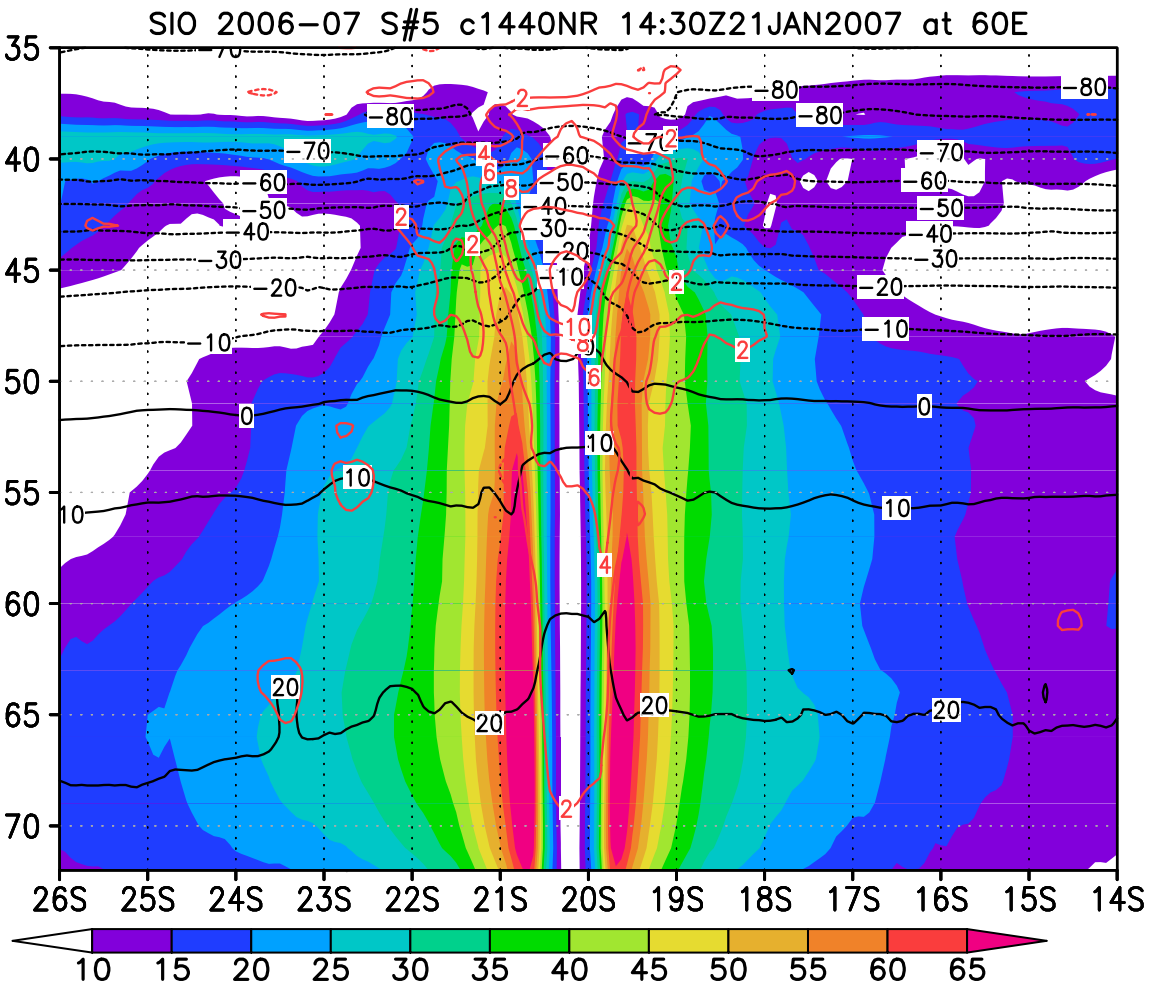

Figure 4.29: Zonal vertical cross-sections of winds (shaded, m s^{-1}) and temperature (black contours, °C) of a Southern Indian Ocean tropical cyclone (TC 5, from Figure 4.27 reference map) in the G5NR. Temperature anomalies (°C, red contours) are computed by subtracting a zonal mean temperature for that latitude, spanning across 20° in longitude.

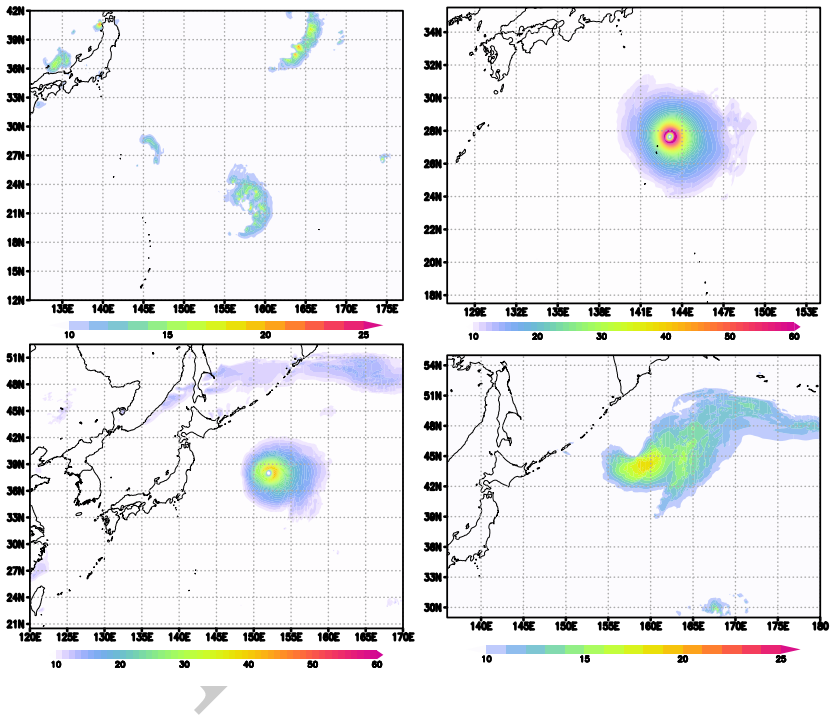

Figure 4.30: Four-panel depiction of near-surface wind speed at various stages of the tropical cyclone's life-cycle in the G5NR, highlighting wind intensity and structural changes during. Upper left: initial tropical genesis at 1100 UTC 03 Aug 2005. Upper right: peak tropical cyclone intensity at 08 Aug. 2005, 0600 UTC. Lower left: early extratropical transition at 1100 UTC 13 Aug 2005. Lower right: mature extratropical transition at 2300 UTC 15 Aug 2005.

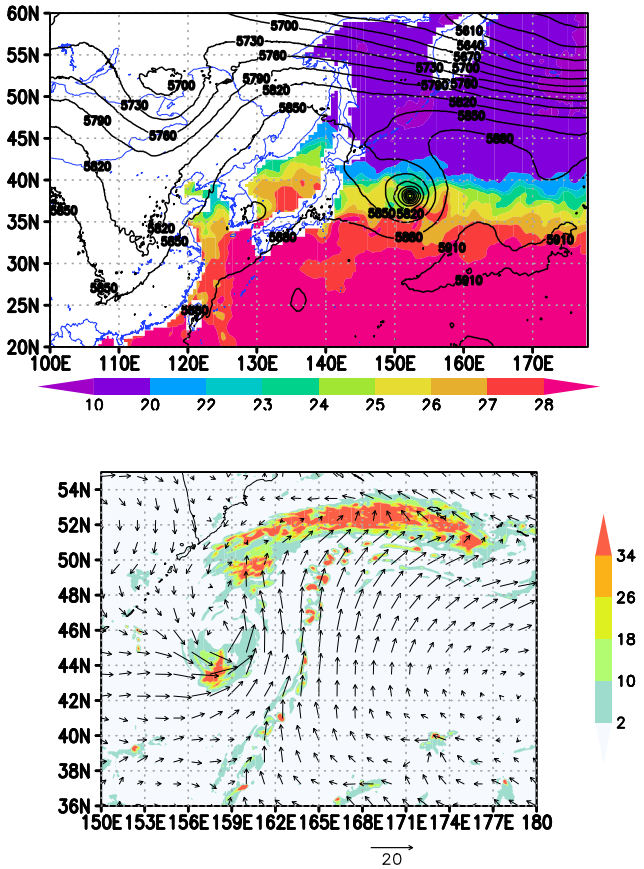

Figure 4.31: Extra tropical transition of a tropical cyclone in the G5NR. Top: 500hpa geopotential height (contour, m) and sea-surface temperature (shaded, C) showing favorable positioning of tropical cyclone to upstream mid-latitude longwave trough 13 Aug. 2005, 2300 UTC. Bottom: 30-minute average rainfall rate (shaded, mm d^{-1}) and 10m wind vectors at full ET maturity 2300 UTC 15 Aug 2005.

Chapter 5

Surface Characteristics

Clara Draper, Richard Cullather, Randal Koster, Guillaume Vernieres and Yuri Vikhliaev

In this chapter, the surface characteristics of the G5NR simulation are investigated, by separately considering the land (Sections 5.1-5.2), ocean (5.3), and polar (5.4.2) regions. The realism of the G5NR simulation is tested by comparison to independent estimates, and known problems with the G5NR model and output are identified.

5.1 Land Surface - Hydrological Processes

Along with its atmospheric output, the G5NR offers a tremendous amount of high resolution, globally gridded land surface hydrological data. Users interested in these particular data should acquaint themselves with the issues highlighted in the subsections below, some of which may limit the data's usefulness for certain applications.

5.1.1 Relationship of G5NR Land Surface Hydrological Data to LDAS Products

In general, land data assimilation systems (LDAS) consist of a global or continental-scale array of land surface model elements driven with observations-based meteorological forcing over a period of years to decades. Output from these systems, which occasionally live up to their name by assimilating land surface states along the way, consist of hydrological and energy fluxes and states at

high spatial and temporal resolution. Numerous LDAS systems are currently operational (Mitchell et al. 2004, Rodell et al. 2004, Xia et al. 2012, Reichle et al. 2011) and offer data to a wide variety of users.

For those interested in hydrological studies requiring high resolution land surface data, it is worth contrasting LDAS products with G5NR land surface products. For certain applications, the LDAS products have distinct advantages. The first advantage involves biases in the meteorological forcings produced by the G5NR's atmospheric model, which will necessarily produce biases in the land surface model output. LDAS products are much less limited by this problem, given that the meteorological forcings they use come from reanalysis and, for precipitation, from datasets corrected with rain gauge measurements. Biases in the G5NR's precipitation and other surface forcings are addressed elsewhere in this volume (and briefly in Section 5.1.2); suffice it to say that these biases can, in certain regions and seasons, be significant.

The second issue involves chaotic atmospheric dynamics. The G5NR is a free-running simulation rather than an analysis. Thus, even though the nominal dates for the simulation span 2005-2007, and even though the atmosphere was forced by sea surface temperatures for those dates, the simulated atmosphere was free to follow any number of diverging trajectories. The nature of chaotic atmospheric dynamics implies that even if the atmospheric and land models were perfect, a given simulation would necessarily produce a time series of precipitation fields not seen in the real world, though not necessarily unrealistic. It is therefore inappropriate to use G5NR land surface output to examine specific, historical real-world flooding events or droughts. LDAS data are better suited for such studies.

This said, the G5NR land surface hydrological dataset does have its advantages. These data, for example, are fully consistent with the rest of the G5NR dataset. During the G5NR, the land states were allowed to feed back on the atmospheric states, and vice versa; the resulting mutual consistency, arguably absent from LDAS products, allows an unprecedented joint analysis of land variables with any number of atmospheric variables – that is, it allows studies of how these variables evolve together. Another important advantage involves the spatial resolution of the G5NR data, which is somewhat finer that of standard LDAS products; for example, the north American LDAS project (Xia et al. 2012) offers data at a resolution of 1/8 degree, and the MERRA-Land global product (Reichle et al. 2011) has a resolution of 0.5 degree.

5.1.2 Hydrological Land Surface Forcing

To get a first-order handle on the degree to which forcing biases affect the G5NR's land products, we turn to Budyko's dryness index, defined as $\mathrm{DI} = R_{\mathrm{net}}/\lambda P$, where R_{net} is the annual net radiation at the surface, λ is the latent heat of vaporization, and P is annual precipitation. Budyko (1974) showed that DI serves as a chief control over long-term surface hydrology, even more so than precipitation does by itself. The top panel of Figure 5.1 shows the global field of DI derived from observations (Koster et al. 2006), which is in essence the field associated, by construct, with LDAS

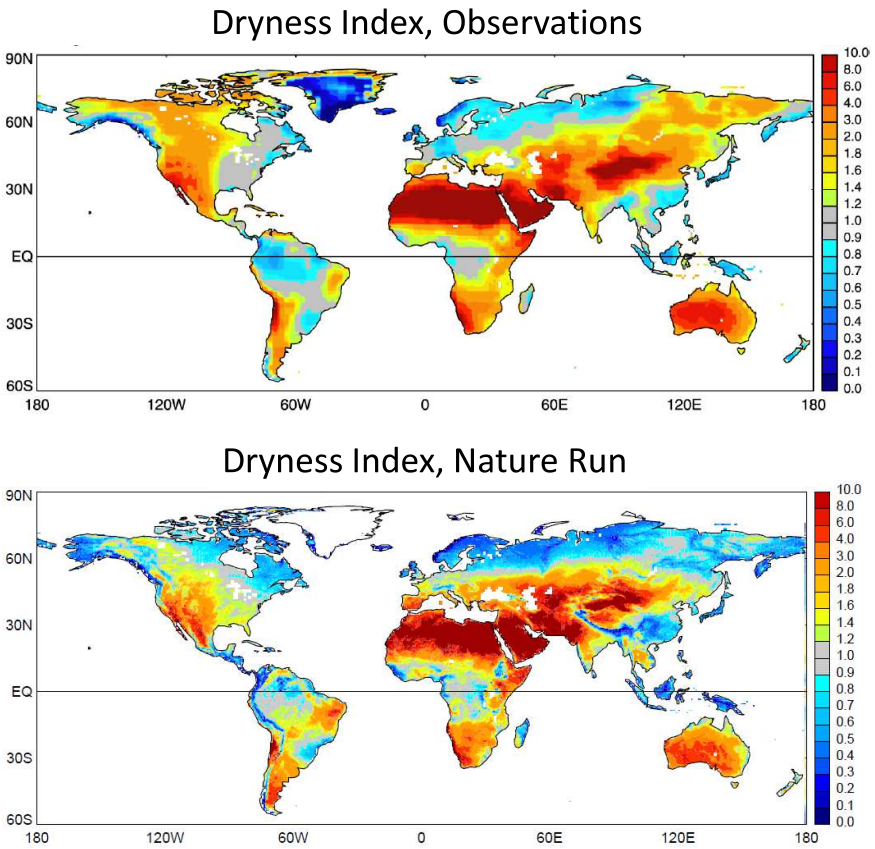

Figure 5.1: Top: Dryness index distribution, as determined from observed precipitation and net radiation fields. Figure reprinted from Koster et al. (2006); see that paper for details. Bottom: Corresponding distribution based on two years of G5NR output.

Overall, the G5NR's simulation of DI looks good, certainly to first order. The locations of energy-limited evaporation (low DI) and water-limited evaporation (high DI) are, for the most part, correctly positioned. One must also keep in mind that some of the differences between the two plots probably result from the short (2-year) averaging period used for the G5NR plot. In addition, the large differences seen in near-polar latitudes are likely associated with poor precipitation observations in these areas; we do not have a good sense for what the correct values of DI in these areas should be.

At least in terms of this bulk forcing diagnostic, the G5NR results look reasonable. Forcing biases at shorter time scales, however, will not be as good. Again, a more complete description of forcing biases is provided elsewhere in this report (including an analysis of the bulk land surface energy budget in the G5NR in Section 5.2).

5.1.3 Inconsistency Between Land-Only and Total-Grid Diagnostics

An inconsistency in the production of grid-averaged hydrological fluxes was discovered midway through the G5NR simulation. The problem is illustrated in Figure 5.2 as it pertains to the production of the 0.5 degree aggregated product. In the figure, precipitation in the 0.5 degree box is seen to be large over the land subset of the box. Prior to fixing the problem, the 0.5 degree runoff product was computed for only the land fraction of the 0.5 degree box; as a result, the 0.5 degree runoff value in this particular example would be high. The precipitation product, on the other hand, was computed for the entire 0.5 degree box (land plus ocean) and its average value would be relatively lc .

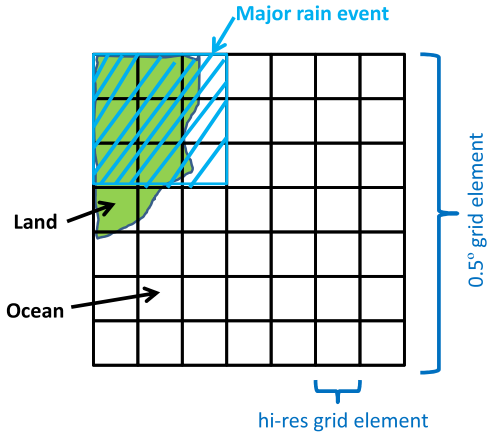

Figure 5.2: Illustration of a situation that leads to an inconsistency in the 0.5 degree output diagnostics, during the first half of the G5NR. Precipitation falls heavily over the land fraction of the 0.5 degree cell. The runoff diagostic represents the average runoff over the land only and will be large; the precipitation diagnostic represents the precipitation over the entire 0.5 degree area and will be relatively small.

Based on this strategy, it is quite possible, especially along coastlines but also in areas with lakes, for grid-averaged precipitation amounts to be fundamentally inconsistent with grid-averaged runoff amounts. Figure 5.3 shows regions where, in the 0.5 degree dataset, surface runoff production exceeds precipitation – a condition that should be impossible and indeed does not occur on the G5NR's native cube grid. While this post-processing problem is especially present in the 0.5 degree dataset, it must also be implicit in the high resolution gridded G5NR dataset, given that the surface elements defined by the cube are not the same as those in the high resolution latitude-longitude grid.

The problem was corrected midway through the G5NR simulation. For G5NR output dated after 9 May 2006, a new precipitation diagnostic is included, one that provides the precipitation falling over the land fraction of a grid element.

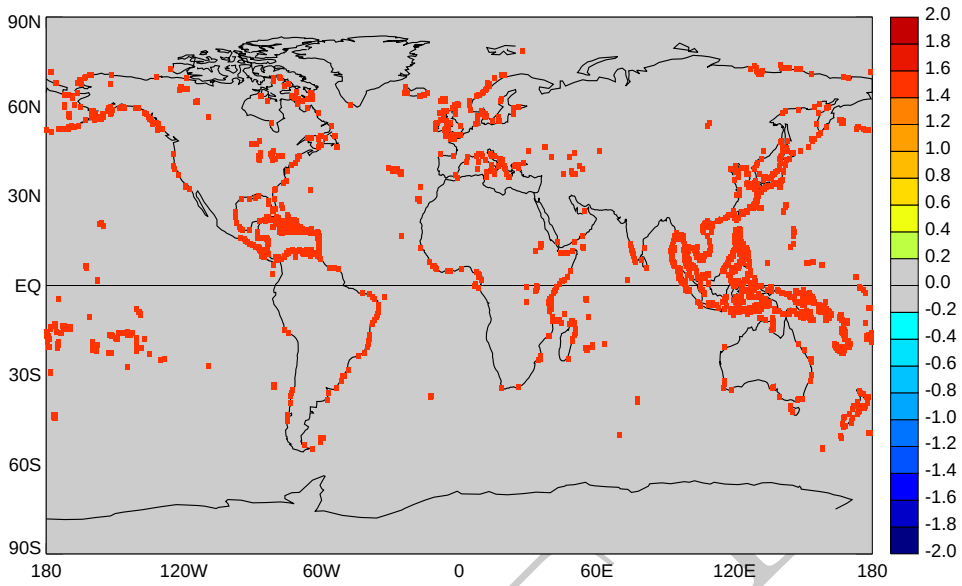

Figure 5.3: Locations (marked as red dots) where the output diagnostics for land surface runoff and precipitation are found to be inconsistent during a 16-day period in May, for reasons outlined in the text. The processing of the diagnostics was corrected in the latter half of the G5NR.

5.1.4 Singularities in Parameter Estimation

A problem with a certain set of land surface model parameters was discovered after the G5NR was launched. In essence, a curve fitting routine used to parameterize the net results of some complex calculations produced, in certain situations, an unwanted singularity. During the G5NR simulation, the singularity manifests itself as an excessive areal fraction of saturated soil, which in turn induces excessive runoff ratios. In other words, for a given input of precipitation, too much of the rainwater runs off.

The problem is somewhat rare. Roughly 4% of the land elements in the G5NR are potentially affected by the problem, but tests show that the actual manifestation of the problem appears in an even smaller percentage, of order 2%. Though much of the water runs off from the affected tiles, evapotranspiration from the tiles still proceeds. The impact of the problem on the atmosphere should be small and should certainly be non-singular.

5.1.5 Snowfall Forcing

A curious feature of the G5NR is the occasional generation of significant amounts of snow during warm periods in the tropics and midlatitudes. The map in Figure 5.4, constructed from 0.5 degree

G5NR data, shows the total amount of snow reaching the surface during the 16-day period spanning May 1 through May 16 of the first simulation year. The counterintuitive snowfall is likely the result of temporal truncation in the sequence of processes in the moist physics, whereby one process that results in a strong cooling is followed in the model by a process that produces a compensating large heating, and the rain/snow determination is made between the two steps.

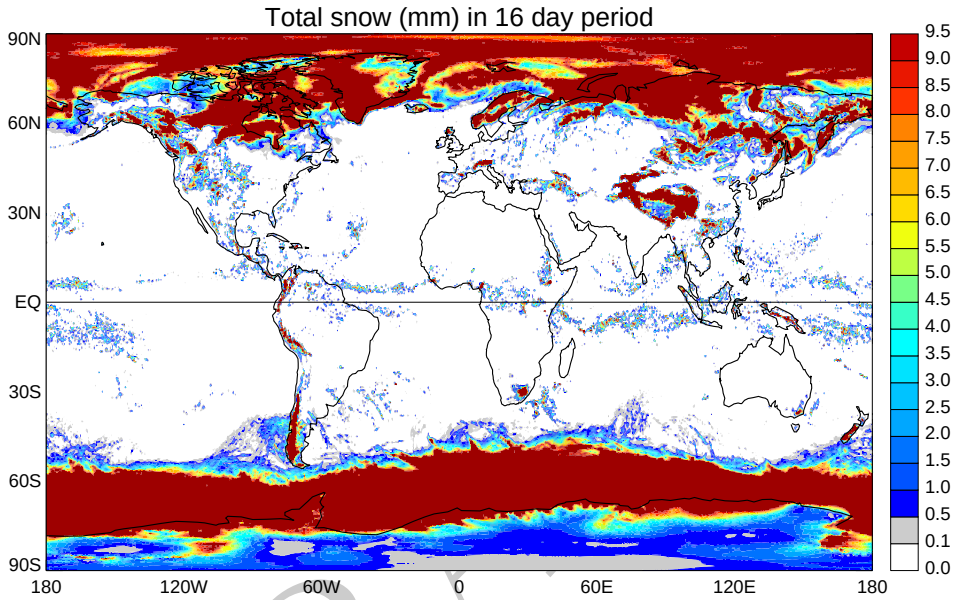

Figure 5.4: Amount of snow reaching the surface during a 16-day period in May. Values as high as 67 mm, for example, are seen in the Tropical Pacific.

Figure 5.5 shows time series covering two days in July for a high-resolution grid cell in Mexico. In most tropical/subtropical areas, unrealistic snow amounts on the surface melt rapidly. Here, though, even though the near-surface air temperatures remain above 280K, the deposited snow remains on the ground into the next day, having a strong and unrealistic impact on albedo and thus on the absorbed radiation at the surface.

Probably the most important impact of having spurious snow on the ground is the need for energy to melt it. Presumably that energy should have been taken out of the atmosphere, melting the snow before it reaches the surface. As it is, the energy comes from the land surface energy budget at the expense of other terms.

An additional technical point should be made about snow budgets in the model. The model naturally conserves snow, but there will be instances in the G5NR data when time-integrated snowmelt appears to exceed time-integrated snowfall. This occurs because liquid water falling onto a snowpack is allowed to freeze into the snowpack, increasing the snow mass.

5.1.6 Reduction of Solar Radiation During Rainfall Events

Reichle et al. (2011) identified an issue with the coupled land-atmosphere system used for the MERRA reanalysis (Rienecker et al. 2011). Overestimates of land surface evapotranspiration, particularly the interception loss component, were induced by three unrealistic behaviors of the coupled system, working together: (i) rain tended to fall only during daylight hours, (ii) the rain tended to fall as drizzle during the day rather than as high-intensity, episodic events, and (iii) incoming solar radiation at the land surface tended to be high during the drizzle. All three issues are apparent in the comparison of MERRA results with observations in Figure 5.6, taken from Reichle et al. (2011). Notice, for example, the significant reduction in downward solar radiation on June 21 in the observations, during a daytime rainstorm; similar reductions are not seen in the MERRA data. The MERRA-Land collection (Reichle et al. 2011) was created largely to account for improved precipitation estimates but also in part to overcome the interception loss deficiency associated with these three behaviors.

It is reasonable to investigate whether these issues also appear in the G5NR; it is possible that they are ameliorated by this simulation's increased spatial resolution and its concomitant changes in rainfall and radiation behavior. Figure 5.7 shows some corresponding time series taken from the high resolution G5NR data. These plots indicate that, indeed, the indicated problems are reduced. Rain does fall at night in the G5NR, and when it falls during the day, it can be more episodic. Days with significant rain now show a significant decrease in incoming solar radiation (e.g., on day 3), though days with tiny amounts of drizzle still show low reductions. Overall, the G5NR appears to behave more accurately in this context than MERRA, giving more credence to its calculation of land surface evapotranspiration.

5.1.7 Evaporation Instabilities

Figure 5.8 shows 3-day time series of precipitation, net radiation, and total evapotranspiration at a specific high resolution grid cell. Shown at the end of day 2 is a jump in the evaporation rate that is unrelated to any contemporaneous precipitation or net radiation input. The jump results from an instability in the land surface model's energy budget calculation.

The degree to which such instabilities occur in the G5NR over a representative 2-week summer period in central-north America is indicated in Figure 5.9. The problem, while ugly, is not rampant. Instabilities are absent over most of the area, and they happen at most about once per day in a few grid cells in the southern and northwestern U.S.

Furthermore, such instabilities have been analyzed before and are known to be connected, in large part, to the transfer of information between the atmosphere and land surface. To compute the surface fluxes, the land surface model requires the atmosphere to provide initial estimates of evaporation and sensible heat flux as well as the derivatives of these fluxes with respect to near-surface

air temperature and specific humidity, which themselves depend on the derivatives of aerodynamic resistance (a strongly nonlinear function) with respect to temperature and specific humidity. For various logistical reasons, the aerodynamic resistance derivatives are not produced by the atmospheric model, meaning that the land surface model cannot utilize this information. This leads to potential instabilities.

This is demonstrated here using two offline calculations with the land surface model (i.e., the land model is not connected to the atmospheric model but is instead driven with meteorological forcings derived from observations). In the first offline simulation, employing the offline set-up described by Koster and Mahanama (2012), the aerodynamic resistance derivatives are implicit in the forcing. The second simulation is identical to the first except for the zeroing of these particular derivatives. Figure 5.10 shows, for a 15-day summertime period, the relative incidences of instabilities in the two simulations. The occurrence of instability clearly increases when the derivative information is not provided. Again, the information regarding the aerodynamic resistance derivatives is also lacking in the G5NR; indeed, the regions where instability occurs in the second offline simulation are quite similar to those shown in Figure 5.9.

5.1.8 Occasional High Levels of Rainfall Forcing

Precipitation intensities in the G5NR are sometimes very high. To construct Figure 5.11, a representative 2-week period during the summer was chosen, and the precipitation rates computed at each high resolution grid cell were aggregated to half-hour totals. The figure shows the locations for which, during that 2-week period, a full 4 cm of water reached the surface during a single half-hour period. While a comparison with observed rainfall intensities is not provided here, these high simulated rainfall intensities seem unrealistically common. Users should be aware of their potential existence when doing hydrological analyses with G5NR data.

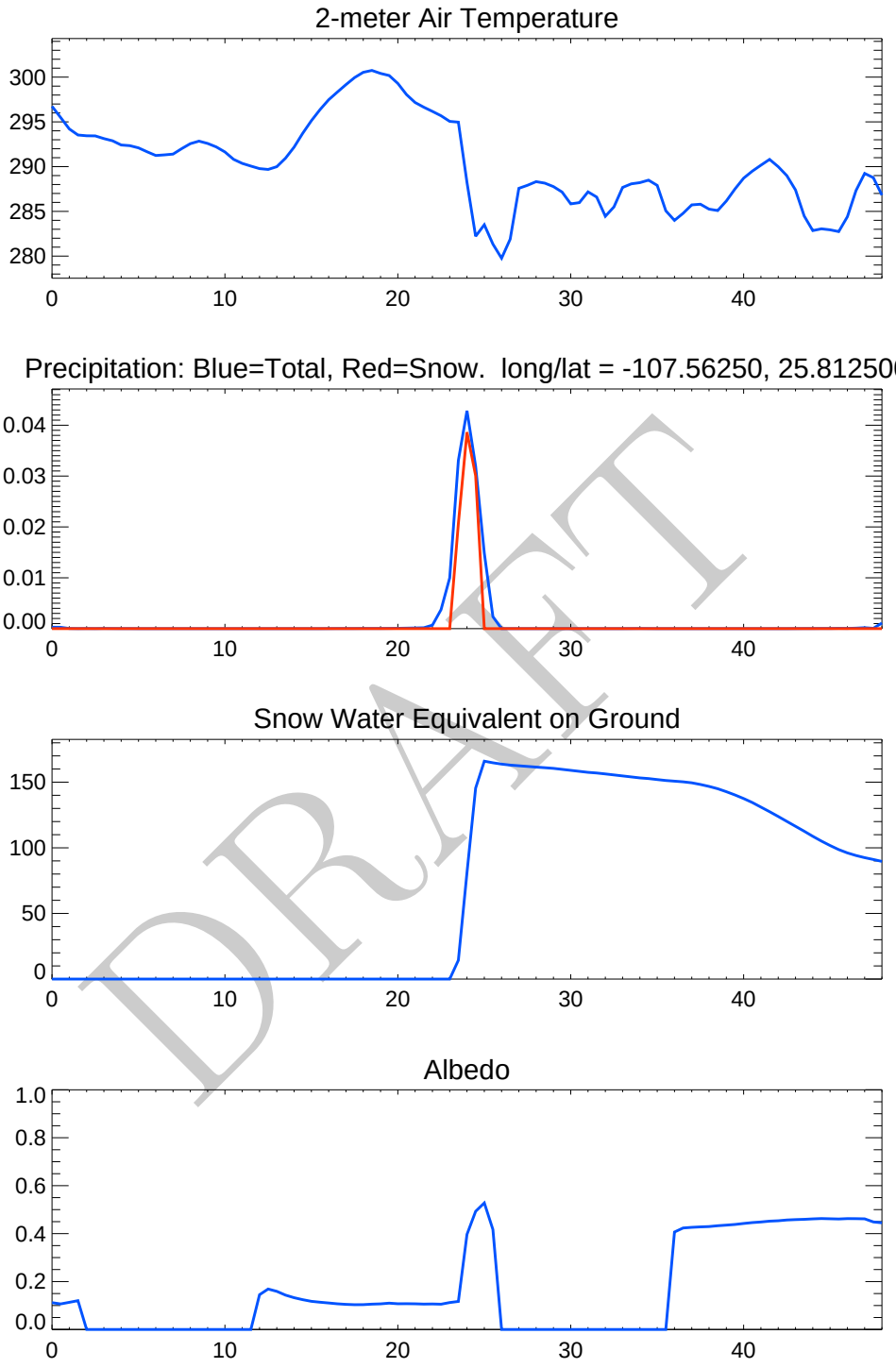

Figure 5.5: Time series (in hours) of 2-meter air temperature (K), precipitation ($kgm^{-2}s^{-1}$; total in blue and snow in red), snow water equivalent (kgm^{-2}), and albedo (-) over a 48-hour period in summer (centered on the snowfall event) at a grid cell in northern Mexico. Albedo by construct has a value of zero at night.

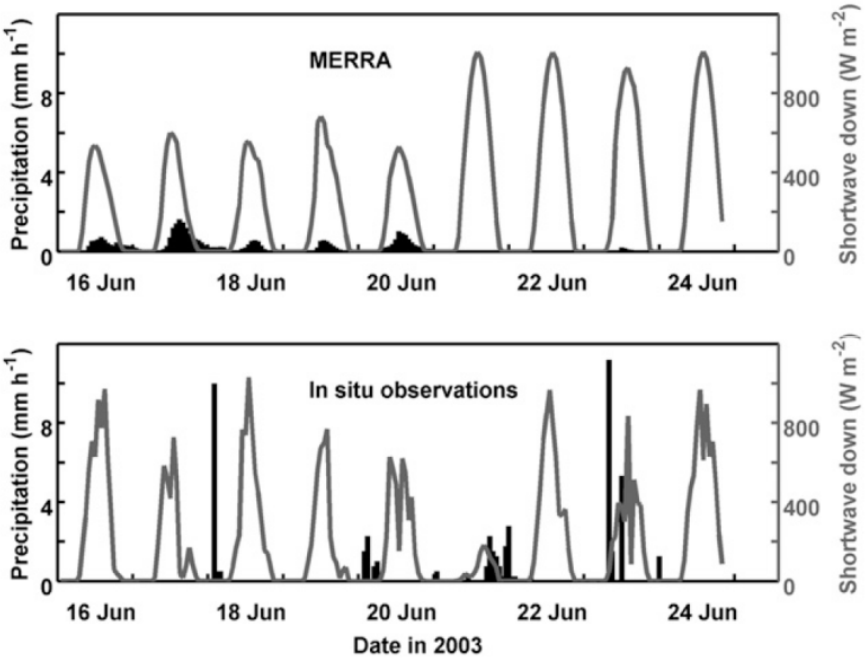

Figure 5.6: (Gray lines) Downward shortwave radiation and (black bars) precipitation from (top) MERRA for a grid cell near Gainesville, Florida (centered at 308N, 828W), and (bottom) in situ observations taken at the US-SP3 FLUXNET site (29.758N, 82.168W) located within the grid cell. Reprinted from Reichle et al. (2011).

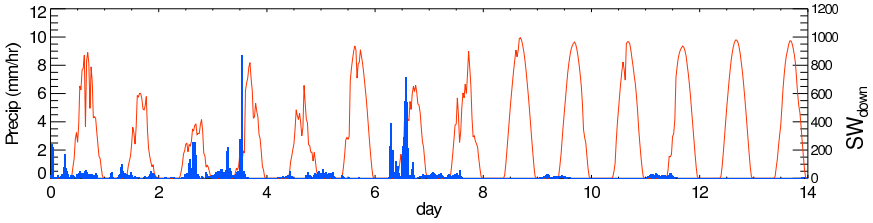

Figure 5.7: As in Figure 5.6, but for a representative high resolution grid cell in the G5NR. The blue histogram bars show the precipitation, and the red curves show the downward shortwave radiation.

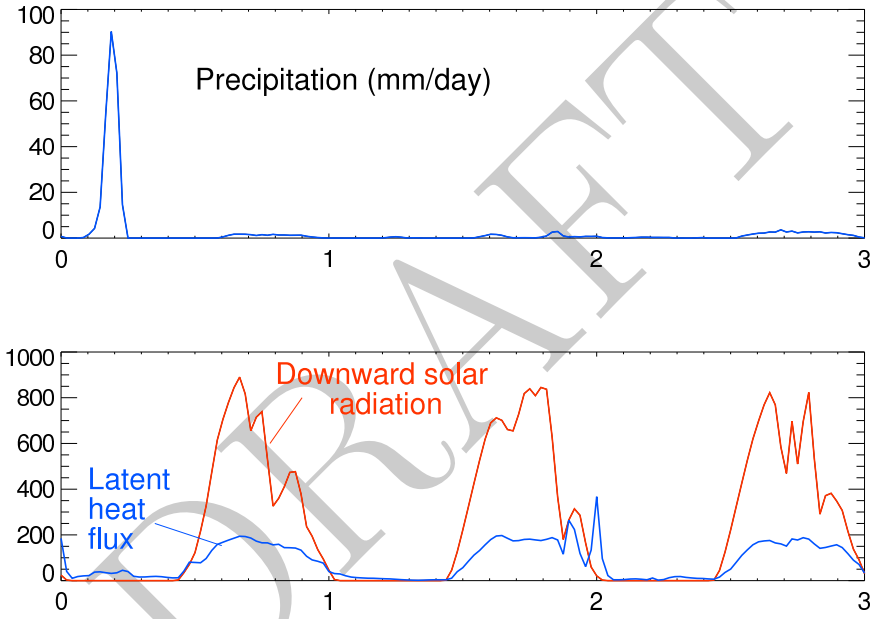

Figure 5.8: Top panel: Time series of precipitation, in mm/day, from the G5NR at a specific high-resolution grid cell. Bottom panel: Corresponding time series of downward solar radiation and latent heat flux, in Wm^{-2}.

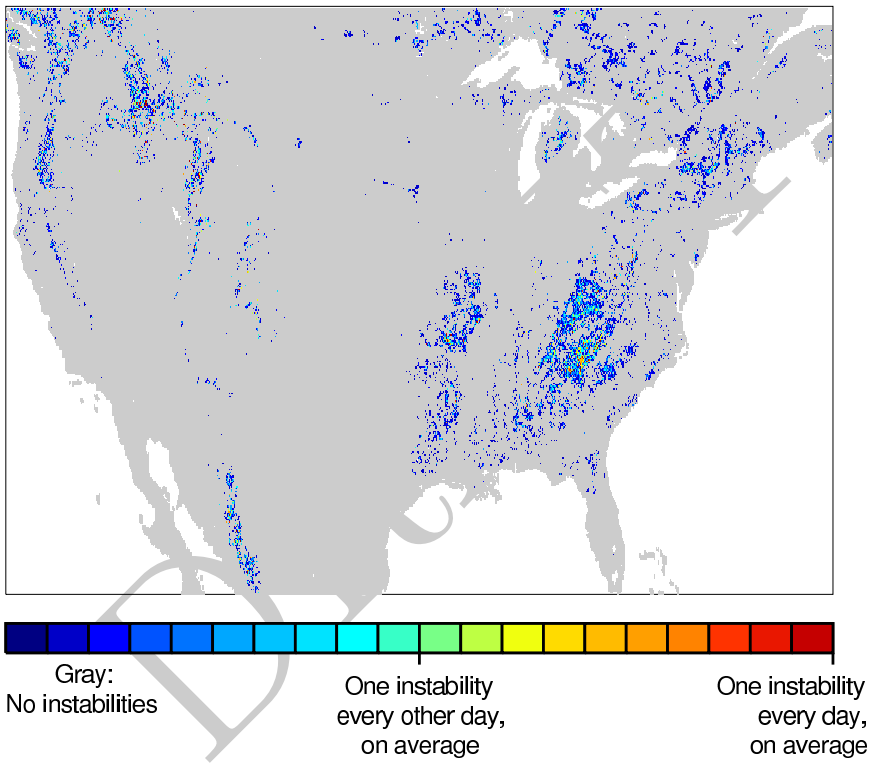

Figure 5.9: Locations where evaporation instabilities are found in the G5NR during a representative 14-day period during summer.

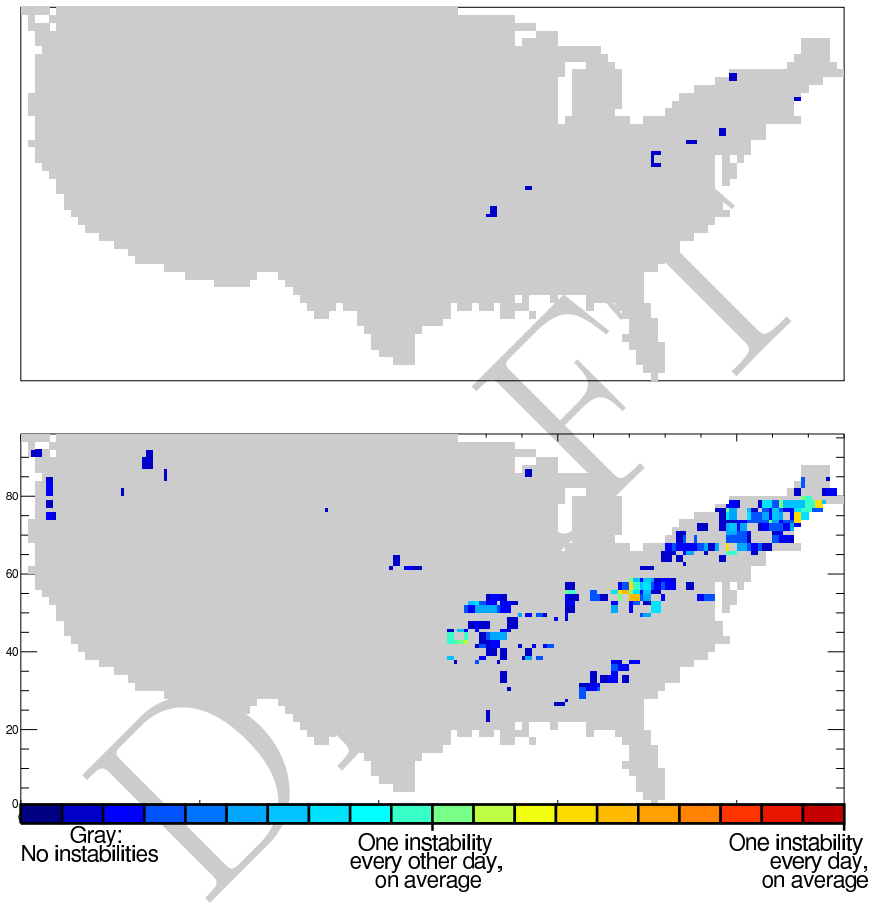

Figure 5.10: Locations where evaporation instabilities are found in two offline land surface model simulations using prescribed, observations-based meteorological forcing. Top panel: simulation in which information regarding the derivatives of aerodynamic resistance with respect to temperature and specific humidity is provided to the land model. Bottom panel: simulation in which this information is not provided to the land model. Results are shown for a representative 15-day summer period.

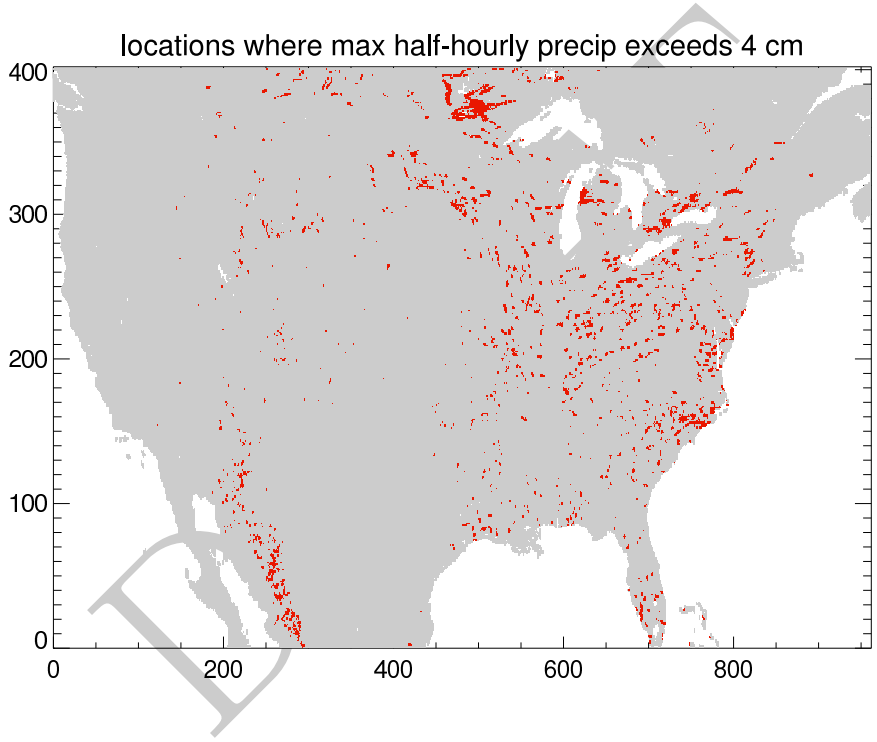

Figure 5.11: Locations for which the maximum of half-hourly precipitation totals during a representative 2-week period in summer exceeds 4 cm.

5.2 Land Surface - Energy Processes

In this Chapter, the realism of the long term mean land surface energy budget and low-level atmospheric temperatures over land in the G5NR are tested by comparison to independent estimates. For both, the means of the two-year free-running G5NR simulations are compared to the mean of the observed climate over a 10-year time period. In addition to being directly relevant to land surface applications of the G5NR output, these comparisons also provide a useful diagnostic for the realism of the physical processes modeled by the G5NR, in terms of both land surface processes, and the atmospheric processes that interact with the land surface.

5.2.1 Surface Energy Budget

The G5NR surface energy budget is compared to estimates from the NASA Energy and Water cycle Studies (NEWS) project (L'Ecuyer et al. 2014). Recall that the water budget component of the G5NR was compared to NEWS estimates in Chapter 3. The NEWS project has produced a 10-year climatology (covering approximately 2000–2009) of the global and continental/basin-scale water and energy budget terms. These budget terms are based on satellite observations, with model products used where observations are unavailable, and have been adjusted to satisfy water and energy balance constraints, with reference to the estimated uncertainty of each term.

Table 5.1 shows the annual mean continental surface energy budget from the G5NR and NEWS (the equivalent comparison will be made over the oceans in Section 5.3.1). The continental G5NR energy budget estimates are quite close to those from NEWS, although typically just outside the NEWS uncertainty estimates. Compared to NEWS, both the downwelling and upwelling components of longwave radiation are underestimated by 2.5–2.6 PetaWatts (PW, 17–18 Wm^{-2}), while both components of the shortwave are slightly overestimated, by 0.6–0.7 PW (4–5 Wm^{-2}). The G5NR turbulent fluxes are reasonably close to those from NEWS, although the partition of radiative energy between the latent and sensible heating differs very slightly, with the G5NR favoring slightly higher sensible heat fluxes (0.5 PW, 4 Wm^{-2}), balanced by slightly lower latent heat fluxes (by 0.4 PW, 3 Wm^{-2}). Note that the NEWS and G5NR land surface turbulent fluxes are not independent, since the NEWS estimates are partly based on land surface turbulent fluxes from MERRA (also a GEOS-5 system).

5.2.2 Land Surface Temperatures

The monthly mean 2 m air temperatures (T_{2m}) from the G5NR are compared to observations from the Integrated Surface Hourly (ISH) collection, collated by the National Climatic Data Center (NCDC, Lott, 2004). Approximately 2000 ISH station are included in the comparison (Figure 5.12), and while these stations span the globe, their coverage is sparse outside of north America

and Europe. For each calendar month, Figure 5.12 shows very good agreement between the mean T_{2m} over the station locations from the G5NR and the ISH data (solid lines). The G5NR monthly mean T_{2m} is consistently within 2 K of the ISH mean, and with the exception of April, is within one temporal standard deviation of the ISH 10-year monthly mean.

Also included in Figure 5.12 are the monthly mean T_{2m} from 10 years of ERA-I reanalyses (Dee et al. 2011). The very close agreement between the ISH and ERA-I mean T_{2m} at the station locations is expected, since ERA-I includes a surface analysis which adjusts the model land surface state variables to reduce the errors in 2m temperature and relative humidity forecasts. However, the high accuracy of the ERA-I monthly mean T_{2m} at the ISH station locations may not extrapolate to regions that are less well observed by T_{2m} stations (even if the same stations are not used in ERA-I and ISH, the same regions will be over-represented by both). Consequently, while we use ERA-I as a global reference for the G5NR T_{2m}, some caution is required in interpreting these results. Nonetheless, Figure 5.12 does show a very strong agreement between the global mean T_{2m} over land from ERA-I and the G5NR (dashed lines).

Figure 5.13 shows the monthly mean T_{2m} over each continent from ISH, ERA-I, and the G5NR. In general, the monthly mean G5NR T_{2m} tracks the ISH time series very well over each continent. The G5NR T_{2m} is within one temporal standard deviation of the ISH 10-year monthly means, and only occasionally differs by more than 2 K. The exceptions are north America in Dec-Jan-Feb and in Europe in Apr-May-Jun, when the G5NR T_{2m} is cooler than ISH. Comparing the dashed and solid lines in Figure 5.13, the poor sampling of the ISH stations (note the number of stations in the subplot title) is reflected by the differences between the station-only time series and continental mean time series. Despite this, the difference between the ERA-I and G5NR time series are consistent between the station-only and continental mean time series, lending some support to the use of ERA-I to infer the continental-scale T_{2m} biases in the G5NR. As with comparison to the ISH observations, comparison to the continental mean ERA-I T_{2m} indicates that the G5NR monthly mean T_{2m} are reasonable. The G5NR monthly mean T_{2m} are consistently within 2 K of the ERA-I values, except for the two instances identified above, in which the G5NR is cooler than other estimates.

Figure 5.14 shows global maps of the bias between the ERA-I and G5NR mean T_{2m} for Dec-Jan-Feb and Jun-Jul-Aug. The cool T_{2m} in the G5NR mention above, during boreal winter over north America and boreal summer over Europe, are both due to the G5NR being consistently cooler across the continent in question. However, other regions stand out in Figure 5.14 as having larger differences between the ERA-I and G5NR T_{2m}. Most notably the G5NR is much cooler over north Africa, and it is much warmer in the northern high latitudes (the latter is associated with differences in cloud-cover between the two models). Unfortunately, neither of these regions is well observed by validating observations, and it is difficult to say which model (if either) is more accurate at these locations.

Finally, since land surface temperature biases are important to microwave forward modeling of the land surface (e.g., to retrieve soil moisture), Figure 5.14 also shows the difference between the monthly mean ERA-I and the G5NR mean land surface temperatures. The differences in

the low-level atmospheric temperature and land surface temperature between the two models are very similar, in terms of both spatial patterns and magnitude. Consequently, the above examination of the G5NR mean T_{2m} also provides an indication of the biases in the G5NR land surface temperatures.

In summary, while it is difficult to evaluate land surface energy processes at large scales the above comparison suggests that the G5NR land surface energy processes are reasonable, in terms of simulating a realistic climate. Globally, the differences between the annual mean surface energy budget, and the monthly mean low-level atmospheric temperatures from the two year G5NR simulation and the 10-year observations-based estimates are within the expected variability, given the short period of the G5NR simulation. The temperatures also appear to be quite realistic when averaged over individual continents, however there are possible instances of large temperature biases ($> 5K$) at the regional scale.

	G5NR	**NEWS**
Sensible heat flux	5.3	4.8±0.5
Latent heat flux	5.6	6±0.2
Downward shortwave radiation	27.7	27±0.6
Upward shortwave radiation	6.8	6±0.2
Downward longwave radiation	42.9	45±0.5
Upward longwave radiation	52.8	55±0.6
Net change in heat storage	0.2	-0.1

Table 5.1: Comparison of G5NR and the NEWS project annual mean surface energy budget terms, in PetaWatts, over continental regions. *Courtesy of Michael Bosilovich.*

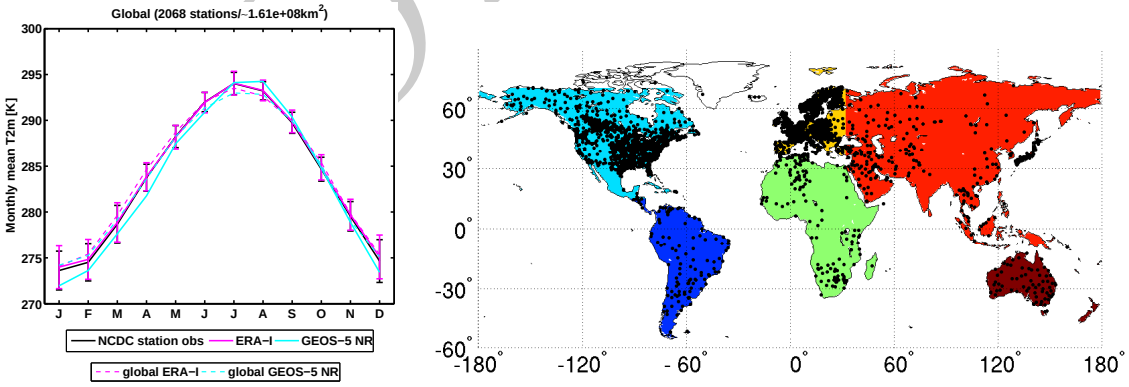

Figure 5.12: Left panel: Monthly mean T_{2m} from the G5NR, ISH station observations, and ERA-I. Solid lines show mean across station locations, and dashed lines show mean across global land. For the station comparison, the error bars give the standard deviation of the 10-year monthly mean. Right panel: Locations of the ISH T_{2m} stations.

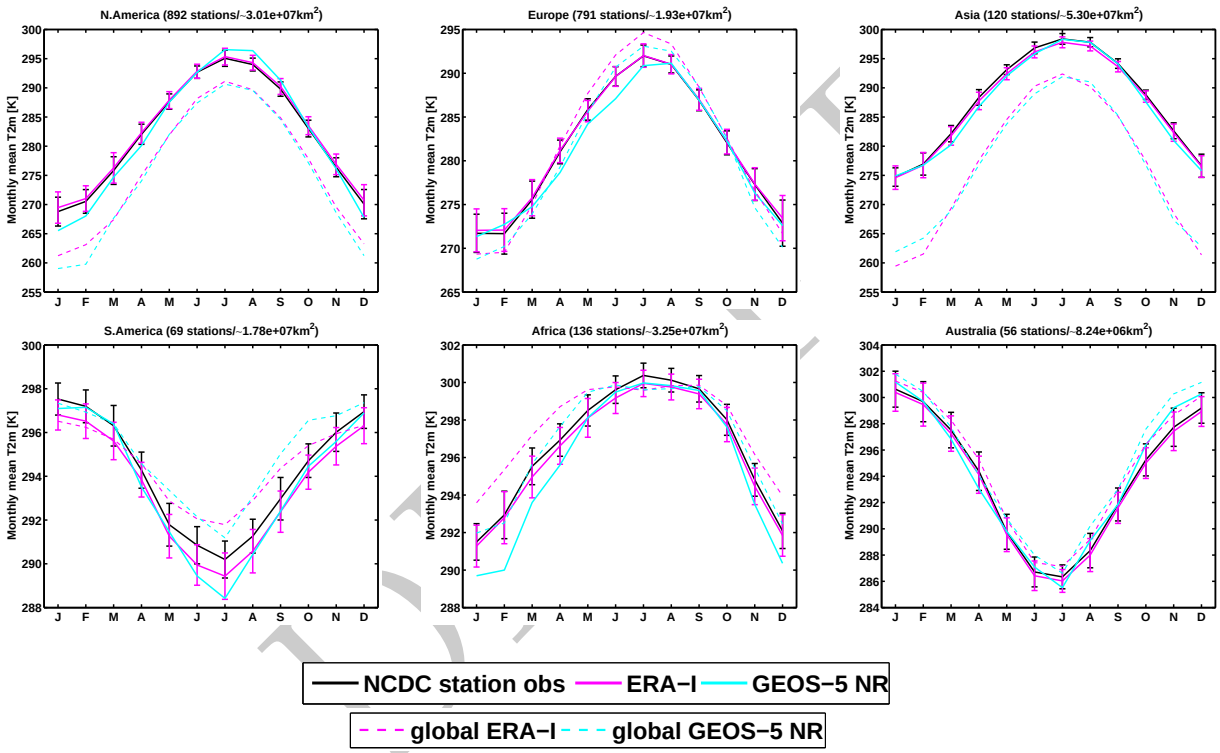

Figure 5.13: Monthly mean T_{2m} from the G5NR, ISH station observations and ERA-I, by continent. Solid lines show mean across station locations, and dashed lines show mean across global land. For the station comparison, the error bars give the standard deviation of the 10-year monthly means.

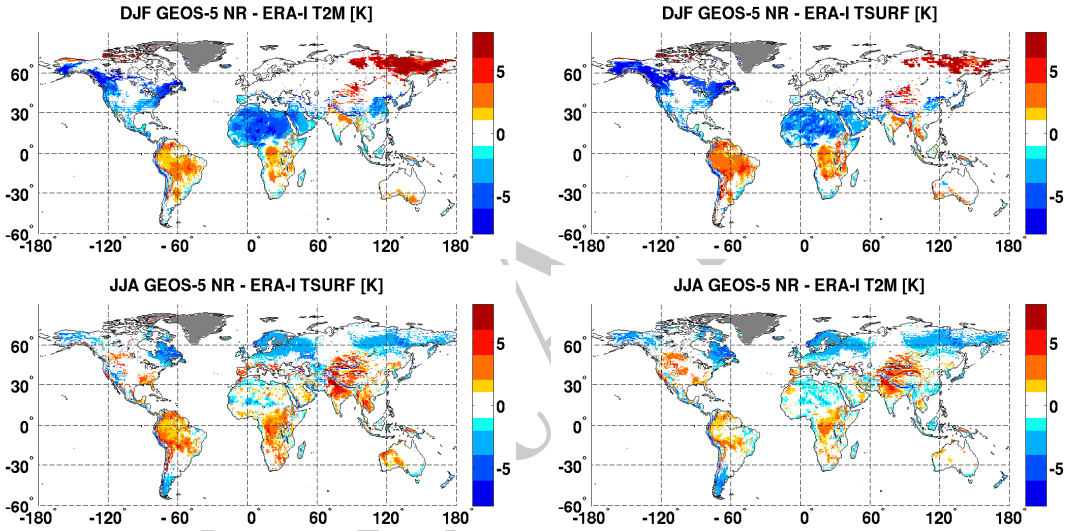

Figure 5.14: G5NR minus ERA-I mean temperature differences, averaged over Dec-Jan-Feb (upper) and Jun-Jul-Aug (lower), for T_{2m} (left) and land surface temperature (right). Colors are only plotted where the difference is greater than $2\times$ the standard deviation of the ERA-I 10-year monthly mean.

5.3 Ocean Surface

5.3.1 Ocean Energy Budget

In the G5NR, the atmosphere is forced by a SST analysis. The net energy budget over the ocean surface can be expressed as

$$F_{SW\downarrow} - F_{SW\uparrow} + F_{LW\downarrow} - F_{LW\uparrow} - F_{SH} - F_{LH} = Q \tag{5.1}$$

where SW and LW are upward and downward shortwave and longwave radiation fluxes, SH is the sensible heat flux, LH is the latent heat flux and Q is the energy storage in the ocean. Table 5.2 shows the components of equation (5.1) from the G5NR integrated over the ocean surface along with their estimates from the NEWS project (recall that the continental component of the NEWS and G5NR energy budget were compared in Section 5.2.1). All balance terms from the G5NR, except for the latent heat flux, are within the uncertainty of the observations. Latent heat flux is over-estimated by several Watts per meter squared, and the net ocean heat loss is 3.4 Wm^{-2}.

The spatial pattern of the net surface radiation from the G5NR, compared to GEWEX Surface Radiation Balance data (Stackhouse et al. 2001), is shown in Figure 5.15. There is an excess of shortwave radiation along midlatitudes and over subtropical regions near the west coasts of Africa and America of up to 40 Wm^{-2}, and a lack of shortwave radiation in the subtropical regions of up to 20 Wm^{-2}. The bottom row in Figure 5.15 shows the error in surface cloud radiative forcing. It is clear that the cloud radiative forcing error pattern closely corresponds to the radiation error pattern with opposite sign, which leads us to conclude that bias in simulated surface radiation is mainly due to cloud radiative effects. The net surface longwave radiation mostly adjusts for shortwave errors due to warmer SST in the regions with excessive shortwave, and colder SST in the regions with insufficient shortwave radiation. Since the G5NR simulation was only two years long, our estimate of annual mean errors can be biased due to inter-annual variability of estimated fields. Gray areas in Figure 5.15 show the 5% significance level calculated using two-sided student t-test.

Figure 5.16 shows the spatial pattern of latent and sensible heat fluxes compared to Goddard Satellite-based Surface Turbulent Fluxes (GSSTF) data (Shie et al. 2009). Latent heat is determined by evaporation and is greatest over subtropical oceans where the atmosphere above the surface is dry. Latent heat flux in the G5NR is higher than the GSSTF estimates over most of the tropical-subtropical oceans by up to 50 Wm^{-2}, and lower than the GSSTF by up to 30 Wm^{-2} in high latitudes. It is known that in GEOS-5 errors in evaporation and, hence, the latent heat flux are consistent with the errors in near surface humidity gradient (Molod et al. 2012). The sensible heat flux in the G5NR is almost everywhere stronger than in GSSTF, with maximum values up to 40 Wm^{-2} in the north Atlantic, which corresponds to the wind stress error patterns (see Section 5.3.2).

Figure 5.17 shows the implied northward heat transport estimated from the G5NR and from observations (Ganachaud and Wunsch, 2000, Trenberth and Caron, 2001). The northward heat transport at a given latitude is the sum of the fluxes on the left-hand side of equation (5.1), integrated zonally and from the north Pole to that latitude. Poleward heat transport is overestimated in the northern hemisphere mid-latitudes, and slightly underestimated compared to Trenberth and Caron (2001) in the subtropics in both hemispheres.

5.3.2 Ocean Winds

In this Section, we look at the 2 year average (from May 2005 to May 2007) 10 m ocean winds and surface wind stresses of the G5NR. The analysis uses monthly fields that are interpolated on a 0.5 degree grid and are compared to estimates from the Cross-Calibrated Multi-Platform (CCMP, Atlas et al. 2011) and from the Scatterometer Climatology of Ocean Winds (SCOW, Risien et al. 2008).

As a first step towards understanding some of the climatological features of the G5NR surface winds, we compare the global wind rose of the G5NR to that of CCMP. The wind roses for CCMP are shown in Figure 5.18. The eastern sector clearly identifies the southeasterly and northeasterly trade winds while the strong westerlies are observed in the western sector. Figure 5.19 depicts the 10 m wind rose for the G5NR. The direction of the trade winds is similar to that in the observations (see eastern sector), except that the trade winds above 15 knots (brown color) are nearly absent. This problem is directly related to the weak Hadley cell circulation described in Section XXX. The prevailing westerlies' strength, observed in the western quadrant of Figure 5.19, is similar to the that observed by CCMP. However, the G5NR statistics indicate an unusual northward component. This northward bias is caused by the strong northwesterlies observed in the North Atlantic, depicted in Figure 5.20. In the north Atlantic region, the meridional and zonal G5NR winds (see the two left-most top panels of Figure 5.20) are significantly stronger than those from SCOW (middle panels of Figure 5.20) and CCMP (bottom panels of Figure 5.20). These strong north Atlantic northwesterlies are the probable cause of the large bias observed in the sensible heat flux discussed in section 5.3.1. Figure 5.21 shows the wind stress from the G5NR and SCOW. Note that in this case, while we highlighted the weakness of the G5NR trade winds, this somehow did not translate into weak stresses. Within the trades regions in Figure 5.21 the G5NR wind stress (top panel) is of similar magnitude than the SCOW wind stress (bottom panel), while in the same region, the G5NR wind speed (top right panel of Figure 5.21) is clearly weaker than in the SCOW (middle right panel of Figure 5.21). This indicates an issue in the surface wind stress calculation. Finally, the stress induced by the westerlies is considerably stronger than the climatology. This is observed above the circumpolar current in the Southern hemisphere as well as over the Gulf stream extension in the north Atlantic.

	G5NR	**NEWS**
Sensible heat flux	5.6	6.8±1.3
Latent heat flux	38.6	34.8±1.8
Downward shortwave radiation	66.4	68.5±1.7
Upward shortwave radiation	5.0	5.3±0.5
Downward longwave radiation	127.9	128.0±2.0
Upward longwave radiation	148.5	149.0±1.7
Net change in heat storage	-3.4	0.7

Table 5.2: Comparison of G5NR and the NEWS project annual mean surface energy budget terms, in PetaWatts, over oceans. *Courtesy of Michael Bosilovich.*

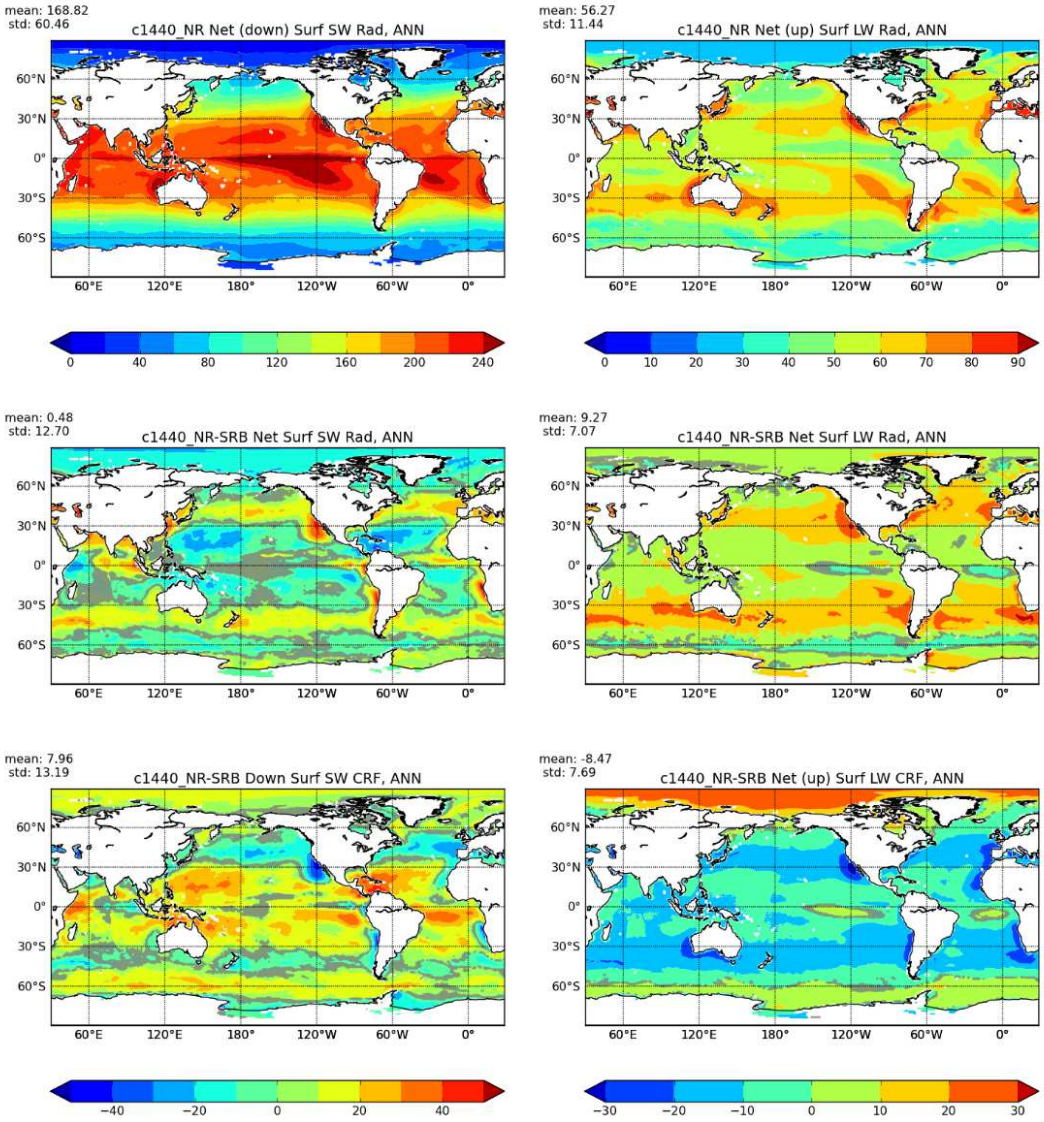

Figure 5.15: Annual mean of net surface shortwave (left) and longwave (right) radiation in Wm^{-2}. Top row shows the radiation from the G5NR, middle row shows the difference between the G5NR and SRB data and the bottom row shows the difference of cloud radiative forcing between the G5NR and SRB data.

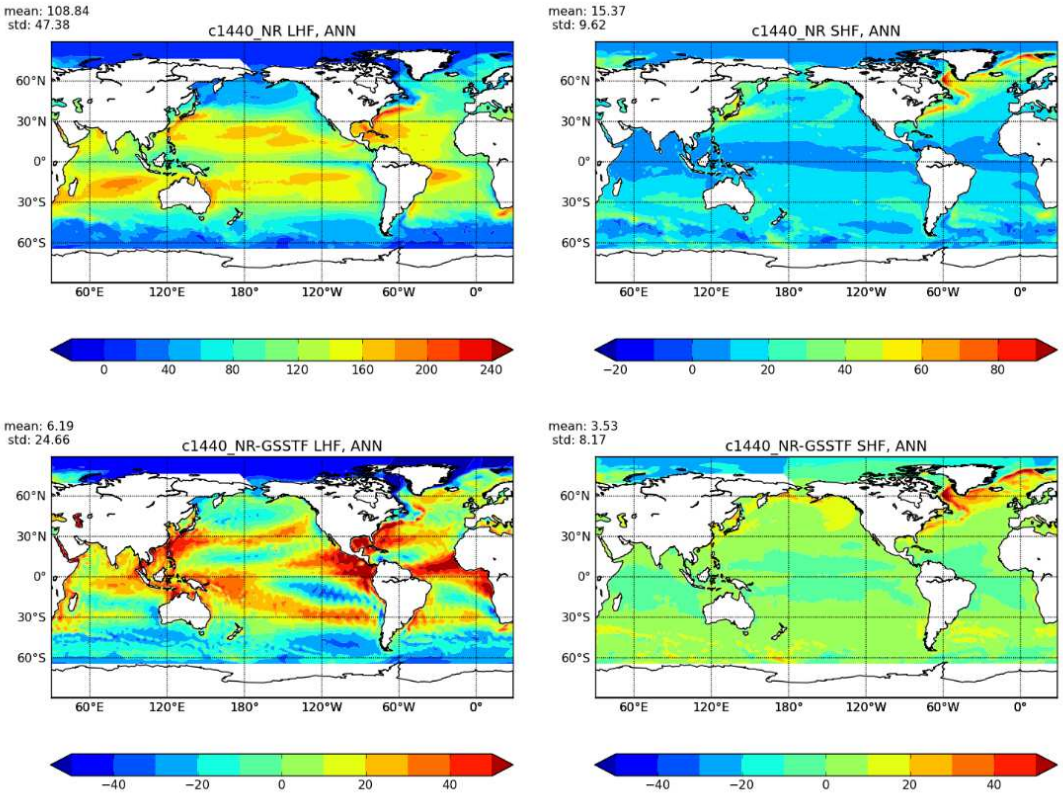

Figure 5.16: Annual mean of latent (left) and sensible (right) heat flux in Wm^{-2} from the G5NR (top) and difference between G5NR and GSSTF data (bottom).

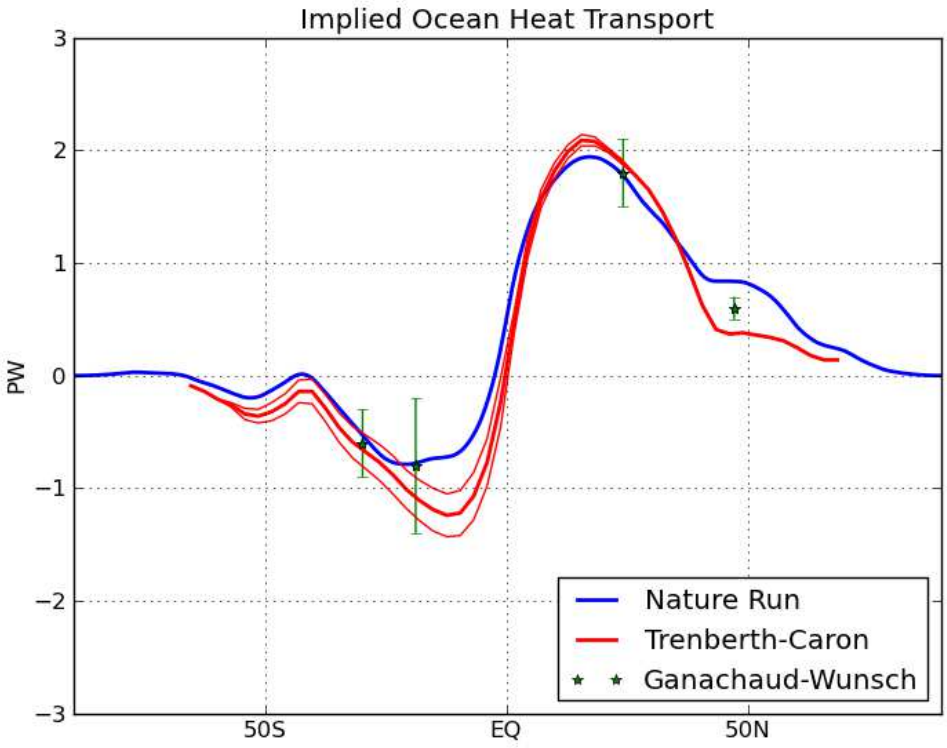

Figure 5.17: Implied ocean heat transport in PetaWatts.

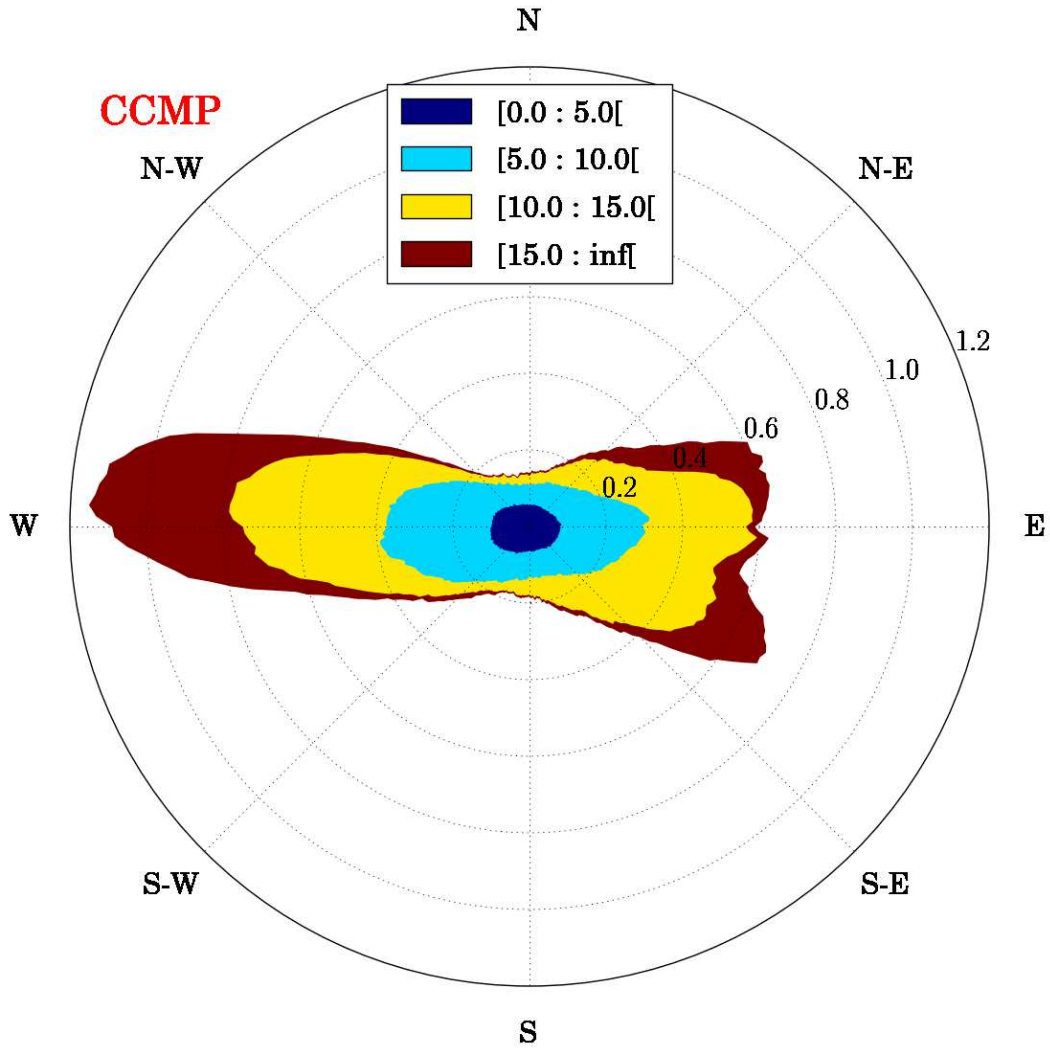

Figure 5.18: CCMP 10 meter wind rose from May 2005 to May 2007, the wind rose is divided in 128 sectors. For clarity, the sector's boundary are not shown. The radius of a sector indicates the percentage of data that have the direction given by the corresponding sector. Colors represent bins of wind speed in knots within a given sector.

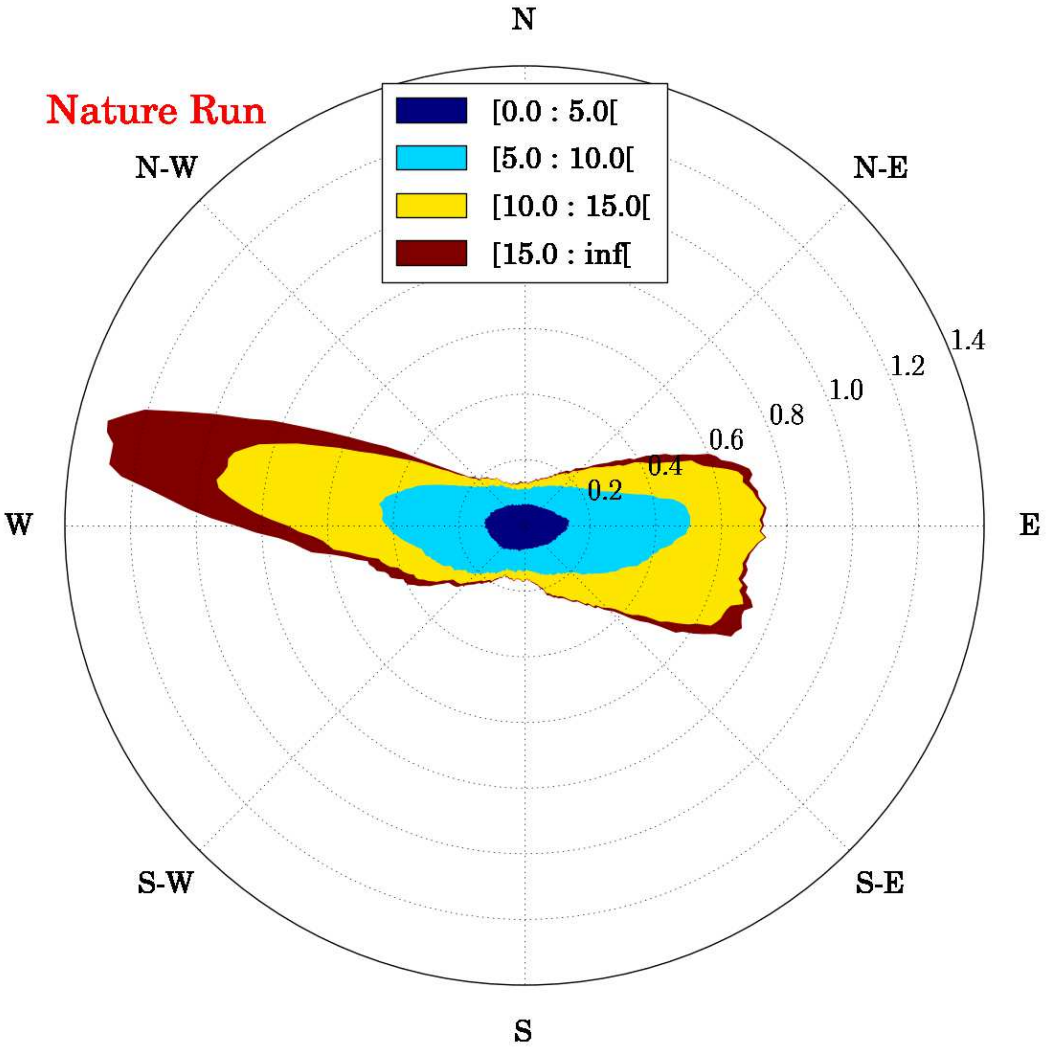

Figure 5.19: Same as 5.18 but for the G5NR 10 m winds.

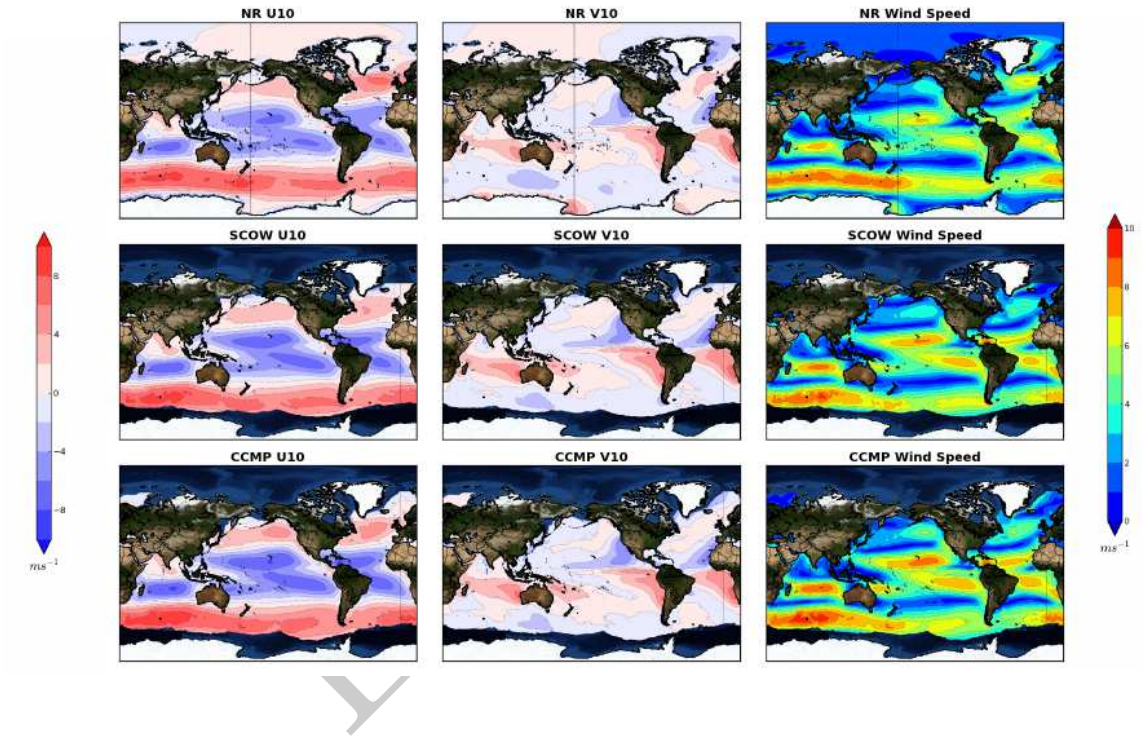

Figure 5.20: From left to right: Zonal wind speed, meridional winds speed and wind speed. From top to bottom: 2 year average from the G5NR, SCOW winds and CCMP winds during the same period as the G5NR.

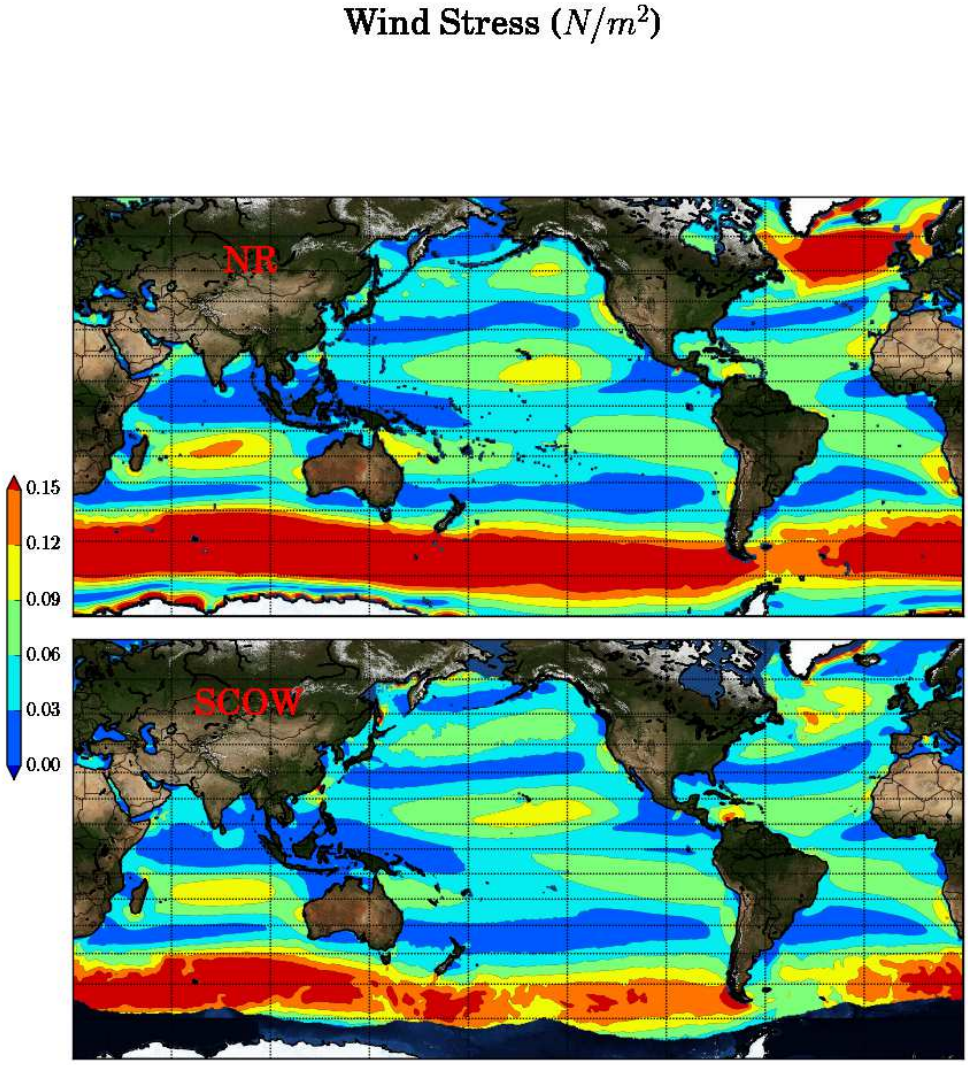

Figure 5.21: Top panel: Two year average wind stress magnitude from the G5NR. Bottom panel: Wind stress magnitude from SCOW.

5.4 Polar Regions

The G5NR provides an opportunity for the examination of simulated atmospheric phenomena in polar regions at very high spatial resolution and in the context of a global model integration. A general validation is performed with a focus on atmospheric moisture and energy budgets, which are frequently used as diagnostics for understanding the changing climate of the polar regions. A few topics related to high spatial resolution are of particular interest in polar regions. These include the simulated surface mass balance over polar ice sheets, and the representation of the near-surface wind field.

5.4.1 Polar Atmospheric Moisture and Energy Budgets

Atmospheric reanalyses have been frequently used to provide a quantitative depiction of energy and moisture budgets (e.g., Serreze et al., 2005), although their performance in polar regions contains significant caveats. A comparison of G5NR energy budget components with three contemporary atmospheric reanalyses for the North Polar Cap (70 °N - 90 °N) is nevertheless informative. The North Polar Cap roughly corresponds to the periphery of the Arctic Ocean and is a frequently-used region in polar studies. The reanalyses used for the evaluation include ERA-I (Dee et al., 2011), the Climate Forecast System Reanalysis of the National Centers for Environmental Prediction (CFSR; Saha et al., 2010), and MERRA (Rienecker et al., 2011). First, it is found that the G5NR net surface energy flux exceeds reanalyses estimates by an average of 19 Wm^{-2} in winter months of December-January-February and 13 Wm^{-2} in the summer months of June-July-August, while transitional seasons compare more favorably (Figure 5.22a). These seasonal discrepancies in the net surface energy flux occur from differing components, with winter differences associated with turbulent heat fluxes and summer discrepancies associated with the solar radiative flux. There is substantial disagreement among the reanalyses in the magnitude and even the sign of the Arctic sensible heat flux (Figure 5.22b), but the G5NR is a clear outlier to these disparate estimates in winter by an average of 15 Wm^{-2}. In summer, the G5NR net solar flux at the surface is less than reanalyses values by about 7 Wm^{-2}. Comparisons of surface solar fluxes illustrate some of the deficiencies in the reanalyses that need to be kept in mind. The MERRA product used a fixed surface albedo over sea ice that was too low in comparison to observation for the early summer period (Cullather and Bosilovich, 2012). This accounts for the large differences between MERRA and other reanalyses shown in Figure 5.22c. Subsequent improvements to the surface representation over sea ice and grounded ice sheets in GEOS-5 are incorporated in the G5NR simulation, but discrepancies between the G5NR net solar flux and the other two reanalyses are associated with an underestimate of the solar downwelling component. This is suggestive of differences in cloud cover. Discrepancies between the G5NR and reanalyses radiative fluxes at the top of the atmosphere (not shown) indicate a simulated atmosphere that reflects about 9 Wm^{-2} more than reanalyses shortwave radiative flux values in summer. The South Polar Cap (70°S - 90°S) encompasses most of the Antarctic continent. Here, differences among the reanalyses are large and conclusions regarding the relative performance of the G5NR are less straightforward. While the net surface energy flux of the G5NR is within the broad range of reanalysis values, the surface downwelling shortwave

radiative flux of the G5NR for the south polar region is less than reanalysis estimates by an average of 30 Wm^{-2} during summer months. This is consistent with the underestimate of the net solar flux in comparison to reanalyses for Northern Hemisphere high latitudes. Despite these differences in energy flux components, there is generally good agreement between the G5NR and station near-surface air temperatures. For example, Figure 5.23a shows a comparison with Amundsen Scott (90°S, 2835m). Over the Antarctic ice sheet, the orography is typically smooth and discrepancies with the G5NR surface geopotential are negligible at this spatial resolution. Other Antarctic stations examined show similar agreement with the exception of Halley Bay (76°S, 26°W, 30m), where the G5NR is 5°C warmer than corresponding station values in winter. This exceeds the range found in inter-annual variability, and appears to be associated with differences in the local circulation. For the Northern Hemisphere, comparisons with several stations indicate the G5NR is too warm in winter. This includes Barrow (71°N, 157°W, 40m), where the G5NR exceeds the station value by 4°C in winter (Figure 5.23b).

Atmospheric reanalyses have also been frequently used for the evaluation of the polar atmospheric moisture budget (e.g., Serreze et al., 2006), but these estimates have been substantiated with studies using rawinsonde observations, and with glaciological data. The net surface moisture flux — equivalent to precipitation minus evaporation (P−E) — is typically evaluated with reanalysis prognostic fields, however the atmospheric budget computation —vertically-integrated atmospheric moisture convergence minus precipitable water tendency — has been found to be a more robust estimate. The budget computation is often referred to as the 'aerological' estimate in contrast to values from prognostic fields. Reanalysis aerological values have been obtained from the Climate Analysis Section of the National Center for Atmospheric Research (NCAR) and are shown for the polar caps in Figure 5.24 in comparison to prognostic values and the G5NR. It is seen in Figure 5.24 that aerological values from the reanalyses agree closely for both regions, and that the G5NR exceeds these values. For the Arctic, the G5NR produces a net surface flux of 265 mm yr^{-1}, which compares to reanalysis estimates of 205±45 mm yr^{-1} from prognostic fields and 203±6 mm yr^{-1} from the aerological method. The largest discrepancies are found to occur in transitional seasons. For the Antarctic polar cap, the G5NR value is 220 mm yr^{-1} as compared to average reanalysis values of 186±24 mm yr^{-1} from prognostic fields and 191±12 mm yr^{-1} from the aerological method.

A further validation of the moisture budget may be obtained through evaluation of the surface mass balance (SMB) of the polar ice sheets. Significant efforts have been made in recent years to constrain SMB estimates though increased in situ glaciological measurements, remote sensing methods, and the employment of high-resolution regional climate models. Shown in Figure 5.25 are computed SMB fields from the G5NR for (a.) the Greenland Ice Sheet (GrIS) and (b.) the Antarctic Ice Sheet (AIS). The SMB is computed as the net of annual precipitation minus evaporation and runoff. Other wastage terms including blowing snow processes are not considered in the G5NR. For the GrIS, the G5NR produces a mean SMB of 30.4 cm yr^{-1} water-equivalent. This is somewhat larger than available contemporary estimates including 27.4±2.4 cm yr^{-1} and 25.3 cm yr^{-1} from the MAR and RACMO2 regional climate models (Ettema et al., 2009; Fettweis et al., 2007). The spatial patterns of G5NR SMB are nevertheless intriguing and agree reasonably well with regional climate model fields. Of particular interest are the peripheral ablation zones that exceed 2 m yr^{-1} in the southwest, and localized areas of accumulation above the equilibrium line along the western GrIS. Similarly, the AIS field shows excellent spatial agreement with the accumulation

field as it is known. The G5NR values for interior plateau are generally between 5 and 10 cm yr^{-1}. Historical stake measurements obtained from South Pole have found an average accumulation of about 8.4 cm yr^{-1} (e.g., Mosley-Thompson et al., 1999). The G5NR simulation also correctly indicates ablation on the western edge of the Lambert glacier adjacent to the Amery Ice Shelf. A negative surface moisture flux is also shown over adjacent oceanic areas of the southwestern Ross Sea and to the northeast of the Antarctic Peninsula. While this would appear to be reasonable for the Ross Sea region, ablation along the northeastern peninsula seems unusual in comparison to available climatologies and requires further study. An additional area of ablation in the area of Roi Baudouin that is featured in earlier compilations is absent in the G5NR field. A preliminary comparison has been made between the G5NR field and observed radio echo sounding observations in the high accumulation zones of West Antarctica. These comparisons suggest that the G5NR values are somewhat high, in agreement with the comparison with reanalyses for the South Polar Cap.

5.4.2 Near-Surface Wind Field Over Polar Ice Sheets

Surface winds over polar ice sheets are a principal feature of the general circulation and climate of the high latitudes. In the polar night, the near-surface atmosphere cools rapidly, loses buoyancy, and descends along the topographic gradient. Over ice sheets, these katabatic winds are sustained over continental scales and become directionally modified by the Coriolis force. The Antarctic 10 m wind field simulated by the G5NR for the month of July 2005 (Figure 5.26) compares closely with the diagnostic model field of Parish and Bromwich (1991). Of particular note is the excellent directional agreement over the Antarctic plateau and concurrence in the location of wind maxima in confluence zones at Cape Denison (67°S, 143°E) the southwestern edge of the Amery Ice Shelf (70°S, 71°E), and the Wilhelm II Coast (∼90°E). A cyclonic circulation feature over the Ross embayment and the adjacent area of West Antarctica is more robust in the G5NR than in the diagnostic model, which may be specific to the time period simulated. Southerly winds along the eastern side of the Antarctic Peninsula are simulated in the G5NR with monthly-averaged magnitudes of less than 6 ms^{-1}. This contrasts with the prevalence of barrier winds associated with the area (Parish, 1983), but may also result from inter-annual variability.

A close-up of the G5NR simulated winds for the southwestern Ross Sea (Figure 5.27) finds a local maxima in the vicinity of the Terra Nova Bay confluence zone, but the magnitude contours appear to indicate two airstreams that do not converge. Two factors may hinder the simulation for Terra Nova Bay. First, the area is a confluence zone for airstreams following four glaciers which have spatial resolutions that are not resolved by the G5NR. Second, the resulting polynya modifies the atmosphere and induces a local ice-breeze effect that may act to consolidate and enhance the airstreams over the bay (e.g., Gallée, 1997). For the G5NR simulation, the temporal and spatial extent of the polynya is not adequately resolved by the ocean surface forcing field. Coarse resolution models and atmospheric reanalyses typically indicate a maxima that is farther inland. With monthly averaged contours of greater than 12 ms^{-1} extending into the bay, the G5NR simulation clearly benefits from the enhanced spatial resolution. Additional features including the Ross airstream and the influence of Ross Island on the wind field are seen in the G5NR simulation.

For Greenland, the near-surface wind field is more directly influenced by synoptic activity. Nevertheless topography also plays an important role here in the directionality of the winds. The G5NR simulation (Figure 5.28) agrees well with the Ettema et al. (2010) regional climate model in indicating the northeast as the area of maximum wind magnitude, with additional areas of averaged magnitudes greater than 9 ms^{-1} along the western and southeastern periphery of the ice sheet. Notably the G5NR also agrees with Ettema et al. (2010) in showing the offshore synoptically-forced northeasterly winds acting as an inhibiting barrier to katabatic winds along the southeastern coast. A particular difference with the regional models is the wind magnitude at Summit. The G5NR shows calm conditions while Ettema et al. (2010) contour values greater than 6 ms^{-1}. Station observations show better agreement with the regional climate model. Magnitudes of less than 2 ms^{-1} are also shown at the top of South Dome in the G5NR. While inter-annual variability may also play a role, these becalmed areas are intriguing and warrant further investigation.

A cursory assessment of variability in the wind field may be seen by examining different synoptic conditions. In Figure 5.29a, a surface low is located SSW of Greenland and results in enhanced flow along the southwestern periphery of the ice sheet, and locally reversed, 'up-hill' wind flow along the southeastern coast. In Figure 5.29b, a surface low is located north of Iceland. Here, enhanced northerly barrier flow is found along the northeastern coast of Greenland which inhibits katabatic winds along the coastal escarpment. The synoptic condition enhances westerly wind flow over the southern part of the ice sheet, and particularly along the southeastern coast. A wedge-shaped feature in wind magnitude contours in Figure 5.29b extending from Cape Farewell generally resembles the analysis of Doyle and Shapiro (1999) in identifying a tip jet associated with the steep topography of the southernmost edge of Greenland. It may be seen that in both cases, the directionality of the wind in the northern half of the ice sheet stays fairly constant, in agreement with the study of Heinemann and Klein (2002).

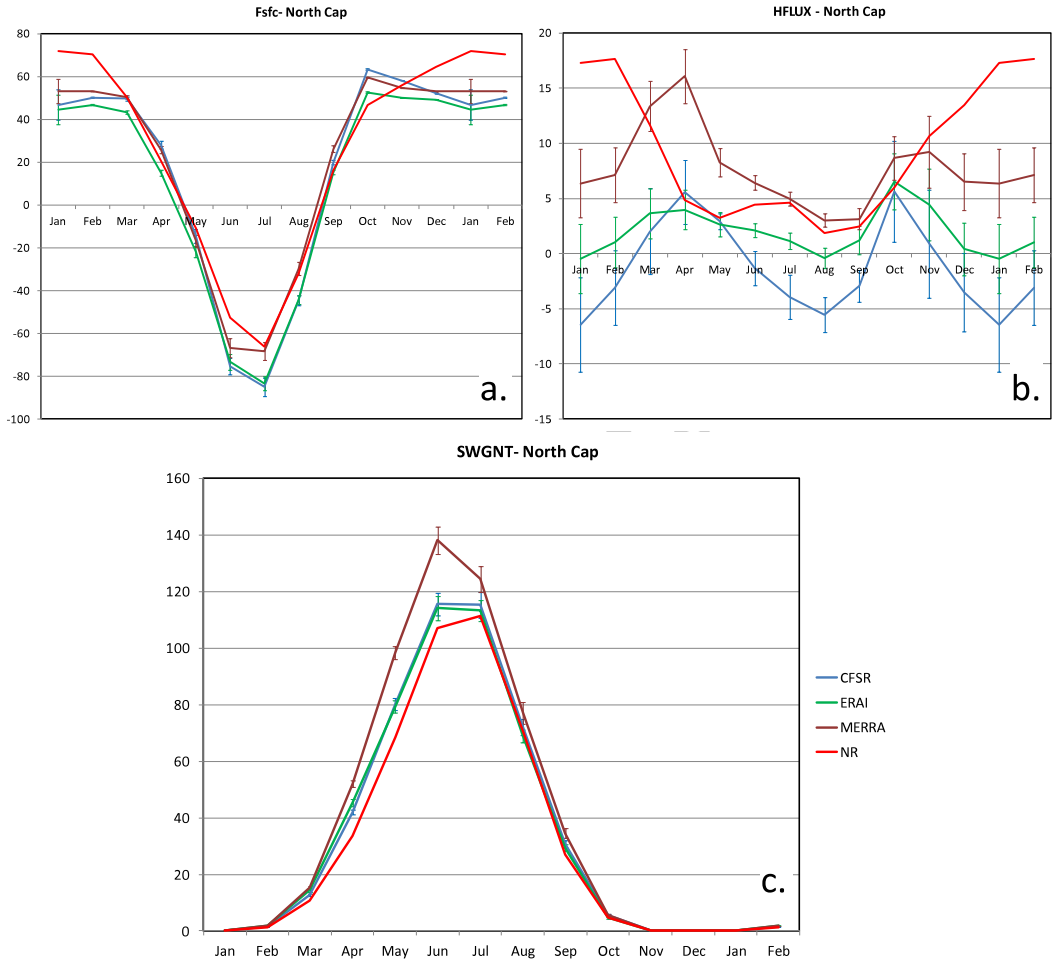

Figure 5.22: Net surface energy flux components from the G5NR for the North Polar Cap, averaged for the annual cycle from available years 2005-2007, and corresponding values from atmospheric reanalyses, in Wm^{-2}. Vertical bars indicate plus and minus one standard deviation of reanalysis values for the period 1989-2009. Shown are the net surface energy flux (a., positive upwards), sensible heat flux (b., positive upwards), and net surface shortwave radiative flux (c., positive downwards).

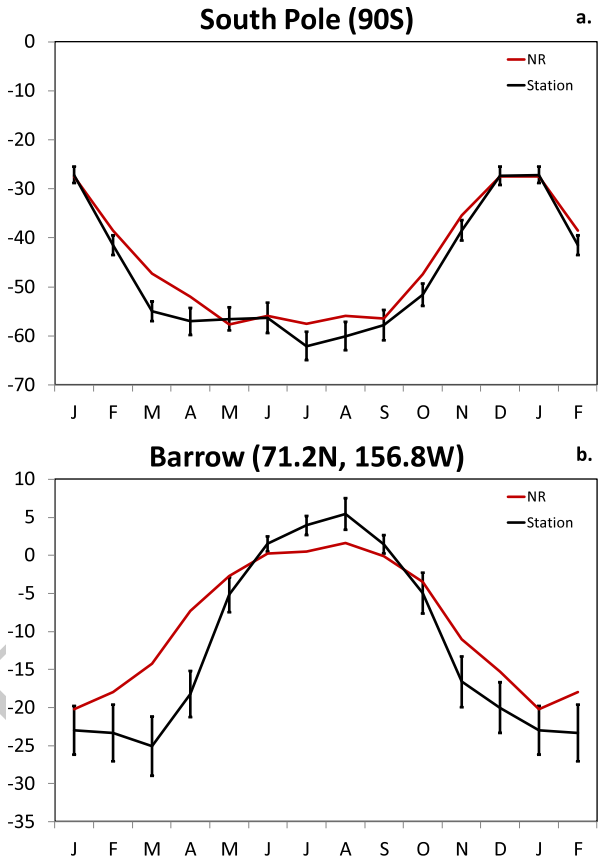

Figure 5.23: Comparison of G5NR 2m temperature and corresponding station temperature for (a.) South Pole and (b.) Barrow, in °C. Error bars correspond to the plus and minus the inter-annual standard deviation for the available station record.

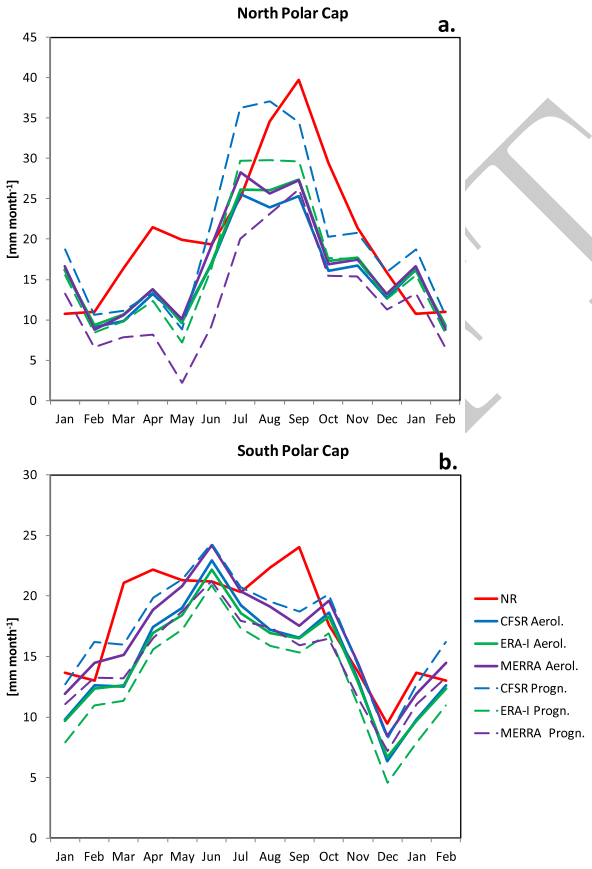

Figure 5.24: Average annual cycle for net surface moisture flux from G5NR and corresponding values from reanalyses for (a.) North Polar Cap and (b.) South Polar Cap, in mm month^{-1} water-equivalent.

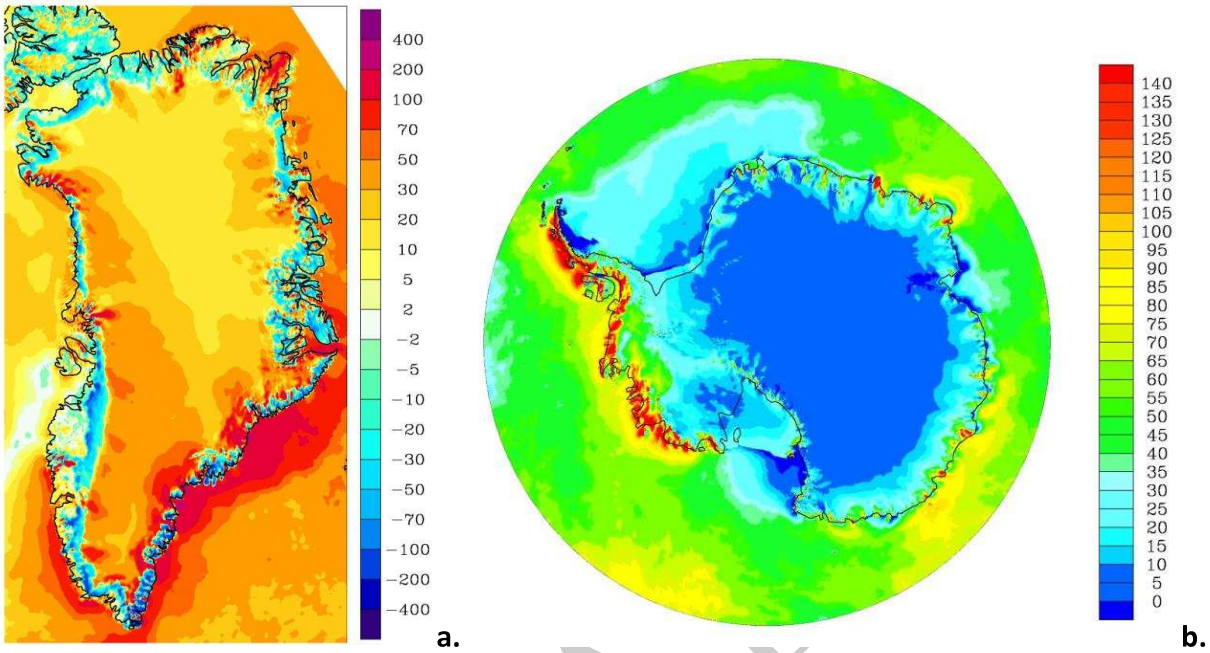

Figure 5.25: G5NR surface mass balance for (a.) Greenland and (b.) Antarctica, in cm yr^{-1} water-equivalent.

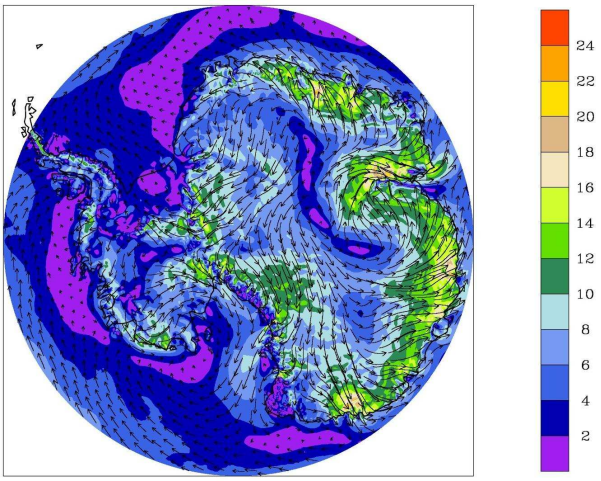

Figure 5.26: G5NR 10 m wind vectors over the Antarctic averaged for July 2005 and contours of vector magnitude in ms^{-1}.

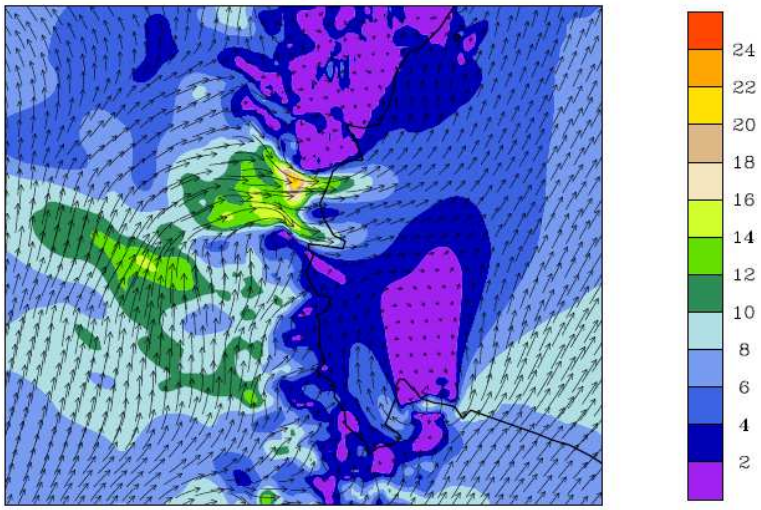

Figure 5.27: G5NR 10 m wind vectors averaged for July 2005 and contours of vector magnitude in ms^{-1} for the southwestern Ross Sea.

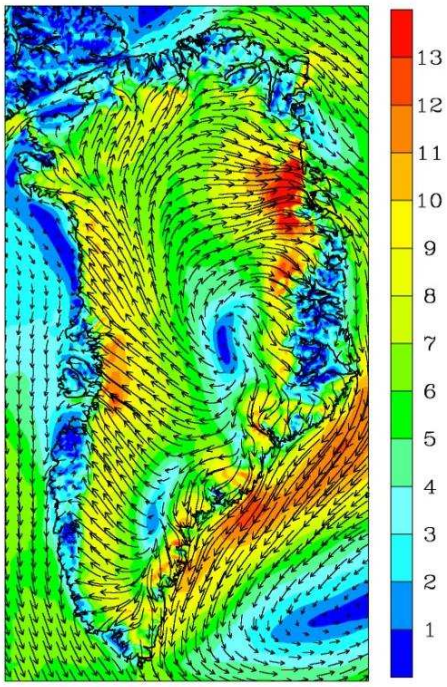

Figure 5.28: G5NR near-surface wind field over Greenland for January 2005, in ms^{-1}.

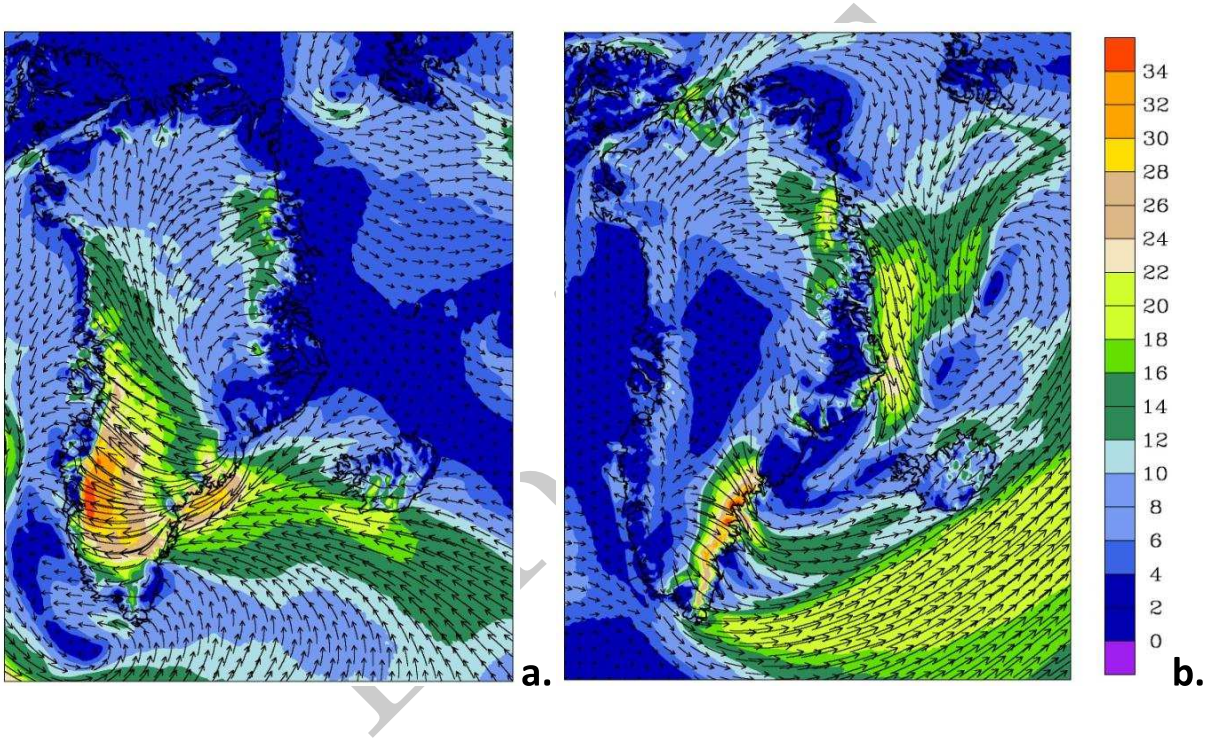

Figure 5.29: Daily-averaged G5NR 10 m wind field over Greenland and surrounding area for (a) 1 Jan 2006 and (b) 30 Jan 2006, in ms^{-1}.

Chapter 6

Clouds and Radiation

Peter M. Norris, Will McCarty and Ronald M. Errico

The following is a validation of the G5NR clouds and top-of-atmosphere (TOA) radiation against CERES (Clouds and the Earth's Radiant Energy System) observations aboard the Aqua and Terra satellites and against CALIOP (Cloud-Aerosol Lidar with Orthogonal Polarization) observations aboard the CALIPSO satellite.

Section 6.1 uses CERES Single Scanner Footprints (SSF) data. This is the highest resolution Level II CERES product, comprised of individual 20 km footprints. Our validation procedure uses only the G5NR averages at the Single Scanner Footprints from Terra and Aqua (which sample in the daytime at 10:30 am and 1:30 pm local time, respectively, and 10:30 pm and 1:30 am in the nighttime.) This validation is therefore valid for the atmosphere averaged only over the sampled local times — no diurnal temporal model is employed to attempt full diurnal means. This is the most accurate validation we can make, but is time consuming, so it is performed only for June 2005.

In contrast, Section 6.2 performs full diurnally averaged validation for four months (June, September, December, 2005 and March 2006) using CERES EBAF products. The EBAF dataset ("Balanced Top-of-Atmosphere Fluxes") is a Level III CERES product primarily used for climate model evaluation. It constrains the global net TOA flux to the ocean heat storage term and also spatially interpolates (fills) clear-sky fluxes in non-observed regions. Finally, it employs a diurnal temporal model to produce full diurnal average estimates from the Aqua and Terra observations. The differences from the validations in Section 6.1 appear small, so the EBAF validation is preferred in terms of speed and its full diurnal averages. Conclusions from Sections 6.1 and 6.2 are summarized

in Section 6.3.

Section 6.4 compares the G5NR cloud top pressure (CTP) and cloud fraction (total and low, mid and high bands) against a multiyear DJF observations from the active lidar instrument CALIOP (Cloud-Aerosol Lidar with Orthogonal Polarization) aboard the CALIPSO satellite. For the G5NR, the first (pseudo 2005–06) season is compared against the CALIPSO data. Since the G5NR exists at a lower resolution than the CALIPSO data (7.5 km vs 1 km), a maximum-random overlap assumption was employed to sample the G5NR at a sub-gridscale resolution and locations consistent with the lidar data. This overlap assumption was essential to properly compensate for instances where dense low clouds are only partially covered by higher clouds in a multilayered cloud environment.

6.1 June 2005 Validation Against CERES SSF: Not Diurnally Averaged

This first section uses CERES Single Scanner Footprints (SSF) data for June 2005. This is the Level II CERES product, comprised of individual 20 km footprints. This validation uses only the G5NR averages over the Single Scanner Footprints from Terra and Aqua (which sample in the daytime at 10:30 am and 1:30 pm local time, respectively, and 10:30 pm and 1:30 am in the nighttime.) No diurnal temporal model is employed. All results are monthly averages for June 2005. The notations "nC" or "nC (masked)" both mean the *Coarsened* G5NR sampled at the locations of valid SSF data, while the notations "nN" or "nN (masked)" mean the *Native* resolution G5NR sampled at the locations of valid SSF data.

6.1.1 TOA Outgoing Longwave Radiation

Figure 6.1 shows the zonal average OLR validation against CERES. The agreement is very good. Figure 6.2 shows the corresponding global map comparison. The differences are unremarkable, except that the G5NR has a distinct bifurcation in the ITCZ in the Western to Central Pacific.

6.1.2 TOA Outgoing Shortwave Radiation

Figures 6.3 and 6.4 show the corresponding comparisons for TOA Outgoing Shortwave Radiation (OSR). [Note that, like OLR, the comparisons includes both daytime and nighttime samples, but for OSR the nighttime zero values are averaged in.] It appears that the OSR is being overestimated at almost all latitudes, likely because the model clouds are too reflective (see later). From the global map comparison, we can make several observations:

- The cloud minima in the sub-tropical subsidence zones is less intense in the G5NR, indicating a potentially weaker Hadley circulation. At the same time, it is also broader in latitude, with the transition to northern stratus being further north in the G5NR, although after the transition the stratus is brighter. This gives the feature in the zonal OSR plot where a positive bias in the northern subtropics switches to a negative bias in northern mid-latitudes, then to positive again at northern high latitudes.
- The low cloud (marine stratocumulus) shields off the western continental coasts are different in nature. This is particularly evident off the North American coast, but also off Africa and South America. It seems that the G5NR has a tendency to produce clear swaths near these coasts, possibly indicating that the marine boundary layer height is too low near the coast, or its inversion is too weak, or surface latent heat fluxes are too weak, maybe due to insufficient strength of the subtropical highs. The SST should not be a factor since it is forced from daily data based on observations.

6.1.3 Cloud Properties

Cloud Fraction

Figure 6.5 shows the zonal average total column cloud fraction. Ignore the polar regions, where CERES may not be correct, due to ice issues. The agreement is generally good, but the G5NR has a more pronounced southern branch of ITCZ, and subtropical subsidence zone cloud minima displaced a little poleward. Clearly, cloud fraction cannot explain the over-bright zonal OSR.

The global map (Figure 6.6) highlights the same problems seen for OSR, and in particular, the sparcity of low cloud off western continental coasts is especially evident. It looks like the reduced cloud cover features off the western continental interiors are being "leaked out" to the nearby marine environments in some way, as though dry subsiding air over the land is moving out over the ocean and the normal marine boundary layer mechanisms of maintaining a strong elevated inversion are not strong enough to resist. The arcs of high cloud fraction SW off the Southern US / Mexico and West of Southern and Central Africa are evidence of this effect.

Figure 6.7 shows the frequency distribution of cloud fraction on the coarse grid over the month of June 2005. This study was spearheaded by Ron Errico for his work on radiance assimilation. Note the logarithmic scale necessitated by the strong binary character of cloud fraction (which becomes more pronounced as the grid size decreases). There is good agreement, but we note these differences:

- From 30S to 30N the pattern is similar: the G5NR tends to underestimate small cloud fractions and overestimate large cloud fractions, though the overcast cases are again underestimated.

- The pattern is similar but less extreme for 30N-60N.
- For the Southern Ocean region 60S-30S, both small and large cloud fractions are overestimated, overcast is underestimated, and clear is overestimated.

The cumulative frequency distributions (Figure 6.8) show another perspective: In the 30S-30N equatorial/subtropical region, the G5NR has a deficit of partial cloud fraction, made up for only by an excess at high and overcast partial cloud fractions. For mid-to-high latitudes, the situation is reversed: the G5NR has an excess of partial cloudiness across the cloud fractions, especially in the southern ocean, but made up for by an underestimate of overcast cases.

Cloud Top Pressure

Cloud Top Pressure (CTP) is a quantity that has quite different definitions in the model (layer optical thickness threshold) and in CERES (IR-based), so we will not put much credence in differing magnitudes between the G5NR and CERES. Specifically the IR method mixes high thin cloud with lower thicker cloud, while the model method does not as much. Nevertheless, we show the global map comparison (Figure 6.9) because it reveals some interesting qualitative details. What is most evident for the low cloud comparison we have been discussing is that the CTP shows a clear land/ocean contrast, mostly right up to the coast, unlike the cloud fraction just mentioned. This tends to argue against a marine boundary layer height problem, but rather that the near coast cloud fraction / cloud occurence is too low, not the height per se. This argues more for a weak inversion in the G5NR, and/or reduced surface latent heat flux.

Cloud Optical Thickness

Figure 6.10 shows the total in-cloud visible optical thickness (COT). In this case, the model diagnostic TAUTOT is incorrect, because it basically adds TAULOW, TAUMID and TAUHGH. This is not correct, because these are the *in-cloud* low, mid and high band optical depths, not the grid-box band means. [Note: the "128" on the ordinate label indicates limiting of the model values to the CERES maximum value. This is a small effect.]

In Figure 6.11 we use a replacement diagnostic for total in-cloud COT, namely:

$$\text{TAUTTN} = \frac{\text{TAULOW} * \text{CLDLOW} + \text{TAUMID} * \text{CLDMID} + \text{TAUHGH} * \text{CLDHGH}}{\text{CLDTOT}}.$$

This should be a corrected and acceptable replacement for the random band overlap assumed by the model. COT is nevertheless still overestimated, and likely explains the over-bright OSR.

We also show the global map comparison (Figure 6.12) just to look at qualitative features, since the

magnitude is incorrect. Specifically for the issue of the paucity of low marine cloud, the in-cloud optical depths are under-predicted in these marine regions, not just the cloud fraction.

In summary, for the stratocumulus issue, there are less low clouds over Eastern Pacific and Atlantic boundaries, and they are thinner, but their height is not so problematic.

Condensed Water Path

The grid-mean condensed water path (Figure 6.13, this time at full native resolution) shows a significant over prediction of condensed water path at most latitudes, that may at least partially explain the optical depth and OSR overprediction. Other factors, such as effective radius may also play a role. The global map (Figure 6.14) shows very clear differences:

- Cloud minima in subtropical subsidence zones are clearly more distinct for CERES. The G5NR has too much cloud water in these latitudes.
- The ITCZ is more distinct in the observations, partly because of the previous item. Also the ITCZ appears to bifurcate in Pacific in the G5NR; and
- Western continental coast cloudiness seems to have a clear swath near coast in the G5NR, particularly off North America.

These are grid-column condensed mean water paths. We can divide by the total column cloud fraction (Figure 6.15) to get an idea of the average in-cloud condensed water path. In preparation, Figure 6.16 show the total column cloud fraction at full native G5NR resolution. As discussed earlier, outside of the unreliable polar regions, the comparison is reasonable, except that the subtropical cloud fraction minima are more distinct and less broad (closer to the equator) in the observations. Finally, the "in-cloud" cloud water paths (grid-column mean CWP / total column cloud fraction) are shown in Figures 6.17 and 6.18. We can now clearly summarize the issue: subtropical and mid-latitude clouds have too much condensed water in them in the G5NR (except in the waters adjacent to western continental margins, where they do not have enough). The first effect dominates the climate, giving too much cloud albedo and an over-bright planet.

6.1.4 Albedo vs. OLR Joint Histograms

In Figures (6.19)–(6.22) we show joint histograms of TOA solar albedo versus OLR for different latitude bands. We choose these variables because they are direct radiative outputs from the model and rather direct observations from CERES SSF, and are therefore less susceptible to varying definitions (cf. cloud top pressure) between model and retrievals. A drawback of this choice is that we are folding in clear-sky and surface albedo effects (the pure cloud radiative effect is not available

from CERES SSF). To mitigate this complication, we consider ocean-only results, where the albedo is low and reasonably constant. All results are again for the June 2005 period.

The OLR axis is inverted, so that the y-axis is a proxy for cloud height. Contours are proportional to probability density. The filled contours are for CERES SSF. The dashed contours are for the CERES-SSF-masked coarse G5NR (nC). The five dashed (blue, cyan, green, orange and red) contours delineate the boundaries of the four filled color regions. All results are for daytime only. The results are build up from individual hourly averages.

Figure 6.19 is for the two tropical bands. The southern tropics show reasonable agreement, but with a bright bias in thicker cloud, and some evidence of a low bias. The northern equatorial region, which contains the dominant ITCZ branch, shows interesting behavior: (1) Two distinct cloud types are seen: low clouds and high clouds; (2) Both types are biased bright and warm. Note that if the clouds are gray, not black, a bright bias will, in of itself, lead to a cold bias. So this warm bias is likely to be a true low bias.

Figure 6.20 is for mid-latitudes bands (again over ocean only). The southern mid-latitudes have a pronounced bright and low bias. The northern mid-latitudes have similar bias, but to a much lesser degree. Note that a distinct low vs. high cloud type bifurcation is not present in the southern midlatitudes, in the observations or the G5NR.

Figure 6.21 shows the higher-latitudes from 40-60 degrees. The southern branch contains the Southern Ocean in austral winter. Clouds tend to be thicker and higher in the G5NR. More precisely, it seems that the low clouds are lower and thicker, while there is a population of higher, very thick clouds not seen in the observations. It is possible that the latter represents contamination from the northern edge of the winter Antarctic ice sheet. The northern (summer) higher latitudes show distinct low bias, and a narrower range of OLR at cloudy albedos, indicating less variability in cloud height.

Finally, Figure 6.22 shows the global joint probability density. Note: All these joint histograms are weighted by the cosine of latitude, so this plot avoids an undue polar influence. About all we can say in general is that the G5NR has a bright bias for clouds (consistent with our other findings) and somewhat of a low bias. This is for both the low and high cloud branches. It is still possible some sea-ice influence is showing in the high cloud branch, but this requires further investigation.

6.2 Diurnally-Averaged Validation Against CERES EBAF

Next we conduct monthly and diurnally averaged validation for four months (June, September, December, 2005 and March 2006) using CERES EBAF products (see Section 1) . Because the EBAF dataset also uses a temporal model to create a full diurnal cycle, there is no masking of the G5NR results along the swath in this section, as contrasted with the previous SSF section.

The appearance of "nC" or "nC(unmasked)" in any of the figures for this section both refer to full diurnal averages of the coarsened G5NR.

6.2.1 TOA Outgoing Longwave Radiation

June 2005 (Figure 6.23) is one of the best validations, with a global mean difference of only 0.1 Wm^{-2}! September 2005 (Figure 6.24) is one of the worst, but is still very good, with a global mean difference of only 1.4 Wm^{-2}. The corresponding global map (Figure 6.25) evidences the double ITCZ issue and the concomitant pushing of the southern subtropical subsidence zone (and paucity of cloud) further to the South. Table 6.1 summarizes the four monthly global mean OLR differences. Clearly the differences are small.

6.2.2 TOA Outgoing Shortwave Radiation

The OSR comparison for June shows much the same features as above in Section 6.1. December shows similar behavior: a weaker but slightly broader subtropical/midlatitude cloud minima and brighter Southern Ocean stratus. A double Pacific ITCZ is somewhat evident in both model and CERES. As an equinoctial example we show the results for September (Figures 6.26 and 6.27). Many of the differences have already been noted: tropical differences including the definition and bifurcation of the ITCZ; the intensity of subtropical subsidence zones; western continental coast cloudiness; and the brightness of Southern Ocean cloud.

For each month there is a bright bias, as Table 6.2 of global means shows. The almost 7 Wm^{-2} overestimate of outgoing solar flux is significant considering that a net $2\times CO_2$ forcing is on the order of 4 Wm^{-2}. The global mean OLR bias of 1.0 Wm^{-2} adds to this, giving a combined excess global cooling of about 7.8 Wm^{-2}. A similar bright bias was found for 2006 in the G5NR (Table 6.3). The bright bias appears consistent from year to year, and maps (not shown) show very similar features, indicating that these differences cannot be assigned to inter-annual variability, but appear to be climatic biases.

Note that these values are reasonably consistent with a NASA Energy and Water cycle Study (NEWS) analysis of TOA energy balance provided by Dr. Michael Bosilovich (Figure 6.28), although the NEWS values are for a longer period, 2001–2010. For comparison, Table 6.4 provides the summarized global TOA energy balance numbers from the G5NR. Table 6.5 provides the equivalent numbers for CERES EBAF.

What is the cause of this general bright bias, if it is more than just the sum of the noted specific cloud problems, as it seems it might be? First, we need to discount the possibility that CERES and the G5NR have different incoming solar radiation (ISR). There is negligible difference, as per Tables 6.4 and 6.5. So the OSR bias is *not* due to incoming solar. Still, it is useful to normalize

the OSR by the ISR as an albedo, since the ISR strongly varies with latitude, especially in the summer/winter seasons. Figures 6.29 and 6.30 show the TOA albedo for June 2005. The zonal plot shows that the albedo is biased high over almost all the latitudes. The CERES outlier at the southernmost latitude should be ignored, where the incoming solar goes to zero. The global map shows all the features we have been discussing very clearly.

The next issue we would like to eliminate is non-cloud affects, such as differences in surface albedo. Figure 6.31 shows the radiative cloud forcing SCF = OSR_{clr} - OSR. The definition gives negative values, meaning that cloudy regions generally reflect more solar energy than clear regions, thereby acting to cool the planet. Evidently for June 2005, clouds in the G5NR are cooling the planet in the global mean by an excessive amount, about 7.4 Wm^{-2} extra compared with CERES EBAF. Table 6.6 shows the numbers for Jun, Sep, Dec 2005 and Mar 2006. The average is an excessive cooling due to clouds of about 8 Wm^{-2}.

[Note: the global mean longwave cloud forcing, LCF = OLR_{clr} - OLR, for the four month average is 25.87 Wm^{-2} for the G5NR and 26.24 Wm^{-2} for EBAF, a difference of only -0.37 Wm^{-2}.]

Finally, we scale the SCF by the incoming solar radiation (ISR), in order to remove the latitudinal variation in insolation. Figures 6.32 and 6.33 show the June 2005 results. All the features we have been discussing are clearly evident in the G5NR: tropical differences including the definition and Pacific bifurcation of the ITCZ; reduced intensity of subtropical subsidence zones; more northerly but more intense northern high latitude stratus; western continental coast cloudiness has clear swaths near the coast; and excessive brightness and broadness of Southern Ocean cloud.

6.3 CERES Validation Summary

From the validation work in Sections 6.1 and 6.2, we can draw the following conclusions:

- The G5NR outgoing long wave radiation (OLR) at top-of-atmosphere (TOA) is very good. Differences from CERES are unremarkable, except for the cloud signature of a more active southern branch of the ITCZ in the Western to Central Pacific. The average global mean difference was only about 1 Wm^{-2}.
- In contrast, the outgoing shortwave radiation (OSR) at TOA is overestimated by the G5NR at almost all latitudes. The average global mean excess was about 7 Wm^{-2}, which is significant considering that a net $2\times CO_2$ forcing is on the order of 4 Wm^{-2}. This problem appears to be due to excessive cloud optical depth in the G5NR. Excess in-cloud condensed water is at least partially responsible, although other as yet unknown factors must also exist. An examination of shortwave cloud forcing scaled by the incoming solar radiation for June 2005 shows these qualitative features: a less well-defined and more bifurcated ITCZ; reduced intensity of subtropical subsidence zones; more northerly but more intense northern high latitude stratus;

clear swaths in marine cloud near Western continental coasts; and excessive brightness and broadness of Southern Ocean cloud.

- The total column cloud fraction validation is reasonable to good. The main differences are a more pronounced southern branch of ITCZ in the nature, a sparsity of low cloud off western continental coasts, and the subtropical subsidence zone cloud minima being displaced a little poleward. By contrast these cloud minima are more distinct and less broad (closer to the equator) in the observations. Note that these cloud fraction differences cannot explain the over-bright zonal OSR.

- An analysis of the cumulative distribution of partial cloud fractions shows that in the 30S-30N equatorial/subtropical region, the G5NR has a deficit of partial cloud fraction, made up for only by an excess at high and overcast partial cloud fractions, while for mid-to-high latitudes, the situation is reversed: the G5NR has an excess of partial cloudiness across the cloud fractions, especially in the southern ocean, but made up for by an understimate of overcast cases.

- There are less low clouds (marine stratocumulus) over the Eastern Pacific and Atlantic boundaries, and they are thinner, but their height is not so problematic. The most likely explanation is a weaker capping inversion in the G5NR.

- The in-cloud condensed water path is significantly over predicted at most latitudes, and this at least partially explains the optical depth and OSR over predictions. In qualitative terms, subtropical and mid-latitude clouds have too much condensed water in them in the G5NR (except in the waters adjacent to western continental margins, where they do not have enough). In contrast, the cloud water minima in the subtropical subsidence zones are clearly more distinct for CERES.

- A study of joint histograms of TOA SW Albedo and OLR reveals that not only do G5NR clouds tend to be biased brighter, but they also tend to be biased lower, both for high and low clouds.

6.4 Cloud Top Pressure and Cloud Fraction Validation Against CALIPSO

Many OSSEs are fundamentally built upon a foundation of synthetically-generated observations. Typically, a forward model (e.g. a radiative transfer model, a lidar instrument simulator) is used to generate the more complicated measurements (e.g. radiances, lidar backscatter) from the core atmospheric fields modeled in the G5NR. Fundamental to these simulated observations is the inclusion of realistic cloud effects. Clouds have varying scattering and absorptive/emissive effects through the entire electromagnetic spectrum, from the ultraviolet to the microwave, which has a significant effect in the realistic relationship between synthetic and real observations. Without the inclusion of these effects, simulated observations can be unrealistically cloud-free, and this can result in the over- or under-selling of a platform's scientific impact. This study performed a validation

on the underlying cloud fields that will be sampled in the generation of remotely sensed satellite observations.

6.4.1 Data and Sampling

The primary data used in the validation of the G5NR clouds is every December-January-February (DJF) season over the course of the currently-existing data record (2006–07 to 2013–14) of the Cloud-Aerosol Lidar with Orthogonal Polarization (CALIOP) instrument onboard the Cloud-Aerosol Lidar and Infrared Pathfinder Satellite Observations (CALIPSO) platform. Specifically, the G5NR was compared against cloud top pressure (CTP) retrievals at 1 km from the version 3.3 release, known as the CAL_LID_L2_01kmCLay-ValStage1-V3-30 data record.

For the G5NR, the first (pseudo 2005–06) season was compared against the CALIPSO data. Specifically, the cloud fraction field was validated. Since the G5NR exists at a lower resolution than the CALIPSO data (7.5 km vs 1 km), a maximum-random overlap assumption was employed to sample the G5NR at a sub-gridscale resolution and locations consistent with the lidar data. This overlap assumption was essential to properly compensate for instances where dense low clouds are only partially covered by higher clouds in a multilayered cloud environment.

Finally, CALIPSO data were used as reference because, as a visible lidar, the instrument has the highest sensitivity to thin, high clouds. This was the most accurate observation to directly compare to the G5NR cloud fraction fields without having to incorporate an instrument model. These active lidar measurements have significantly higher sensitivity to optically thin clouds compared to other options, namely observations and retrievals from measurements in the infrared and microwave as well as for passive shortwave measurements.

6.4.2 Mean Cloud Height

The zonal mean cloud top pressure for the G5NR and CALIPSO DJF seasons is presented in Figure 6.34. The G5NR clouds were higher than the distribution measured by CALIPSO. In the Southern Hemisphere, Tropics, and Arctic, the mean cloud top pressure was beyond the spread of the eight years of CALIPSO measurements. It is only in the northern midlatitudes that the G5NR neared the spread of the CALIPSO measurements, though the G5NR was on the vertically higher end of the distribution and was above the CALIPSO mean.

6.4.3 Spatial Distribution of Cloud Fraction

In addition to the mean height of the clouds, the spatial distribution of cloud amount was considered. To compare the sampling of the nadir-sampling CALIPSO data spatially, all measurements over the DJF period were aggregated into cloud fractions on a $5^\circ \times 5^\circ$ grid. The same was done for the G5NR fields sampled coincidentally along the CALIPSO tracks at the 1 km sub-grid resolution with the maximum-random overlap. The spatial maps of cloud fraction and their corresponding difference are shown in Figure 6.35. The G5NR generally has more clouds than the CALIPSO measurements in the poles and less in the extratropics. The Tropics appears to have a zonal mean near zero but differ from positive to negative as a function of longitude. There are also two large minima off the west coasts of Australia and South America. To further understand the various regions where there was either an overabundance or deficiency in cloud cover, the cloud fractions were further investigated by height as a function of the ISSCP definitions of high (CTP $<$ 440 hPa), midlayer (440 hPa $<$ CTP $<$ 700 hPa), and low (CTP $>$ 700 hPa) cloud.

Spatial Distribution of High Clouds (CTP $<$ 440 hPa)

When considering the spatial distribution of high clouds, as shown in Figure 6.36, the largest agreement between the high cloud differences and the total differences is in the Tropics. The areas of excess cloud overall seen in Figure 6.35 agree in sign and location with the areas of excess high cloud, though the magnitude of these differences does not fully explain the difference in total cloud fraction. Both the Arctic and Antarctic have excess high cloud, though not in complete agreement with the regions of excessive total cloud fraction. An example of this is over the Arctic north of Eurasia. In total clouds, the G5NR and CALIPSO means differ on the order of 5–20%, while in high cloud, the difference is in excess of 50%. In contrast, north of Siberia and Alaska, the discrepancy between the G5NR and CALIPSO data in high clouds is less than the discrepancy seen in total clouds. Finally, the G5NR does not have a strong deficiency in high clouds in the midlatitudes corresponding to that seen in total clouds.

Spatial Distribution of Mid-Layer Clouds (440 hPa $<$ CTP $<$ 700 hPa)

The spatial distribution of mid-layer clouds is shown in Figure 6.37. A general lack of clouds in this region in the G5NR is seen relative to the CALIPSO data through most of the globe. This is apparent through the Tropics where there mid-layer cloud fraction over ocean is generally less than 5% and the general deficit continues, though to a lesser extent, over land. The most spatially consistent deficiency is over the Southern Ocean. This largely matches the overabundance of high clouds shown in Figure 6.36. This corresponds to a general upward shift of the highest cloud tops in the G5NR relative to CALIPSO.

Spatial Distribution of Low Clouds (CTP > 700 hPa)

In the spatial distribution of low clouds shown in Figure 6.38, it is once again seen that the model has a general lack of clouds relative to the CALIPSO data record, with the some exceptions being regions over Northern Hemisphere snow and ice. The clearest deficits are in the marine stratocumulus regions off the west coasts of South America and Australia, and these areas correspond with the areas of overall cloud fraction deficits in Figure 6.35. A strong deficit is also seen in the Arctic region north of Eurasia. This is related to a "shadowing" effect, as there ias an over-abundance in high clouds in this region as shown in Figure 6.36 which obscures the potential low clouds in a top-downward, highest cloud only, CTP analysis.

6.5 CALIPSO Validation Summary

The zonal mean CTP shows a consistent displacement between the G5NR and the CALIPSO data record. There are three possible ways to explain the displacement between the CALIPSO and G5NR fields: the G5NR has excessive high clouds, a shortage of low clouds, or a similar distribution that is displaced vertically upwards. In considering the overall cloud fraction, it is seen that the distribution varies regionally across the globe. By further comparing the cloud fraction figures as a function of cloud height layer, it was seen that some areas were simply deficient throughout, some areas were "shadowed" by excess high clouds, and others still were dramatically lacking low clouds.

It is noted that the methods of this section are consistent with those of McCarty et al. (2012). That study performed a similar analysis on the ECMWF NR, though with a shorter CALIPSO record and different version of CALIPSO cloud height retrievals. While both comparisons reveal shortcomings relative to observations, the G5NR shows better agreement in terms of high-level clouds, which were found to be deficient in the ECMWF NR. In contrast, the G5NR shows a greater deficiency in low-level clouds than the ECMWF NR, particularly in areas of marine stratocumulus. The conclusions of McCarty et al. (2012), however, still hold true. In an OSSE context, the user should be aware of these patterns, as too few or too many clouds may result in a synthetic dataset that does not fully represent the observations from a real, space-borne platform.

OLR validation against CERES EBAF for 2005

	Jun	**Sep**	**Dec**	**Mar**	**Avg**
nC	242.51	243.55	238.41	238.74	240.80
EBAF	242.61	242.12	236.75	237.66	239.79
nC-EBAF	-0.10	1.43	1.66	1.08	1.02

Table 6.1: Global means of OLR for four months of 2005 for the coarsened nature run and CERES EBAF. The "Avg" field is the average of the four months.

OSR validation against CERES EBAF for 2005

	Jun	**Sep**	**Dec**	**Mar**	**Avg**
nC	102.78	100.62	114.32	107.41	106.28
EBAF	96.70	94.65	107.03	99.44	99.46
nC-EBAF	6.08	5.97	7.29	7.97	6.83

Table 6.2: Global means of OSR for four months of 2005 for the coarsened nature run and CERES EBAF. The "Avg" field is the average of the four months.

OSR validation against CERES EBAF for 2006

	Jun	**Sep**	**Dec**	**Mar**	**Avg**
nC	101.79	100.73	114.22	107.07	105.96
EBAF	95.75	94.39	108.10	99.45	99.42
nC-EBAF	6.04	6.34	6.12	7.62	6.53

Table 6.3: Global means of OSR for four months of 2006 for the coarsened nature run and CERES EBAF. The "Avg" field is the average of the four months.

G5NR run global TOA energy balance

nC	ISR	OLR	OSR	Onet
2005-2006	340.38	240.80	106.28	6.70
2006-2007	340.37	240.59	105.96	6.18

Table 6.4: G5NR global mean TOA energy balance summary. All the numbers are for Jun, Sep, Dec, Mar averages (in W/m^2).

CERES EBAF global TOA energy balance

EBAF	ISR	OLR	OSR	Onet
2005-2006	340.30	239.79	99.46	-1.05
2006-2007	340.29	240.10	99.42	-0.77

Table 6.5: CERES EBAF global mean TOA energy balance summary. All the numbers are for Jun, Sep, Dec, Mar averages (in W/m^2).

SCF validation against CERES EBAF for 2005

	Jun	Sep	Dec	Mar	Avg
nC	-52.57	-53.46	-59.70	-55.50	-55.31
EBAF	-45.21	-45.55	-52.58	-46.09	-47.36
nC-EBAF	-7.36	-7.91	-7.12	-9.41	-7.95

Table 6.6: Global means of shortwave cloud forcing (SCF) for four months of 2005 for the coarsened nature run and CERES EBAF. The "Avg" field is the average of the four months.

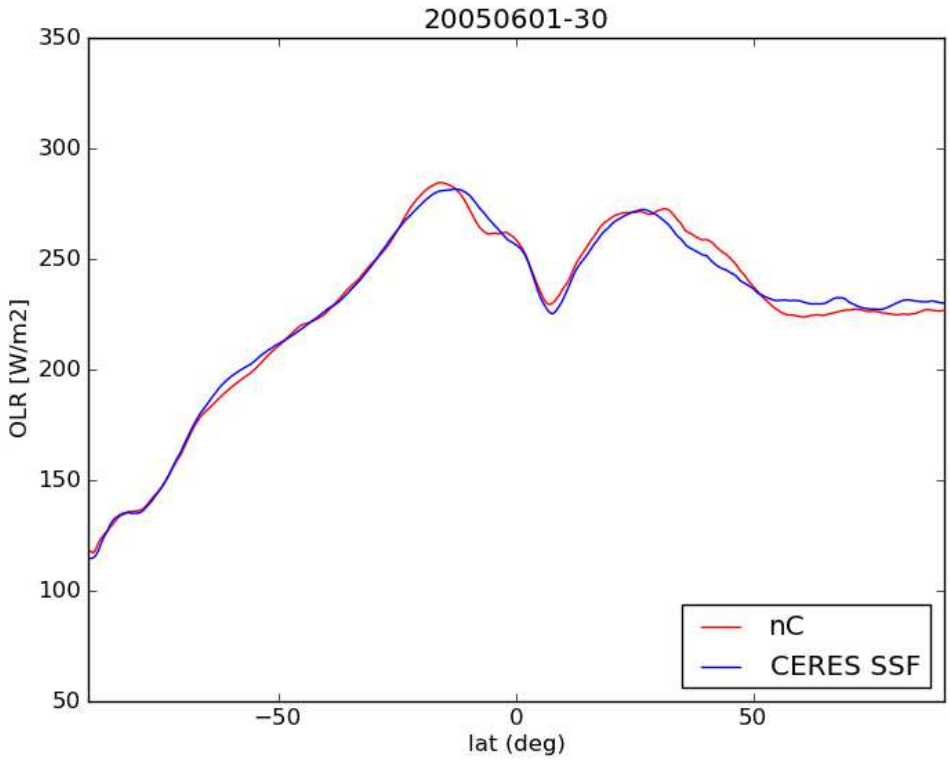

Figure 6.1: Zonal average OLR validation against CERES SSF. "nC" means the *Coarsened* G5NR sampled at the locations of valid SSF data.

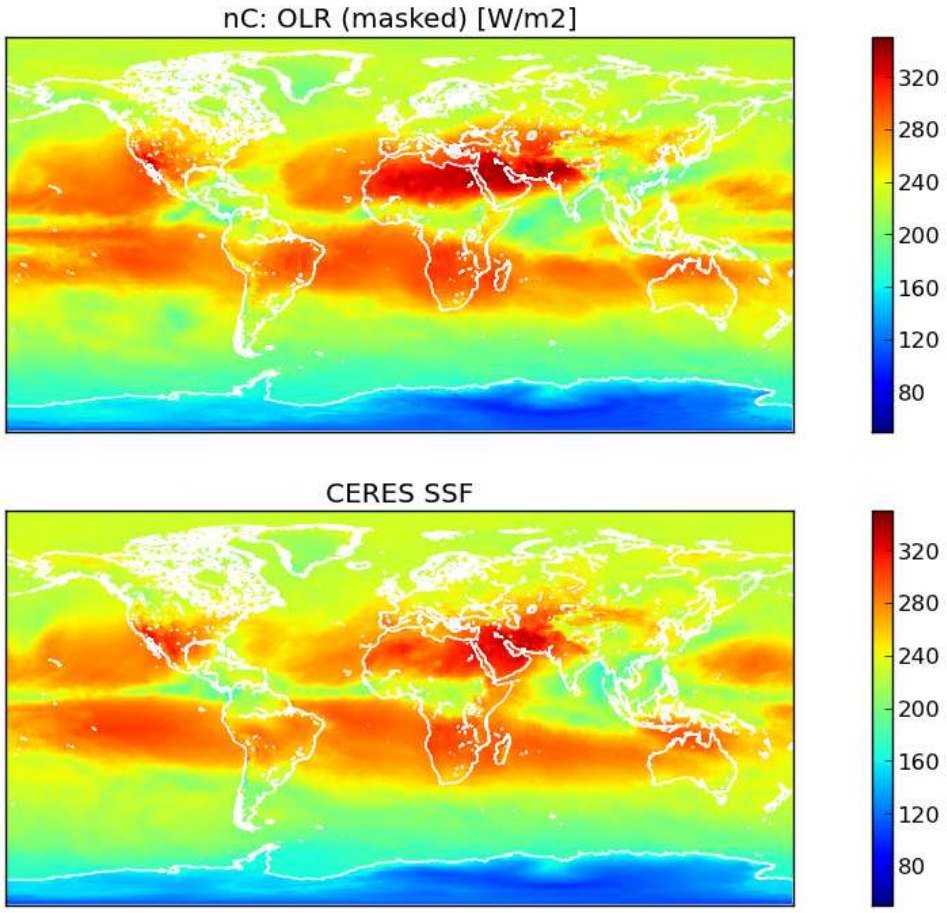

Figure 6.2: Global map OLR validation against CERES SSF. "nC" means the *Coarsened* G5NR sampled at the locations of valid SSF data. "(masked)" emphasizes that the G5NR output is averaged only over the locations of valid SSF data.

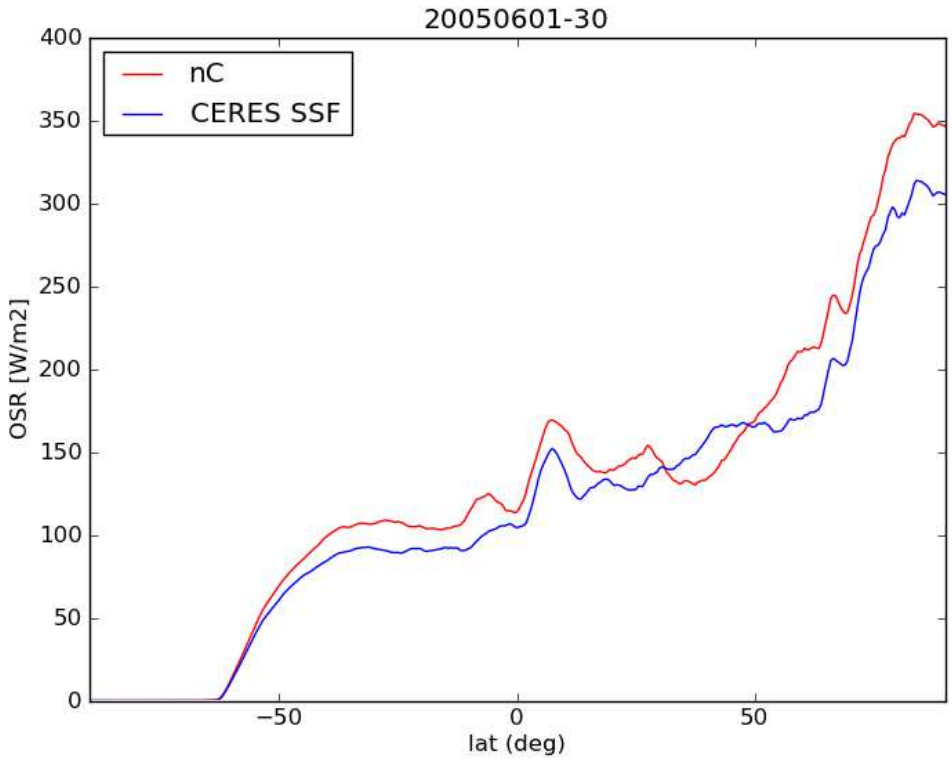

Figure 6.3: Zonal average OSR validation against CERES SSF. "nC" means the *Coarsened* G5NR sampled at the locations of valid SSF data.

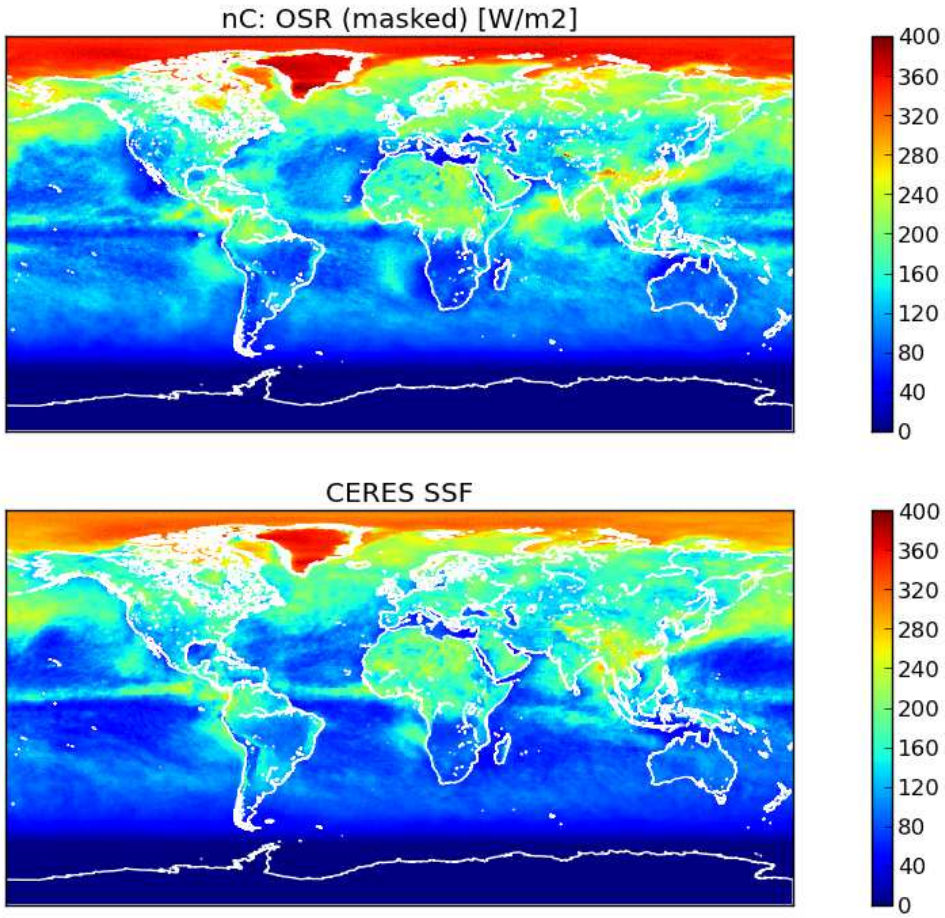

Figure 6.4: Global map OSR validation against CERES SSF. "nC" means the *Coarsened* G5NR sampled at the locations of valid SSF data. "(masked)" emphasizes that the G5NR output is averaged only over the locations of valid SSF data.

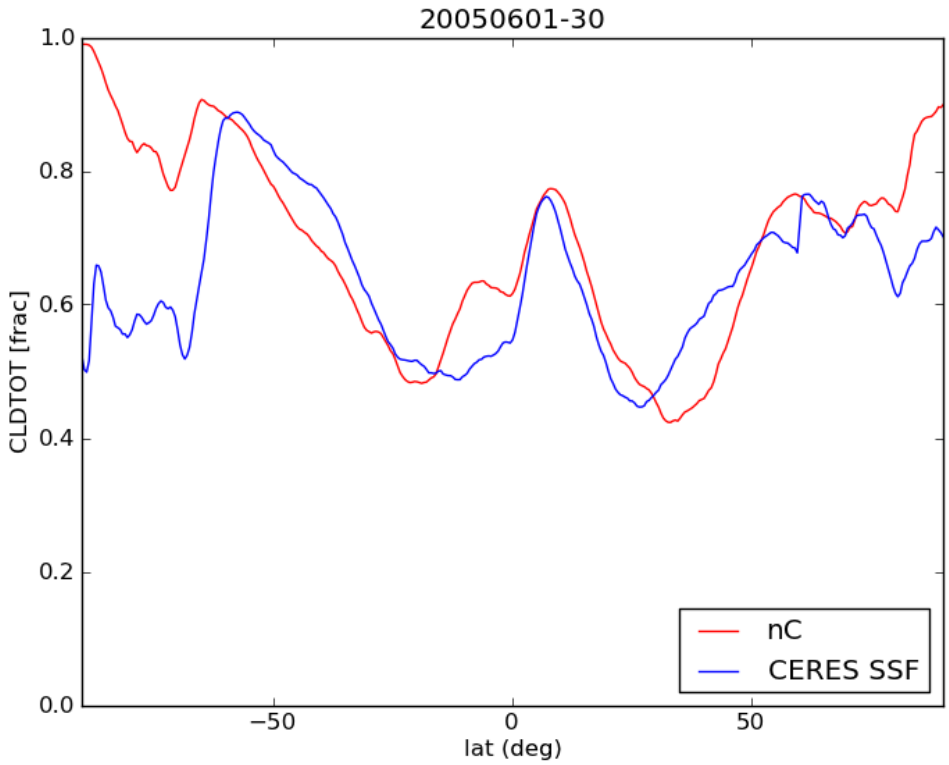

Figure 6.5: Zonal average total column cloud fraction validation against CERES SSF. "nC" means the *Coarsened* G5NR sampled at the locations of valid SSF data.

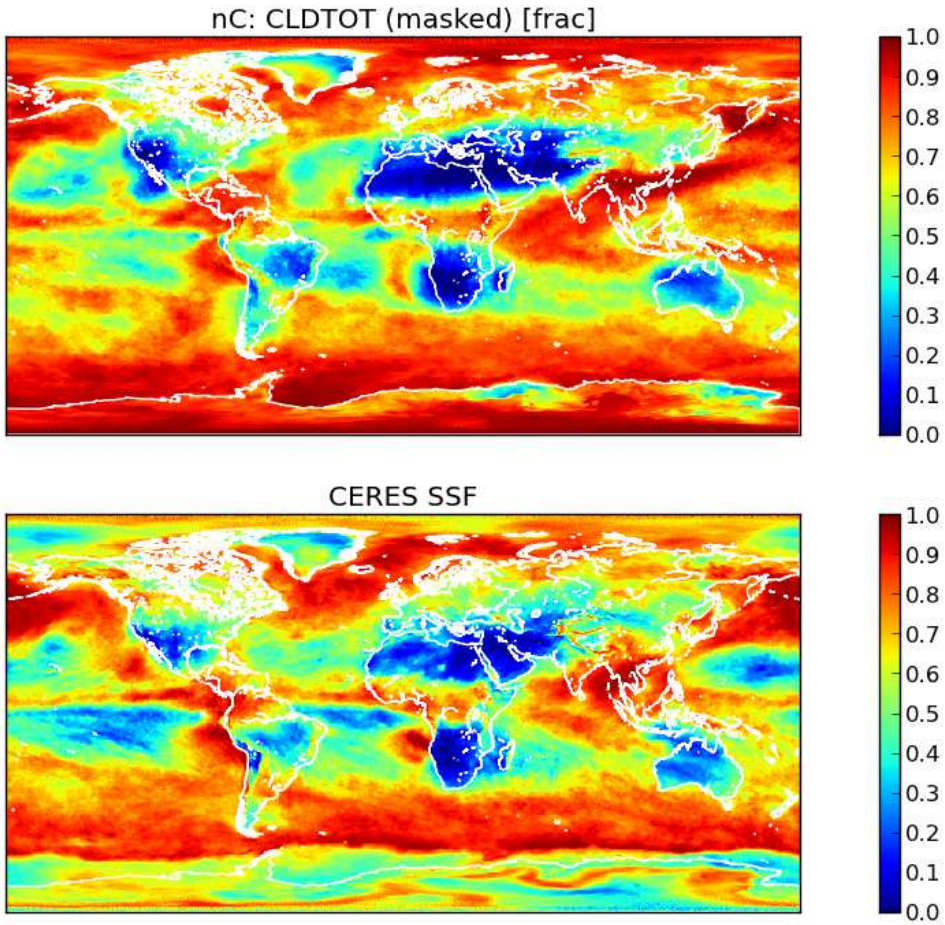

Figure 6.6: Global map total column cloud fraction validation against CERES SSF. "nC" means the *Coarsened* G5NR sampled at the locations of valid SSF data. "(masked)" emphasizes that the G5NR output is averaged only over the locations of valid SSF data.

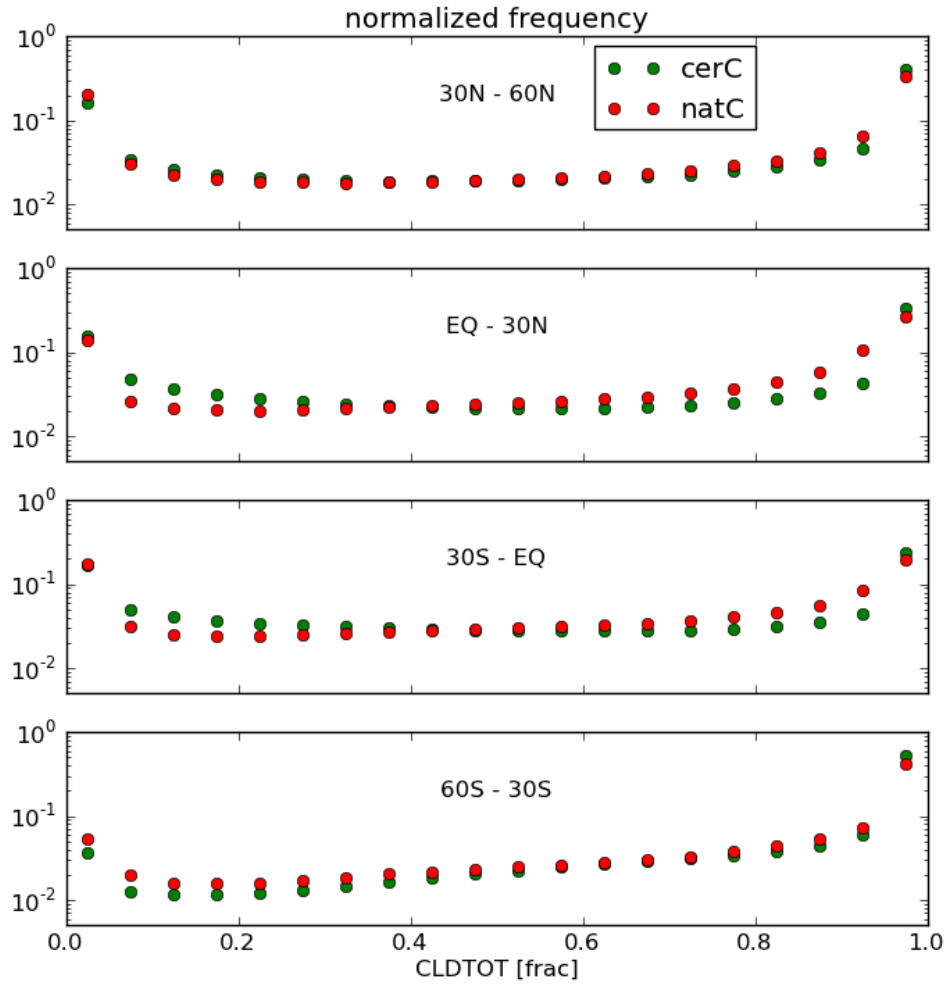

Figure 6.7: Frequency distribution of cloud fraction on the coarse grid over the month of June 2005. "cerC" are the CERES total column cloud fractions binned to the coarse grid, and "natC" are the corresponding coarsened G5NR values. Note the logarithmic scale necessitated by the strong binarity of cloud fraction.

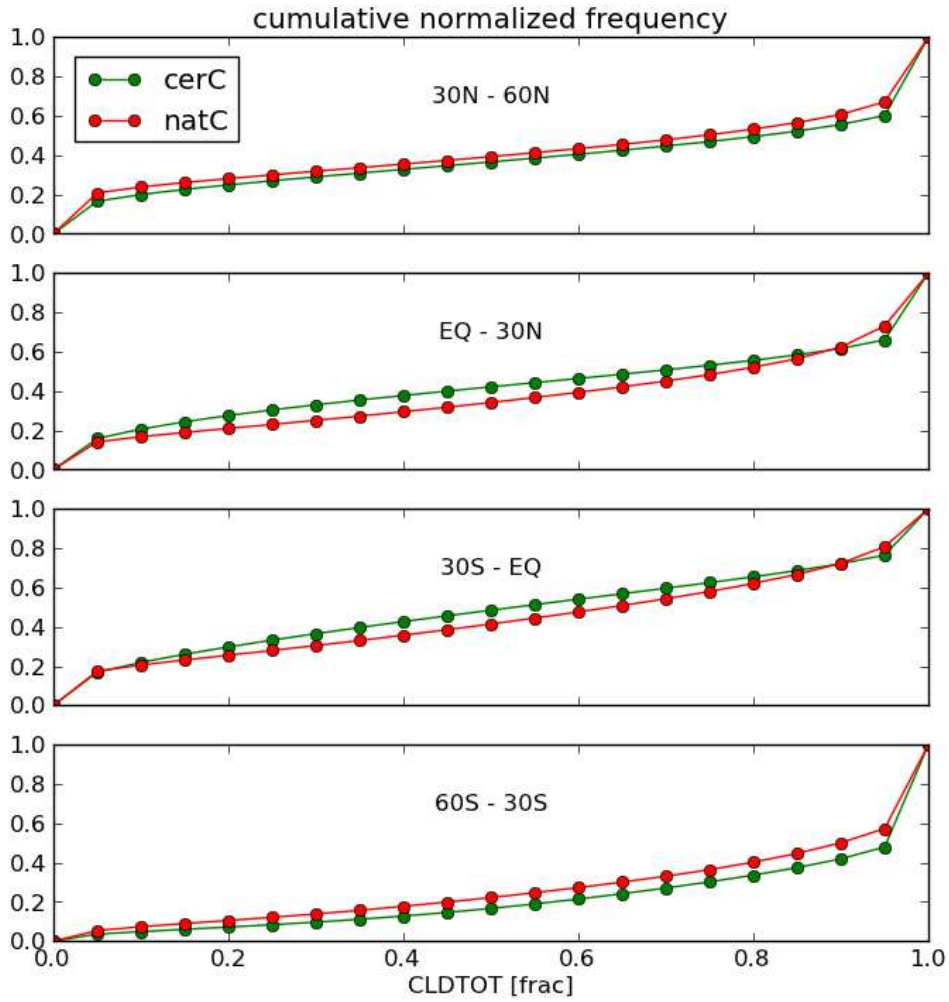

Figure 6.8: As for Figure 6.7 but the *cumulative* frequency distributions.

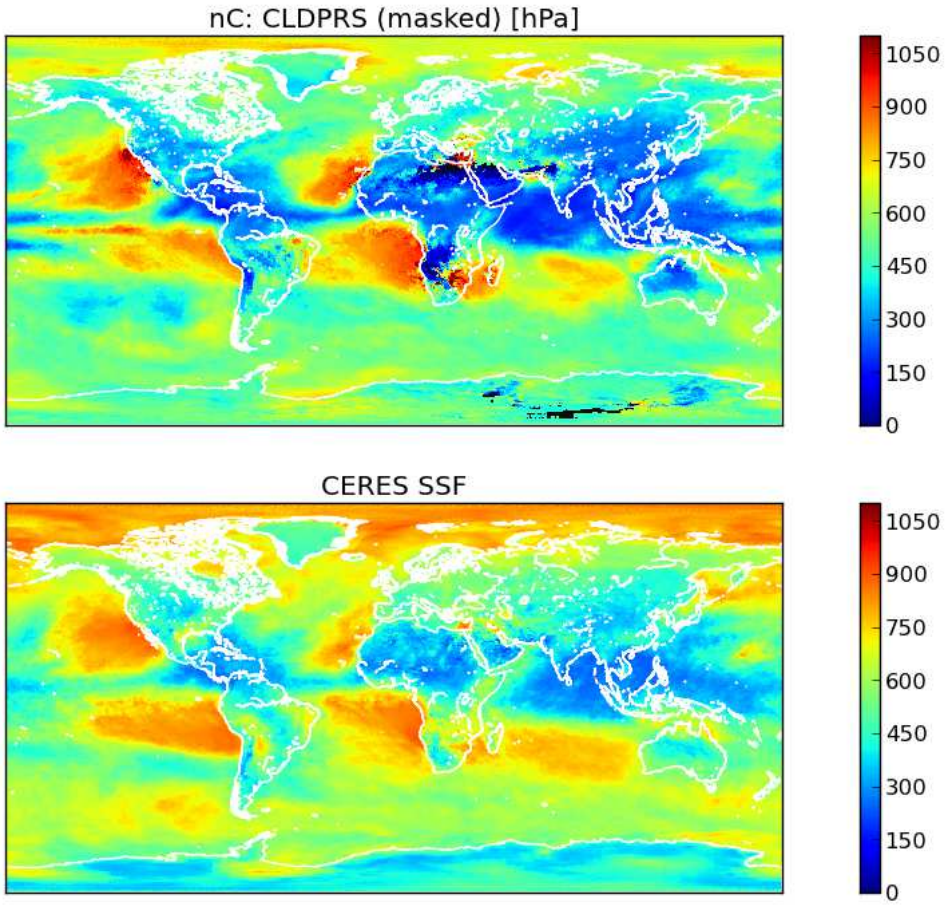

Figure 6.9: Global map cloud top pressure comparison against CERES SSF. "nC" means the *Coarsened* G5NR sampled at the locations of valid SSF data. "(masked)" emphasizes that the G5NR output is averaged only over the locations of valid SSF data.

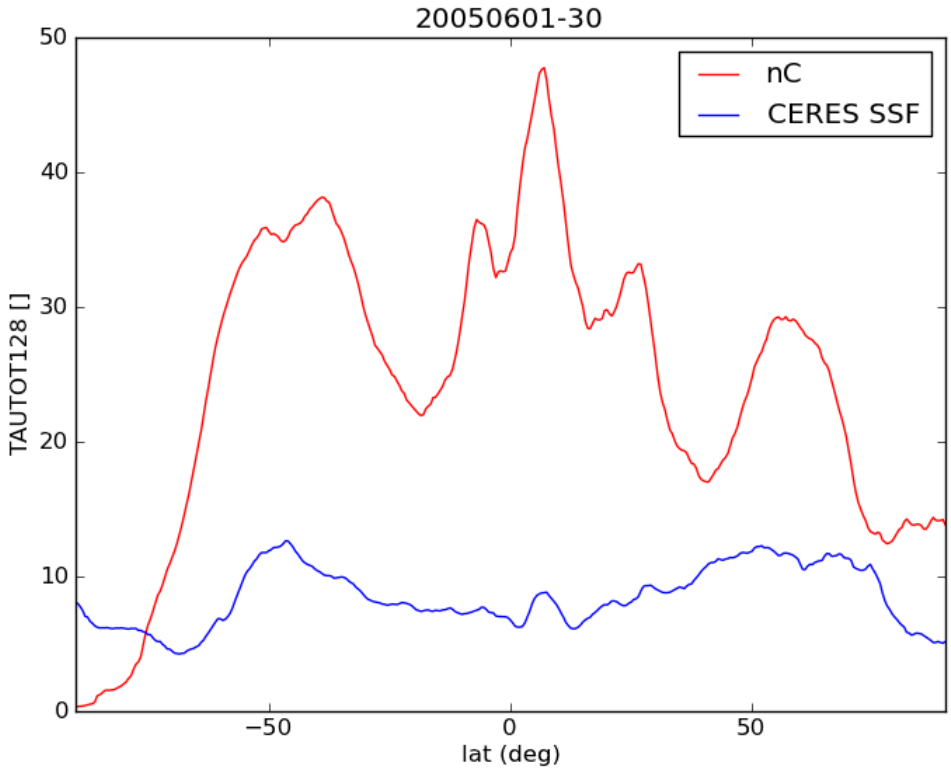

Figure 6.10: Zonal average in-cloud cloud optical thickness validation against CERES SSF. "nC" means the *Coarsened* G5NR sampled at the locations of valid SSF data.

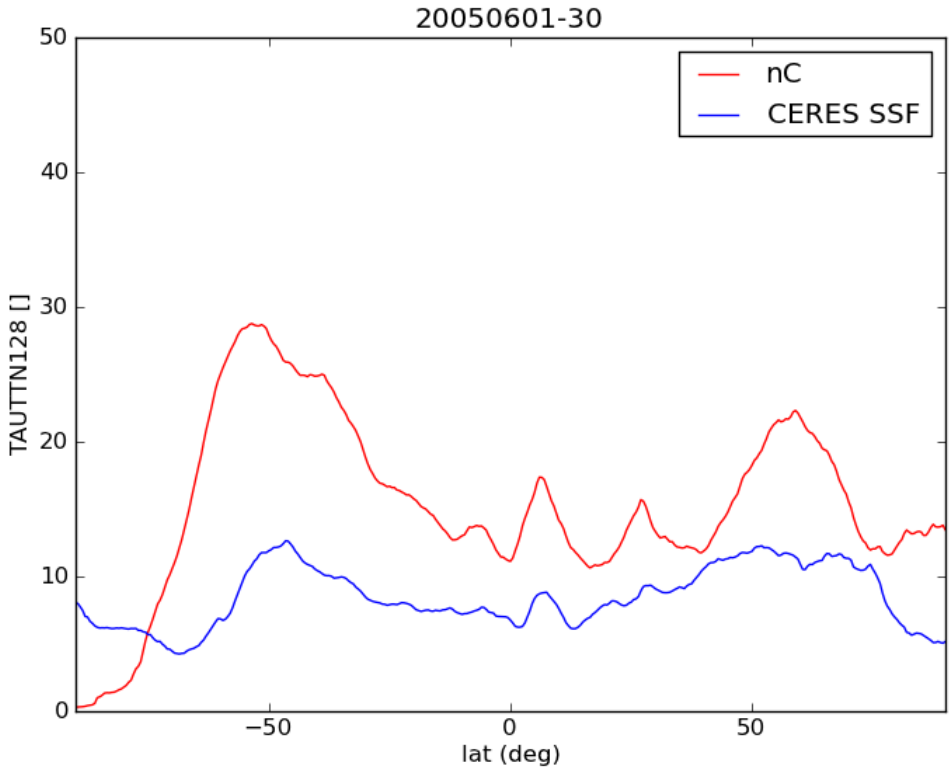

Figure 6.11: Zonal average corrected in-cloud cloud optical thickness validation against CERES SSF. "nC" means the *Coarsened* G5NR sampled at the locations of valid SSF data.

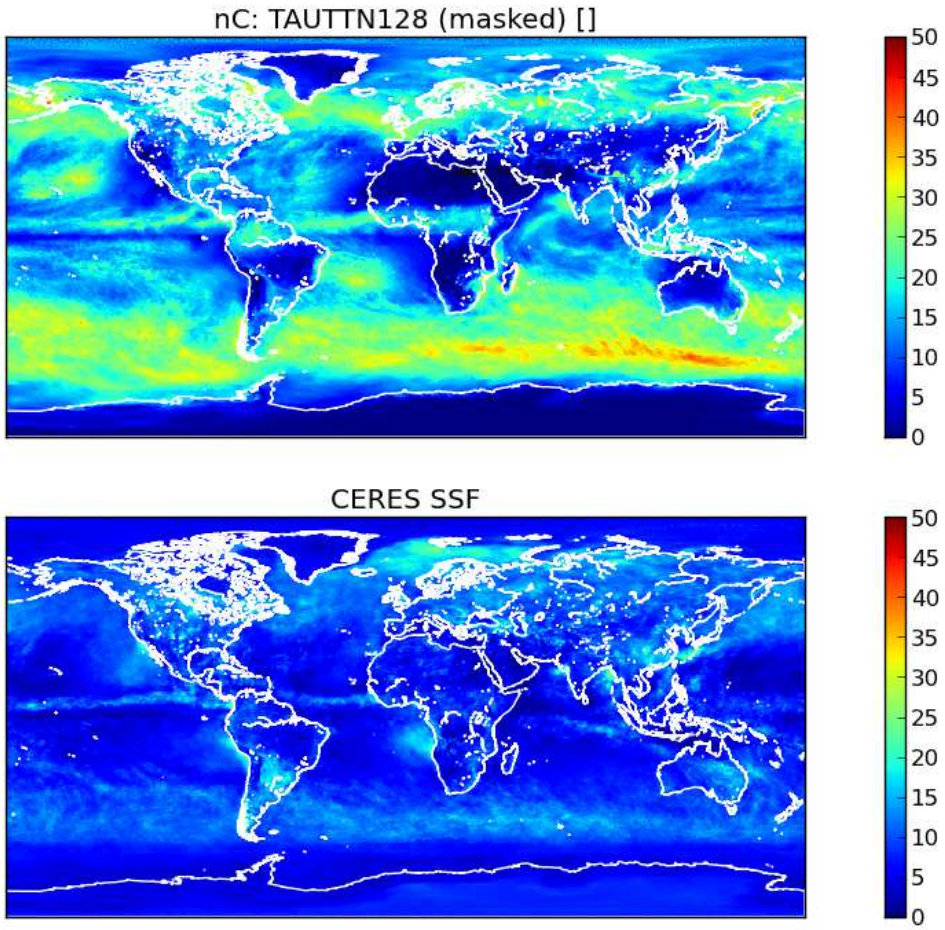

Figure 6.12: Global map corrected in-cloud cloud optical thickness comparison against CERES SSF. "nC" means the *Coarsened* G5NR sampled at the locations of valid SSF data. "(masked)" emphasizes that the G5NR output is averaged only over the locations of valid SSF data.

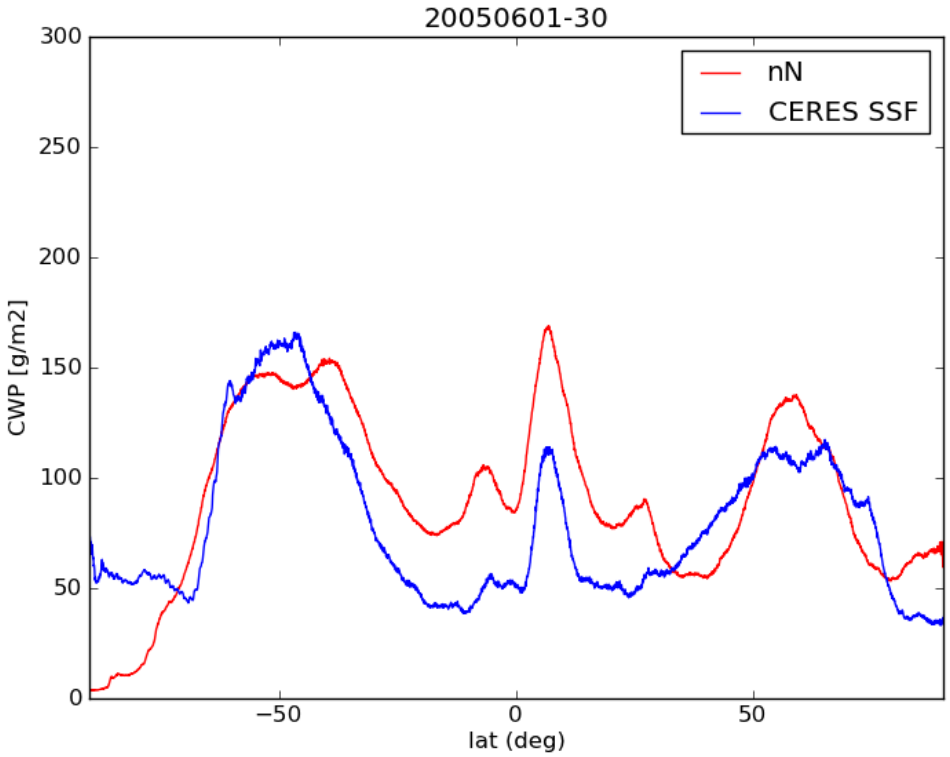

Figure 6.13: Zonal average grid-column mean condensed water path validation against CERES SSF. "nN" means the *Native resolution* G5NR sampled at the locations of valid SSF data.

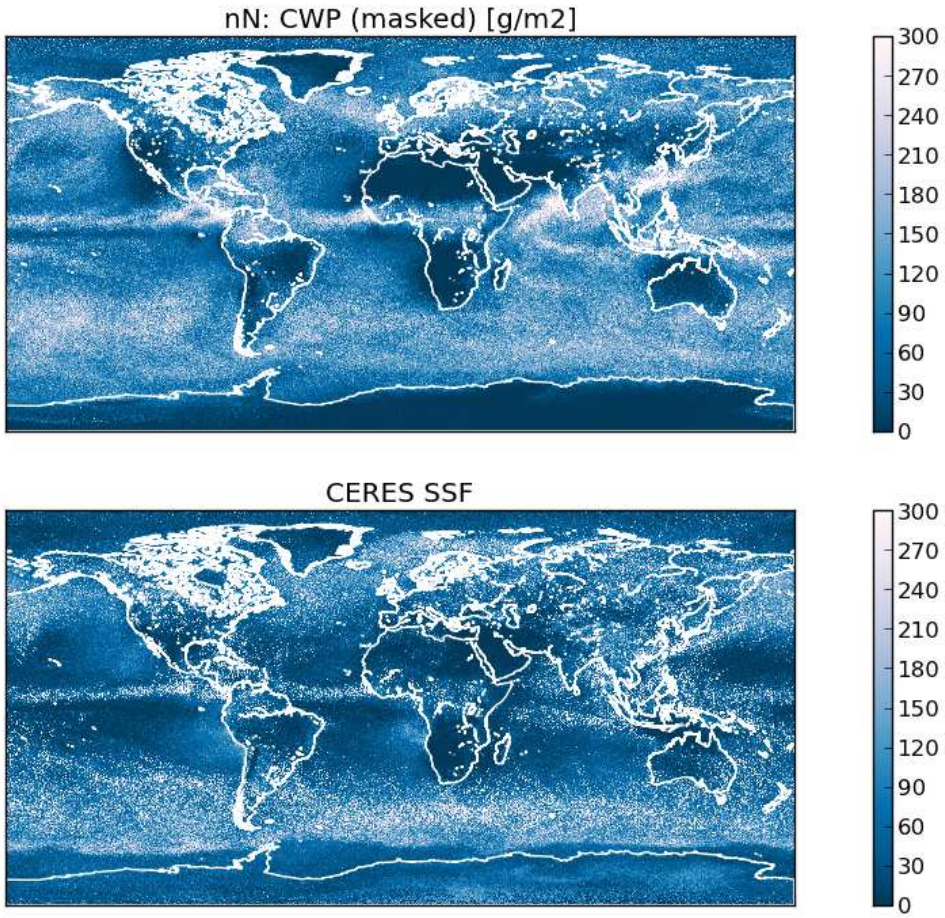

Figure 6.14: Global map grid-column mean condensed water path validation against CERES SSF. "nN" means the *Native resolution* G5NR sampled at the locations of valid SSF data. "(masked)" emphasizes that the G5NR output is averaged only over the locations of valid SSF data.

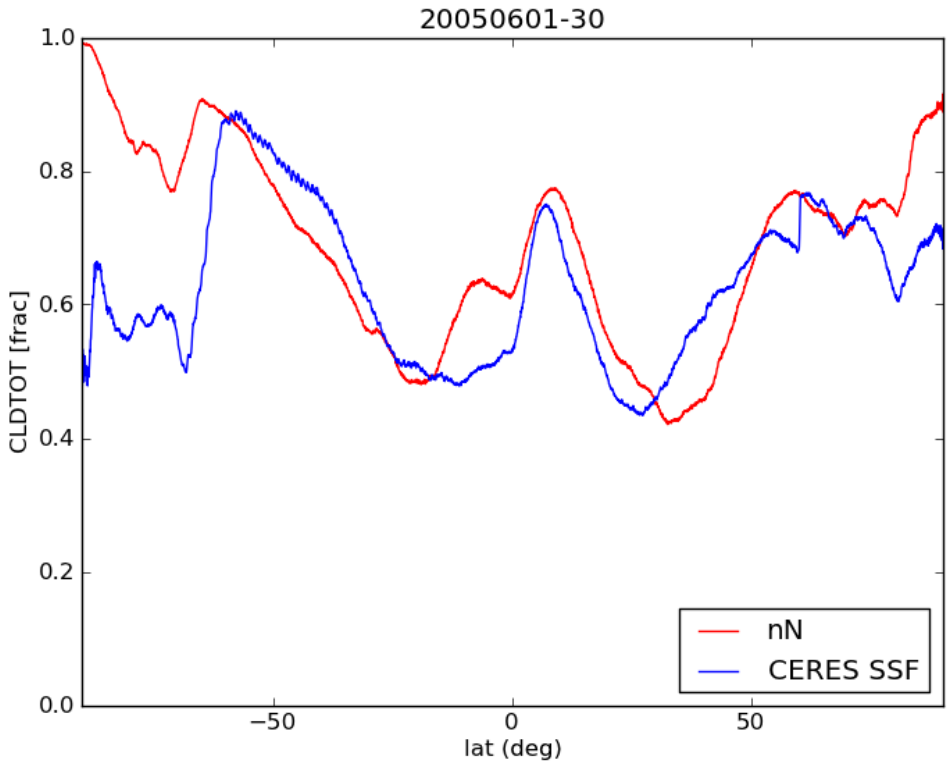

Figure 6.15: Zonal average cloud fraction validation against CERES SSF at native G5NR resolution. Otherwise like Figure 6.5.

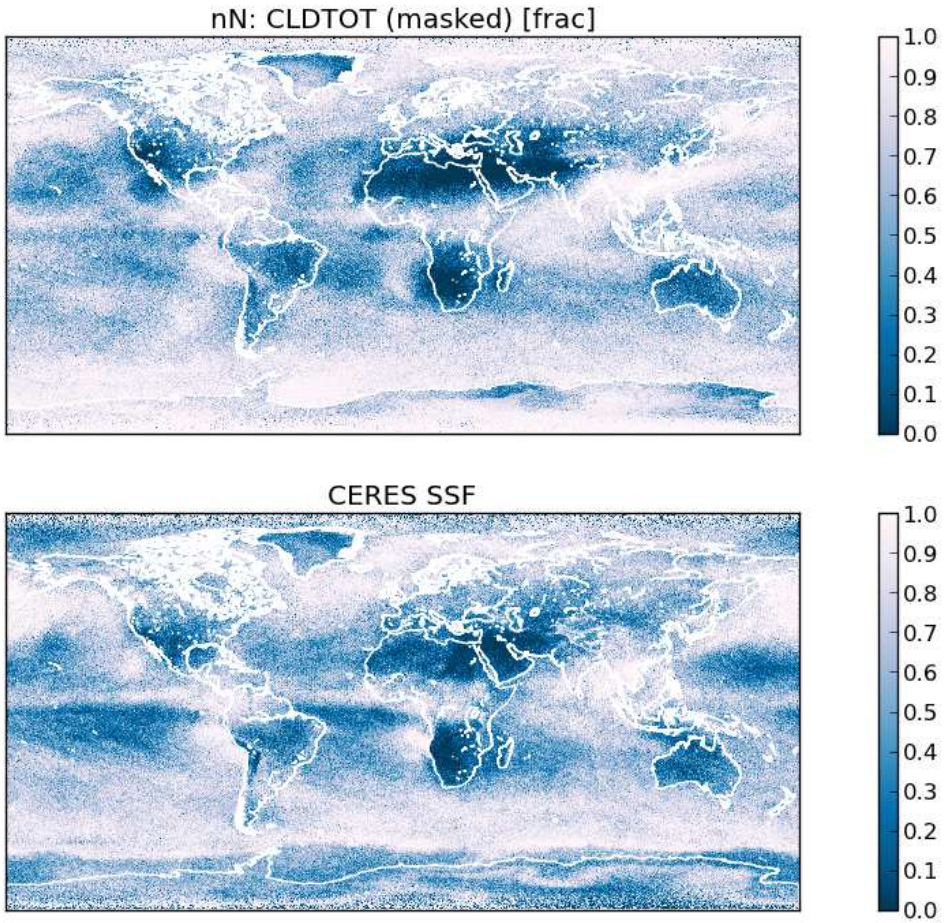

Figure 6.16: Global map cloud fraction validation against CERES SSF at native G5NR resolution. Otherwise like Figure 6.6.

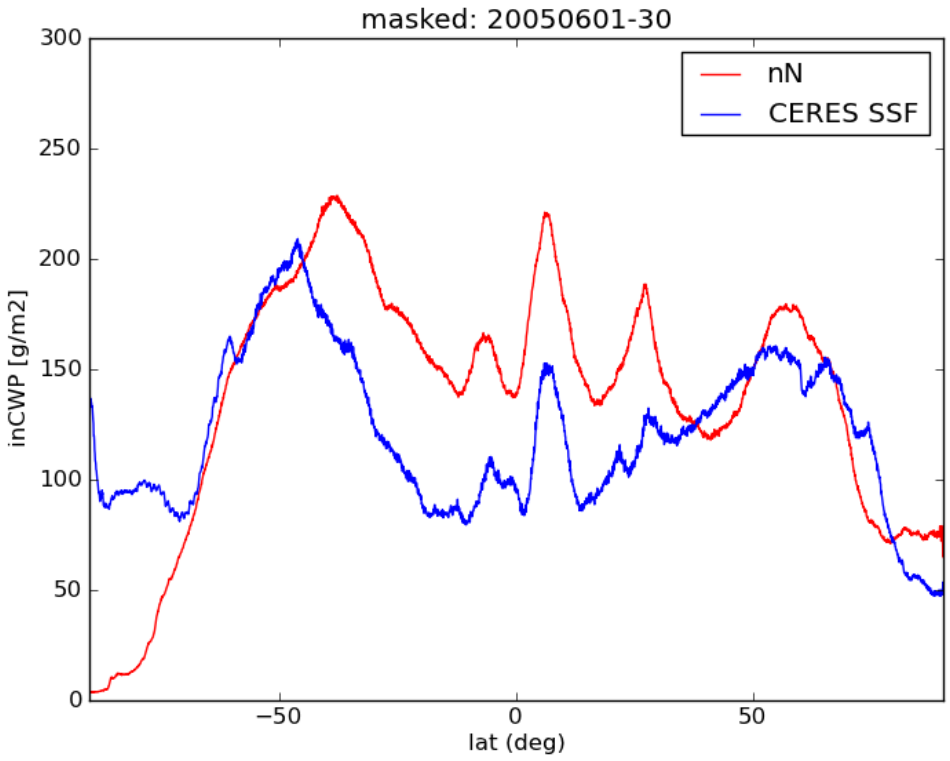

Figure 6.17: Zonal average in-cloud condensed water path validation against CERES SSF. "nN" means the *Native resolution* G5NR sampled at the locations of valid SSF data.

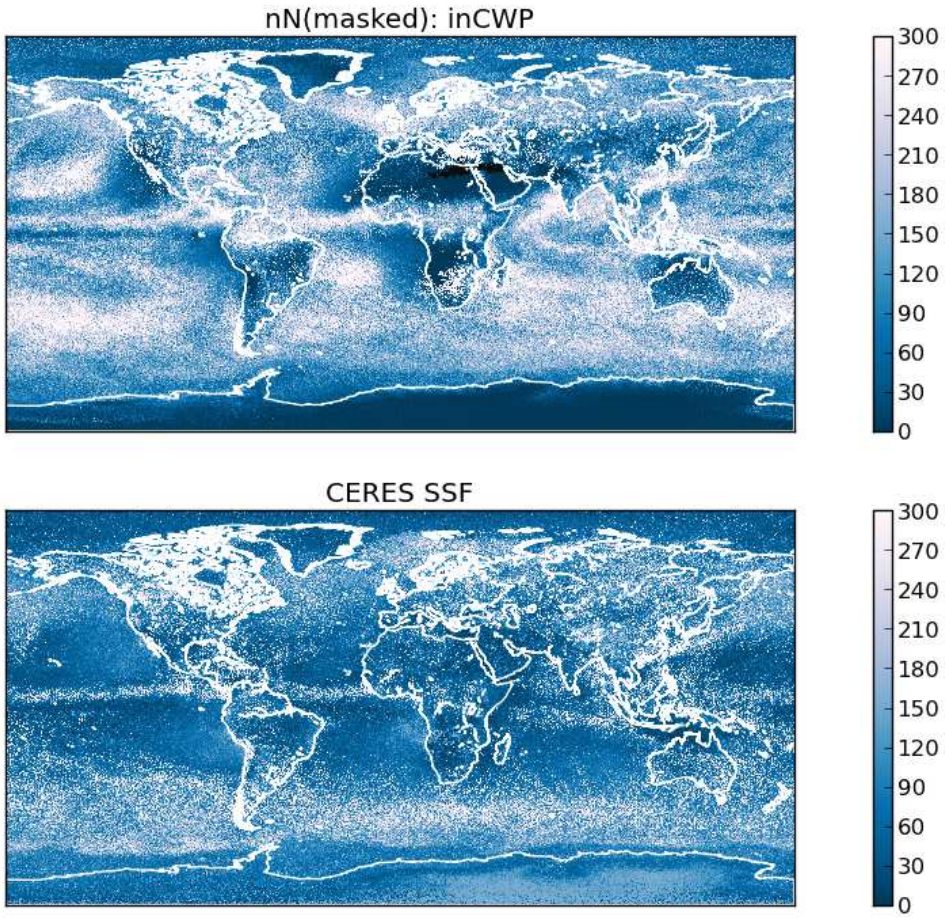

Figure 6.18: Global map in-cloud condensed water path validation against CERES SSF. "nN" means the *Native resolution* G5NR sampled at the locations of valid SSF data. "(masked)" emphasizes that the G5NR output is averaged only over the locations of valid SSF data.

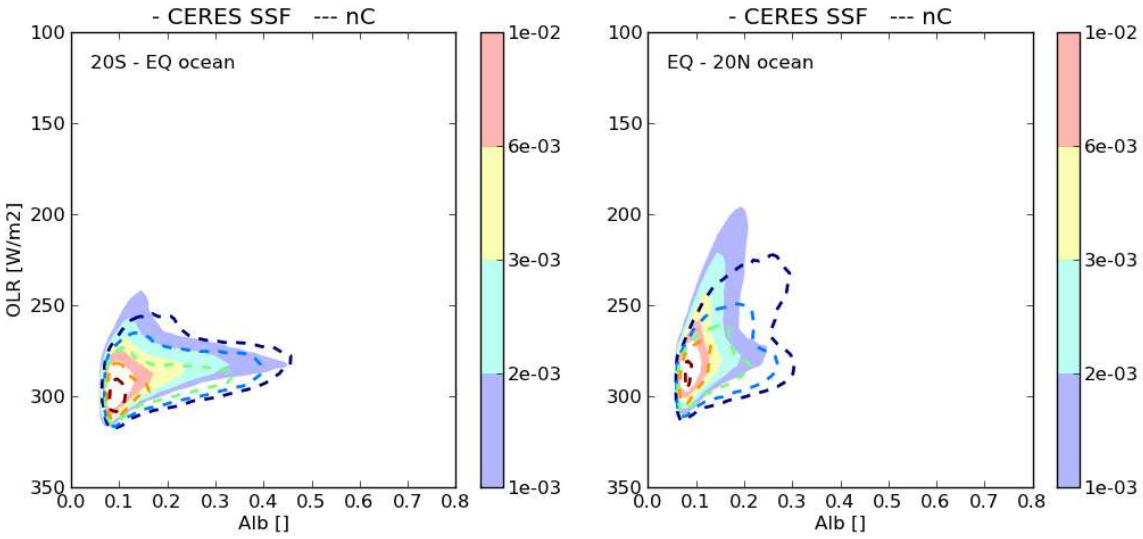

Figure 6.19: Joint histogram of TOA Cloud Albedo vs. OLR for the tropical ocean. Contours are proportional to probability density. The filled contours are for CERES SSF. The dashed contours are for the CERES-SSF-masked coarse G5NR (nC). The five dashed (blue, cyan, green, orange and red) contours delineate the boundaries of the four filled color regions. All results are for daytime only. The results are build up from individual hourly averages.

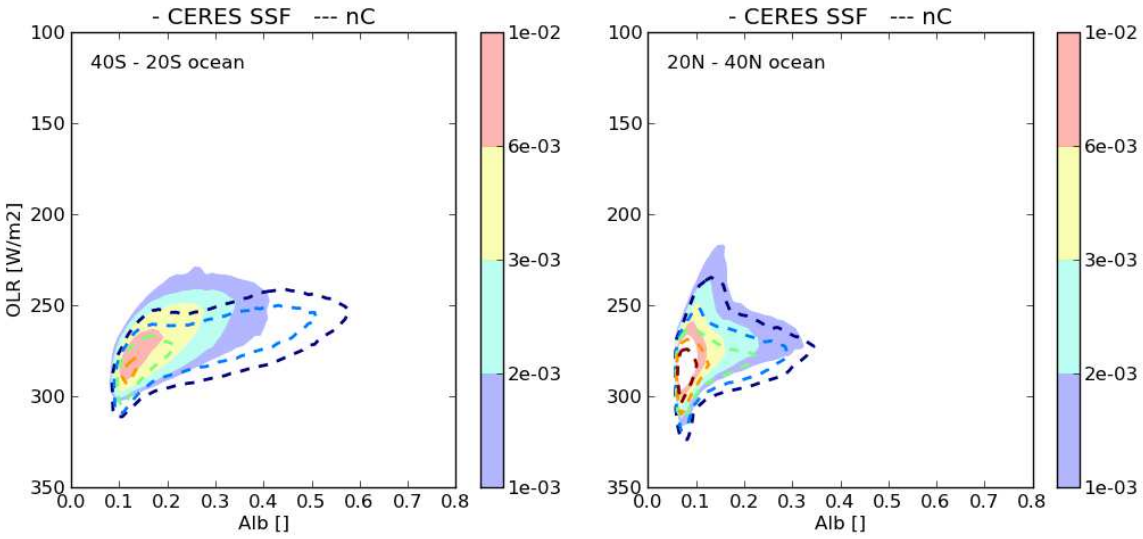

Figure 6.20: Joint histogram of TOA Cloud Albedo vs. OLR for the mid-latitude ocean. Otherwise, as in Figure 6.19.

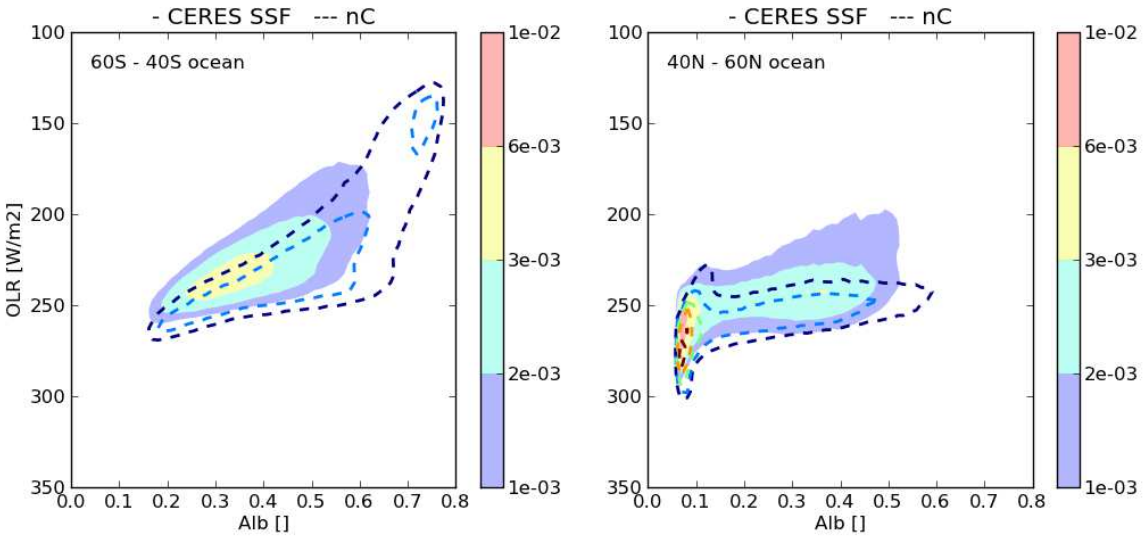

Figure 6.21: Joint histogram of TOA Cloud Albedo vs. OLR for the higher-latitude oceans. Otherwise, as in Figure 6.19.

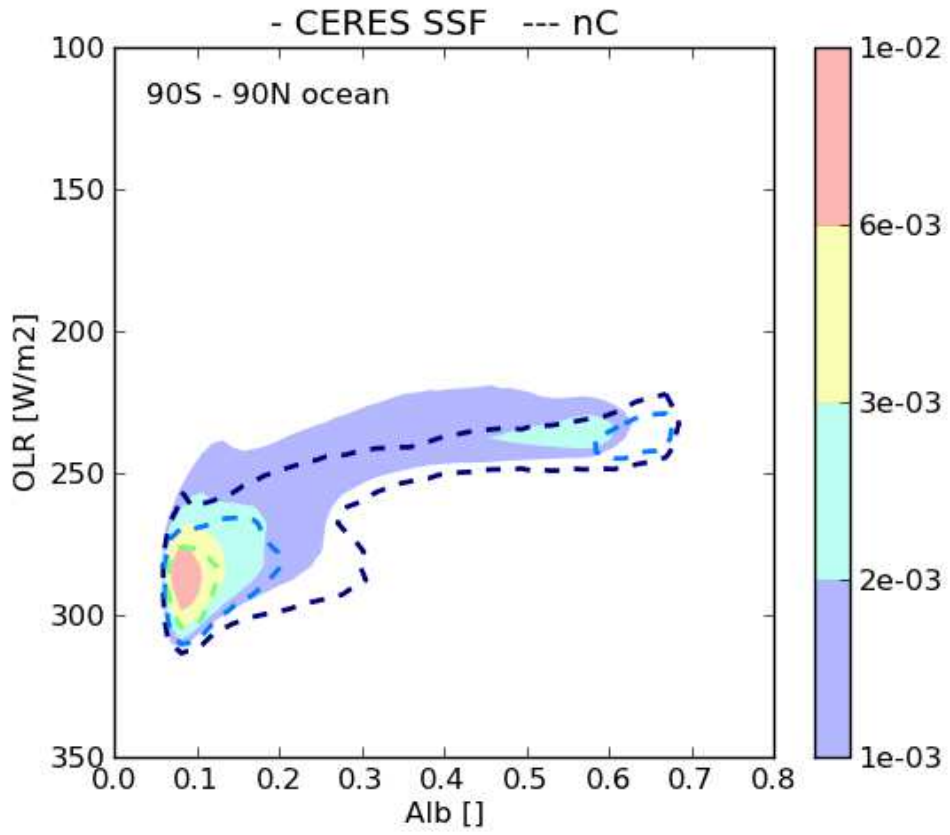

Figure 6.22: Joint histogram of TOA Cloud Albedo vs. OLR for the global oceans. Otherwise, as in Figure 6.19.

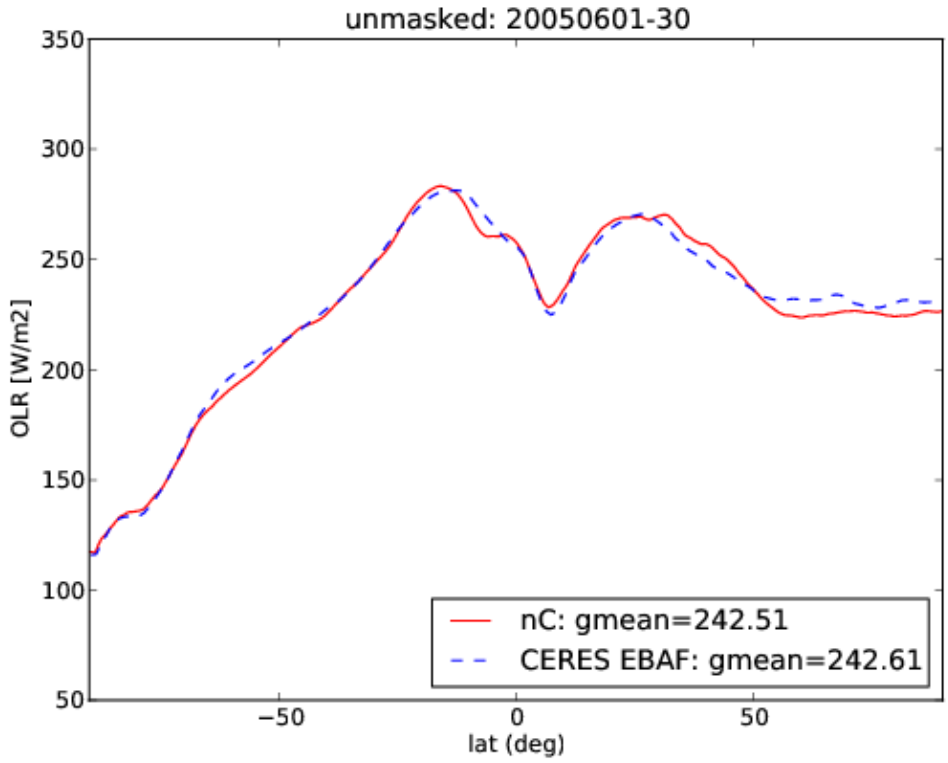

Figure 6.23: Zonal average OLR validation against CERES EBAF for June 2005. "nC" is the full diurnally and monthly averaged *Coarsened* G5NR (see text). The "gmean" are the global mean values.

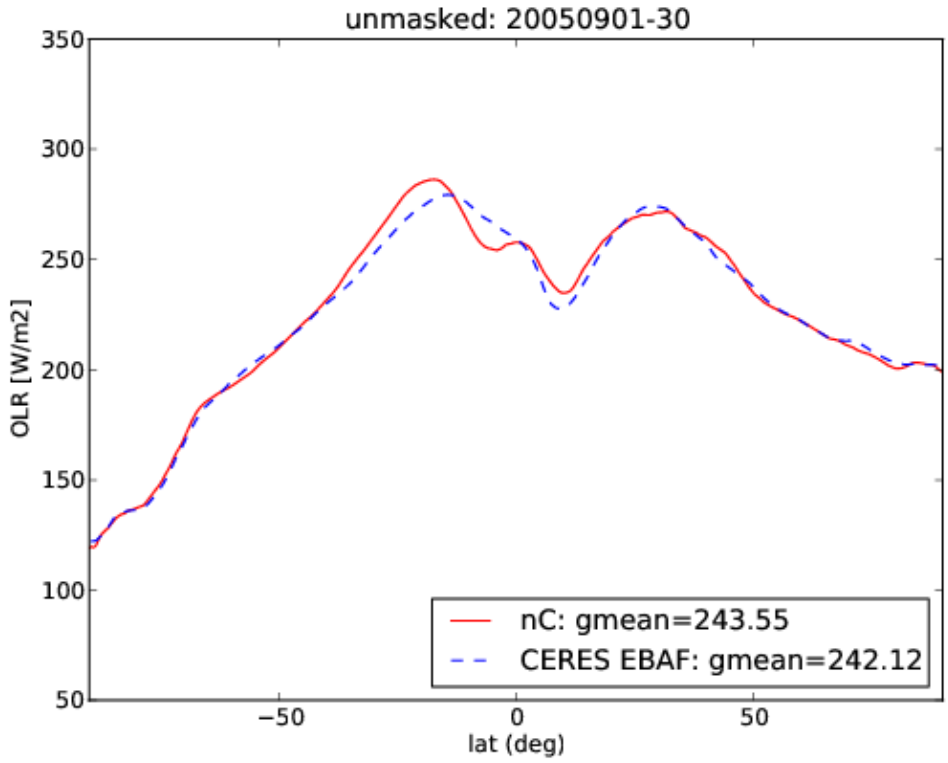

Figure 6.24: Zonal average OLR validation against CERES EBAF for September 2005. "nC" is the full diurnally and monthly averaged *Coarsened* G5NR (see text). The "gmean" are the global mean values.

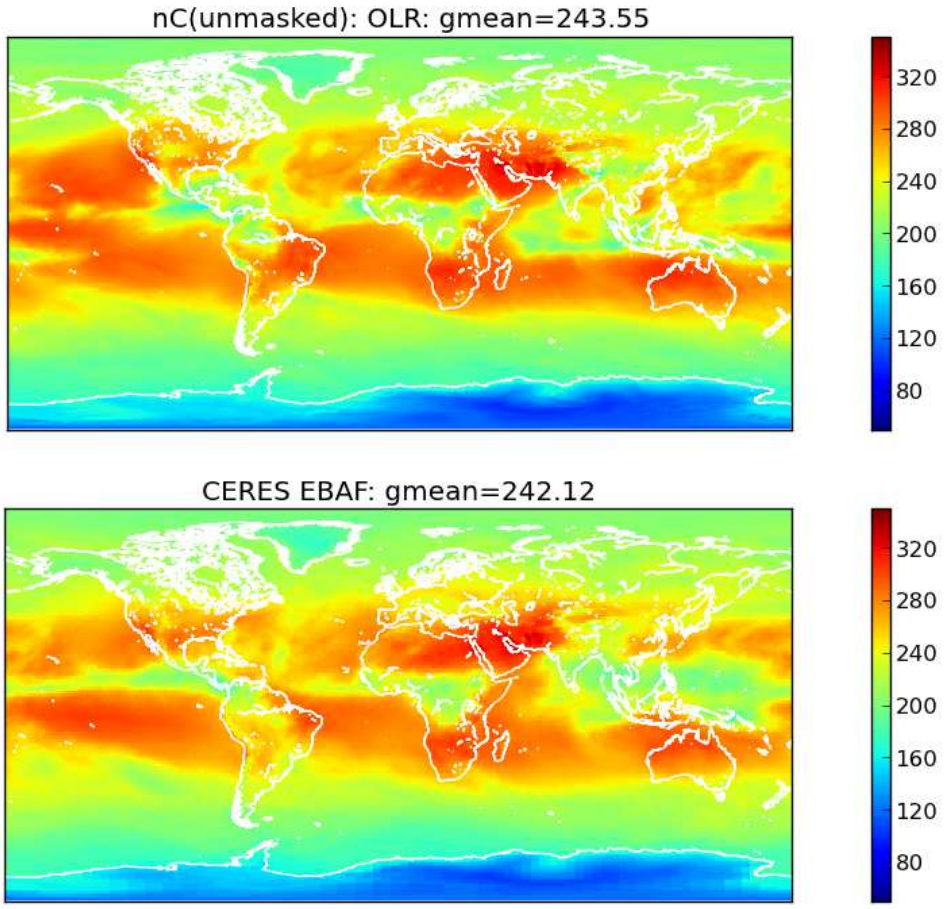

Figure 6.25: Global map OLR validation against CERES EBAF for September 2005. "nC(unmasked)" is the full diurnally and monthly averaged *Coarsened* G5NR (see text). The "gmean" are the global mean values.

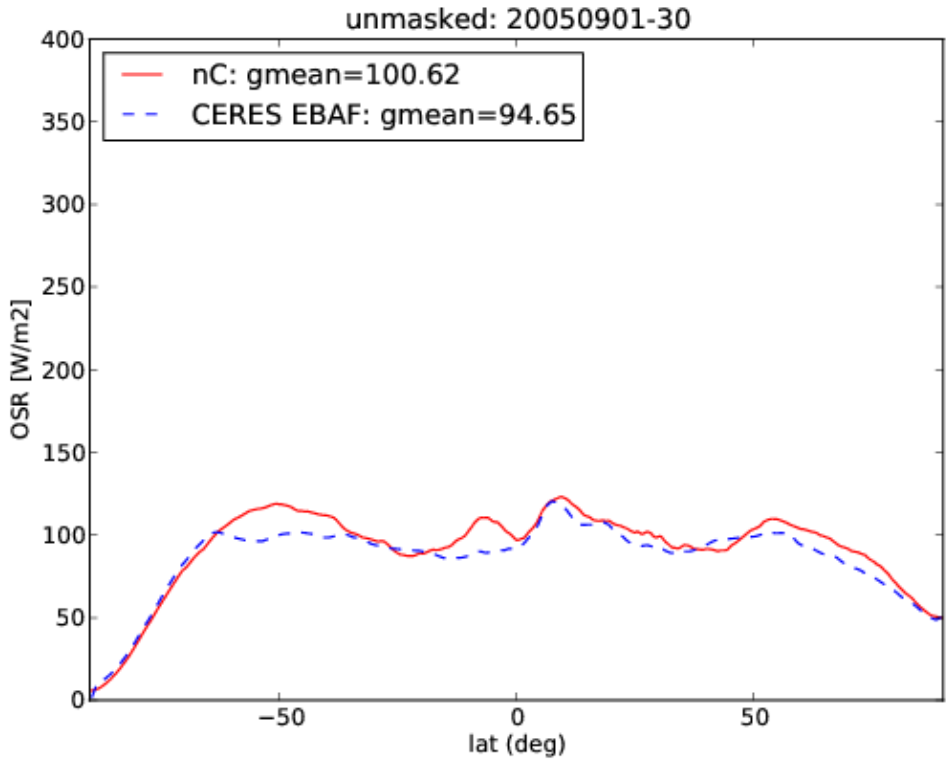

Figure 6.26: Zonal average OSR validation against CERES EBAF for September 2005. "nC" is the full diurnally and monthly averaged *Coarsened* G5NR (see text). The "gmean" are the global mean values.

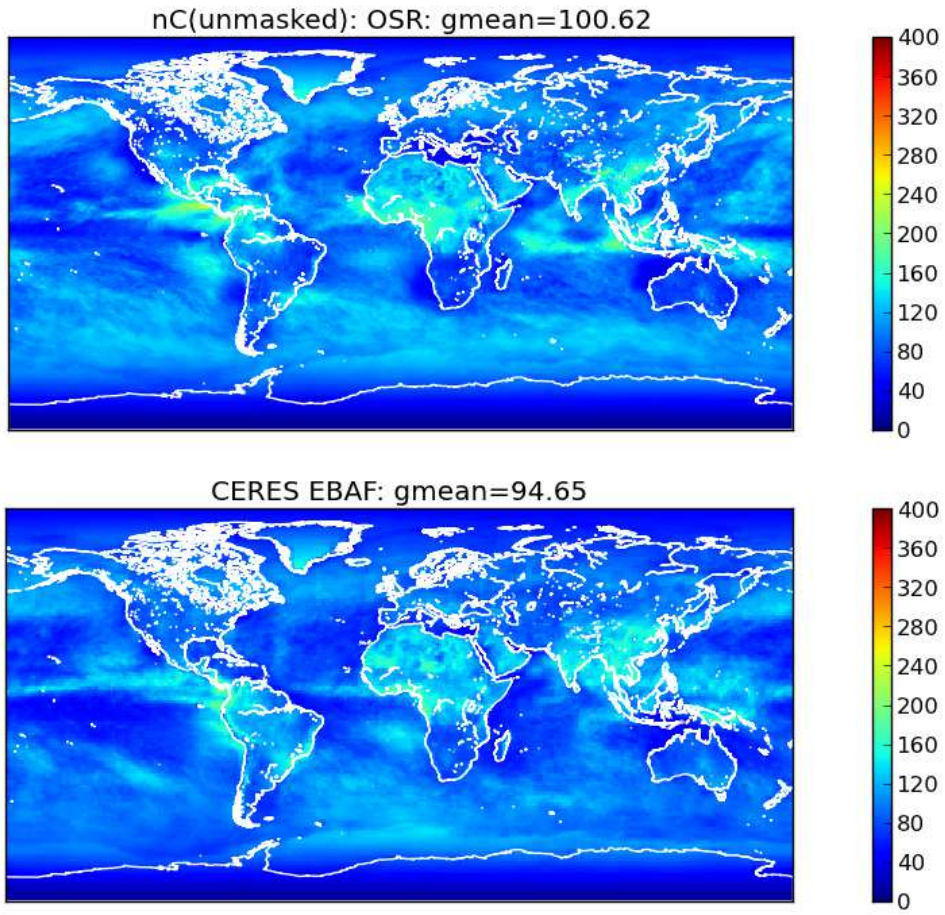

Figure 6.27: Global map OSR validation against CERES EBAF for September 2005. "nC(unmasked)" is the full diurnally and monthly averaged *Coarsened* G5NR (see text). The "gmean" are the global mean values.

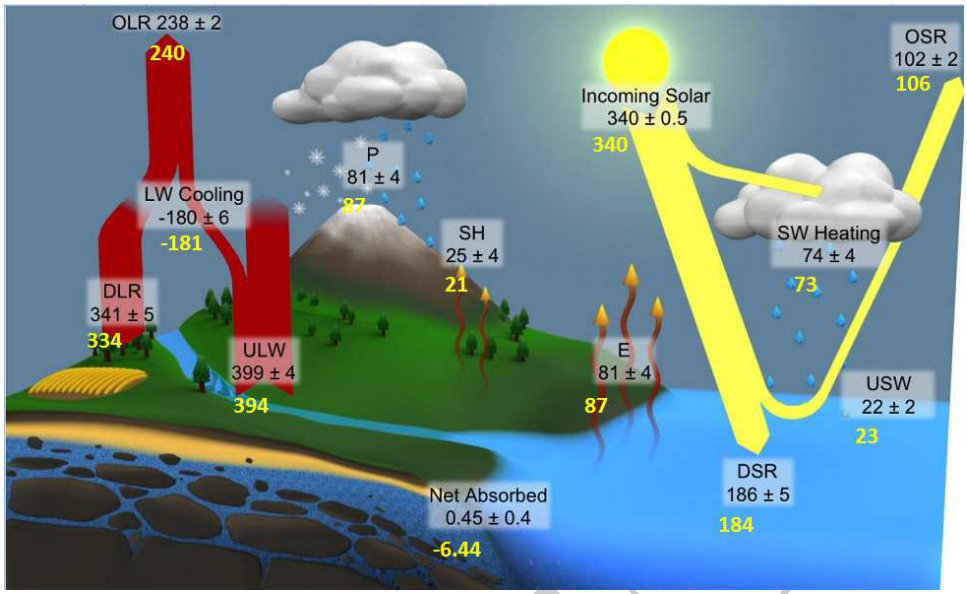

Figure 6.28: NASA Energy and Water cycle Study (NEWS) analysis of TOA energy balance (credit: Dr. Michael Bosilovich).

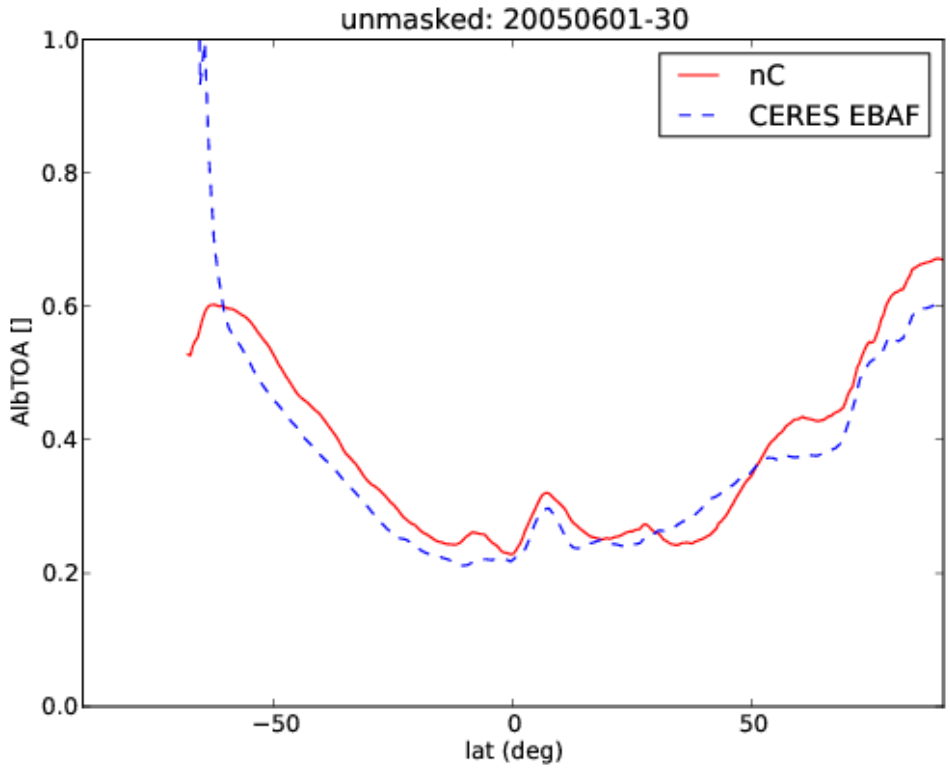

Figure 6.29: Zonal average shortwave TOA albedo validation against CERES EBAF for June 2005. "nC" is the full diurnally and monthly averaged *Coarsened* G5NR. The CERES outlier at the southernmost latitude should be ignored, where the incoming solar goes to zero.

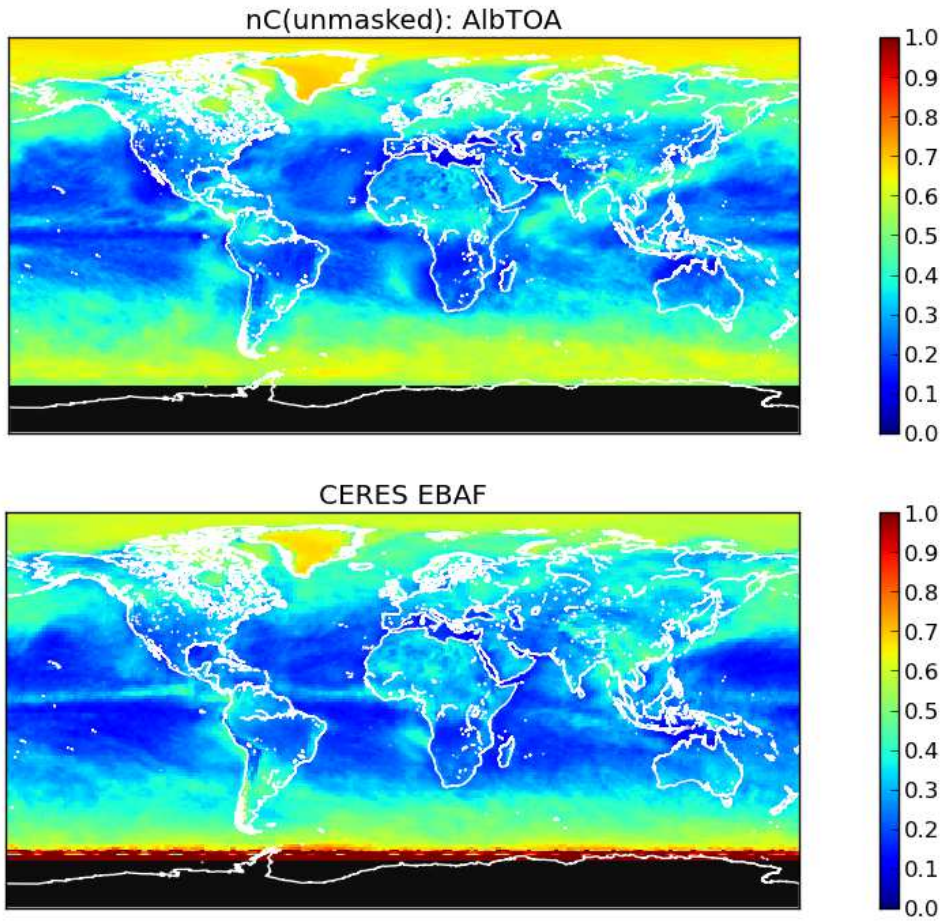

Figure 6.30: Global map shortwave TOA albedo validation against CERES EBAF for June 2005. "nC(unmasked)" is the full diurnally and monthly averaged *Coarsened* G5NR.

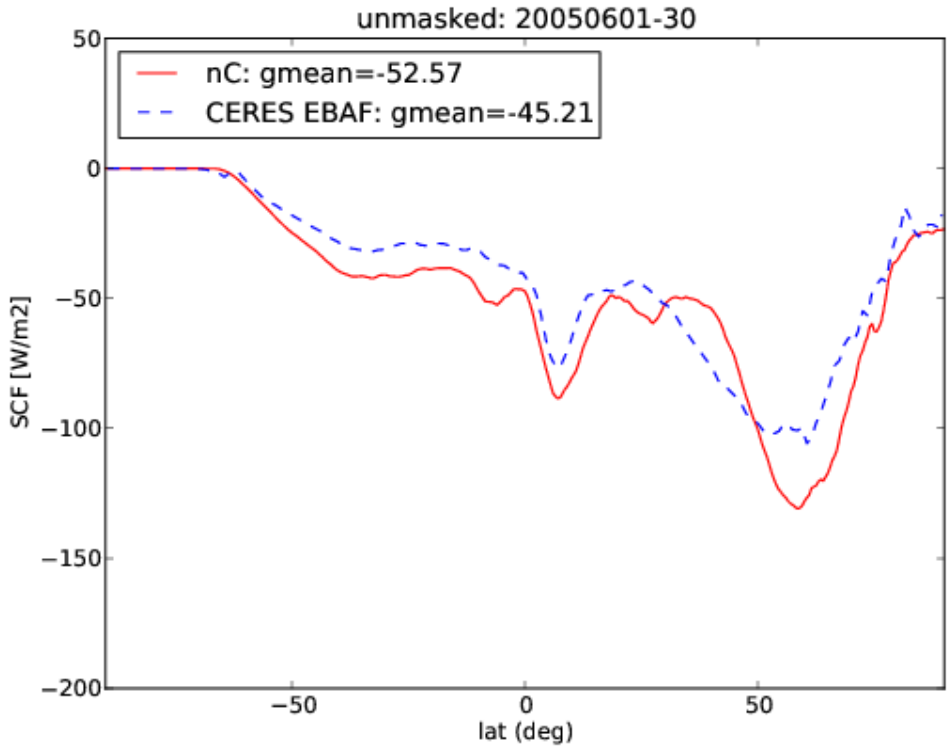

Figure 6.31: Zonal average shortwave cloud forcing (SCF) validation against CERES EBAF for June 2005. "nC" is the full diurnally and monthly averaged *Coarsened* G5NR. The "gmean" are the global mean values.

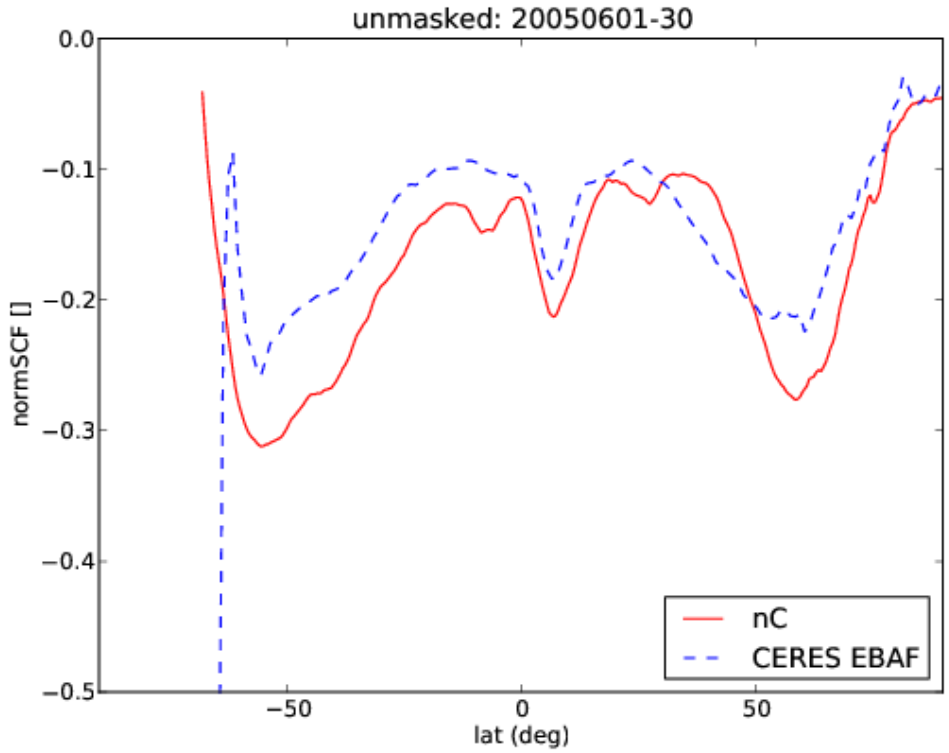

Figure 6.32: Zonal average shortwave cloud forcing (SCF) normalized by ISR: validation against CERES EBAF for June 2005. "nC" is the full diurnally and monthly averaged coarsened G5NR.

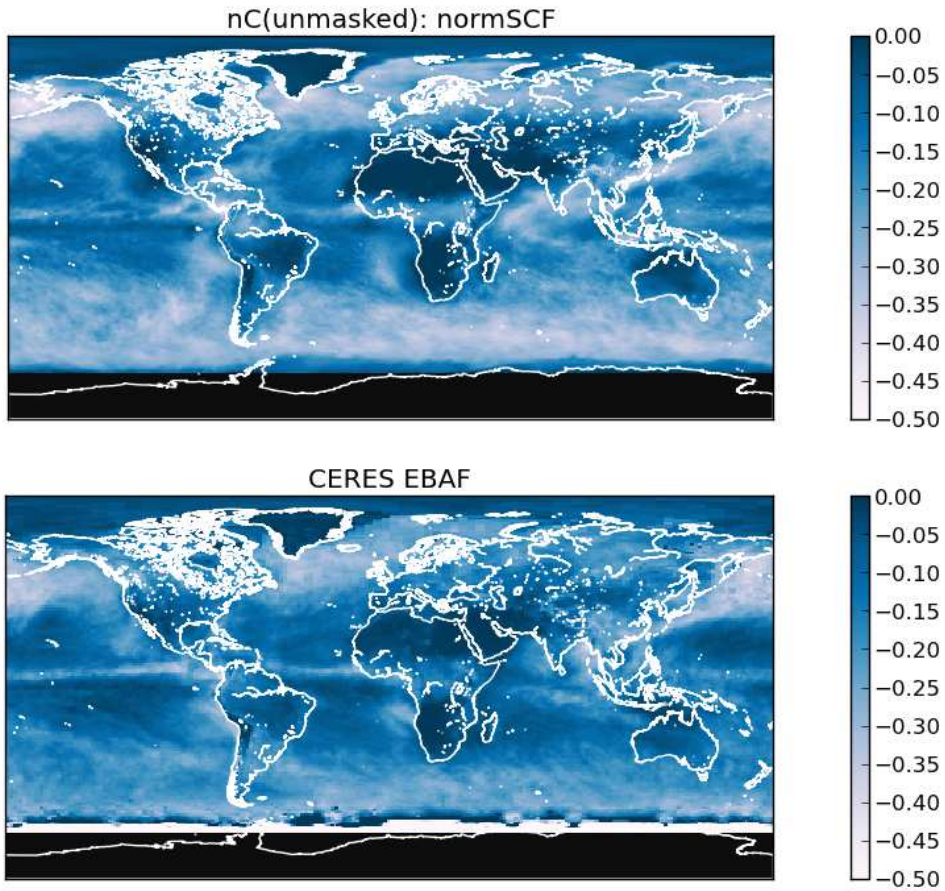

Figure 6.33: Global map average shortwave cloud forcing (SCF) normalized by ISR: validation against CERES EBAF for June 2005. "nC" is the full diurnally and monthly averaged coarsened G5NR.

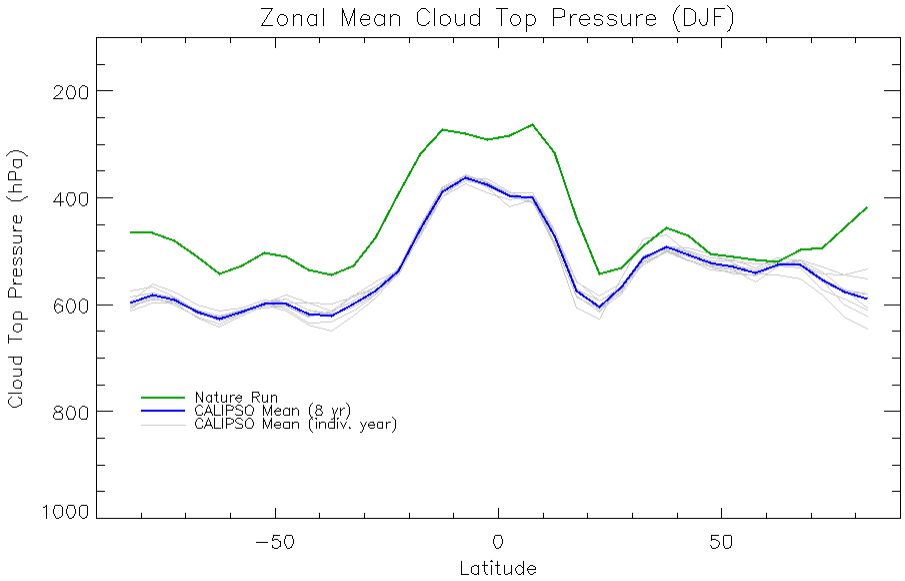

Figure 6.34: The mean cloud top pressure as a function of latitude for DJF for the G5NR (green), each CALIPSO DJF from 2006–07 through 2013–14 (gray), and the CALIPSO DJF 8 year average (blue).

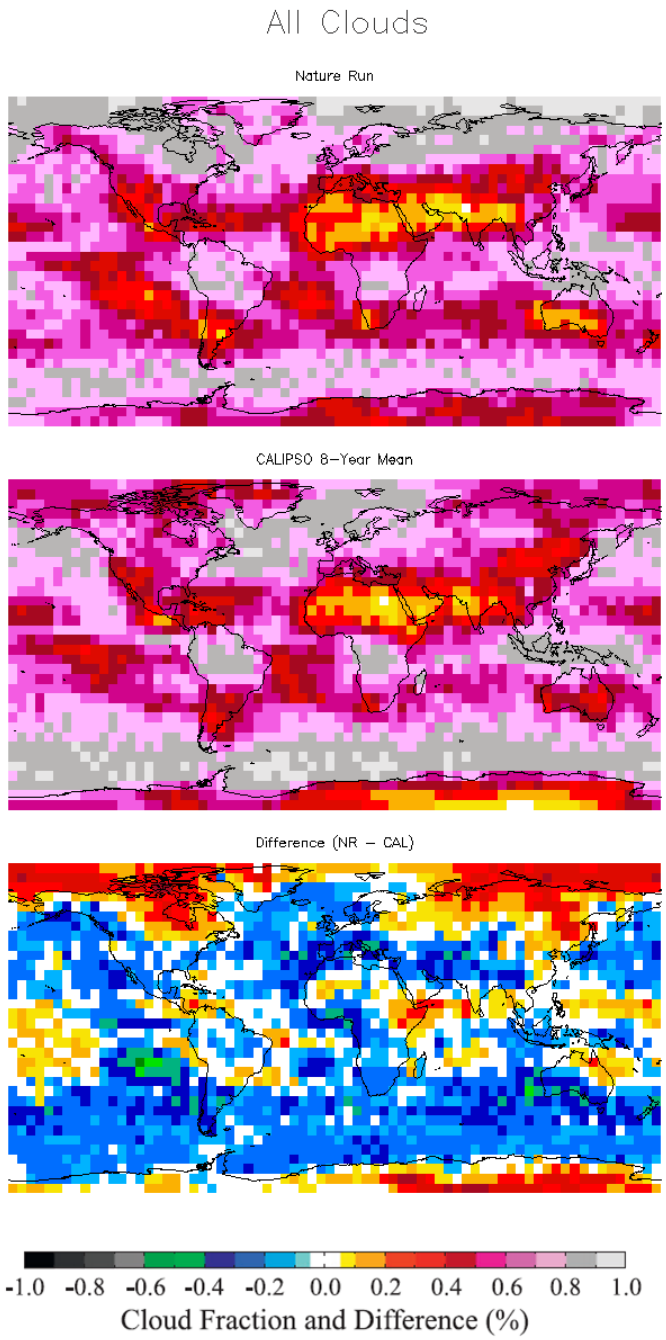

Figure 6.35: Spatial distribution of DJF cloud fraction for $5° \times 5°$ bins for the G5NR (top), the CALIPSO 8-year mean (middle), and the difference of the two (G5NR minus CALIPSO, bottom).

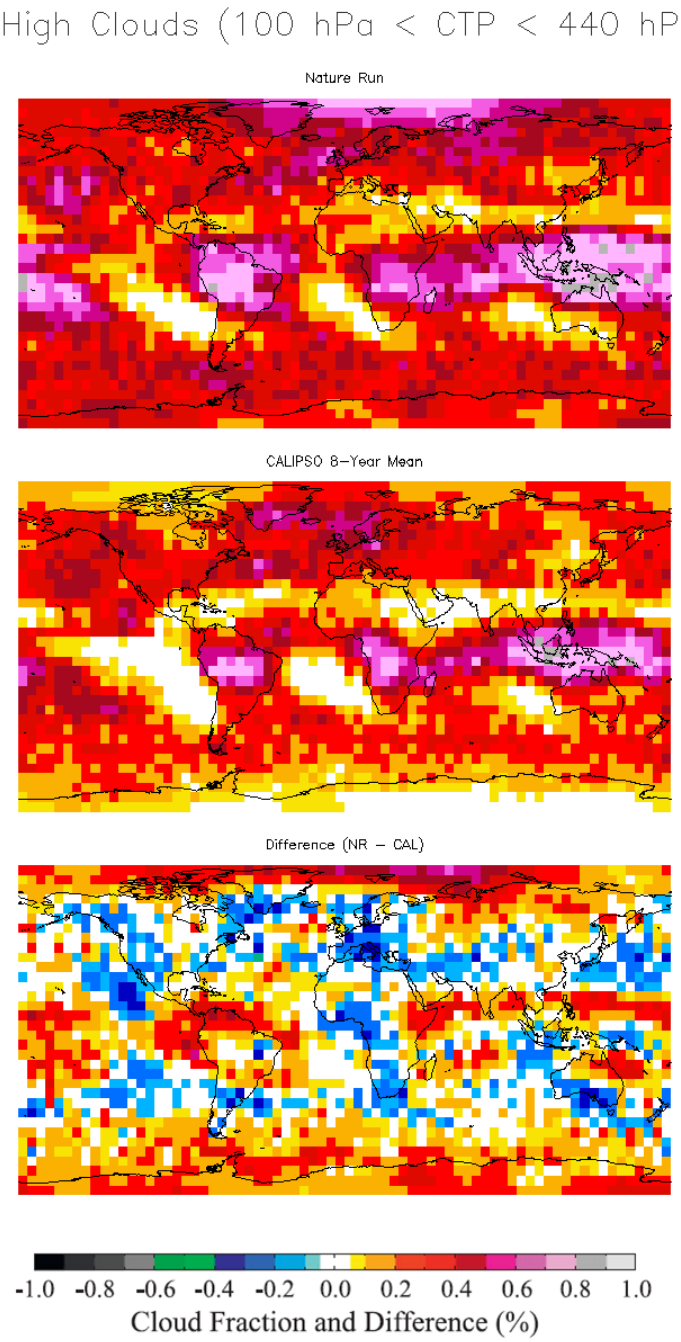

Figure 6.36: Same as Figure 6.35, but for high clouds (CTP < 440 hPa).

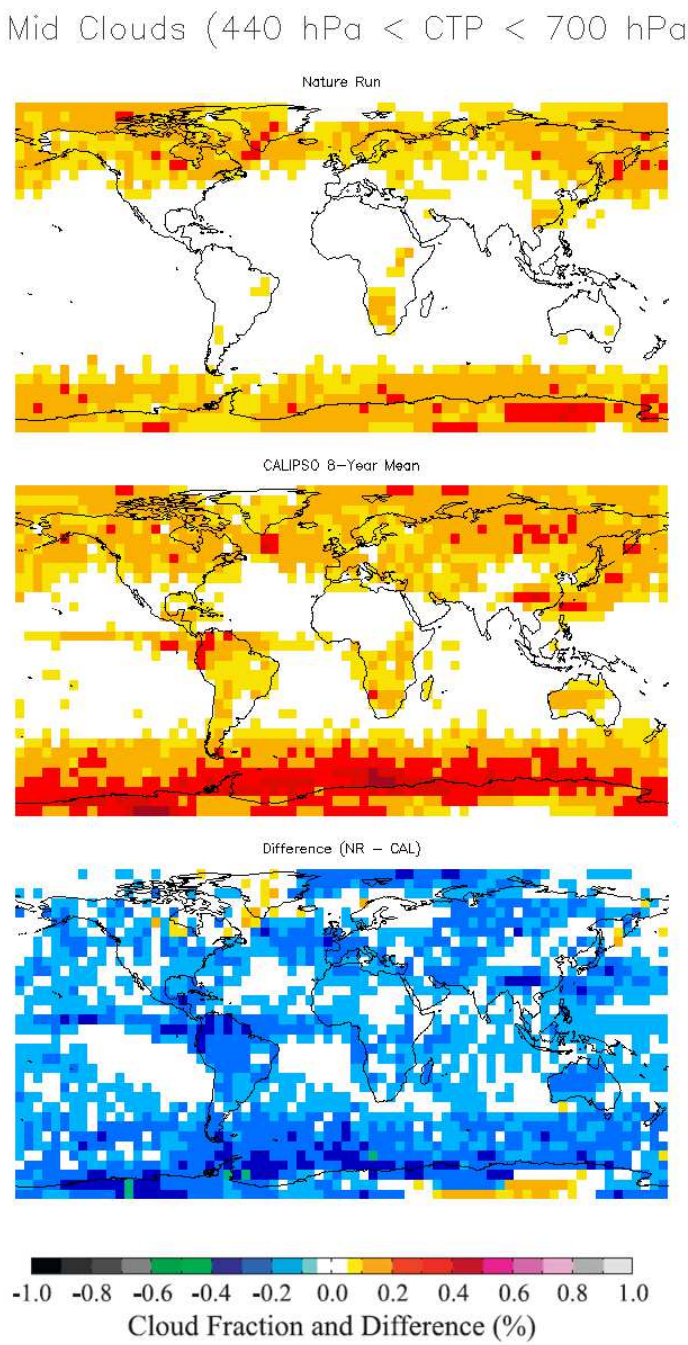

Figure 6.37: Same as Figure 6.35, but for mid-layer clouds (440 hPa < CTP < 700 hPa).

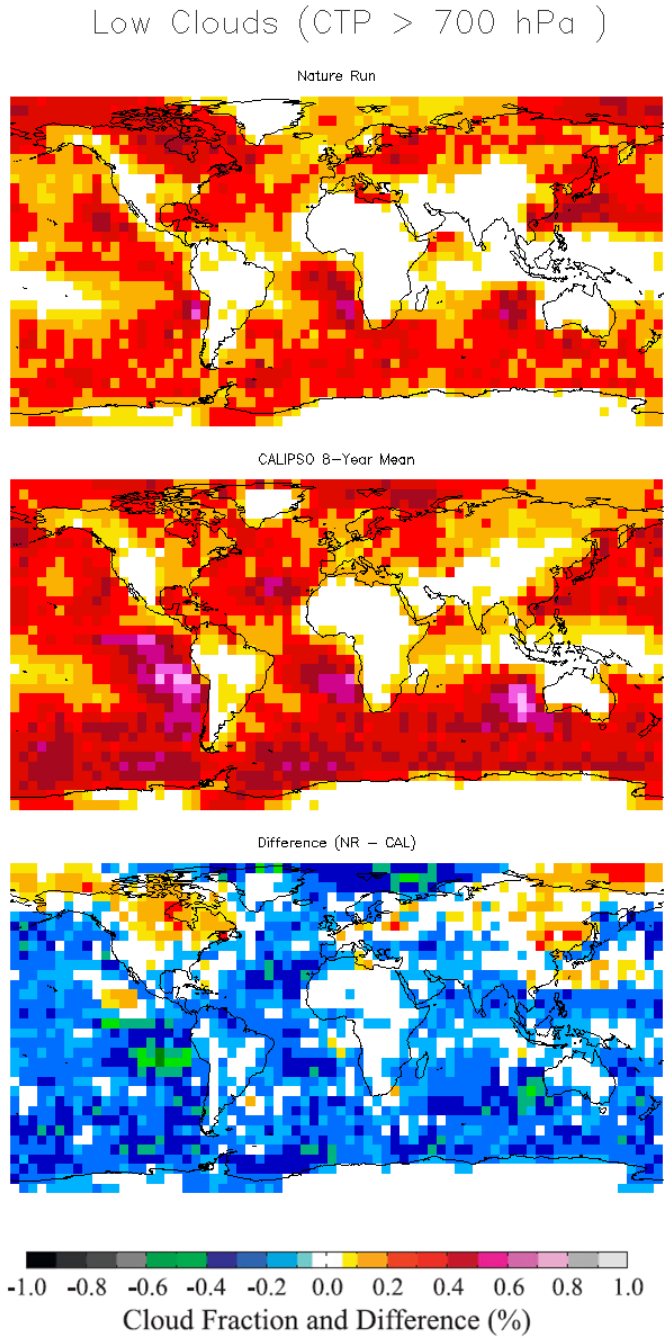

Figure 6.38: Same as Figure 6.35, but for low clouds (CTP > 700 hPa).

Chapter 7

Aerosols and Trace Gases

Lesley Ott, Anton Darmenov, Arlindo da Silva, Virginie Buchard and Krzysztof Wargan

Aerosols and atmospheric trace gases exert strong influences on both human health and climate. Satellite observations of aerosols and carbon monoxide have long been used by the scientific community to study the transport and fate of air pollution. Increasingly, satellite data are also playing a role in understanding air quality and its potential health impacts. Carbon dioxide and ozone observations are used to understand the distributions of these gases in the atmosphere and the processes governing them. While ozone observations have been available for over 30 years, carbon dioxide observations from satellites are relatively new. We expect that the high spatial resolution of the G5NR will aid users conducting studies to both better observe and model atmospheric trace gases and aerosols. In addition, because aerosols affect the ability to observe meteorological parameters, the realistic aerosol simulation provided by the G5NR should aid users with a wide variety of research goals. The following chapter provides an evaluation of the performance of aerosols and trace gases in the G5NR as well as recommendations for users.

7.1 Aerosols

Aerosols in the G5NR are simulated with an online version of the the Goddard Chemistry, Aerosol, Radiation, and Transport model (GOCART, Chin et al., 2002) and are radiatively active. Emissions of organic carbon (OC), black carbon (BC), sulfur dioxide (SO_2), carbon monoxide (CO) and carbon dioxide (CO_2) from biomass burning are from the Quick Fire Emissions Dataset (QFED) version 2.4-r6. The QFED methodology is based on the fire radiative power (top-down) approach and draws on the cloud correction approach utilized in the Global Fire Assimilation System (GFAS,

Kaiser et al., 2012). QFED, however, employs a more sophisticated treatment of non-observed land areas (Darmenov et al., 2014). Location and fire radiative power of fires are obtained from the Moderate Resolution Imaging Spectroradiometer (MODIS) Level 2 fire products and the MODIS Geolocation products. Volcanic emissions of SO_2 are prescribed following Diehl et al. (2012). Parameterization of sea salt production follows the formulation of size dependent number flux in Gong et al., 2003) but with a wind dependent term equal to $u_*^{2.41}$, where u_* is the friction velocity. Similarly to the work of Jaegle et al. (2011) we apply an independently derived SST correction term which modulates the strength of the emissions. More details on anthropogenic and biomass burning emissions and aerosol optical properties used in the G5NR are provided in Putman et al. (2014).

Evaluation of aerosols in the G5NR includes comparison with the aerosol climatology from the NASA/GMAO MERRA Aerosol Reanalysis (MERRAero, da Silva et al., 2012), statistics from the Aerosol Comparisons between Observations and Models (AeroCom) initiative and satellite observations. Evaluation mainly focuses on basic performance metrics that included residence times of tropospheric aerosols, aerosol optical thickness, composition and vertical distribution of the simulated aerosols.

7.1.1 Residence Times of Aerosols

To compare the net effect of aerosol properties and parameterizations of physical processes controlling the aerosol burden to other models, we compute the residence times of the aerosols in the G5NR simulation. Residence times and wet and dry removal rates are listed in Table 7.1. Also included in the table are the AeroCom multi-model mean parameters and their standard deviation reported in Textor et al. (2006). Residence times of sea salt (0.4 days), dust (4.2 days) and BC (7.3 days) agree very well with the AeroCom statistics. Residence time of OC in the G5NR Run is 5.33 days which is about one day less than the AeroCom mean value of 6.54 days but is well within one standard deviation from the reported mean. The residence time of sulfate aerosol is 2.7 days whereas the AeroCom mean and standard deviation are 4.12 days and 18, respectively. The shorter residence time in the G5NR simulation is due to relatively high wet removal rate of 0.34 $days^{-1}$. In comparison, the residence time of sulfate aerosol in GEOS-5 simulations performed at 0.5° horizontal resolution, with replayed meteorology and precipitation, were 3.4 days and 3.9 days - values which are at the lower range of the AeroCom results.

7.1.2 Aerosol Optical Thickness

Time series of global monthly mean aerosol optical thickness (AOT) are computed and compared with aerosol climatology from the MERRAero reanalysis. Monthly varying total and speciated global mean AOTs are shown in Figure 7.1. Results from the G5NR simulation are plotted as open

Residence times and removal rates of aerosols

Species	residence time (days)	dry removal rate (day^{-1})	Wet removal rate (day^{-1})
OC	5.33 (6.54 ± 27%)	3.55×10^{-2}	1.52×10^{-1}
BC	7.31 (7.12 ± 33%)	3.08×10^{-2}	1.06×10^{-1}
Sulfate	2.67 (4.12 ± 18%)	3.18×10^{-2}	3.43×10^{-1}
Sea-salt	0.42 (0.48 ± 58%)	1.13	1.24
Dust	4.22 (4.14 ± 43%)	1.55×10^{-1}	8.16×10^{-2}

Table 7.1: The accompanying residence times in parenthesis are the multi-model mean and standard deviation from the AeroCom initiative reported in Textor et al. (2006).

circles connected with solid black lines. The gray shaded area represents the range of minimum and maximum values from the MERRAero climatology. The mean and median values of the latter are plotted as solid and dashed gray lines.

The time series of the G5NR and the aerosol climatology are similar, which is expected, given the similarities in the primary emissions. On the other hand, differences in the annual mean AOTs due to OC, BC, sulfate and dust are clearly present. The observed similarities in the temporal patterns of the speciated AOTs enables us to derive global scaling factors for each of the aerosol species and also to assess how well tuned were the global magnitude of the wind driven and resolution dependent sea salt and dust emissions. Global scaling factors were computed from linear regression of the G5NR and MERRAero AOTs while constraining the intercept to zero. Because of the small sample size, we also computed global scaling factors as the ratio of the annual mean AOTs. The two methods resulted in very similar values. Here we report the scaling factors found from the linear regression of AOTs.

On a global scale, the AOT due to BC is 1.36 times smaller when compared to the aerosol climatology. Similarly, factors of 1.43 and 1.3 were computed for the OC and sulfate species. In contrast, dust AOT is overestimated by a factor of about 1.5 which suggests that magnitude of global dust emissions in simulations at similar horizontal resolutions needs to be reduced by a factor of about 0.7. Sea-salt AOT is underestimated slightly but the results suggest that scaling up the global magnitude of sea salt emissions by a factor of 1.08 will improve the sea salt burden. Our findings from the AOT comparison are summarized in Table 7.2.

The underestimated AOT due to BC, OC, sea salt and sulfate aerosols is compensated by the overestimated AOT from dust. The net effect is that the G5NR and the MERRAero reanalysis

Aerosol species	Scaling factor
OC	1.43
BC	1.36
Sulfate	1.30
Sea-salt	1.08
Dust	0.67

Table 7.2: Global aerosol scaling factors

agree very well in terms of total AOT on a global scale (Figure 7.1).

Early in the simulation (Figure 7.1), dust AOT is slightly higher than the aerosol climatology. As the simulation progresses, the dust AOT increases and then appears to stabilize, following the seasonal climatology pattern. This behavior suggests that the tuning of the strength of global dust emissions was performed over an insufficiently long period, which did not allow for the model physics and feedback mechanisms to adjust fully. Tuning of dust emissions in future global mesoscale simulations need to account for this behavior in order to reduce biases in dust loadings.

7.1.3 Spatial Patterns of AOT

Maps of annual- and seasonal-mean AOT from the G5NR and MERRAero are included in Figures 7.2 and 7.3. Time-averaged values were computed using model outputs for the time period December 2005 – December 2006. Comparison of the G5NR annual-mean total AOTs with MERRAero reveal very similar pattens of global aerosol loading. The overestimated dust emissions in the G5NR result in higher aerosol loading over Africa and along the westward transport route of Saharan dust. Similar observations are true for the regions affected by dust that originate from sources in the Middle East. In contrast, emissions from Asian dust sources result in very similar AOT. Over the oceans, the G5NR AOT tends to be lower compared to MERRAero. AOT is also lower over the land masses in the Northern Hemisphere.

In the winter months (DJF), dust mixed with smoke from fires results in slightly overestimated AOT in the Sahel region. Aerosol loadings across North America are similar. AOT in the West coast of USA is larger than the mean over the continent, mostly due to anthropogenic emissions in this region. AOT over East Asia are also very similar. In the Southern Hemisphere, MERRAero

AOT is spatially more uniform in comparison to the G5NR. In the G5NR simulation, regions affected by strong sea salt emissions are well defined and located between 45°S and 65°S.

In the spring (MAM) and summer (JJA) months, there are remarkable similarities in the spatial patters of AOT from the G5NR and the aerosols reanalysis. Aerosol loadings downwind of major fire sources in central and southern Africa, and South America are also very similar. In the fall (SON), the patterns of AOT due to smoke from fires in South America remain in a good agreement. MERRAero AOT in central Africa, Indonesia and the boreal forests of North America is slightly higher in comparison to the results from the G5NR.

7.1.4 Aerosol Speciation

We used the speciated AOT to compute the fractional contribution of individual aerosol species to the total AOT. The resulting maps of column integrated aerosol speciation are shown in Figure 7.4. The panels are organized by species (rows) and seasons (columns). Seasonal variations of OC and BC follow the active fire seasons. A high fraction of OC is observed over the major sources of fire emissions in sub-Saharan Africa, South America, North America and northern Eurasia. Maximum values of about 0.7 are observed in JJA and SON. Patterns of high sulfate fraction are associated with anthropogenic and volcanic sources of SO_2. Regions that are dominated by anthropogenic sulfate aerosols include the western US, Europe and China. The contribution of dimethyl sulfide (DMS), released naturally over oceans, peaks in the Southern Hemisphere during DJF when the sea salt emissions are relatively weak. The contribution of sea salt aerosol is large in the marine environments throughout the year especially in the Southern Hemisphere. In MAM and JJA sea salt fraction exceeds 0.7 over the regions with high sea salt emissions. Dust is the other major contributor to natural aerosols. It influences the aerosol burden in the Northern Hemisphere. It dominates the arid regions in Africa, Asia and Australia and downwind of dust transport routes.

Patterns of the column integrated aerosol speciation agree well with the major sources and transport routes of aerosol. Information about aerosol speciation (Figure 7.4) is easy to digest and compliments the global spatial distribution of AOT (Figure 7.3). It can provide guidance for end users of the aerosol products from the G5NR simulation about the aerosol composition.

7.1.5 Vertical Distribution

Aerosol mass mixing ratios were initialized to zero at the start of the G5NR simulation and therefore the vertical distribution and loadings of aerosols are not very realistic early in the simulation. A spin-up period of about two weeks is needed for the aerosols to reach realistic concentrations in the troposphere. Reaching equilibrium in the stratosphere requires a longer time period on the order of several months. Analysis of the time series of aerosol burden in the stratosphere (not shown) indicates that dust reaches equilibrium in approximately two months, whereas four to five months were needed for OC, BC and sulfate concentrations to stabilize. The short residence time of sea salt aerosol and effective wet removal processes restrict them to the lower atmosphere and inhibit vertical transport to the upper troposphere. Consequently the stratosphere is practically free of sea salt aerosol.

To investigate the model skill in representing the aerosol vertical distribution, we analyze zonal-mean aerosol mass concentration in the troposphere and low- to mid-stratosphere. Snapshots early in the simulation and one year later are shown in Figures 7.5 and 7.6. Mass concentrations plots are organized by species and time. Results about a month into the simulation are shown in the left column, and results from one year later are shown in the right column. Except for sea salt, aerosols exhibit a slight increase in concentration in the higher troposphere and lower stratosphere; however, there is no indication of excessive collection of aerosols in the mid and high stratosphere. Independently, we also examined the time series of aerosol burden in the stratosphere (not shown) and reached a similar conclusion.

The vertical distributions of OC and BC share similar features because of the similar patterns of anthropogenic and fire emissions. Concentrations in the Northern Hemisphere are higher than the Southern Hemisphere with a well pronounced collection of OC and BC over the north pole driven by transport from mid-latitude regions.

The concentration of sulfate aerosol near the surface follows the major sources of anthropogenic and fire emissions in the Northern Hemisphere and DMS emissions in the Southern Hemisphere. A poleward transport and collection at the poles is also evident. The observed high concentrations in the stratosphere near the equator one year into the simulation were traced back to volcanic activity. Compared to the carbonaceous aerosols, the concentration of sulfate is higher in the stratosphere.

Dust and sea salt concentrations are largest near the surface which reflects the injection of freshly emitted particles in the surface model layer. Concentrations of sea salt reflect the pattern of strong wind driven emissions along mid-latitude storm tracks and frontal systems in the Southern Ocean. Deeper boundary layers over source regions and less effective wet removal result in high dust concentrations in the upper troposphere and low stratosphere driven by vertical transport due to the general circulation patterns.

7.1.6 Comparison with CALIOP Retrievals

In this section, we analyze the vertical distribution of the simulated aerosols and perform a qualitative comparison with data from the Cloud Aerosol Lidar with Orthogonal Polarization (CALIOP), carried by CALIPSO as part of the NASA A-Train (Winker et al., 2007, 2010). We use CALIPSO's level 1.5 profile product (i.e., 'expedited') adapted for forecasting applications, that have been cloud-cleared (Vaughan et al., 2011).

We focus our analysis on two different specific regions dominated by dust and biomass burning aerosols. For the dust case study, we chose an area over the Sahara and the North Atlantic Ocean (60°W – 20°E, 0°N – 30 °N) during the month of July. For biomass burning aerosols, we select a region over southern Africa (10 °W – 30 °E, 0 °S – 30 °S) to analyze during the month of July.

Figure 7.7 shows monthly mean comparisons between CALIOP and the G5NR-derived attenuated backscatter at 532 nm over the Saharan dust region for the month of July 2006 for the model and July 2011 for CALIOP. For the sake of comparison, the molecular scattering was removed from the CALIOP profiles. This comparison should be approached as qualitative because of the differences in the data collection times due to CALIOP's level 1.5 data availability, and also note that the G5NR has not been sampled along the CALIPSO orbit track.

We can see that the G5NR and CALIOP have a similar vertical structure with a dust plume that extends up to a little bit above 6 km for CALIOP and around 6 km for the G5NR over the Saharan region and descends as it travels west to the Caribbean over a shallow marine aerosols layer. However, when looking at the magnitude of the attenuated backscatter coefficient, we can see that the simulated signal of the G5NR is higher than the CALIOP estimates for the dust plume. For the marine aerosols layer, the attenuated backscatter coefficient is generally in the range of

CALIOP values, except at some longitudes where the G5NR values appear to be lower. As seen previously, these discrepancies in the magnitude of the signal might be explained by an excess of dust and slightly underestimated sea salt emissions in the model. Applying the AOT derived factors moderately improved the comparison (not shown).

Figure 7.8 shows comparisons similar to the ones on Figure 7.7 but over the southern Africa biomass burning region. We can see a similar vertical structure between the G5NR and CALIOP. The smoke plume extends up to 4 km above a marine aerosol layer that can reach an altitude around 1.5 km for both the model and CALIOP. While the magnitude of the simulated signal for the smoke plume is in the range of the CALIOP estimates, the simulated signal for the marine aerosol layer tends to be weaker. Applying the coefficients suggested above does not improve the comparison (not shown), suggesting that the modeled sea salt emissions in this region are very weak.

7.1.7 Summary and Recommendations

In this investigation, the aim was to assess the quality of aerosols in the 7-km GEOS-5 G5NR global mesoscale AGCM simulation with interactive aerosol chemistry. Analysis of tropospheric residence times, aerosol optical thickness and vertical distribution of aerosols indicates that the skill of the G5NR simulation to produce realistic aerosols is very good (Figure 7.9). The following conclusions and recommendations can be drawn from the present evaluation:

- The G5NR AOT reproduced well the spatial and temporal patters of AOT from the MERRAerosol reanalysis. The observed similarities in the AOT patterns enabled us to derive global factors for each of the aerosol species (see Table 7.2) that can be applied to scale the predicted aerosol mass mixing ratios and improve the agreement with the aerosol reanalysis.
- The vertical distribution of tropospheric aerosols in the G5NR simulation agreed well with CALIOP profiles. We found that the aerosol load in the stratosphere tends to increase as the simulation progresses, but there does not appear to be excessive accumulation of aerosols in the upper stratosphere during the simulated time period. For simulations involving aerosols in the high troposphere and low- and mid-stratosphere we recommend to use model output in the second half of 2006 and onwards.
- Users of the instantaneous aerosol fields at 7-km horizontal resolution need to be aware that

there are indications of unrealistically high aerosol loadings at times in isolated grid cells. Examination of the instantaneous aerosol loading at 7-km horizontal resolution revealed that in some instances AOT can exceed values of 10. The simulated extreme AOT values were associated with strong emissions from fires or from anthropogenic sources of sulfate aerosol.

7.2 Trace Gases

7.2.1 CO

Atmospheric carbon monoxide (CO) is an important air pollutant who presence can affect human health, the production of tropospheric ozone, and the oxidizing capacity of the atmosphere. The 1-2 month lifetime of CO also makes it a useful tracer for atmospheric transport. A simplified version of CO chemistry, described in Ott et al. (2010), was used in the G5NR to increase computational efficiency. Detailed descriptions of emissions are given in Putman et al. (2014). Biogenic and methane sources of CO are taken from coarse resolution chemical transport model simulations while biomass burning and fossil fuel emissions were produced at 0.1° in order to introduce spatial heterogeneity into the simulations.

G5NR CO mixing ratios were evaluated using a combination of surface and satellite observations. NOAA's Earth System Research Laboratory (ESRL) maintains a global network of remote surface sites that measure CO and CO_2 mixing ratios weekly. Figure 7.10 shows a map of sites operational during the 2005-2007 G5NR period. For comparison to surface stations, the GEOS-5 grid cell containing each station location was sampled at the time that an observation was collected and simulated CO mixing ratios then vertically interpolated to the altitude of the observing station. Observations and pseudo-data are averaged over the course of a day (when multiple observations are present) and daily simulated and observed CO mixing ratios at six stations representing a variety of latitudes are shown in Figure 7.11. In general, the G5NR tends to underestimate CO at extratropical northern hemisphere stations with the largest underestimates occurring during spring months. This is evident in Figure 7.11 at Ny Alesund, Sweden (ZEP) and Cold Bay, Alaska (CBA). Underestimates of this magnitude are common in CO simulations as demonstrated by Shindell et al. (2006) who compared fields generated by 26 chemical transport models using an earlier version of the EDGAR inventory. Based on an analysis of radon and CO observations over the western North Pacific, Wada et al. (2012) suggest that the version of EDGAR used in this study may

underestimate emissions over China by as much as 45%.

These underestimates can be significantly improved through application of an empirically derived bias correction based on latitude and the simulated mixing ratio given by

$$CO_{corr}(lat, CO_{sim}) = CO_{sim} - 28.2 - 0.28 \times lat + 0.4 \times CO_{sim} + 0.0032 \times lat \times CO_{sim}$$

where CO_{corr} is the bias corrected value, CO_{sim} is the G5NR simulated CO value, and lat is the latitude of the simulated value. As shown in Figure 7.11 and Figure 7.12, the bias correction improves the model result at extratropical northern hemisphere stations by reducing the large negative bias; performance at southern hemisphere tropical and subtropical stations is slightly degraded as the bias correction causes larger underestimates.

Satellite observations of CO are provided by a number of satellites with the longest and most complete observational record provided by thermal infrared (TIR) observations from MOPITT and AIRS, which have peak sensitivity in the mid-troposphere. Newer releases of MOPITT also include retrievals from near infrared (NIR) observation (Deeter et al., 2012), which have greater sensitivity near the surface. MOPITT version 6, level 3 monthly mean observations are compared to simulated CO from the G5NR by first regridding model output from the native 7-km resolution to the 1° MOPITT grid. Model profiles are then averaged over each month, interpolated to MOPITT pressure-defined layers, and convolved with the MOPITT averaging kernel and a priori profiles following Deeter et al. (2012).

Comparisons between observed and simulated mid-tropospheric CO for April and October (Figure 7.13) show that the model tends to underestimate CO in the northern hemisphere mid-troposphere during spring, consistent with the comparison with surface observations. In the mid-troposphere, this underestimate is slightly improved with the bias correction derived from surface model data comparisons, but the improvement is limited. The model succeeds in capturing the major features of the MOPITT observations, including a strong gradient between northern and southern hemisphere due to fossil fuel emissions, and biomass burning over Africa and South America. During October, 2006, model-data discrepancies are smaller in most regions relative to April, though the model strongly underestimates the influence of Indonesian fire emissions in the mid-troposphere. This is likely because of an underestimate in emissions, which are particularly

difficult to estimate for the type of peat fires that occurred over Indonesia during 2006 (e.g. Ott et al., 2010). The QFED emissions used in the G5NR, which rely on fire radiative power, may underestimate emissions that occur during the smoldering phase of fires or when fires are obscured by particularly thick aerosol loading.

Figure 7.14 shows comparisons of monthly zonal mean MOPITT observations of CO with those from the two-year duration of the G5NR. In the mid-troposphere, GEOS-5 reproduces the major features of the observed distribution with the exception of underestimates in extratropical northern hemisphere CO during spring. Underestimates of 40 ppbv are of similar magnitudes to surface underestimates indicating that they are not likely to be a result of transport errors, but are more likely associated with underestimates in fossil fuel emissions derived from the EDGAR inventory. Comparisons against NIR column CO observations indicate that the G5NR underestimates northern hemisphere spring CO by 10%. MOPITT NIR column CO is also characterized by maxima slightly south (north) of the equator in September (December) caused by biomass burning emissions in South America (Africa). GEOS-5 reproduces both the timing and location of these biomass burning features well, though their magnitude is slightly underestimated.

Comparisons with surface and MOPITT observations demonstrate that the performance of the G5NR in reproducing observed distributions of atmospheric CO is similar to many contemporary chemical transport models. Models in general, and the GEOS-5 G5NR, tend to underestimate extratropical northern hemisphere CO. This is typically attributed to underestimates in fossil fuel emission inventories such as EDGAR. The use of archived hydroxyl radical fields used to calculate CO loss may also contribute to underestimates. As its performance is similar to other chemical transport models, the G5NR CO fields should be suitable for most uses. For applications particularly interested in northern hemisphere and/or anthropogenic CO emissions, users may wish to apply a bias correction. The bias correction provided significantly improves model results at remote surface sites, though its impact is limited in comparisons with MOPITT observations because of the influence of a priori information.

7.2.2 CO_2

Carbon dioxide (CO_2) is the greenhouse gas most strongly influenced by anthropogenic emissions. While contemporary fossil fuel emissions are considered to be reasonably well constrained, land and

ocean carbon fluxes are less well understood leading to large uncertainties in model projections of climate change over the coming century. In the G5NR, fossil fuel and biomass burning emissions, and land fluxes are prescribed and provided at 0.1° resolution in order to introduce spatial heterogeneity into the simulations. Ocean fluxes are computed within GEOS-5 using as input ocean partial pressure of CO_2 (provided at 1° resolution from NASA's Ocean Biogeochemical Model; Gregg et al., 2013) and G5NR-simulated 10-meter wind speeds and atmospheric CO_2. Detailed descriptions of emissions are given in Putman et al. (2014).

G5NR CO_2 mixing ratios are evaluated primarily through comparison with surface observing stations. Figure 7.15 shows simulated and observed CO_2 mixing ratios at the same 6 stations shown for CO in Figure 7.11. At northern hemisphere stations, the seasonal cycle in atmospheric CO_2 is driven primarily by the seasonal cycle in land biosphere flux, which is characterized by drawdown by plants during summer months and release of CO_2 from decaying vegetation during winter. G5NR CO_2 mixing ratios reproduce observations well at these stations, represented here by ZEP, CBA, and Mauna Loa (MLO). Model performance is also reasonable at southern hemisphere mid- and high latitude stations, represented by Crozet Island (CRZ) and Palmer Station, Antarctica (PSA). At these locations, seasonal variations in CO_2 tend to be much weaker because they are farther removed from the bulk of biomass flux and anthropogenic emissions. The largest CO_2 discrepancies in the G5NR occur at tropical ocean locations, represented here by Ascension Island (ASC), located in the Atlantic Ocean between Africa and South America. Here, the simulation underestimates CO_2 by 3-4 ppmv throughout the 2-year simulation. Figure 7.16 shows that this underestimate is characteristic of the majority of remote tropical stations. These underestimates are likely associated with a stronger ocean sink in this region than indicated by observation-based estimates from Takahashi et al. (2002, 2009) and by ensemble-based budget estimates from Le Quere et al. (2013). Because ocean flux is calculated online in the G5NR using the square of the 10-meter wind speed, it can be strongly influenced by wind differences between the simulated and observed atmospheres. As noted in previous chapters, some characteristics of the ITCZ differ substantially from observations which is likely contributing to the underestimate in CO_2 at remote marine sites.

Because of the high degree of accuracy required for useful measurements, the availability of satellite observations of CO_2 is more limited than for CO. Several instruments, including AIRS and TES, provide information on CO_2 variability in the mid- and upper troposphere, but these observations capture little of the information about surface fluxes that is of primary interest (Ott et al., 2014,

submitted). SCIAMACHY provided NIR observations of CO_2 from 2003 through 2012 which provided greater sensitivity to near surface CO_2 mixing ratios, but measurements were characterized by scatter and systematic biases that limited their utility (Breon and Ciais, 2010). The Japanese Greenhouses gases Observing SATellite (GOSAT, Kuze et al., 2009), launched in June, 2009 provides increased reliability and sensitivity to near surface CO_2, though data are sparse because of an inability to observe in the presence of clouds. Several different retrievals of column averaged CO_2 dry air mole fraction (XCO_2) based on GOSAT observations are currently being produced. In this work, we use data produced by NASA's Atmospheric CO_2 Observations from Space (ACOS) effort, a collaboration between the original JAXA GOSAT team and NASA's Orbiting Carbon Observatory (OCO) science team (Crisp et al., 2012). These data are produced using a modified version of the OCO retrieval algorithm applied to GOSAT observed spectra as described in O'Dell et al. (2012) and have been validated extensively. Dated used here are ACOS version 3.4.

Because observations were not available during the 2005-2007 period, we created a monthly climatology to evaluate the ability of the G5NR to reproduce observed spatial patterns of XCO_2. Monthly means were calculated from 2009 through 2013, detrended to remove the annual increase in global CO_2 mixing ratio, and then averaged. The G5NR is compared by calculating monthly mean fields, detrending, and then applying a global adjustment of 6.5 ppmv to account for the difference between 2005 and 2009 atmospheric mixing ratios. Figure 7.17 shows comparisons of simulated CO_2 with the GOSAT climatology for February and August. While the G5NR cannot be expected to exactly match the GOSAT observations, which represents different years and weather features, the spatial distributions of XCO_2 in the simulation and observations are quite similar. Disparities between simulated and observed tropical ocean CO_2 found at the surface are not evident in the column. Figure 7.18 shows the seasonal cycle of zonal mean ACOS XCO_2 and XCO_2 from the G5NR. The simulation also reproduces the major features of the seasonal cycle of XCO_2 well.

Comparisons between surface observations and G5NR CO_2 show that the model effectively reproduces observed time series at remote locations in the extratropics of both hemispheres. The largest model-data discrepancies are found at tropical ocean locations and result from the coupled ocean flux calculation included in the simulation. These are likely caused by differences in near surface ITCZ wind speeds. While reliable satellite CO_2 observations have only recently become available, comparisons between G5NR XCO_2 and a climatology compiled from 4 years of detrended GOSAT observations shows the model reproduces observed spatial and seasonal variations well.

7.2.3 O_3

The G5NR produces 3-dimensional ozone fields subject to advection by the model winds and relaxation to a prescribed time-dependent zonal climatology with a relaxation time of three days. The climatology used here is described in Cionni et al. (2011).

A typical wintertime ozone map at 100 hPa is shown in Figure 7.19 along with Ertel's potential vorticity (EPV) from the model. The figure illustrates that the morphology of the ozone field exhibits a large-scale structure similar to that seen in EPV. Because of the uniform and relatively short (especially in the lower stratosphere and troposphere) relaxation, only large-scale features in ozone can develop in the G5NR. Fourier analysis reveals that, in terms of power spectra, ozone variability is up to 10 times less than in GMAO's operational analyses for wave numbers greater than 10. Therefore, this analysis focuses on assessing the realism of the representation of ozone fields in terms of monthly and spatial averages.

Monthly maps of total ozone (not shown) display a realistic distribution and seasonal cycle with maximum values in the boreal spring in high latitudes, elevated ozone over Alaska and north-eastern Russia, low values over Antarctica in austral spring accompanied by a wave one ozone crescent feature with the maximum located south of Australia.

Figure 7.20 shows the difference between the monthly zonal mean total ozone from the G5NR and a climatology derived from the Ozone Monitoring Instrument (OMI) on the EOS-Aura satellite. The climatology was obtained by averaging the OMI data in each calendar month between 2005 and 2013. In the tropics and in the northern hemisphere the overall agreement is quite good. The differences are typically less than 3% and never greater than about 10%. In the southern high latitudes the agreement is also within 10%. However, the Antarctic spring ozone depletion is underestimated (relative to the OMI climatology) by up to 40%.

We will now discuss the vertical distribution of zonal mean ozone in the G5NR. We use a climatology computed by averaging monthly data from the Microwave Limb Sounder onboard Aura (MLS) over the period of 9 years from 2005 to 2013. Version 3.3 of MLS retrievals is used. We begin the discussion with June 2006 as this is when the G5NR departs from the MLS data more than in other months. Figure 7.21 shows the zonal mean G5NR ozone mixing ratio and the corresponding MLS climatology. The two data sets match each other very closely everywhere except in

the winter upper stratosphere where the G5NR ozone is less than MLS by up to 1 ppmv (15%) and around the tropical ozone maximum, which is sharper than in MLS and slightly shifted upward. The underestimation in the upper stratosphere is caused by the model meridional circulation pushing the climatological ozone isopleths downward. We note that the climatological profile (not shown)is indeed closer to the MLS climatology than the resulting profile in Figure 7.21, indicative of a downward motion. The Brewer-Dobson circulation is the strongest in winter hemispheres, consistent with the observation that the upper-stratospheric low bias in the G5NR ozone is most pronounced during winter. The shape of the tropical ozone maximum in the G5NR is the same as in the climatology used in the model. We note that the G5NR ozone in other months also exhibits a low bias in the upper stratosphere in the middle latitudes but the bias is less pronounced. There is an overall excellent agreement between these data sets in the lower stratosphere and everywhere in the summer stratosphere.

Finally, we note that, while the vertical structure of the tropospheric ozone is not expected to be realistic in the G5NR, the seasonal cycle of the tropospheric ozone column (not shown) is well represented with the maximum values of about 60 Dobson Units in northern high latitudes in spring and early summer.

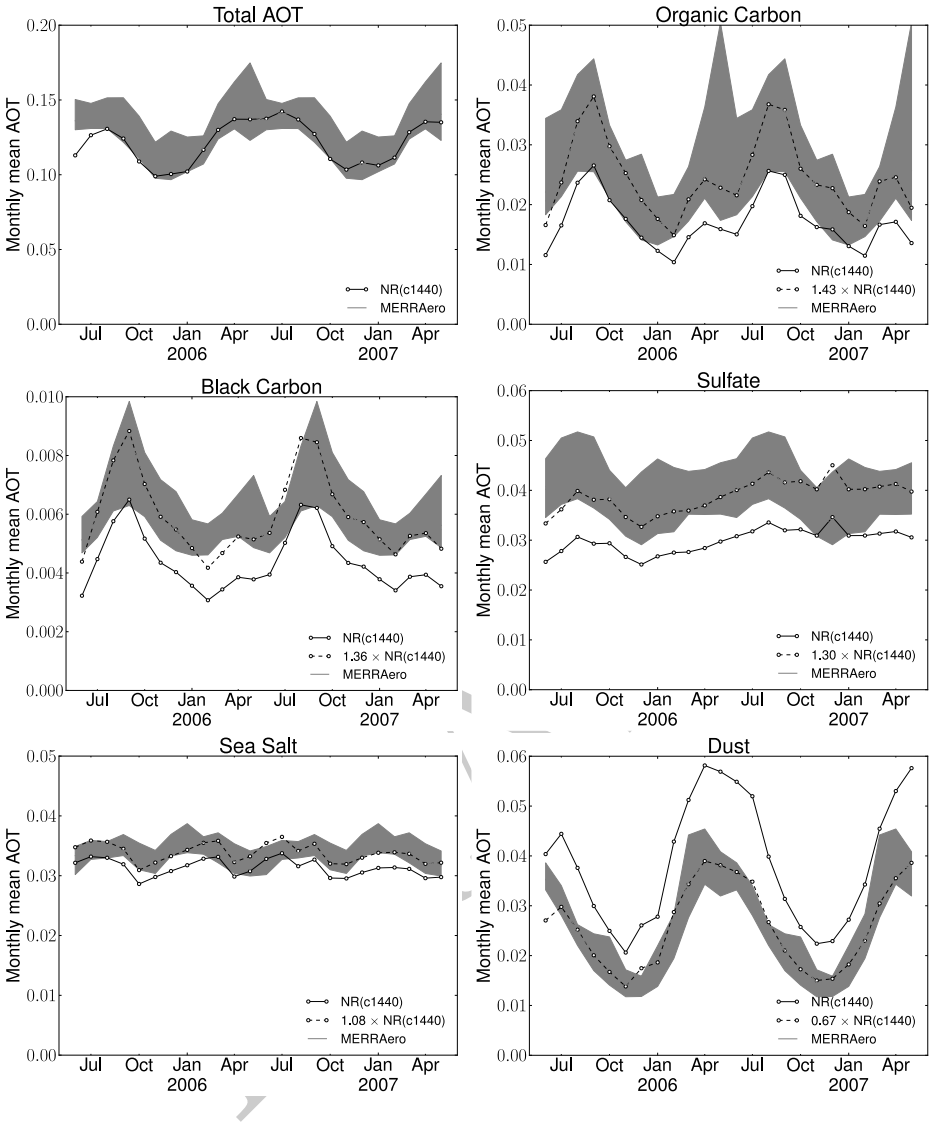

Figure 7.1: Time series of global monthly mean aerosol optical thickness. Results from the G5NR run are shown as open circles connected by solid black lines. Monthly aerosol climatology from the MERRAero aerosol reanalysis is shown in gray - the shaded area enclose the minimum and maximum values, solid and dashed lines depict mean and median values.

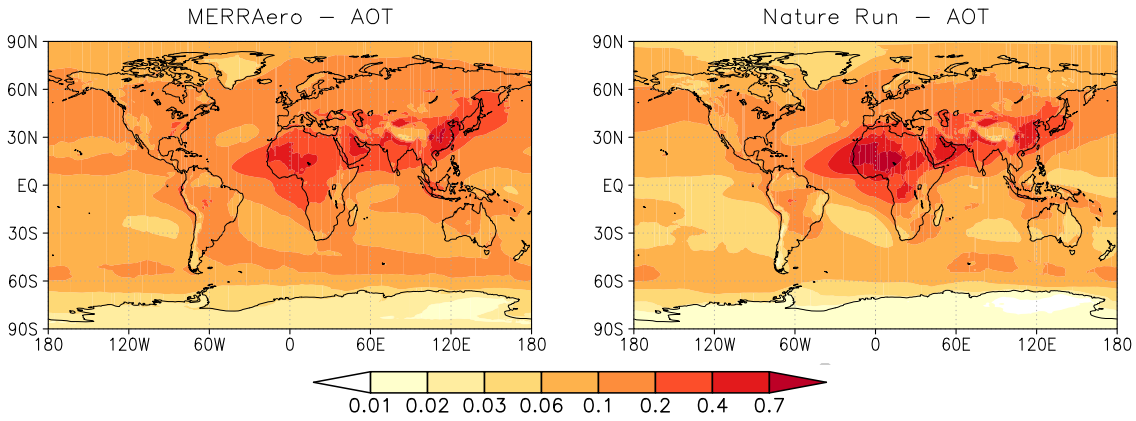

Figure 7.2: Annual-mean AOT from the MERRAero aerosol reanalysis (left panel) and the G5NR simulation (right panel).

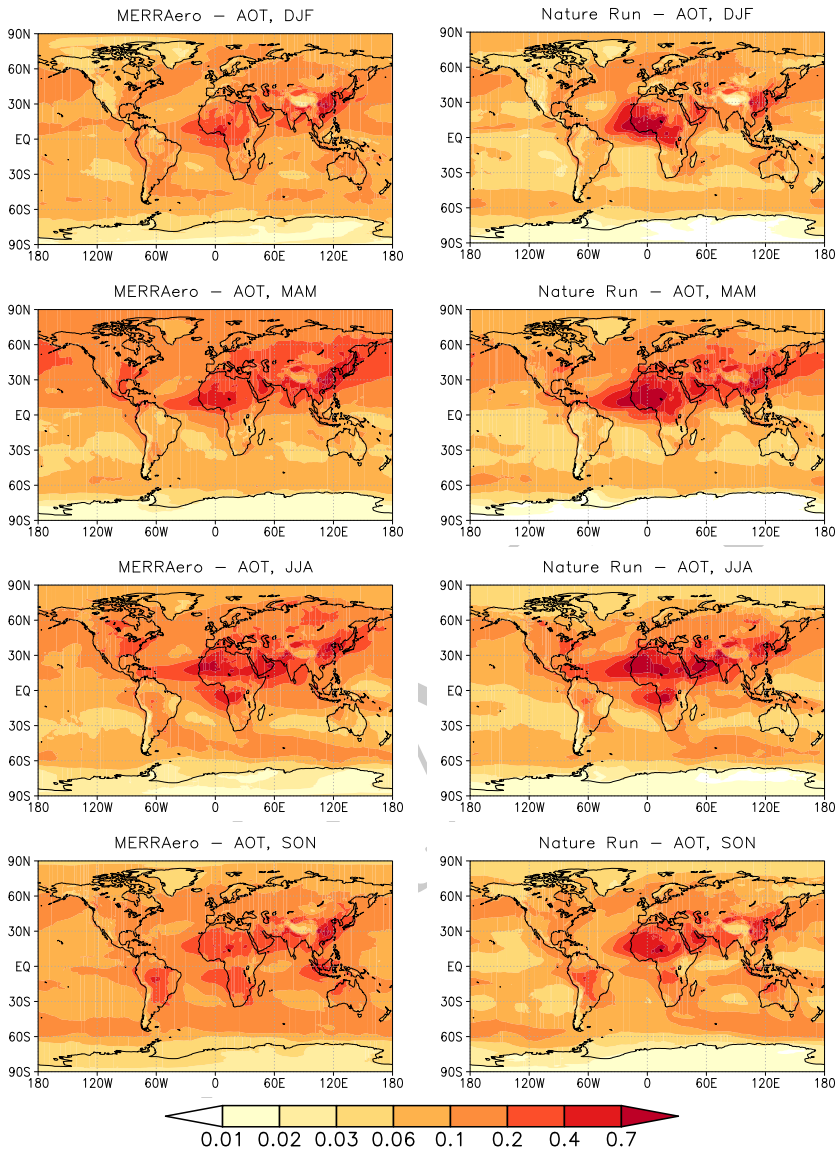

Figure 7.3: Seasonal-mean AOT from the MERRAero aerosol reanalysis (left column panels) and the G5NR simulation (right column panels). Time-averaged values for DJF, MAM, JJA and SON in 2006 are organized in rows from top to bottom.

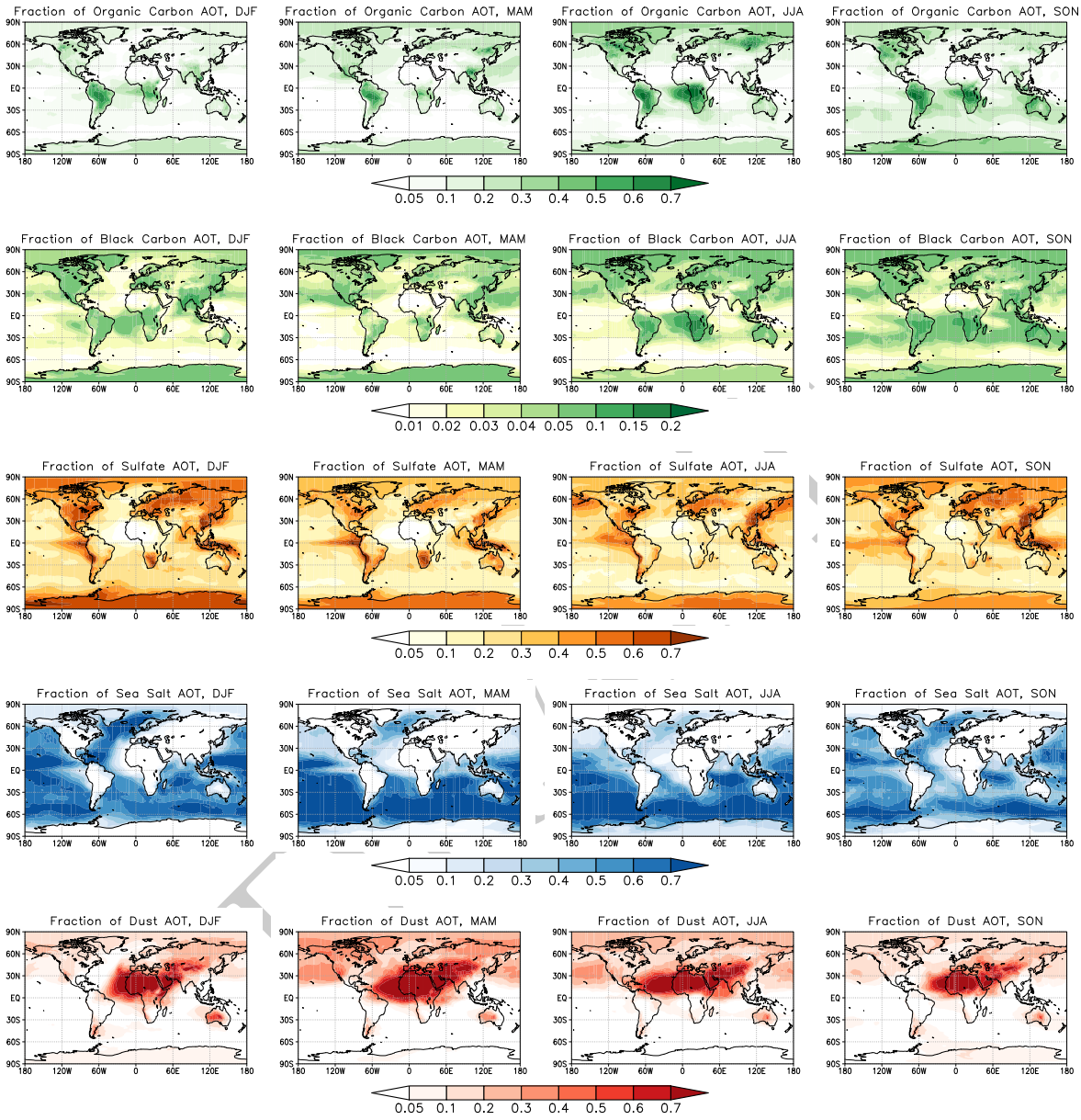

Figure 7.4: Seasonal variations of aerosol speciation based on the fractional contribution to total AOT. From left to right are shown maps for DJF, MAM, JJA and SON, and from top to bottom are maps for OC, BC, sulfate, sea salt and dust.

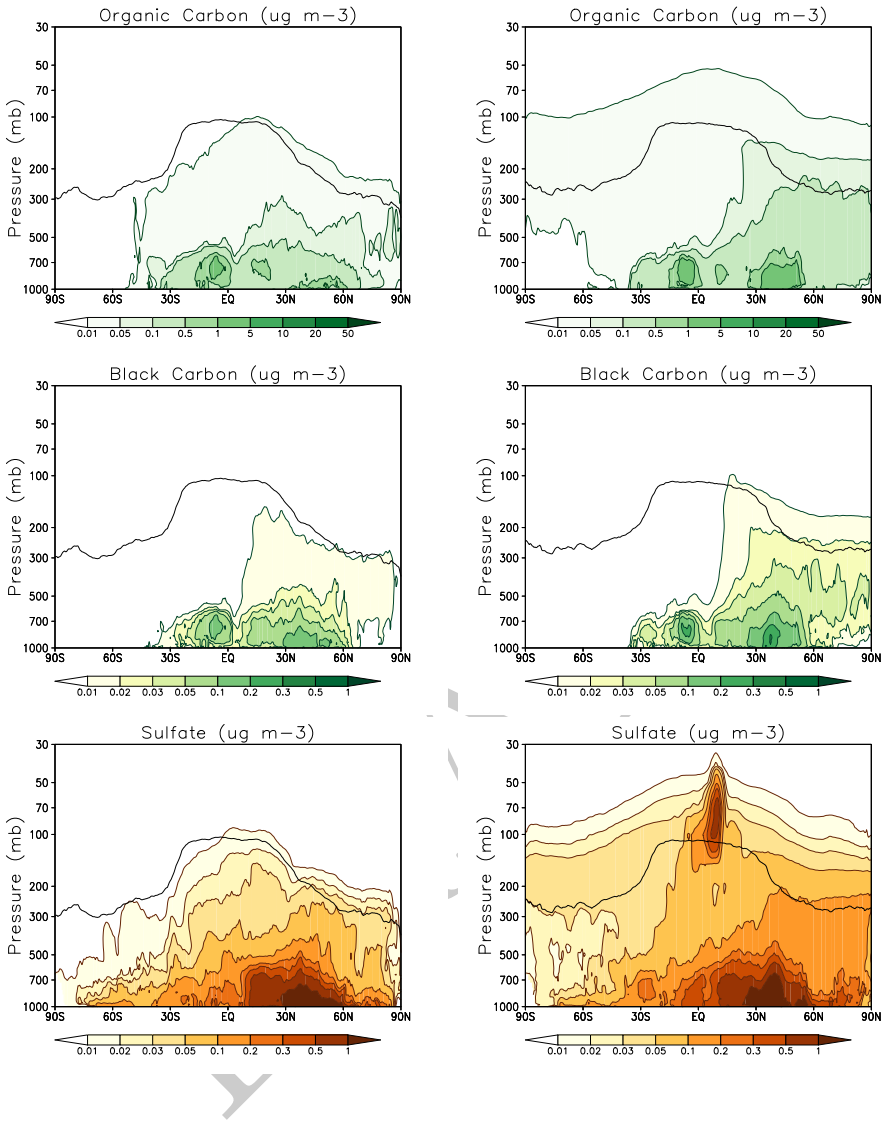

Figure 7.5: Zonal mean mass concentrations of (top to bottom) OC, BC, sulfate and aerosols early into the simulation (left column) and one year into the simulation (right column). Also shown in each panel is the zonal-mean tropopause height as a solid black line.

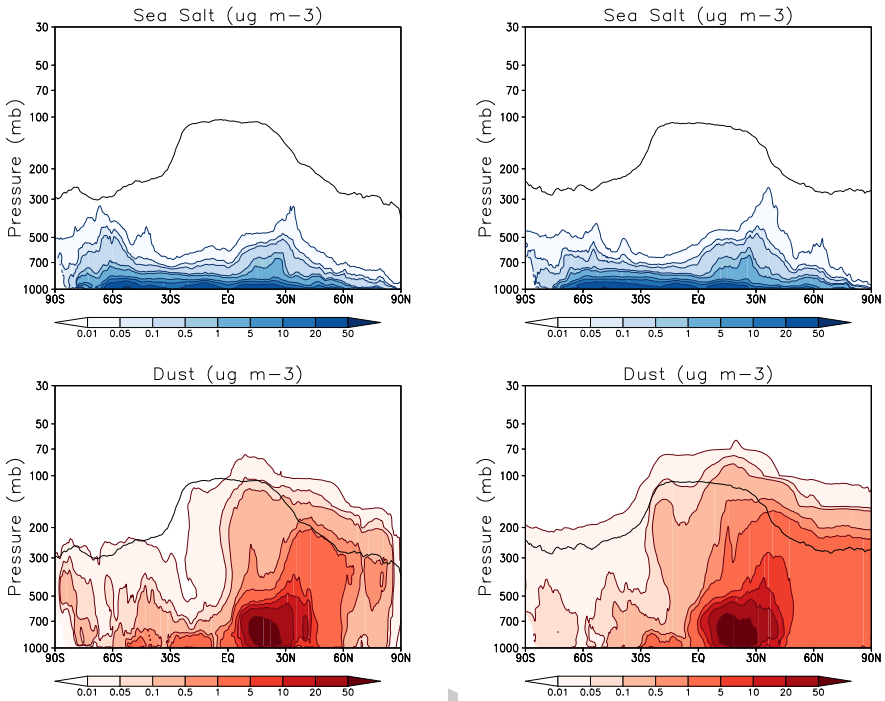

Figure 7.6: Similar to Figure 7.5 but for sea salt (top) and dust (bottom).

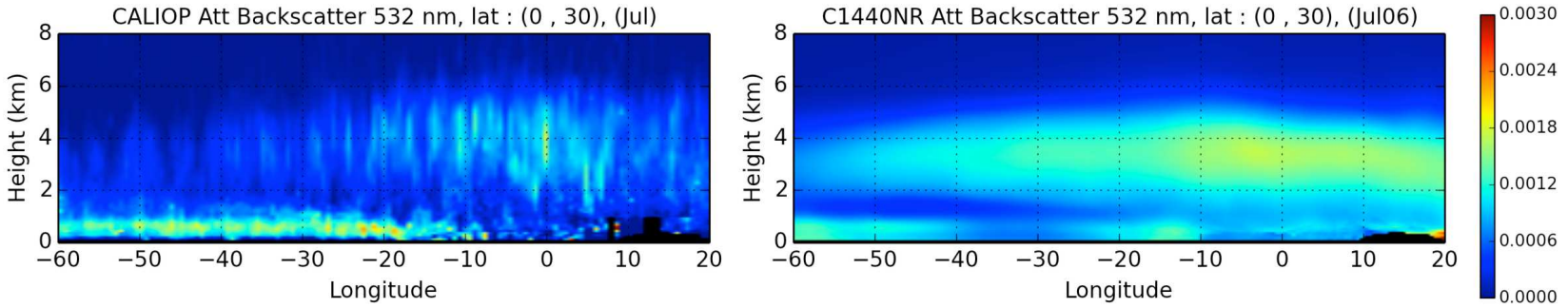

Figure 7.7: Vertical profiles of attenuated backscatter coefficient only due to aerosols at 532 nm over the African dust region (60°W–20°E, 0°N–30°N). On the left are time-averaged retrievals from CALIOP for July 2011. On the right are results from the G5NR simulation but for July 2006.

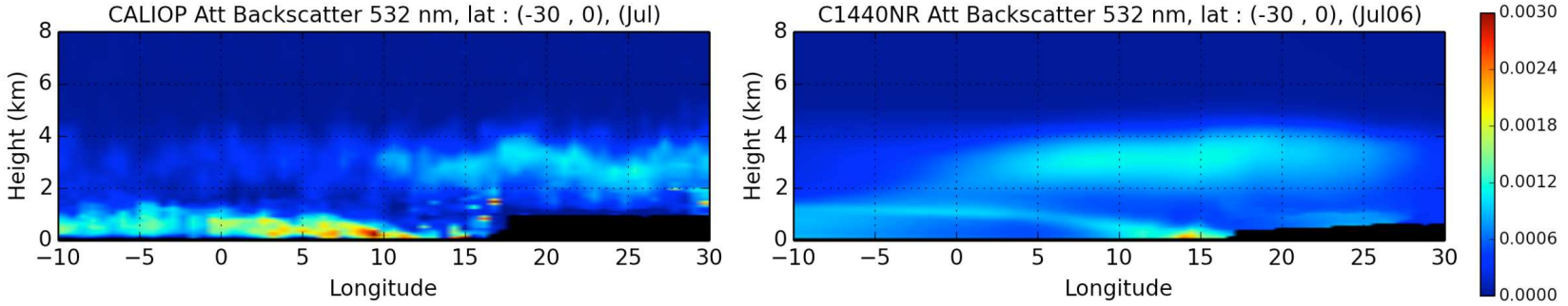

Figure 7.8: Same as Figure 7.7 but for the southern Africa biomass burning region (10°W–30°E, 0°S–30°S).

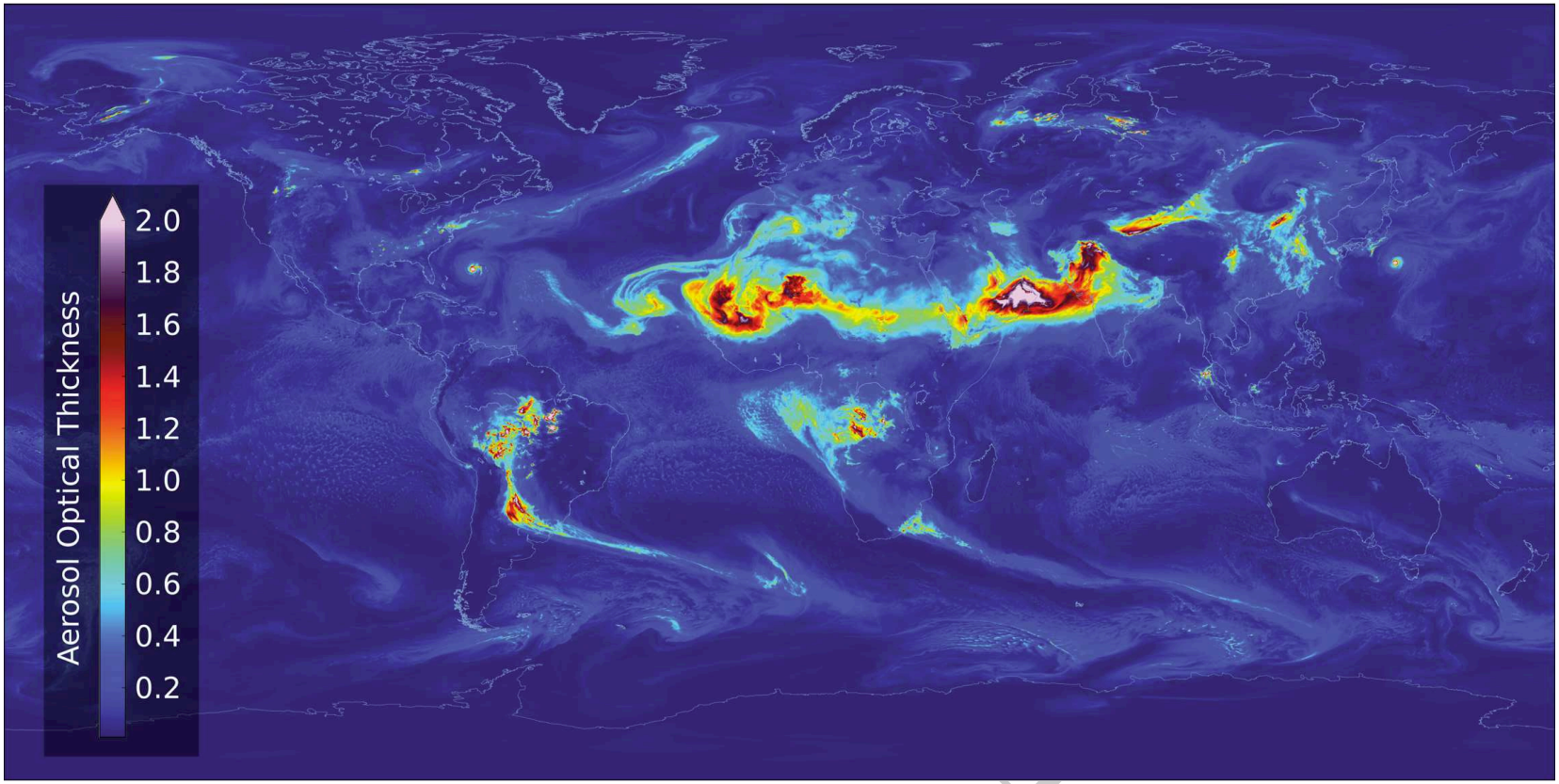

Figure 7.9: Global distribution of AOT from the G5NR simulation on 8 Aug 2005 00UTC. The image shows long range transport of smoke from fires in Africa, South America and Alaska; Saharan dust off the West coast of Africa and Europe; pollution in Asia, Europe and the USA.

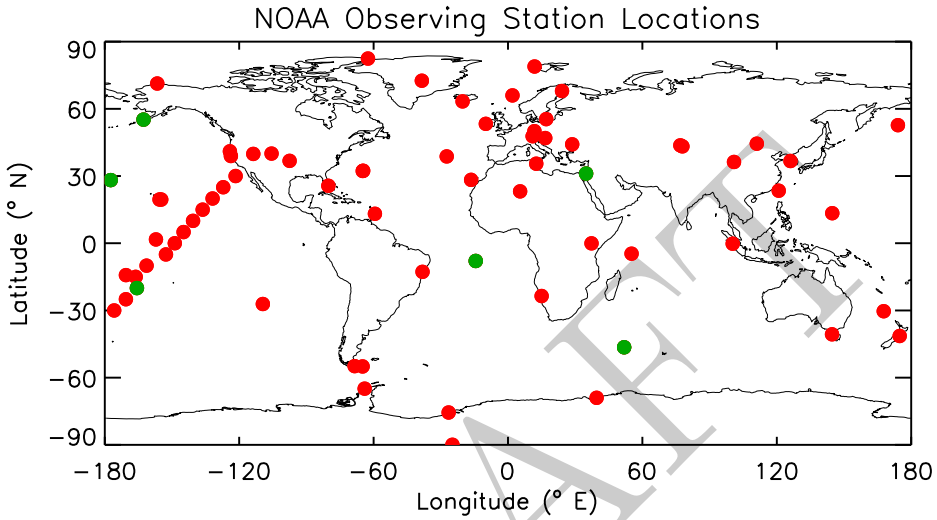

Figure 7.10: Map of NOAA surface trace gas observing stations (red). Sites shown in Figures 7.11 and 7.15 are indicated by green dots.

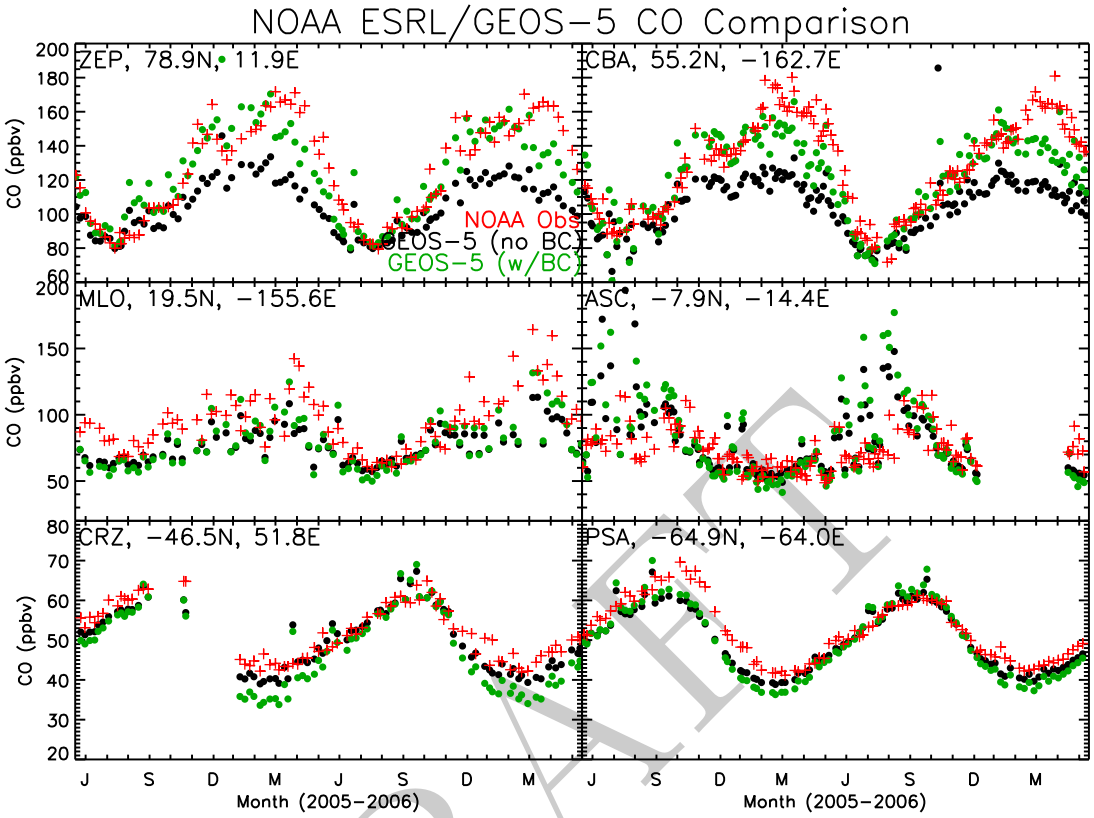

Figure 7.11: .

Simulated and observed surface CO (ppbv) at NOAA stations indicated on Figure 7.10. Red crosses indicate observations while black (blue) dots show model results without (with) a bias correction applied.

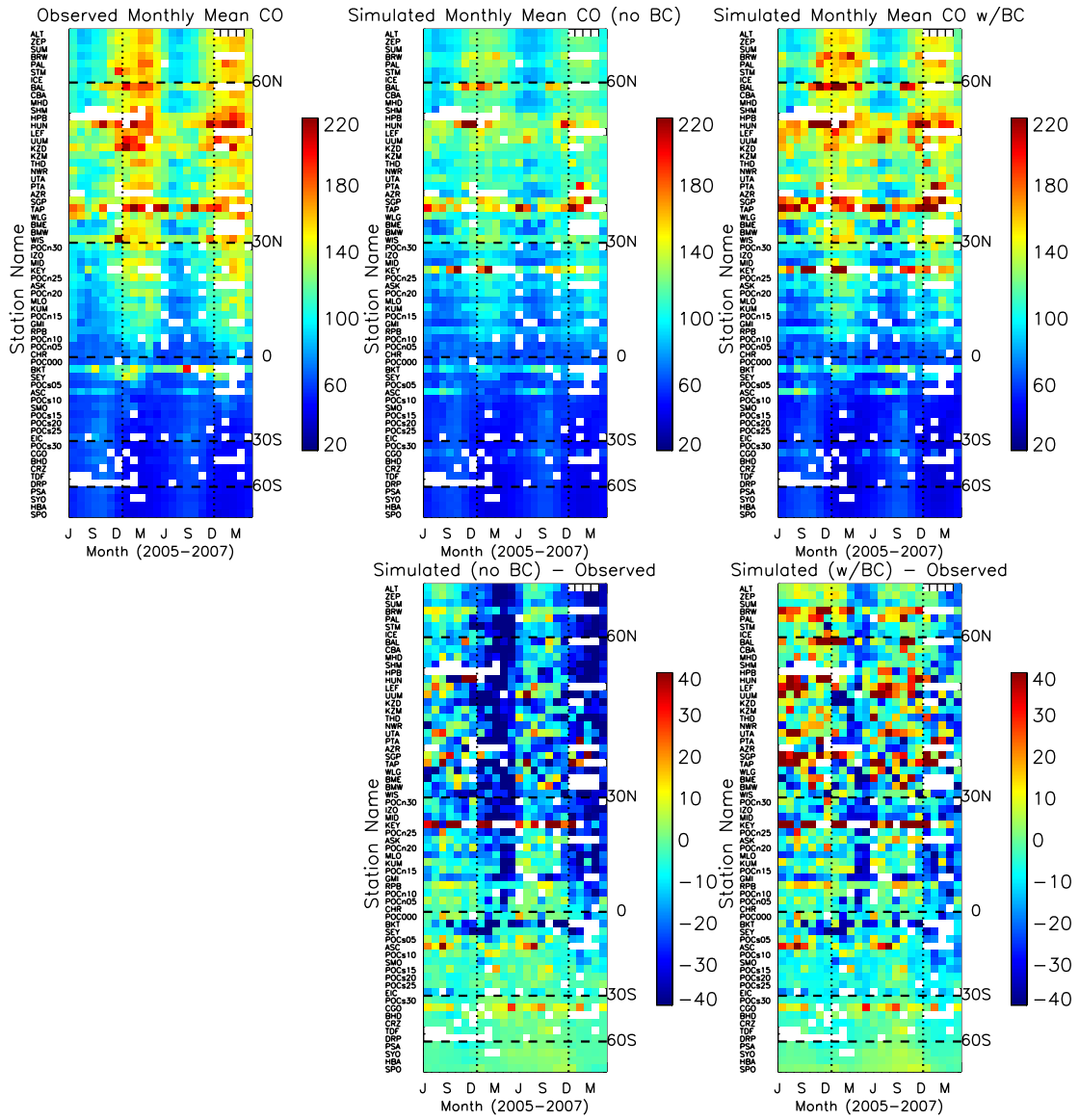

Figure 7.12: Monthly mean CO (ppbv) at each NOAA surface site for the 2005-2007 period. Observations are shown in left top panel while simulated mixing ratios without (with) a bias correction are shown in the middle (right) panel. Bottom plots show the difference between the simulation, with and without bias correction, and observations.

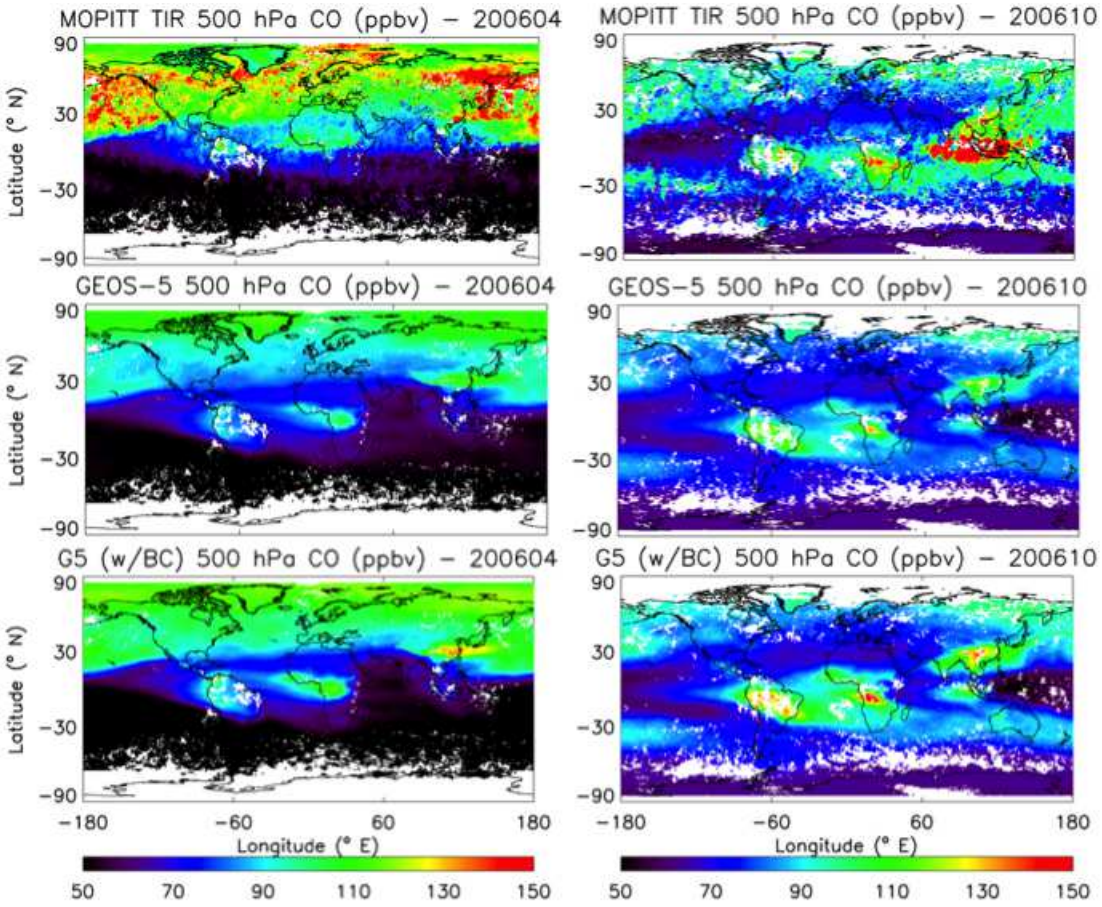

Figure 7.13: Monthly mean mid-tropospheric CO (ppbv) observed by MOPITT TIR measurements (top) for April (left) and October (right), 2006. Middle (bottom) plots show simulated mixing ratios without (with) a bias correction.

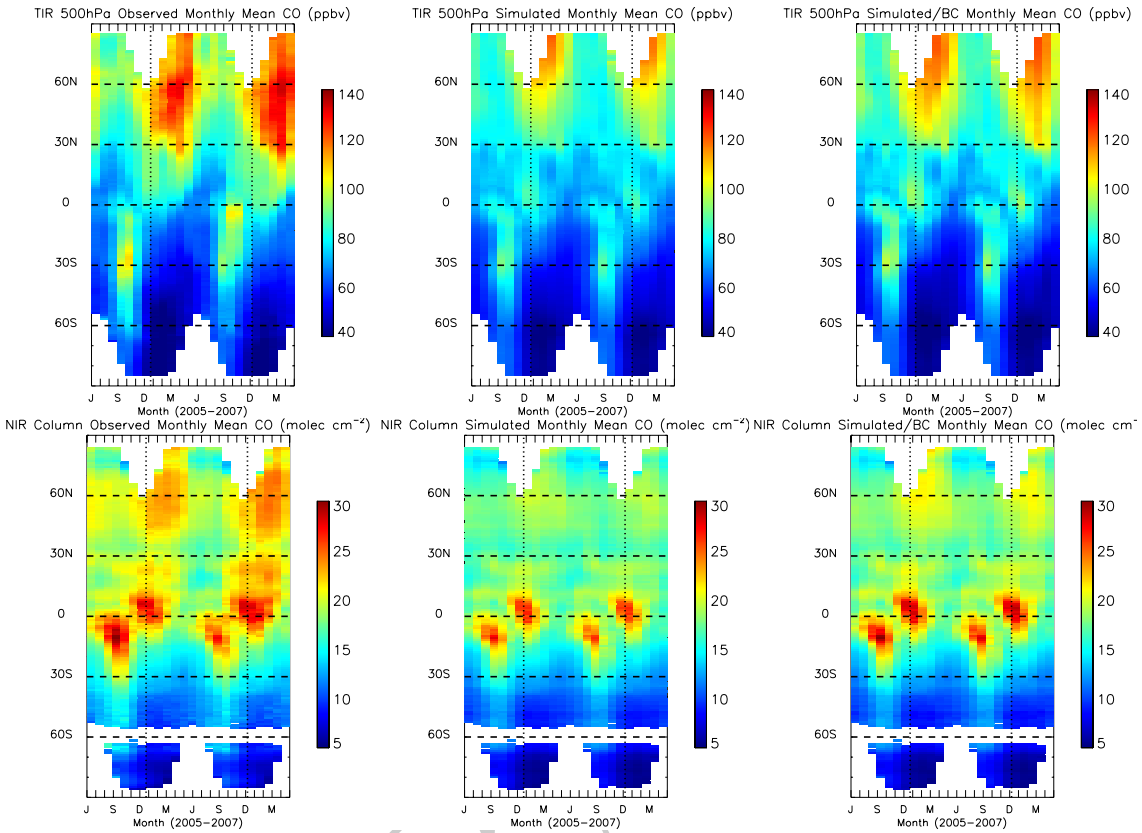

Figure 7.14: Zonal monthly mean CO calculated from MOPITT (left) TIR (top) and NIR (bottom) observations. Middle (right) plots show equivalent quantities calculated from the G5NR simulation without (with) a bias correction applied.

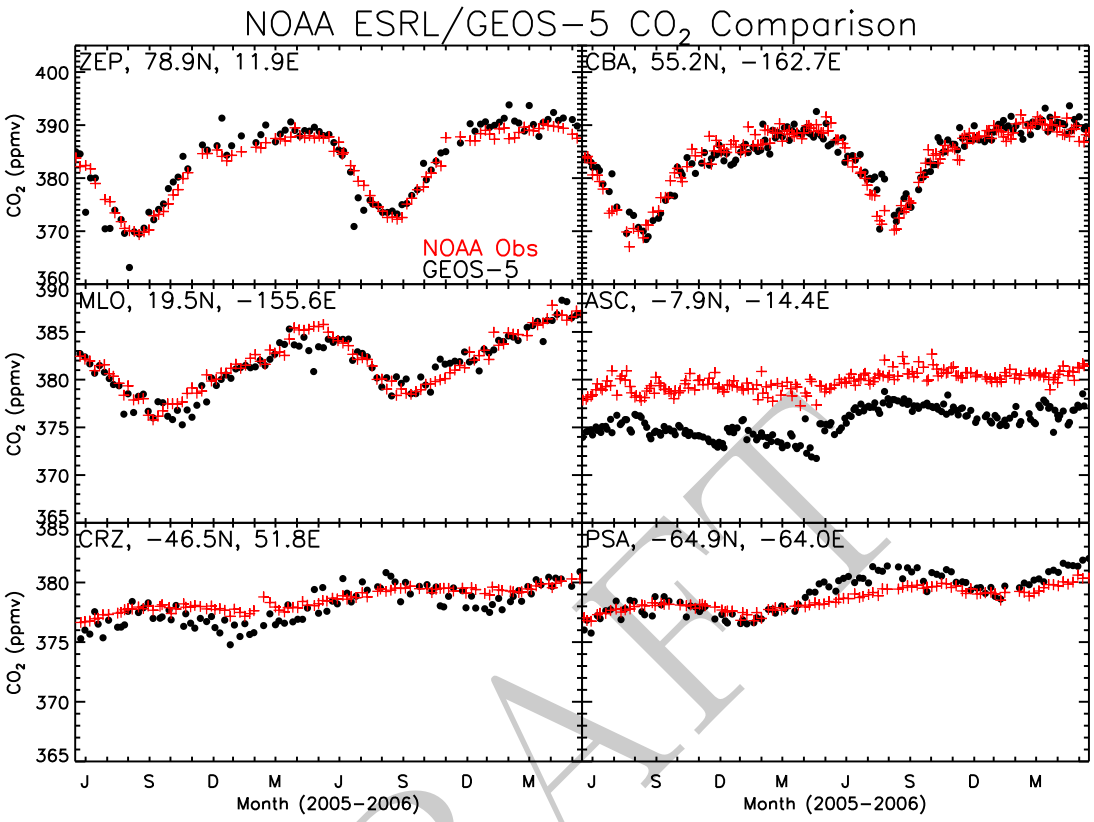

Figure 7.15: Simulated and observed surface CO_2 (ppmv) at NOAA stations indicated on Figure 7.10. Red crosses indicate observations while black dots show model derived values.

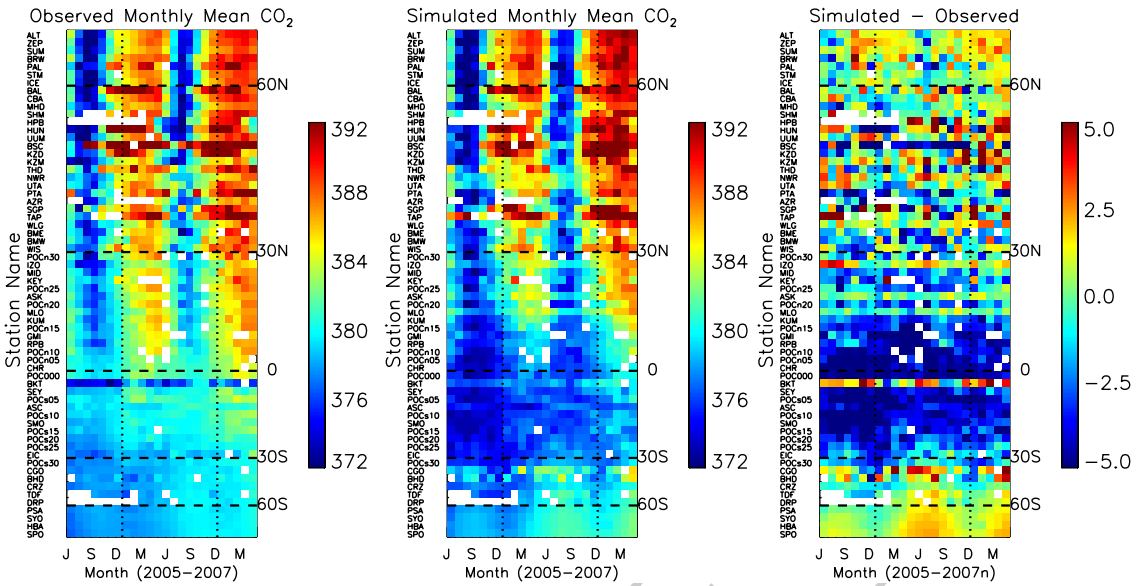

Figure 7.16: Monthly mean CO_2 (ppmv) at each NOAA surface site for the 2005-2007 period. Observations are shown in left panel while simulated mixing ratios are shown in the middle panel. Right panel shows the difference between the simulation and observations.

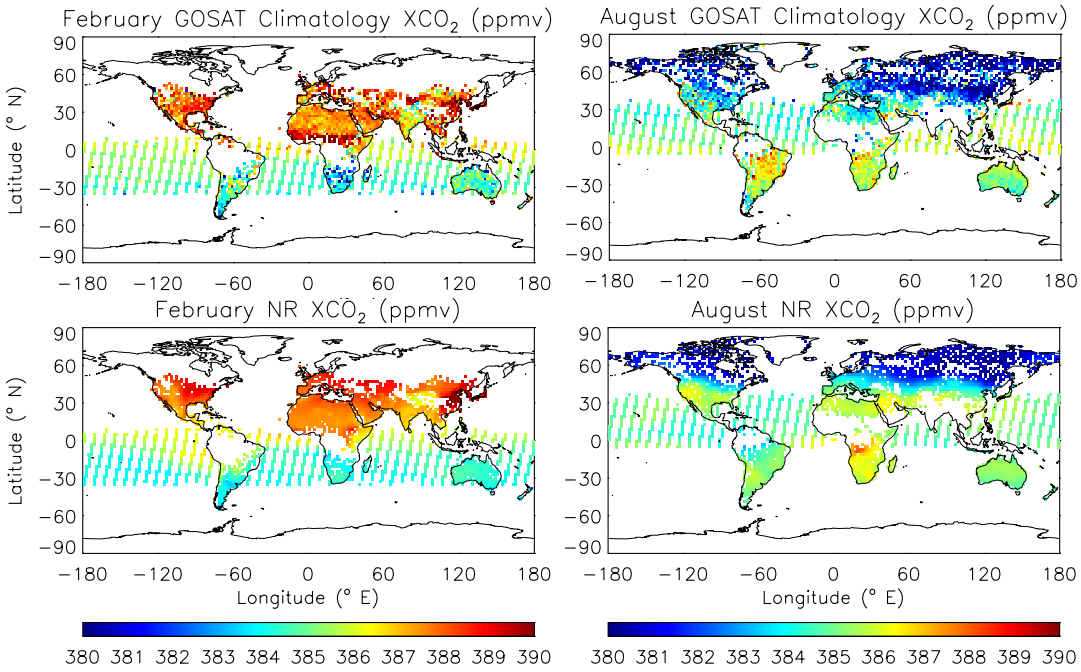

Figure 7.17: Monthly mean XCO_2 (ppmv) calculated from climatology of ACOS GOSAT observations (top) for February (left) and August (right). Bottom plots show G5NR simulated XCO_2 from 2006.

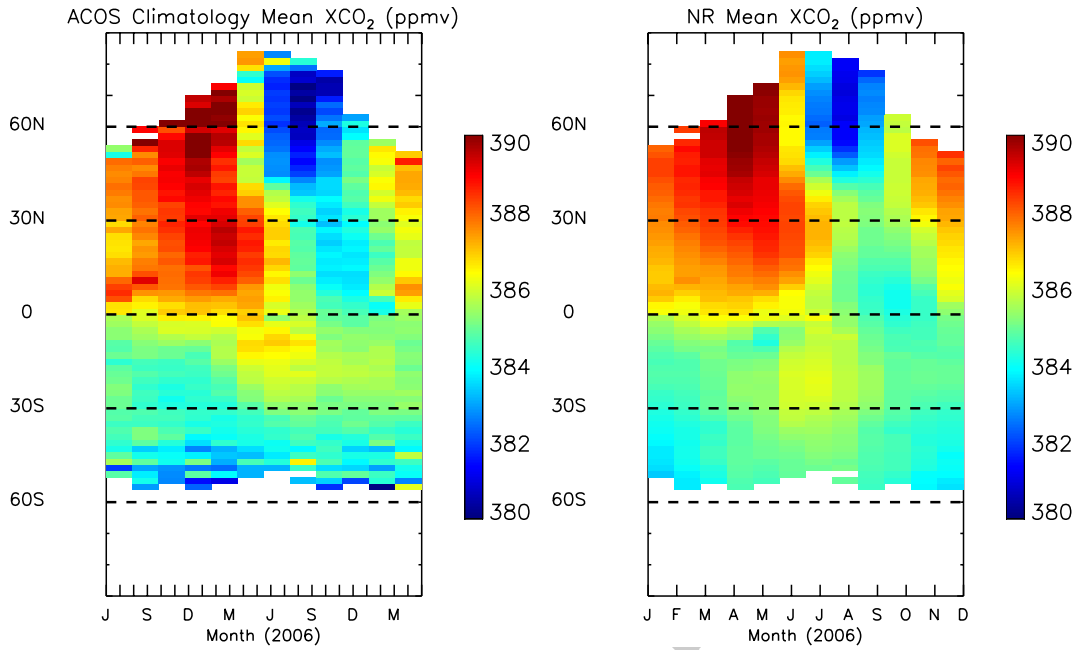

Figure 7.18: Zonal monthly mean XCO_2 (ppmv) calculated from ACOS GOSAT climatology (left) and from the G5NR simulation (right).

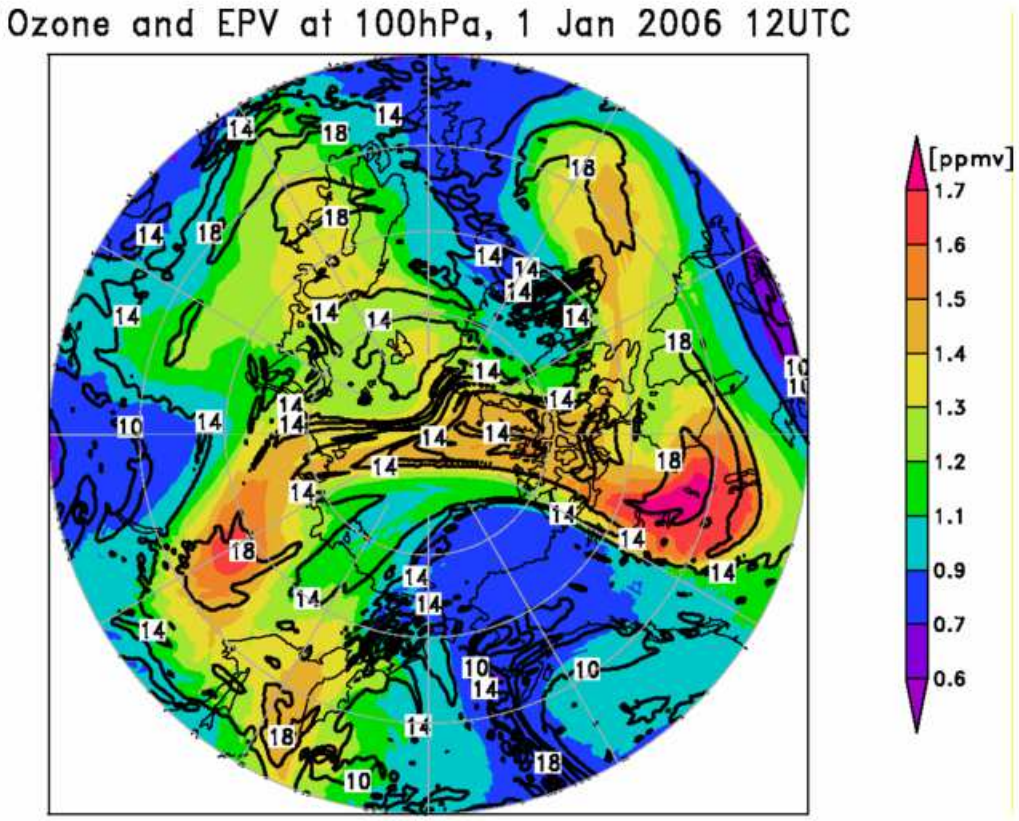

Figure 7.19: Ozone volume mixing ratio (colors) from the G5NR at 100hPa on January 1st 2006 at 12UTC and Ertels potential vorticity (contours). The latitude range is 45°- 90°N.

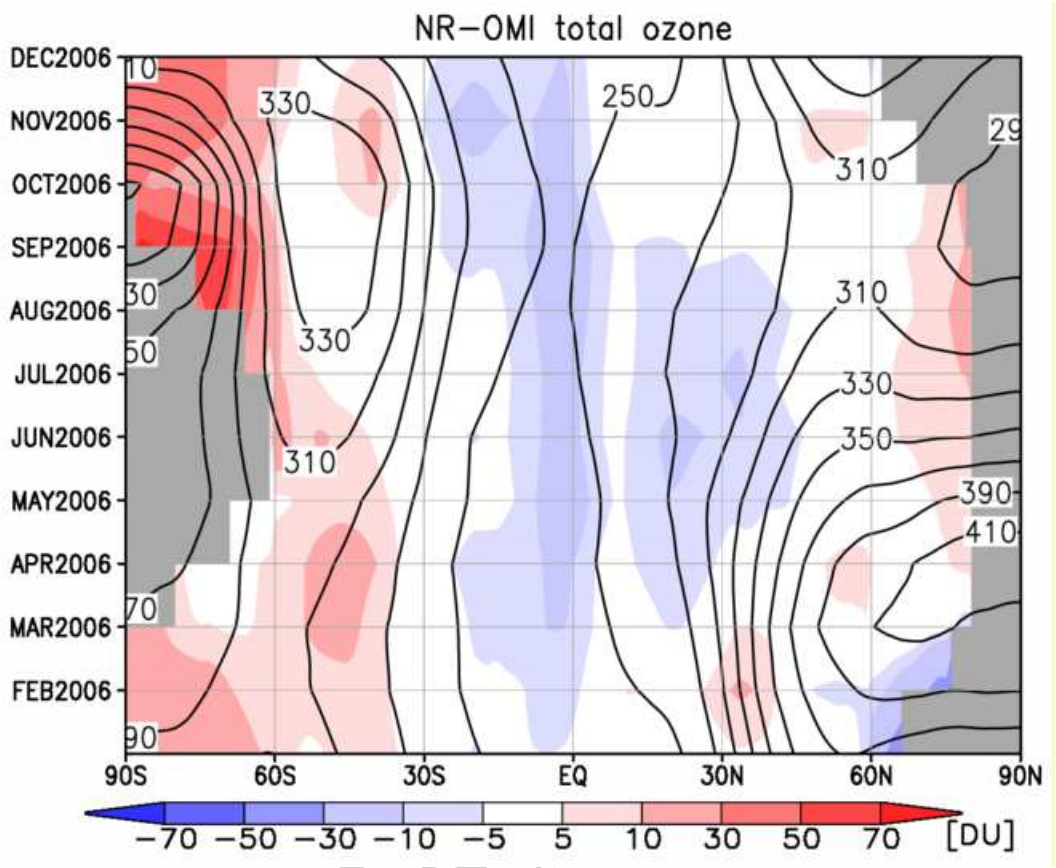

Figure 7.20: The monthly zonal mean difference between the G5NR total ozone in 2006 and 2005-2013 climatology calculated from EOS-OMI data.

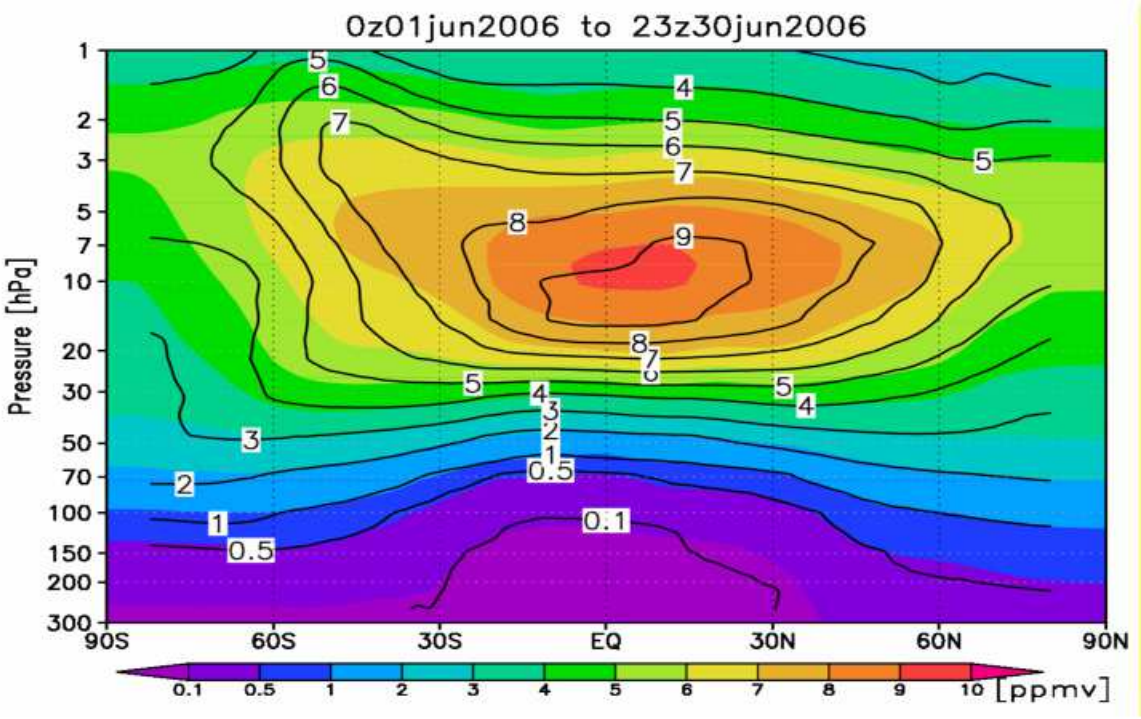

Figure 7.21: June 2006 zonal mean G5NR ozone (colors) and 2005-2013 June climatology computed from version 3.3 EOS-MLS data (contours).

References

Andrews, D. G., J. R. Holton, and C. B. Leovy, 1987: *Middle Atmosphere Dynamics*. Academic Press.

Asnani, G. C., 2005: *Tropical Meteorology*. Publisher: Indian Institute of Tropical Meteorology, Pashan, Pune-411008, India. 3 vols.

Atlas, R., R. N. Hoffman, J. Ardizzone, S. M. Leidner, J. C. Jusem, D. K. Smith, D. Gombos, 2011: A cross-calibrated, multiplatform ocean surface wind velocity product for meteorological and oceanographic applications. Bull. Amer. Meteor. Soc., 92, D157, doi: 10.1175/2010BAMS2946.1.

Augier, P. and E. Lindborg, 2013: A new formulation of the spectral energy budget of the atmosphere, with application to two high-resolution general circulation models. *J. Atmos. Sci.*, **70**, 2293–2308.

Bacmeister, J. T., M. J. Suarez and F. R. Robertson, 2006:Rain Re-evaporation, boundary layer convection interactions, and Pacific rainfall patterns in an AGCM.*J. Atmos. Sci.*, **63**, 3383–3403.

Berry, G., Thorncroft, C. and Hewson, T. 2006: African easterly waves in 2004 Analysis using objective techniques. *Mon. Wea. Rev.,* **133,** 752–766.

Blazica, V., N. Žagar, B. Strajnar, and J. Cedilnik, 2013: Rotational and divergent kinetic energy in the mesoscale model ALADIN. *Tellus*, **65**, doi:tellusa.v65i0.18918.

Bony, S, and co-authors, 2004: On dynamic and thermodynamic components of cloud changes. *Cli. Dyn.*, **22**, 71-82.

Breon, J.-F., and P. Ciais, 2010: Spaceborne remote sensing of greenhouse gas concentrations. *Comptes Rendus Geoscience*, **342**, 4-5, 412-424.

Budyko, M. I., 1974: Climate and Life. Academic Press, New York, 508 pp.

Burgess, N., A. Ehler, and T. Shepherd, 2013: The troposphere-to-stratosphere transition in kinetic energy spectra and nonlinear spectral fluxes as seen in ECMWF analyses. *J. Atmos. Sci.*, **70**, 669–687.

Chakraborty, A., Nanjundiah, R. S. and Srinivasan, J., 2009: Impact of African orography and the

Indian summer monsoon on the low-level Somali jet. *Int. J. Climatol.,* **29,** 983992. doi: 10.1002/joc.1720

Chang, E., 1999: Characteristics of wave packets in the upper troposphere. Part II: seasonal and hemispheric variations. J. Atmos. Sci., **56**, 1729–1747.

Chang, E. and D. Yu, 1999: Characteristics of wave packets in the upper troposphere. Part I: northern hemisphere winter. *J. Atmos. Sci.*, **56**, 1708-1728.

Charney, J., 1971: Geostrophic turbulence. *J. Atmos. Sci.*, **28**, 1087-1095.

Chen, T-C., and H. van Loon, 1987: Interannual variation of the tropical easterly jet. *Mon. Wea. Rev.,* **115,** 17391759.

Chin, M., P. Ginoux, S. Kinne, O. Torres, B. N. Holben, B. N. Duncan, R. V. Martin, J. A. Logan, A. Higurashi, and T. Nakajima, 2002: Tropospheric Aerosol Optical Thickness from the GOCART Model and Comparisons with Satellite and Sun Photometer Measurements.*J. Atmos. Sci.*, **59**, 461483.

Cionni, I., V. Eyring, J. F. Lamarque, W. J. Randel, D. S. Stevenson, F. Wu, G. E. Bodeker, T. G. Shepherd, D. T. Shindell, and D. W. Waugh (2011): Ozone database in support of CMIP5 simulations: results and corresponding radiative forcing. *Atmos. Chem. Phys.*, **11**, 11267-11292, doi:10.5194/acp-11-11267-2011.

Colarco, P., A. da Silva, M. Chin, and T. Diehl, 2010: Online simulations of global aerosol distributions in the NASA GEOS-4 model and comparisons to satellite and ground-based aerosol optical depth,*J. Geophys. Res.*, **115**, D14207, doi:10.1029/2009JD012820.

Crisp, D., et al., 2012: The ACOS CO2 retrieval algorithm Part II: Global XCO2 data characterization. *Atmos. Meas. Tech.*, **5**, 687-707, doi:10.5194/amt-5-687-2012.

Cullather, R.I., and M.G. Bosilovich, 2012. The energy budget of the polar atmosphere in MERRA. J. Climate, 25, 5-24, doi:10.1175/2011JCLI4138.1

Darmenov, A. and A. da Silva, 2014: The Quick Fire Emissions Dataset (QFED) - Documentation of versions 2.1, 2.2 and 2.4, Technical Report Series on Global Modeling and Data Assimilation, NASA.

da Silva, A. and P. Colarco, A. Darmenov, V. Buchard-Marchant, C. Randles, and R. Govinaradju, 2012: Overview of the MERRA Aerosol Reanalysis: Toward an Integrated Earth System Analysis. 4th WCRP International Conference on Reanalyses.

da Silva, Arlindo, W. Putman and J. Nattala, 2014: File Specification for the 7-km GEOS-5 Nature Run, Ganymed Release (Non-hydrostatic 7-km Global Mesoscale Simulation). *GMAO Office Note No. 6 (Version 1.0)*, 199 pp, available from http://gmao.gsfc.nasa.gov/pubs/office_notes.

Dee, DP, and coauthors, 2011: The ERA-Interim reanalysis: configuration and performance of the data assimilation system. *Q. J. R. Meteorol. Soc.* **137**, 553-597.

Deeter, M. N., H. M. Worden, D. P. Edwards, J. C. Gille, and A. E. Andrews, 2012: Evaluation

of MOPITT retrievals of lower-tropospheric carbon monoxide over the United States. *J. Geophys. Res.*, **117**, D13306, doi:10.1029/2012JD017553.

Dell'Aquila, A., V. Lucarini, P. Ruti, and S. Calmanti, 2005: Hayashi spectra of the northern hemisphere mid-latitude atmospheric variability in the NCEP-NCAR and ECMWF reanalyses. *Climate Dynamics*, **25**, 639-652.

Delsole, T., and Chang, P., 2003: Predictable Component Analysis, Canonical Correlation Analysis, and Autoregressive Models. *J. Atm. Sciences*, **60**, 409-416.

Delsole, T., and Tippett, M. K.: Statistical Methods in Climate Research.

Doyle, J.D., and M.A. Shapiro, 1999. Flow response to large-scale topography. The Greenland tip jet. Tellus, Ser. A., 51, 728-748, doi:10.1034/j.1600-0870.1996.00014.x

Errico, R. and N. Privé, 2014: An estimate of some analysis error statistics using the GMAO observing system simulation framework. *Quart. J. Roy. Meteor. Soc.*, **140**, 1005–1012.

Ettema, J., M.R. van den Broeke, E. van Meijgaard, and W.J. van de Berg, 2010. Climate of the Greenland ice sheet using a high-resolution climate model Part 2: Near-surface climate and energy balance. The Cryosphere, 4, 529-544, doi:10.5194/tc-4-529-2010

Fettweis, X., 2007. Reconstruction of the 19792006 Greenland ice sheet surface mass balance using the regional climate model MAR. The Cryosphere, 1, 21-40, doi:10.5194/tc-1-21-2007

Gallée, H., 1997. Air-sea interactions over Terra Nova Bay during winter: Simulation with a coupled atmosphere-polynya model. J. Geophys. Res., 102, 1383513849, doi:10.1029/96JD03098

Ganachaud, A., and C. Wunsch, 2000: Improved estimates of global ocean circulation, heat transport and mixing from hydrological data. Nature, 408, 453-457.

Garcia, R. R., and B. A. Boville, 1994: Downward control of the mean meridional circulation and temperature distribution of the polar winter stratosphere. *J. Atmos. Sci.*, **51**, 2238–2245.

Gregg, W. W., N. W. Casey, and C. S. Rousseaux, 2013: Global surface ocean carbon estimates in a model forced by MERRA. NASA Technical Report Series on Global Modeling and Data Assimilation, NASA TM-2013-104606, Vol. 31, 39 pp.

Gong, S. L., 2003: A parameterization of sea-salt aerosol source function for sub- and super-micron particles. *Global Biogeochem. Cycles*, **17**, 1097, doi:10.1029/2003GB002079.

Hall, N. M. J., G. N. Kiladis, and C. D. Thorncroft, 2006: Three-Dimensional Structure and Dynamics of African Easterly Waves. Part II: Dynamical Modes. *J. Atmos. Sci.,* **63,** 2231-2245.

Halpern, D., and P. M. Woiceshyn, 2001: Somali Jet in the Arabian Sea, El Niño, and India Rainfall. *J. Climate,* **14,** 434441.

Hamilton, K., Y. Takahasi, and W. Ohfuchi, 2008: Mesoscale spectrum of atmospheric motions investigated in a very fine resolution global general circulation model. *J. Geophys. Res.*, **113**, doi:10.1029/2008JD009785.

Hartmann, D. L., H. H. Hendon, and R. A. Houze, J.r, 1984: Some implications of the mesoscale circulations in tropical cloud clusters for large-scale dynamics and climate. *J. Atmos. Sci.*, **41**, 113-121

Hayashi, Y., 1971: A generalized method of resolving disturbances into progressive and retrogressive waves by space Fourier and time cross-spectral analyses. *J. Met. Soc. Japan*, **49**, 125–128.

Haynes, P.H. and M. E. McIntyre, 1987: On the evolution of vorticity and potential vorticitiy in the presence of diabatic heating and frictional or other forces. *J. Atmos. Sci.*,**44**, 828-841.

Heinemann, G., and T. Klein, 2002. Modelling and observations of the katabatic flow dynamics over Greenland. Tellus, Ser. A., 54, 542-554, doi:10.1034/j.1600-0870.2002.201401.x

Holt, T., and S. SethuRaman, 1985: Aircraft and ship observations of the mean structure of the marine boundary layer over the Arabian Sea during MONEX 79. *Boundary-Layer Met.,* **33,** 259282.

Houze, R. A., Jr., 1982: Cloud clusters and large-scale vertical motions in the tropics. *J. Meteor. Soc. Japan*, **60**, 396-410

Houze, R. A., Jr., 1989: Observed structure of mesoscale convective systems and implications for large-scale heating. *Quart. J. Royal Meteor. Soc.*, **115**, 425-461

Huffman, G., Adler, R.F., Rudolf, B., Schneider, U. and Keehn, P.R. 1995. Global precipitation estimates based on a technique for combining satellite-based estimates, rain gauge analysis, and NWP model precipitation information. *J. Climate*, **8**, 1284-1295.

Iguchi T., T. Kozu, R. Meneghini, J. Awaka, and K. Okamoto [2000], Rain-profiling algorithm for the TRMM precipitation radar, *J. Appl. Meteor.*, **39**, 2038-2052.

Jaegl, L., P. K. Quinn, T. S. Bates, B. Alexander, and J.-T. Lin, 2011: Global distribution of sea salt aerosols: new constraints from in situ and remote sensing observations. *Atmos. Chem. Phys.*, **11** , 3137-3157, doi:10.5194/acp-11-3137-2011.

Joyce, R. J., J. E. Janowiak, P. A. Arkin, and P. Xie, 2004: CMORPH: A method that produces global precipitation estimates from passive microwave and infrared data at high spatial and temporal resolution.. J. Hydromet., 5, 487-503.

Kaiser, J. W., A. Heil, M. O. Andreae, A. Benedetti, N. Chubarova, L. Jones, J.-J. Morcrette, M. Razinger, M. G. Schultz, M. Suttie, M., and G. R. van der Werf, 2012: Biomass burning emissions estimated with a global fire assimilation system based on observed fire radiative power. *Biogeosciences* , **9**, 527-554, doi:10.5194/bg-9-527-2012.

Kiladis, G. N., C. D. Thorncroft, and N. M. J. Hall, 2006: Three-Dimensional Structure and Dynamics of African Easterly Waves. Part I: Observations, *J. Atmos. Sci.,* **63,** 2212-2230.

Koster, R. D., B. M. Fekete, G. J. Huffman, and P. W. Stackhouse, 2006: Revisiting a hydrological analysis framework with International Satellite Land Surface Climatology Project Initiative 2 rainfall, net radiation, and runoff fields. J. Geophys. Res., 111, D22S05, doi:10.1029/2006JD007182.

Koster, R. D., and S. P. P. Mahanama, 2012: Land surface controls on hydroclimatic means and variability. J. Hydromet., 13, 1604-1620.

Kozu T., T. Kawanishi, H.Kuroiwa, M. Kojima,K. Oikawa, H. Kumagai, K. Okamoto, M. Okumura, H. Nakatuka, and K. Nishikawa[2001], Development of Precipitation Radar Onboard the Tropical Rainfall Measuring Mission (TRMM) Satellite,*Proceedings of the IEEE 2001 trans. Geoscience and Remote Sensing*, **39**,102-116

Krishnamurthy, T. N., J. Molinari, and H.-L. Pan, 1976: Numerical Simulation of the Somali Jet *J. Atmos. Sci.,* **33,** 23502362.

Kuze, A., S. Hiroshi, N. Masakatsu, and H. Takashi, 2009: Thermal and near infrared sensor for carbon observation Fourier-transform spectrometer on the Greenhouse Gases Observing Satellite for greenhouse gases monitoring. *Applied Optics*, **48**, 6716-6733, doi:10.1364/AO.48.006716.

Kyle G. S., L. F. Bosart, 2014: The Extratropical Transition of Tropical Cyclone Edisoana (1990). *Mon. Wea. Rev.,* **142,** 27722793.

Le Quere, C. et al., 2013: The global carbon budget 19592011. Earth Syst. Sci. Data, 5, 165-185, doi:10.5194/essd-5-165-2013.

L'Ecuyer, T. S., H. Beaudoing, M. Rodell, W. Olson, B. Lin, S. Kato, C. A. Clayson, E. Wood, J. Sheffield, R. Adler, G. Huffman, M. Bosilovich, G. Gu, F. Robertson, P. R. Houser, D. Chambers, J. S. Famiglietti, E. Fetzer, W. T. Liu, X. Gao, C. A. Schlosser, E. Clark, D. P. Lettenmaier, K. Hilburn, 2014: Observed State of the Energy Budget in the Early 21st Century. *J. Climate, sub judice.*

Li, J.-L. F., Waliser, D. E., Chen, W.-T., Guan, B., Kubar, T., Stephens, G., Ma, H.-Y., Deng, M., Donner, L., Seman, C., and Horowitz, L., 2012: An observationally based evaluation of cloud ice water in CMIP3 and CMIP5 GCMs and contemporary reanalyses using contemporary satellite data, *J. Geophys. Res.*, **117**, doi:10.1029/2012JD017640.

Li, J.-L. F., Lee, S., Waliser, D. E., Lee, S., Guan, B., Stephens, G., and Teixeira, J., 2013: Assessment of Cloud liquid water in CMIP3, CMIP5, and contemporary GCMs and reanalyses with observations, *J. Geophys. Res., sub judice.*

Lin, S.-J., 2004: A vertically Lagrangian finite-volume dynamical core for global models. *Mon. Wea. Rev.*, **132**, 2293–2307

Lott, N., 2004: The quality control of the integrated surface hourly database. 84th American Meteorological Society Annual Meeting, 2004, Seattle, WA, American Meteorological Society, Boston, MA, 7.8 (7p.)

Madden, R. A. and P. R. Julian, 1971: Detection of a 4050-day oscillation in the zonal wind in the tropical Pacific. *J. Atmos. Sci.,* **28**, 702708.

Madden, R. A. and P. R. Julian, 1972: Description of global-scale circulation cells in the tropics with a 4050 day period. *J. Atmos. Sci.,* **29,** 1109-1123.

Mapes, B. E. and R. A. Houze, Jr. 1995: Diabitic divergence profiles in western Pacific mesoscale

convective systems. *J. Atmos. Sci.*,**52**,1807-1828.

Masutani, M. K., and Coauthors, 2010: Observing system simulation experiments at the National Centers for Environmental Prediction. *J. Geophys. Res.,* **115,** D07101, doi:10.1029/2009JD012528.

McCarty, W., R. M. Errico, R. Gelaro, 2012: Cloud coverage in the Joint OSSE Nature Run. *Mon. Wea. Rev.,* **,** 1863-1871.

McFarlane, N. A., 1987: The effect of orographically excited gravity-wave drag on the circulation of the lower stratosphere and troposphere. *J. Atmos. Sci.*, **44**, 1775–1800.

Mitchell, K.E., and Co-Authors (2004), The multi-institution North American Land Data Assimilation System (NLDAS): Utilizing multiple GCIP products and partners in a continental distributed hydrological modeling system, J. Geophys. Res., 109, D07S90, doi:10.1029/2003JD003823.

Molod, A., 2012: Constraints on the profiles of total water PDF in AGCMs from AIRS and a high-resolution model. *J. Climate*, **25**, 8341–8352.

Molod, A., L. Takacs, M. Suarez and J. Bacmeister, 2014: Development of the GEOS-5 Atmospheric General Circulation Model: Evolution from MERRA to MERRA2. *Geosci. Model Dev. Discuss.* **??**, doi:10.5194/gmd-2014-167.

Molod, A., L. Takacs, M. Suarez, J. Bacmeister, I.-S. Song, and A. Eichmann, 2012: The GEOS-5 Atmospheric General Circulation Model: Mean climate and development from MERRA to Fortuna. NASA Technical Report Series on Global Modeling and Data Assimilation vol. 28, NASA Global Modeling and Assimilation Office.

Moorthi, S., and M. J. Suarez, 1992: Relaxed Arakawa Schubert: A parameterization of moist convection for general circulation models. *Mon. Wea. Rev.*, **120**, 978–1002.

Mosley-Thompson, E., J.F. Paskievitch, A.J. Gow, and L.G. Thompson, 1999. Late 20th Century increase in South Pole snow accumulation. J. Geophys. Res., 104, 38773886, doi:10.1029/1998JD200092

Murray, R.J. and I. Simmonds, 1991: A numerical scheme for tracking cyclone centres from digital data. Part I: Development and operation of the scheme. *Aust. Met. Mag.* **39**, 155–166.

Neale, R. B., and co-authors, 2008: The impact of convection on ENSO: From a Delayed Oscillator to a Series of Events. *J. Climate*, **21**, 5904-5924.

Nicholson, S. E., A. I. Barcilon, M. Challa, J. Baum, 2007: Wave Activity on the Tropical Easterly Jet. *J. Atmos. Sci.,* **64,** 27562763.

O'Dell, C. W. et al., 2012: The ACOS CO2 retrieval algorithm Part 1: Description and validation against synthetic observations. *Atmos. Meas. Tech.*, **5**, 99-121, doi:10.5194/amt-5-99-2012.

Ott, L., B. Duncan, S. Pawson, P. Colarco, M. Chin, C. Randles, T. Diehl, and E. Nielsen, 2010: Influence of the 2006 Indonesian biomass burning aerosols on tropical dynamics studied with the GEOS-5 AGCM. *J. Geophys. Res.*, **115**, D14121, doi:10.1029/2009JD013181.

Ott, L. E., S. Pawson, G. J. Collatz, W. W. Gregg, D. Menemenlis, H. Brix, C. Rousseaux, K. Bowman, J. Liu, A. Eldering, M. Gunson, and S. R. Kawa, 2014: Quantifying the observability of CO2 flux uncertainty in atmospheric CO2 records using products from NASA's Carbon Monitoring Flux Pilot Project. *J. Geophys. Res.*, submitted.

Parish, T.R., 1983. The influence of the Antarctic Peninsula on the wind field over the western Weddell Sea. J. Geophys. Res., 88, 2684-2692, doi:10.1029/JC088iC04p02684

Parish, T.R., and D.H. Bromwich, 1991. Continental-scale simulation of the Antarctic katabatic wind regime. J. Climate, 4, 135-146, doi:10.1175/1520-0442(1991)004<0135:CSSOTA>2.0.CO;2

Putman, W., A. M. da Silva, L. E. Ott, and A. Darmenov, 2014: Model Configuration for the 7-km GEOS-5.12 Nature Run, Ganymed Release (Non-hydrostatic 7 km Global Mesoscale Simulation), GMAO Office Note, 5. (Version 1.0), 86 pp, available from http://gmao.gsfc.nasa.gov/pubs/office_notes.

Putman, W. M., and M. Suarez, 2011: Cloud-system resolving simulations with the NASA Goddard Earth Observing System global atmospheric model (GEOS-5), *Geophys. Res. Lett.,* **38,** L16809, doi:10.1029/2011GL048438.

Rasmussen, E. A., and Turner, J., 2003: *Polar Lows: Mesoscale Weather Systems in the Polar Regions,* Cambridge: Cambridge University Press, p. 612, ISBN 0-521-62430-4.

Reale, O., and R. Atlas, 2001: Tropical Cyclone-like Vortices in the Extratropics: Observational Evidence and Synoptic Analysis. *Wea. Forecasting*, **16,** 7-34.

Reale, O., J. Terry, M. Masutani, E. Andersson, L. P. Riishojgaard, J. C. Jusem, 2007: Preliminary evaluation of the European Centre for Medium-Range Weather Forecasts (ECMWF) Nature Run over the Tropical Atlantic and African Monsoon region. *Geophys. Res. Lett.*, **34**, L22810, doi:10.1029/2007GL31640.

Reale, O., W. K. Lau, J. Susskind, E. Brin, E. Liu, L. P. Riishojgaard, M. Fuentes, R. Rosenberg, 2009: AIRS Impact on the Analysis and Forecast Track of Tropical Cyclone Nargis in a global data assimilation and forecasting system. *Geophys. Res. Lett.,* 36, L06812, doi:10.1029/2008GL037122.

Rienecker, M. M., and coauthors, 2008: The GEOS-5 Data Assimilation System: Documentation of versions 5.0.1 and 5.1.0, and 5.2.0. NASA Tech. Rep. Series on Global Modeling and Data Assimilation, NASA/TM-2008-104606, Vol. 27, 92 pp.

Rienecker, M.M., and coauthors, 2011: MERRA: NASA's Modern-Era Retrospective Analysis for Research and Applications. *J. Climate*, **24**, 3624-3648.

Risien, C. M., and D. B. Chelton, 2008: A Global Climatology of Surface Wind and Wind Stress Fields from Eight Years of QuikSCAT Scatterometer Data.J. Phys. Oceanogr., 38, D2379, doi:10.1175/2008JPO3881.1.

Rodell, M., and Co-Authors, The Global Land Data Assimilation System, Bull. Amer. Meteor. Soc., 85(3), 381-394, 2004.

Rodell, M., H.K. Beaudoing, T. L Ecuyer, W. Olson, J.S. Famiglietti, P.R. Houser, R. Adler, M. Bosilovich, C.A. Clayson, D. Chambers, E. Clark, E. Fetzer, X. Gao, G. Gu, K. Hilburn, G. Huffman, D.P. Lettenmaier, W.T. Liu, F.R. Robertson, C.A. Schlosser, J. Sheffield, and E.F. Wood, 2014: The observed state of the water cycle in the early 21st century. *J. Climate, sub judice*.

Saha, S, and co-authors, 2010: The NCEP Climate Forecast System Reanalysis. *Bull. Amer. Meteor. Soc.* **91**, 1015-1057.

Sampson, C. R., and A. J. Schrader, 2000: The Automated Tropical Cyclone Forecasting System (Version 3.2). *Bull. Amer. Meteor. Soc.,* **81,** 1231-1240.

Serreze, M.C., A.P. Barrett, A.G. Slater, R.A. Woodgate, K. Aagaard, R.B. Lammers, M. Steele, R. Moritz, M. Meredith, and C.M. Lee, 2006. The large-scale freshwater cycle of the Arctic. J. Geophys. Res., 111, C11010, doi:10.1029/2005JC003424.

Shie, C.-L., L. S. Chiu, R. Adler, E. Nelkin, I-I. Lin, P. Xie, F.-C. Wang, R. Chokngamwong, W. Olson, and D. A. Chu, 2009: A Note on reviving the Goddard satellite-based surface turbulent fluxes (GSSTF) dataset. Adv. Atmos. Sci., 26(6), 10711080.

Shindell, D. T., et al. 2006: Multimodel simulations of carbon monoxide: Comparison with observations and projected near-future changes. *J. Geophys. Res.*, **111**, D19306, doi:10.1029/2006JD007100.

Simmonds, I., R.J. Murray and R.M. Leighton, 1999: A refinement of cyclone tracking methods with data from FROST. *Aust. Met. Mag.*, **Spec. Ed.**, 35–49.

Sinclair, M. R., 1993: Synoptic-scale diagnosis of the extratropical transition of a southwest Pacific tropical cyclone. *Mon. Wea. Rev.,* **121,** 941960.

Stachnik, J. and C. Schumacher, 2011: A comparison of the Hadley circulation in modern reanalyses. *J. Geophys. Res.*, **116**, doi:10.1029/2011JD016677.

Stackhouse, Jr., P. W., S. J. Cox, S. Gupta, M. Chiacchio, and J. Mikovitz, 2001: The WCRP/GEWEX surface radiation budget project release 2: An assessment of surface fluxes at 1 degree resolution. IRS 2000: Current Problems in Atmospheric Radiation, W. Smith and Y. Timofeyev, Eds., A. Deepak Publishing.

Takahashi, T., et al., 2002: Global sea-air CO2 flux based on climatological surface ocean pCO2, and seasonal biological and temperature effects. *Deep-Sea Res. II*, **49**, 1601-1622.

Takahashi, T., et al., 2009: Climatological mean and decadal changes in surface ocean pCO2, and net sea-air CO2 flux over the global oceans. *Deep-Sea Res. II*, **56**, 554-577.

Textor, C., M. Schulz, S. Guibert, S. Kinne, Y. Balkanski, S. Bauer, T. Berntsen, T. Berglen, O. Boucher, M. Chin, F. Dentener, T. Diehl, R. Easter, H. Feichter, D. Fillmore, S. Ghan, P. Ginoux, S. Gong, A. Grini, J. Hendricks, L. Horowitz, P. Huang, I. Isaksen, I. Iversen, S. Kloster, D. Koch, A. Kirkevg, J. E. Kristjansson, M. Krol, A. Lauer, J. F. Lamarque, X. Liu, V. Montanaro, G. Myhre, J. Penner, G. Pitari, S. Reddy, O. Seland, P. Stier, T. Takemura, and X. Tie, 2006: Analysis and quantification of the diversities of aerosol life cycles within AeroCom. *Atmos. Chem. Phys.*, **6** , 1777-1813, doi:10.5194/acp-6-1777-2006.

Thorncroft, C. D., J. Hall, and G. N. Kiladis, 2008: Three-dimensional structure and dynamics of African easterly waves. Part III: Genesis. *J. Atmos. Sci.,* **65,** 35963607.

Tokioka, T., K. Yamazaki, A. Kitoh and T. Ose, 1988: The equatorial 30–60 day oscillation and the Arakawa-Schubert penetrative cumulus parameterization. *J. Meteor.Soc. Japan*, **66**, 883–901.

Trenberth, K.E. and J. Caron, 2001: Estimates of Meridional Atmosphere and Ocean Heat Transports. J. Climate, 14, 3433-3443.

Tulloch, R. and K. Smith, 2006: A theory for the atmospheric energy spectrum: depth limited temperature anomalies at the tropopause. *Proc. Nat. Acad. Sci.*, **103**, 14,690–14,694.

Vaughan, M., C. Trepte, D. Winker, M. Averya, J. Campbell, R. Hoff, S. Young, B. Getzewich, J. Tackett, and J. Kar, 2011: Adapting CALIPSO climate measurements for near real time analyses and forecasting. Proceedings of the 34th International Symposium on Remote Sensing of Environment.

Wada, A., H. Matsueda, S. Murayama, S. Taguchi, A. Kamada, M. Nosaka, K. Tsuboi, and Y. Sawa, 2012: Evaluation of anthropogenic emissions of carbon monoxide in East Asia derived from the observations of atmospheric radon-222 over the western North Pacific. *Atmos. Chem. Phys.*, **12**, 12119-12132, doi:10.5194/acp-12-12119-2012.

Wheeler, M. and G. Kiladis, 1999: Convectively coupled equatorial waves: analysis of clouds and temperature in the wavenumber-frequency domain. *J. Atmos. Sci.*, **56**, 374–399.

Winker, D. M., W. H. Hunt, and M. J. McGill, 2007: Initial performance assessment of CALIOP. *Geophys. Res. Lett.*, **34**, L19803, doi:10.1029/2007GL030135.

Winker, D. M., J. Pelon, J. A. Coakley Jr., S. A. Ackerman, R. J. Charlson, P. R. Colarco, P. Flamant, Q. Fu, R. M. Hoff, C. Kittaka, T. L. Kubar, H. Le Treut, M. P. McCormick, G. Mgie, L. Poole, K. Powell, C. Trepte, M. A. Vaughan, and B. A. Wielicki, 2010: The CALIPSO Mission: A Global 3D View of Aerosols and Clouds. *Bull. Amer. Meteor. Soc.*, **91**, 12111229. doi: http://dx.doi.org/10.1175/2010BAMS3009.1

Wu, M.-L, O. Reale, S. Schubert, M. J. Suarez, R. Koster, P. Pegion, 2009: African Easterly Jet: Structure and Maintenance. *J. Climate,* **22**, 4459-4480.

Wu, M.-L, O. Reale, S. Schubert, M. J. Suarez, C. Thorncroft, 2012: African Easterly Jet: barotropic instability, waves and cyclogenesis. *J. Climate,* **25,** 1489-1510.

Wu, M.-L, O. Reale, S. Schubert, 2013: A characterization of African Easterly Waves on 2.5-6 and 6-9 day time scales. *J. Climate,* **26,** 6750-6774.

Xia, Y., and Co-Authors, 2012: Continental-scale water and energy flux analysis and validation for the North American Land Data Assimilation System project phase 2 (NLDAS-2): 1. Intercomparison and application of model products. J. Geophys. Res., 117, doi:10.1029/2011JD016048.

Xie, P., and P. A. Arkin, 1996: Analysis of global monthly precipitation using gauge observations, satellite estimates, and numerical model predictions. *J. Climate*, **9**, 840-858.

Xie, P., and P. A. Arkin, 1997: Global precipitation: A 17-year monthly analysis based on gauge observations, satellite estimates, and numerical model outputs. *Bull. Amer. Meteor. Soc.*, **78**, 2539-2558.

Yin, X, A. Gruber and P. Arkin, 2004: Comparison of the GPCP and CMAP Merged Gauge–Satellite Monthly Precipitation Products for the Period 1979–2001. *J. Hydrometeorol.*, **5**, 1207-1222.

Zimin, A., I. Szunyogh, D. Patil, B. Hunt, and E. Ott, 2003: Extracting envelopes of Rossby wave packets. *Mon. Wea. Rev.*, **131**, 1011–1017.